Modelling and analysis of LRRK2 mutations in iPSC-derived dopaminergic neurons and astrocytes

Heather D.E. Booth

St Anne's College

Department of Physiology, Anatomy and Genetics

University of Oxford

Trinity Term 2017

A thesis submitted towards the degree of Doctor of Philosophy

Abstract

Parkinson's disease (PD) is a common neurodegenerative disorder, characterised by preferential loss of ventral midbrain dopaminergic (vmDA) neurons in the substantia nigra pars compacta (SNc). The majority of PD cases have unknown aetiology; however, between 5-10% arise due to known genetic mutations, the most common of which are found in the *LRRK2* gene. *LRRK2* is expressed in neurons and glia in the human brain; therefore, cell-autonomous and/or non-cell autonomous effects may participate in *LRRK2*-mutation-mediated degeneration of vmDA neurons. This study set out to understand the effects of *LRRK2* mutations on human vmDA neurons and midbrain astrocytes, and to shed new light on the mechanisms of PD pathogenesis. To achieve this goal, differentiation protocols were generated to produce vmDA neurons and midbrain patterned (MP) astrocytes from induced pluripotent stem cells (iPSCs). iPSCs from patients carrying the LRRK2-G2019S mutation were differentiated into both cell types, and hypothesis-driven analysis of cellular functions including autophagy, mitochondrial respiration, glycolysis, and cellular migration was conducted; however, no disease phenotypes were observed. Following this, proteomics and transcriptomics techniques were then used to analyse the effects of the LRRK2-G2019S mutation in an unbiased manner. In the iPSC-derived MP-astrocyte cultures, this technique highlighted stochastic X-chromosome reactivation events that led to difficulties in interpreting the resulting data; however, in the iPSC-derived vmDA-neuron cultures, LRRK2-G2019S-mediated inhibition of endocytosis and axon guidance was identified. These findings were found to be consistent in iPSC-derived vmDA-neuron cultures carrying the LRRK2-R1441C mutation, suggesting that these two mutations exert their pathogenic effects

through similar mechanisms. Finally, phosphoproteomics analysis of iPSC-derived vmDA-neuron cultures was conducted to identify *bone fide* LRRK2-kinase substrates. Eleven potential LRRK2-kinase substrates were identified, nine of which have been previously shown to participate in endocytic vesicle trafficking, neurite outgrowth, and synaptic function. The findings of this study suggest that LRRK2 has neuron-specific functions, and that its mutations contribute to neurodegeneration in a cell-autonomous manner.

Acknowledgements

Many people have been instrumental to the completion of this work, and I would like to thank them for their help and support over the past four years. Firstly, I would like to thank my supervisors; Richard, for working with me to obtain funding, for providing me with the opportunity to study in his group, and for his supervision throughout my DPhil; Paul, for his support in obtaining funding for my studies, and his supervision; and Warren, for his continued support of my project, across companies and oceans.

Secondly, I would like to thank all of my collaborators. Jeff, Benbo, Kejie, Norm, and everyone else at Biogen who has been involved in this project, without whom, I am sure this work would not have yielded such interesting results. Also Sally and Jane, for generating the stem cell lines that have been essential to this work. Additionally, I would like to thank the MRC and Pfizer for funding my studentship.

Over the past four years, many members of the Wade-Martins and Cowley groups have provided their insight, help, and support, and I would like to thank them for this. I would especially like to thank Natalie, Becky, and Cecilia for entertaining my love-hate relationship with LRRK2, and helping to interpret what on earth its function may be. Liz and Hugo for setting our lab off along the road of iPSCs and paving the way for my project. Federica for developing the cortical astrocyte differentiation protocol, which laid the groundwork for the generation of midbrain astrocytes in this thesis. Fede, Charmaine, and Joel, for sharing the burden of weekend feeding of iPSC cultures and for their help in troubleshooting iPSC dilemmas. Brent for teaching me many useful

techniques. Emma for proving that my neurons could indeed fire action potentials. Charmaine, Nora, Dayne, Natalie, Amy, and Brent, for critically commenting on drafts of this thesis, and for making it better than it might have been.

Finally, I would like to thank my family and friends for their support over the past four years. In particular, my husband Mike, who has had to deal with the highs and lows that inevitably arise from studying for a DPhil, and who has read and critically assessed this entire thesis. Without his calming influence, I am doubtful that I would have made it this far. He tells me it will all be worth it, to be Dr & Dr Booth.

Declaration

I hereby declare that the work presented in this thesis was conducted by the author at the University of Oxford and that where others have contributed, proper acknowledgement has been made. This work has not been submitted for any other degree.

Publications and presentations

Publications

Beevers, J. E., M. C. Lai, E. Collins, **H. D. E. Booth**, F. Zambon, L. Parkkinen, J. Vowles, S. A. Cowley, R. Wade-Martins and T. M. Caffrey (2017). "MAPT Genetic Variation and Neuronal Maturity Alter Isoform Expression Affecting Axonal Transport in iPSC-Derived Dopamine Neurons." Stem Cell Reports **9**(2): 587-599.

Booth, H. D. E., W. D. Hirst and R. Wade-Martins (2017). "The Role of Astrocyte Dysfunction in Parkinson's Disease Pathogenesis." Trends Neurosci **40**(6): 358-370.

Sandor, C., P. Robertson, C. Lang, A. Heger, **H. Booth**, J. Vowles, L. Witty, R. Bowden, M. Hu, S. A. Cowley, R. Wade-Martins and C. Webber (2017). "Transcriptomic profiling of purified patient-derived dopamine neurons identifies convergent perturbations and therapeutics for Parkinson's disease." Hum Mol Genet **26**(3): 552-566.

Fernandes, H. J., E. M. Hartfield, H. C. Christian, E. Emmanoulidou, Y. Zheng, **H. Booth**, H. Bogetofte, C. Lang, B. J. Ryan, S. P. Sardi, J. Badger, J. Vowles, S. Evetts, G. K. Tofaris, K. Vekrellis, K. Talbot, M. T. Hu, W. James, S. A. Cowley and R. Wade-Martins (2016). "ER Stress and Autophagic Perturbations Lead to Elevated Extracellular alpha-Synuclein in GBA-N370S Parkinson's iPSC-Derived Dopamine Neurons." Stem Cell Reports **6**(3): 342-356.

Presentations

Booth, H.D.E., J. Martin, B. Gao, P. Juhasz, K. Li, N. Allaire, C. Roberts, J. Vowles, S. Cowley, W.D. Hirst, and R. Wade-Martins R. “Integrated omics analysis reveals functional effects of LRRK2 mutations in dopaminergic neurons.” EMBL Mechanisms of Neurodegeneration, Heidelberg, Germany (2017). Selected flash talk and poster presentation.

Booth, H.D.E., F. Rinaldi, E. Whiteley, J. Vowles, S. Cowley, W.D. Hirst, P. Whiting, and R. Wade-Martins. “Investigating the role of LRRK2 mutations in patient iPSC-derived midbrain neurons and astrocytes.” Leucine Rich Repeat Kinase 2: Ten Years Along the Road to Therapeutic Intervention, Henley, UK (2016). Selected oral presentation.

Booth, H.D.E., F. Rinaldi, R. Flynn, H. Lee, J. Vowles, S. Cowley, W.D. Hirst, P. Whiting, and R. Wade-Martins. “Investigating the role of LRRK2 mutations in patient iPSC-derived midbrain neurons and astrocytes.” Parkinson’s UK Research Conference, Leeds, UK (2016). Selected poster presentation.

Booth, H.D.E., B. Ryan, E. Hartfield, F. Zambon, J. Vowles, S. Cowley, W.D. Hirst, P. Whiting, and R. Wade-Martins. “Uncovering the role of LRRK2 in Parkinson’s using iPSC-derived dopaminergic neurons.” Parkinson’s UK Research Conference, York, UK (2014). Selected poster presentation.

Table of contents

List of figures

List of tables

List of abbreviations

AA	Ascorbic acid
AADC	DOPA Decarboxylase
ABI2	ABL-Interactor 2
ABL1	Abelson Murine Leukaemia Viral Oncogene Homolog 1
ADD1	Alpha-Adducin
AMPAR	Alpha-Amino-3-Hydroxy-5-Methyl-4-Isoxazole Propionate Receptor
ANK	Ankyrin repeat
AP1	Adaptor Protein 1
AQP4	Aquaporin 4
ARMC10	Armadillo Repeat-Containing Protein 10
ATP13A2	Lysosomal Type 5 ATPase
B2M	Beta-2-microglobulin
BAC	Bacterial artificial chromosome
BBB	Blood-brain-barrier
BCA	Bicinchoninic acid
BDNF	Brain Derived Neurotrophic Factor
BMP	Bone Morphogenic Protein
BSA	Bovine Serum Albumin
CAV1	Caveolin-1
CCCP	Carbonyl cyanide m-chlorophenyl hydrazone
CCDC120	Coiled-Coil Domain Containing 120
CDK5	Cyclin-Dependent Kinase 5
CHIR	CHIR99021
CLCs	Clathrin Light Chains
CLINT1	Clathrin Interactor 1
CMA	Chaperone-mediated autophagy
c-Myc	Proto-Oncogene c-Myc
CNTF	Ciliary Neurotrophic Factor
COR	C-terminal of ROC
CPM	Counts per minute
CRMP1	Collapsin-Response Mediator Protein 1
CT-1	Cardiotrophin 1
CXCR4	C-X-C Chemokine Receptor Type 4
DA	Dopaminergic
DAPT	N-[N-(3,5-Difluorophenacetyl)-L-alanyl]-S-phenylglycine t-butyl ester

DAT	Dopamine Transporter
db-cAMP	N6,2′-O-Dibutyryladenosine 3′,5′-cyclic monophosphate sodium salt
DEG	Differentially expressed gene
DIV	Days in vitro
DLP1	Dynamin-Like Protein 1
DMEM	Dulbecco's modified eagle medium
DMV	Dorsal motor nucleus of the vagus
DNM1	Dynamin-1
dNTPs	Deoxynucleoside triphosphates
DPBS	Dulbecco's phosphate buffered saline
EB	Embryoid body
ECAR	Extracellular acidification rate
EDTA	Ethylenediaminetetraacetic acid
EGF	Epidermal Growth Factor
EGSEA	Ensemble of Gene Set Enrichment Analyses
EPHA5	Ephrin Type-A Receptor 5
ERK1/2	Mitogen Activated Protein Kinases
ERM	Ezrin Radixin Moesin
ESCs	Embryonic stem cells
F12	Nutrient mixture F12
FAM107B	Family with Sequence Similarity 107 B
FC	Fold change
FCCP	Carbonyl cyanide-4-(trifluoromethoxy)phenylhydrazone
FDR	False discovery rate
FGF	Fibroblast Growth Factor
FOXA2	Forkhead Box Protein A2
FPKM	Fragments per Kilobase of transcript per Million mapped reads
FYN	FYN Proto-oncogene
GBA	β-Glucocerebrosidase
GBX2	Gastrulation Brain Homeobox 2
GDI1	RAB GDP Dissociation Inhibitor α
GDI2	RAB GDP Dissociation Inhibitor β
GDNF	Glial Derived Neurotrophic Factor
GFAP	Glial Fibrillary Acidic Protein
GIRK2	G-Protein-Regulated Inward-Rectifier Potassium Channel 2
GLAST1	Glutamate-Aspartate Transporter 1
GLUR1	Glutamate Receptor 1
GNAI1	G Protein Subunit Alpha I1

GO	Gene ontology
GPs	Glial progenitors
GRIP	Glutamate Receptor-Interacting Protein
GSK3β	Glycogen Synthase Kinase 3 beta
GTP	Guanosine triphosphate
HACD3	Very-Long-Chain (3R)-3-Hydroxyacyl-CoA Dehydratase 3
HCD	Higher-energy collision dissociation
HCN3	Hyperpolarization Activated Cyclic Nucleotide Gated Potassium Channel 3
Hep	Heparin
hESCs	Human embryonic stem cells
HPRT1	Hypoxanthine-Guanine Phosphoribosyltransferase
hPSCs	Human pluripotent stem cells
IFN-γ	Interferon Gamma
IL-1β	Interleukin 1 Beta
IL6	Interleukin 6
IMAC	Immobilized Metal-Ion Affinity Chromatography
iPSCs	Induced pluripotent stem cells
IVF	In vitro fertilisation
KEGG	Kyoto encyclopedia of genes and genomes
KI	Knock-in
Klf4	Kruppel-Like Factor 4
KO	Knockout
KRAS	KRAS Proto-oncogene GTPase
KSR	Knockout serum replacement
LAMP1	Lysosomal-Associated Membrane Protein 1
LAMP2	Lysosomal-Associated Membrane Protein 2
LAMP2A	Lysosomal-Associated Membrane Protein 2A
LAR-RPTP	LAR Transmembrane Tyrosine Phosphatase
LC	Liquid chromatography
LC	Locus coeruleus
LC3	Microtubule-Associated Proteins 1A/1B Light Chain 3B
LDN	LDN-193189
LIF	Leukaemia inhibitory factor
LIMA1	LIM domain and actin-binding protein 1
LMX1A	Lim Homeobox Transcription Factor 1 Alpha
LMX1B	Lim Homeobox Transcription Factor 1 Beta
LRR	Leucine-rich repeat
Lrrk	Drosophilia leucine-rich repeat kinase

LRRK2	Leucine-Rich Repeat Kinase 2
MALAT1	Metastasis Associated Lung Adenocarcinoma Transcript 1
MAP2	Microtubule-Associated Protein 2
MAPK	Mitogen-activated protein kinase
MAPT	Microtubule-Associated Protein Tau
MARCKSL1	MARCKS-Related Protein
MEFs	Mouse embryonic fibroblasts
mESCs	Mouse embryonic stem cells
MIRO1	Mitochondrial Rho GTPase 1
MMP	Mitochondrial membrane potential
MOAC	Metal Oxide Affinity Chromatography
MP	Midbrain patterned
MPP+	1-methyl-4-phenylpyridinium
MPTP	1-methyl-4-phenyl-1,2,3,6-tetrahydropyridine
MSX1	Msh Homeobox 1
MUNC18-1	Mammalian Uncoordinated-18-1
NANOG	Nanog Homeobox
NBM	Nucleus basalis of Meynert
NCE	Normalized collision energy
NGN2	Neurogenin 2
NGS	Next-generation sequencing
NMDA	*N*-methyl-D-aspartate
NPs	Neural progenitors
NRP1	Neuropilin 1
NS	Not significant
NSF	N-Ethylmaleimide-Sensitive Factor
NUCKS1	Nuclear Casein Kinase and Cyclin Dependent Kinase Substrate 1
NURR1	Nuclear Receptor Related-1
OCR	Oxygen consumption rate
Oct3/4	Octamer-Binding Transcription Factor 3/4
OTX2	Orthodentical Homeobox 2
p-	Phosphorylated
P62	Ubiquitin Binding Protein P62/Sequestosome
PAK	P21-Activated Kinase
PAK3	P21-Activated Kinase 3
PAK6	P21-Activated Kinase 6
PAX6	Paired Box Protein PAX6
PBMCs	Peripheral blood mononuclear cells

PBS	Phosphate buffered saline
PC	Principal component
PCA	Principal component analysis
PCR	Polymerase-chain reaction
PD	Parkinson's disease
PenStrep	Penicillin-Streptomycin
PF475	PF06447475
PFA	Paraformaldehyde
PIF	Parent ion fraction
PINK1	Pten Induced Putatitive Kinase 1
PITX3	Pituitary Homeobox 3
PLA2G6	Phospholipase A2 group VI
PLEKHA5	Pleckstrin Homology Domain Containing A5
PPFIA3	Liprin-α3
PPN	Pedunculopontine nucleus
PSCs	Pluripotent stem cells
qPCR	Quantitative polymerase-chain reaction
RAB	Ras-Related Protein
REM	Rapid eye movement
Ri	Y27632
RIN	RNA integrity number
RN	Raphe nuclei
RNA-seq	RNA sequencing
RO	Reverse-osmosis
ROC	Ras of complex proteins
RRF	Retrorubal field
S100B	S100 Calcium Binding Protein B
SB	SB-431542
SCFD1	Sec1 Family Domain-Containing Protein 1
SD	Standard deviation
SDHA	Succinate Dehydrogenase Complex Flavoprotein Subunit A
SEM3A	Semaphorin 3A
SH3GL3	Endophilin III
SH3GL3	Endophilin III
SHH	Sonic hedgehog
SILAC	Stable isotope labelling by amino-acids in cell culture
SNc	Substantia nigra pars compacta
SNCA	α-Synuclein

SNPs	Single nucleotide polymorphisms
Sox2	SRY (Sex Determining Region Y)-Box 2
SRCIN1	SRC Kinase Signaling Inhibitor 1
SRRM2	Serine/Arginine Repetitive Matrix 2
Tau	Microtubule-Associated Protein Tau
TCEP	Tris(2-carboxyethyl)phosphine
TEAB	Triethylammonium bicarbonate
TGF	Transforming Growth Factor
TGN	Trans-golgi network
TH	Tyrosine Hydroxylase
TMRM	Tetramethylrhodamine methyl ester
TNF-α	Tumour Necrosis Factor Alpha
TPC2	Two-Pore Calcium Channel 2
TUJ1	Beta-III Tubullin
UCP	Mitochondrial Uncoupling Protein
VAMP2	Vesicle-Associated Membrane Protein 2
VIM	Vimentin
VMAT2	Vesicular Monoamine Transporter 2
vmDA	Ventral-midbrain dopaminergic
VPS35	Vacuolar Protein Sorting-Associated Protein 35
VTA	Ventral tegmental area
WAVE2	Wiskott-Aldrich Syndrome Protein Family Member 2
WIPI	WD-repeat Protein Interacting with Phosphoinositides
WNT	Wingless-Type MMTV Integration Site Family
WT	Wildtype
XIST	X-inactive specific transcript

Chapter 1: Introduction

1.1. Parkinson's disease

1.1.1. Parkinson's disease prevalence and impact

Parkinson's disease (PD) is the second most common neurodegenerative disorder worldwide (Pringsheim et al. 2014). Disease prevalence increases with age, occurring in just 0.07% of adults aged 40-59, rising to 0.65% aged 60-79, and 1.90% in those aged over 80. PD has a strong negative effect on the quality of life of those whom it afflicts, and is a burden on healthcare systems and the economy (Boland and Stacy 2012). Development of a disease-modifying treatment, or a cure, for PD is therefore a priority for improving patient quality of life and survival, and will reduce the economic burden of the disease.

1.1.2. Parkinson's disease symptoms

PD was first described in detail in 1817 by Dr James Parkinson in his paper "An essay on the shaking palsy" (Parkinson 1817, reprint 2002). In this essay, he describes not only the motor symptoms that have become known as the hallmark features of PD, but also some of the accompanying non-motor symptoms that affect many patients. The motor component of PD is the most widely recognised aspect of the disease and involves resting tremor, bradykinesia (slowness of movement), and rigidity (Parkinson 1817, reprint 2002). As a result, patients experience difficulty with walking, which can result in falls (Wood et al. 2002). Difficulties with speech also emerge, and as the disease progresses patients experience problems with swallowing (Kalf et al. 2011).

Although PD is primarily considered a motor-neurodegenerative disease, it is now known that it involves multiple systems. In his essay, James Parkinson refers to the sleep disturbances that his patients experience as being caused by their tremors. In addition to this cause, it has now been found that many patients experience REM sleep behaviour disorder, which causes them to act out their dreams, often years before they are diagnosed with PD (Pont-Sunyer et al. 2015). Additionally, patients commonly experience symptoms that arise due to the manifestation of the disease in the autonomic nervous system. Many patients develop problems with urinary control as well as gastrointestinal issues, such as constipation (Jost 2003; Jost and Eckardt 2003). Further effects of the disease on the autonomic system are characterised by orthostatic hypotension—abnormally low blood pressure upon standing—which can lead to dizziness and fainting (Wu and Hohler 2015).

Cognitive decline and dementia are common in PD and manifest at early stages of the disease in some patients, and at later stages in others (Williams-Gray et al. 2006). Patients may also experience depression, anxiety, hallucinations, and more rarely psychosis (Williams-Gray et al. 2006; Reijnders et al. 2008; Pagonabarraga et al. 2016). Many patients also experience sensory symptoms such as unusual sensations and pain, as well as anosmia (loss of sense of smell), which often emerges before the onset of motor symptoms (O'Sullivan et al. 2008; Driver-Dunckley et al. 2014).

1.1.3. Parkinson's disease pathology

Dopaminergic (DA) neurons are present throughout the brain—in the midbrain, hypothalamus, olfactory bulb and lower brain stem (Hegarty et al. 2013). Around 75% of DA neurons are found in the midbrain, where several subtypes—A8, A9 and A10—are present. A8 DA neurons reside in the retrorubal field (RRF), A9 in the substantia nigra pars compacta

(SNc), and A10 in the ventral tegmental area (VTA). Pathologically, PD is characterised by the preferential loss of A9 ventral midbrain DA (vmDA) neurons in the SNc. When patients present to their general practitioner with motor symptoms, typically around 50% of the neurons in this region will have already been lost to degeneration (Kordower et al. 2013) (Figure 1.1A). Death of these neurons results in a reduction in dopamine transmission to the dorsal striatum and causes the motor phenotypes of the disease. Lewy bodies and Lewy neurites (Figure 1.1B) are often found in surviving neurons and the extracellular space, and consist of multiple aggregated proteins including α-Synuclein, ubiquitin, phosphorylated neurofilaments and lipids (Spillantini et al. 1998; Gai et al. 2000).

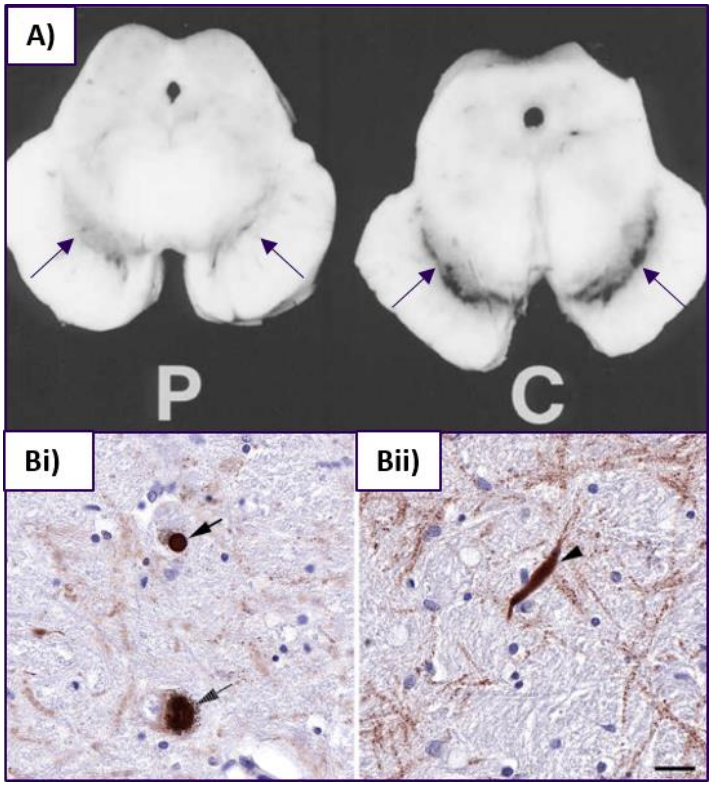

Figure 1.1. Parkinson's disease pathology.
A) Horizontal human brain sections from a PD patient (P) and a healthy control (C) (Mackenzie 2001). Arrows indicate the pigmented cells of the SNc, which are greatly reduced in number in (P) compared to (C). B) Human PD SNc stained with an antibody against α-Synuclein and counterstained with hematoxylin, demonstrating the presence of a Lewy bodies (i: arrows), and Lewy neurites (ii: arrow); scale bar: 25 µm (Vermilyea and Emborg 2015).

Although the pathological hallmark of PD is loss of dopaminergic neurons in the SNc, Lewy bodies and Lewy neurites are often widespread throughout other brain regions. Braak et al., characterised the localisation of these inclusions in post-mortem brains from PD patients with varying degrees of Lewy body and Lewy neurite pathology (Braak et al. 2003). They classified the brains into six categories and found that in the mildest cases the pathology was present only in the dorsal motor nucleus and the anterior olfactory nucleus. As sequentially more severe cases were assessed, the pathology was found to spread upward through the brain stem to the anteromedial temporal cortex, followed by the neocortex.

It is not yet completely understood why Lewy bodies and neurites form, or what their role in the disease is. Brains from many PD patients with mutations in Parkin, and some with mutations LRRK2, exhibit no Lewy body pathology (Doherty and Hardy 2013; Gaig et al. 2007). Furthermore, Lewy bodies have been found in around 8% of neurologically normal post-mortem brains (Gibb and Lees 1988; Parkkinen et al. 2005). These findings suggest that Lewy bodies are not necessarily pathogenic. α-Synuclein, a component of Lewy bodies, has been shown to form toxic oligomeric structures (Chen et al. 2007; Danzer et al. 2007). These have been demonstrated to have a high seeding propensity (Pieri et al. 2016), and have been found in PD patient brains (Sharon et al. 2003; Tokuda et al. 2010). It has therefore been hypothesised that these oligomers are pathogenic in PD, and that formation of Lewy bodies is a protective mechanism for sequestering toxic oligomers and maintaining normal cellular function (Bengoa-Vergniory et al. 2017).

It has not yet been discovered exactly why dopaminergic neurons in the SNc are particularly susceptible to degeneration. Other neuronal cell types also degenerate, but to a lesser extent. These include dopaminergic neurons in the VTA and the RRF, as well as other neuronal

subtypes such as those in the dorsal motor nucleus of the vagus (DMV), locus coeruleus (LC), raphe nuclei (RN), pedunculopontine nucleus (PPN) and nucleus basalis of Meynert (NBM) (Sulzer and Surmeier 2013). There are several commonalities that exist between the neurons that degenerate in PD, and these have been hypothesised to contribute to their propensity to degenerate. Susceptible neurons tend to have unusually highly branched, long, unmyelinated axons that put a high energetic burden on the cell (Braak and Del Tredici 2004; Pissadaki and Bolam 2013). Furthermore, SNc, LC, DMV, and PPN (but not VTA, RN, or NBM) neurons also share an electrical phenotype; they are autonomous pacemakers, which continuously fire action potentials without synaptic input (Williams et al. 1984; Jiang et al. 1994; Takakusaki and Kitai 1997; Krashia et al. 2016). This pacemaking activity is thought to have high energy requirements. Altogether, the high energetic burden that these cells experience may make them more susceptible to degeneration in the presence of PD risk factors such as disease-causing mutations or environmental factors.

1.1.4. Parkinson's disease treatments

L-Dopa, a dopamine precursor, was introduced as a treatment for the motor symptoms of PD in 1970, and still remains the most widely used treatment for the disease (Fahn 2015). It works by elevating dopamine levels in the striatum. Other drugs such as monoamine oxidase B inhibitors, which inhibit the enzyme that degrades dopamine, and catechol-O-methyltransferase inhibitors, which inhibit the enzyme that degrades L-Dopa, can be used together with L-Dopa to improve its effectiveness (Robakis and Fahn 2015; Muller 2015). Dopamine agonists can also be used to directly stimulate neurons in the striatum, and can be used alone or in combination with L-Dopa (Blandini and Armentero 2014). As the disease progresses however, there is decreased capacity for dopamine storage, and the effectiveness

of treatment can diminish. Less commonly used drugs include anticholinergics and glutamate antagonists. Anticholinergics reduce tremor and can be used at the early stages of the disease, before L-Dopa is required (Pagano et al. 2015). Glutamate antagonists are helpful in a minority of patients, and can mildly reduce some of the motor effects of the disease as well as sleepiness (Duty 2012). Additionally, surgery—most commonly in the form of deep brain stimulation—is available to patients. Deep brain stimulation is carried out by implantation of electrodes into subthalamic nucleus or the internal segment of the globas pallidus, which then provide electrical stimulation to modulate neurotransmission (Wichmann and DeLong 2016). This technique has been shown to alleviate motor and non-motor symptoms, for up to 10 years (Deuschl et al. 2013; Collomb-Clerc and Welter 2015).

All of the treatments currently available only treat the symptoms of PD and do not modify disease progression. In order to develop disease modifying treatments, it will be necessary to develop a deeper understanding of the mechanisms underlying the disease, so that treatment can be approached in a more targeted manner.

1.1.5. Parkinson's disease aetiology

For many years it was thought that PD was a purely sporadic disorder, however in 1997 the first PD related mutation was found in *SNCA*, the gene that encodes the α-Synuclein protein (Polymeropoulos et al. 1997). Since then, monogenic mutations in 16 genes have been found to contribute to the genetic aetiology of the disease (Table 1.1) (Fujioka and Wszolek 2012; Saiki et al. 2012; Hernandez et al. 2016); however, these still account for only ~30% of familial and 3-5% of sporadic cases (Kumar et al. 2011). The majority of PD cases have unknown cause. Genome-wide association studies (GWAS) have been conducted in sporadic PD patients in an effort to identify rare variants that increase disease risk (Satake et al. 2009; Simon-

Sanchez et al. 2009; Pankratz et al. 2009; Hamza et al. 2010; Nalls et al. 2014). Twenty-eight genetic loci have now been identified as risk factors for the development of the disease (Table 1.2).

Table 1.1. Genetic loci associated with monogenic PD.
*Table adapted from Hernandez et al. (Hernandez et al. 2016) detailing genetic loci associated with monogenic PD, their corresponding gene and protein, as well as their inheritance pattern. *Genes that have been reproducibly associated with Mendelian PD.*

Locus	Gene	Protein	Inheritance
Park1/4	*SNCA**	α-Synuclein	Autosomal dominant
Park2	*PRKN**	Parkin	Autosomal recessive
Park3	Unknown	Unknown	Autosomal dominant
Park5	*UCHL1*	Ubiquitin C-terminal hydroxylase	Autosomal dominant
Park6	*PINK1**	Pten induced putatitive kinase 1	Autosomal recessive
Park7	*PARK7**	DJ-1	Autosomal recessive
Park8	*LRRK2**	Leucine-rich repeat kinase 2	Autosomal dominant
Park9	*ATP13A2**	Lysosomal type 5 ATPase	Autosomal recessive
Park11	*GIGYF2*	GRB interacting GYF protein 2	Autosomal dominant
Park12	Unknown	Unknown	X-linked
Park13	*HTRA2*	HTRA serine peptidase 2	Autosomal dominant
Park14	*PLA2G6**	Phospholipase A2 group VI	Autosomal recessive
Park15	*FBXO7**	F-box only protein 7	Autosomal recessive
Park17	*VPS35**	Vacuolar protein sorting 35	Autosomal dominant
Park18	*EIF4G1*	Eukaryotic translation initiating factor gamma 1	Autosomal dominant
Park19	*DNAJC16*	DNAJ1 heat shock protein family member C16	Autosomal recessive

Environmental factors may also contribute to the development of PD. A recent umbrella review of meta-analyses assessed the strength of evidence presented for 75 environmental risk factors in PD (Bellou et al. 2016). The study categorised evidence levels as “convincing evidence”, “highly suggestive evidence”, “suggestive evidence”, “weak evidence”, or “no evidence”. It was concluded that there is “suggestive evidence” for exposure to environmental toxins such as pesticides resulting in an increased risk for disease development (Mortimer et al. 2012; Pezzoli and Cereda 2013; van der Mark et al. 2012). They also found “suggestive evidence” that consumption of dairy products may lead to an increased risk of disease (Jiang et al. 2014). Additionally, the conclusion was drawn that treatment with beta-

blockers may increase disease risk ("highly suggestive evidence") (Noyce et al. 2012), but that treatment with calcium channel blockers (Lang et al. 2015) or ibuprofen (Gao et al. 2011) may confer a protective effect ("suggestive evidence"). Smoking ("convincing evidence") (Noyce et al. 2012), alcohol consumption (Zhang et al. 2014) and drinking coffee ("highly suggestive evidence") (Noyce et al. 2012) were all found to be protective against development of PD.

Table 1.2. Alleles associated with PD risk.
Table adapted from Hernandez et al. (Hernandez et al. 2016) detailing single nucleotide polymorphisms (SNPs) identified as risk factors for PD, along with details of their nominated genes, possible alleles, and odds ratio. Conditional SNPs are identified by an asterisk.*

SNP	Nominated gene	Effect allele /alternate allele	Odds ratio
rs35749011	*GBA/SYT11*	A/G	1.824
rs114138760*	*GBA/SYT11*	C/G	1.586
rs823118	*RAB7L1/NUCKS1*	T/C	1.122
rs10797576	*SIPA1L2*	T/C	1.131
rs6430538	*ACMSD/TMEM163*	T/C	0.875
rs1474055	*STK39*	T/C	1.214
rs12637471	*MCCC1*	A/G	0.842
rs34311866	*TMEM175/GAK/DGKQ*	T/C	0.786
rs34884217*	*TMEM175/GAK/DGKQ*	A/C	1.105
rs11724635	*BST1*	A/C	1.126
rs6812193	*FAM47E/SCARB2*	T/C	0.907
rs356182	*SNCA*	A/G	0.760
rs7681154*	*SNCA*	A/C	0.934
rs9275326	*HLA-DQB1*	T/C	0.826
rs13201101*	*HLA-DQB1*	T/C	1.217
rs199347	*GPNMB*	A/G	1.11
rs591323	*FGF20*	A/G	0.916
rs117896735	*INPP5F*	A/G	1.624
rs329648	*MIR4697*	T/C	1.105
rs76904798	*LRRK2*	T/C	1.155
rs11060180	*CCDC62*	A/G	1.105
rs11158026	*GCH1*	T/C	0.904
rs2414739	*VPS13C*	A/G	1.113
rs14235	*BCKDK/STX1B*	A/G	1.103
rs11868035	*SREBF/RAI1*	A/G	0.939
rs17649553	*MAPT*	T/C	0.769
rs12456492	*RIT2*	A/G	0.904
rs8118008	*DDRGK1*	A/G	1.111

It is likely that in many cases, genetic and environmental factors coalesce, resulting in the development of PD. Genetic variants may predispose individuals to the risks inferred by certain environmental factors, and this makes identifying such variants more difficult. Nevertheless, monogenic mutations that give rise to PD may provide us with the information we need to treat the sporadic disease. By studying these mutations to develop an understanding of the mechanisms by which they cause PD, treatments may be developed that can be utilised across the PD patient population.

1.1.6. Astrocyte involvement in Parkinson's disease pathogenesis

Many studies have been conducted in an effort to identify the mechanisms underlying the degeneration of A9 vmDA neurons in PD (Poewe et al. 2017). The majority of these investigate intrinsic cellular mechanisms that could be occurring in A9 neurons themselves. More recently, however, the fact that other cell types in the brain could contribute to the early stages of disease has been recognised. Of particular interest is the role that midbrain astrocytes may play (Rappold and Tieu 2010; Niranjan 2014; Cabezas et al. 2014; Booth et al. 2017). Astrocytes are essential for maintaining neuronal health. They regulate synaptic transmission, water transport, and blood flow; and provide metabolic and structural support (Sofroniew and Vinters 2010). Furthermore, they produce neurotrophic factors, including Glial Derived Neurotrophic Factor (GDNF), which is particularly important for the development and survival of DA neurons (Lin et al. 1993; Schaar et al. 1993). Additionally, astrocytes are involved in blood-brain-barrier (BBB) integrity, which has been demonstrated to be disrupted in PD (Gray and Woulfe 2015). Astrocytes express many of the genes that have been implicated in PD, at levels similar to (or in some cases higher than in) neurons (Figure 1.2) (Zhang et al. 2016). So far, studies have determined that eight of these genes—

SNCA (α-Synuclein), *PARK7* (DJ-1), *PRKN* (Parkin), *PINK1*, *GBA*, *LRRK2*, *PLA2G6*, and *ATP13A2*—play a role in astrocyte biology; the remainder are yet to be investigated.

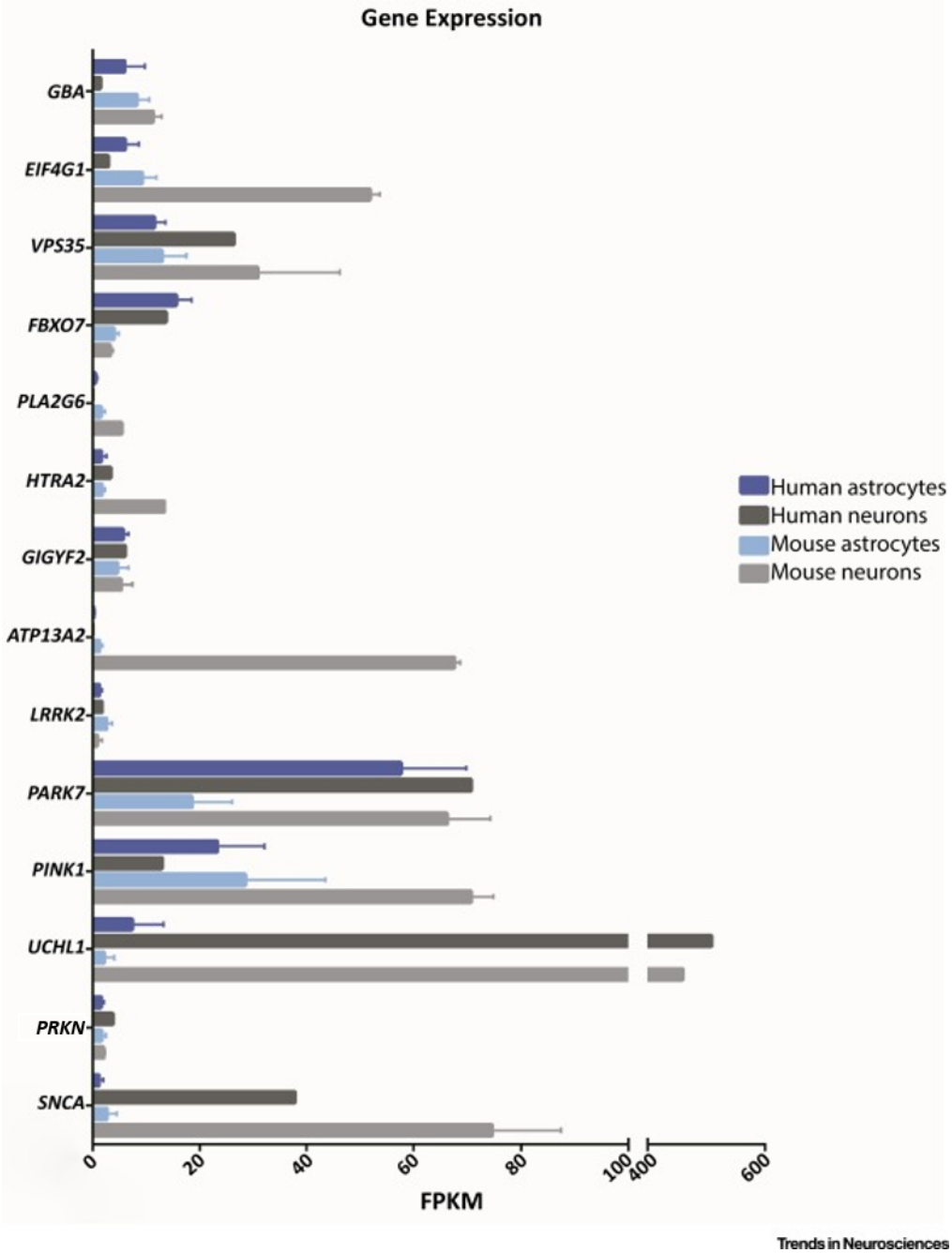

Figure 1.2. Expression levels of key PD genes in astrocytes and neurons.
Transcriptome data from Zhang et al. showing the expression levels of genes known to be causative in PD in astrocytes and neurons from humans and mice. Human astrocytes N = 12 subjects; human neurons N = 1 subject; mouse astrocytes N = 6 animals; mouse neurons N = 2 animals. Abbreviation: FPKM, fragments per kilobase of transcript per million mapped reads. Graph shows mean ± SD. Data obtained from Supplementary Table S4 in the original publication (Zhang et al. 2016), and can be also be found online at http://web.stanford.edu/group/barres_lab/brainseq2/brainseq2.html. Figure originally published in Booth et al. (Booth et al. 2017) https://creativecommons.org/licenses/by/4.0/.

Disruption of mitochondrial function and lysosome biology have been widely implicated in PD. *Lrrk2*, *Gba*, and *Prkn* knockout (KO) models have shown disruption of mitochondrial function in astrocytes (Larsen et al. 2011; Osellame and Duchen 2013; Schmidt et al. 2011), and in the *Gba* and *Prkn* studies, this disruption was found to be more pronounced in astrocytes than in neurons. Furthermore, perturbations in Gba, Atp13a2 and Lrrk2 function have all been shown to be detrimental to lysosome function in astrocytes (Qiao et al. 2016; Henry et al. 2015; Vitner et al. 2010).

PD risk genes have also been demonstrated to play a role in cellular functions that are more specific to astrocytes, including proliferation and inflammatory responses. There is evidence that loss of function mutations in *PINK1* and *PRKN* lead to impairment of astrocyte proliferation during development and in response to insult (Choi et al. 2013; Choi et al. 2016; Solano et al. 2006; Solano et al. 2008). α-Synuclein, DJ-1, and PLA2G6 have been shown to respectively activate (Rannikko et al. 2015; Fellner et al. 2013; Klegeris et al. 2006), modulate (Kim et al. 2013a; Waak et al. 2009; Ashley et al. 2016), and respond to (Strokin et al. 2011) TLR4-inflammatory signalling in astrocytes. It has also been shown that DJ-1 regulates IFN-γ-mediated astrocyte activation (Kim et al. 2013b), IL-1β and TNF-α stimulation regulate Parkin levels (Khasnavis and Pahan 2014), and the presence of functional ATP13A2 at the lysosome prevents a cascade of events that result in activation of the NLRP3 inflammasome (Qiao et al. 2016). Essential astrocyte functions including water transport (Gu et al. 2010), glutamate uptake (Gu et al. 2010; Kim et al. 2016), and neurotrophic capacity (Solano et al. 2008; Mullett and Hinkle 2009; Mullett and Hinkle 2011; Kim et al. 2013; Lev et al. 2013; Qiao et al. 2016), which are important for maintaining neuronal health, are negatively affected by disruption of these inflammatory signalling pathways. Dysregulation of these functions in astrocytes has

been shown to lead to degeneration of neighbouring neurons, demonstrating a potential mechanism for astrocyte-mediated PD pathogenesis.

1.2. iPSC disease modelling

1.2.1. Modelling Parkinson's disease

The study of post-mortem human brain tissue from PD patients has provided many insights into disease pathology (Hartmann 2004). However, such samples can only tell us about the processes that are occurring at the end stage of the disease, they cannot provide information regarding the mechanisms that result in disease initiation (Hartmann 2004). It is therefore necessary to develop models that allow us to study these processes. There are many approaches to modelling PD in the laboratory. One of the simplest approaches is to express disease-causing genes in immortalised, human cell lines (Alegre-Abarrategui et al. 2009). These models tend to be easy to work with, but have their limitations. Immortalised cell lines are generally derived from cancerous cells, and have been cultured for many generations, resulting in changes to their genetic and physiological characteristics; as such, they are not truly representative of their tissue of origin (Horvath et al. 2016). These models often involve the expression of transcripts from plasmids containing only the cDNA sequence of the gene of interest, which lacks regulatory information encoded by intron sequences (Hube and Francastel 2015). Additionally, genes are often overexpressed, and/or fluorescently tagged which can lead to misleading results (Moore et al. 2009, Margolin et al. 2012, Siller et al. 2013). Furthermore, the gene is not expressed in its native cell type. Different cell types express different proteins (Yeger-Lotem and Sharan 2015), and many of the proteins expressed in immortalised cell lines are not present in neurons (or astrocytes), and vice versa. This may lead to the identification of interactions that are irrelevant to the disease.

Primary human fibroblast cultures retain the genetic background of the donor, and therefore provide the opportunity to study disease-causing mutations at physiological expression levels.

Fibroblasts can be obtained from patients via a skin punch biopsy, and can be easily cultured (Vangipuram et al. 2013). They enable the study of mutations across a range of genetic backgrounds and can provide important insight into early disease mechanisms. Although modelling PD in patient-derived fibroblasts provides advantages over the use of immortalised cell lines, proteins of interest still do not interact with the same repertoire of cellular components that they would encounter in a brain cell.

Animal models provide a whole-system approach to studying PD; they can be studied in totality, or primary cell cultures and slice cultures can be derived from them. Rodents can be readily modified to introduce genetic mutations. Gene KO can be achieved by introducing a null mutation into the rodent gene sequence. Similarly, knock-in (KI) mutations can be achieved by replacing a segment of the rodent gene sequence with a fragment containing a mutation. Advantages of these approaches are that the site-specific manipulations do not disrupt the rest of the rodent genome, and gene function can be studied at physiological expression levels. However, disadvantages can arise due to the differences in the effect of a mutation on the rodent gene in comparison to the effect it has on the human gene. A notable example of this is the PD-causing A53T mutation in human α-Synuclein (Polymeropoulos et al. 1997); in mice T53 is the normal amino acid found at this position (Hong et al. 1998). To overcome this issue, whole human genes, including their regulatory sequences, can be introduced into the rodent genome using bacterial artificial chromosomes (BACs). Although this approach allows the study of human genes, it can suffer from the effects that random integration of the BAC can have on other regions of the genome, and often results in multiple copies of the BAC being integrated, resulting in overexpression (Ristevski 2005). Furthermore, once the human gene is incorporated, it interacts with the rodent environment, which may

lead to different phenotypes than those that might arise in a human system. Nevertheless, many rodent models have been developed that closely recapitulate certain aspects of PD. Furthermore, animal models have the advantage that they can be used in preclinical studies to identify candidate drugs; however, results of such studies often do not translate to success in human clinical trials (Hackam and Redelmeier 2006; Perel et al. 2007). Therefore, there is an urgent need for realistic human models to address these problems. The discovery and development of human embryonic stem cells (hESCs) and induced pluripotent stem cells (iPSCs) for use in disease modelling has been a great step towards achieving this goal.

1.2.2. Embryonic stem cells

Embryonic stem cells (ESCs) are pluripotent, meaning that they are capable of differentiating into any of the three germ layers of the body (ectoderm, endoderm, and mesoderm). Differentiation to specific cell types can be achieved by culturing ESCs in the presence of growth factors and small molecules that mimic *in-vivo* development. Differentiated cells can be used to model diseases in the very cell types that are affected in the disease of interest. ESCs were first derived in 1981, by isolating and culturing the inner cell mass from mouse blastocysts (Evans and Kaufman 1981; Martin 1981) (Figure 1.3). These mouse ESCs (mESCs) were maintained on mouse embryonic fibroblasts (MEFs) and their pluripotency was demonstrated through their capacity to differentiate into a range of tissue types *in vitro* and *in vivo*. In 1998, the first hESCs were derived from embryos that had been produced by in vitro fertilisation (IVF) (Thomson et al. 1998). Since the first derivation of hESCs, protocols for their differentiation into a vast array of somatic cell types have been developed. This has enabled researchers to study the biology of specific human cell types that were previously

inaccessible. Furthermore, genetic modification of hESCs has enabled the study of gene function in specific tissues.

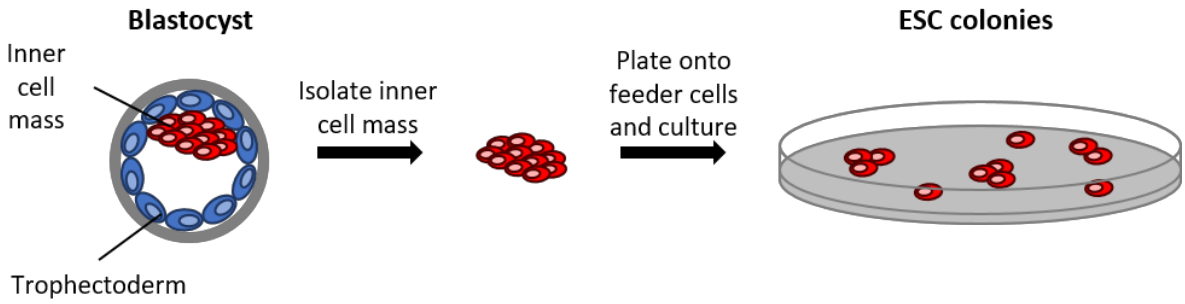

Figure 1.3. Embryonic stem-cell derivation.
By day 5 of embryonic development, the blastocyst is formed. At this stage, cells are segregated into the inner cell mass, which will develop into the foetus; and the trophectoderm, which gives rise to the placenta (Marikawa, Y. 2009). Embryonic stem cells are derived by isolating and culturing the inner-cell mass (Evans and Kaufmann 1981; Martin 1981; Thomson et al. 1998).

1.2.3. Induced pluripotent stem cells

The first evidence that pluripotency could be induced in somatic cells was discovered in 1962 by John Gurdon when he transplanted the nucleus from a *Xenopus* intestinal epithelial cell into a *Xenopus* egg (Gurdon 1962). 1.5% of transfers conducted resulted in the development of healthy tadpoles, demonstrating that the genetic content of the intestinal epithelial cell nucleus was capable of producing all cells of the organism. These experiments were the first demonstration that the specialisation of cells is reversible, and showed that the nuclei of somatic cells contain the genetic information necessary for the proper functioning of any cell type. In 2006, Takahashi and Yamanaka discovered that pluripotent stem cells (PSCs) could be derived from mouse fibroblast cultures by delivery of the 'reprogramming factors' *Oct3/4*, *Sox2*, *c-Myc*, and *Klf4* under mESC culture conditions (Takahashi and Yamanaka 2006). The resulting iPSCs expressed ESC markers, exhibited the morphology and growth properties of ESCs, and were capable of differentiating into cell types of all three germ layers. Just one year

later, Yamanaka's team demonstrated that the same four reprogramming factors could be used to derive iPSCs from human fibroblasts (Takahashi et al. 2007). Reprogramming factors were delivered using a retrovirus, and reprogramming efficiency was ~0.02% by 30 days after retroviral delivery. This discovery hailed a new era in human disease modelling.

A downside to using retroviral delivery for the production of iPSCs is the fact that the reprogramming factors randomly integrate into the host genome. This can lead to disruption of other genes in the cells, and if the reprogramming factors do not become silenced over time, they can impair the capacity of the iPSCs to differentiate. In order to overcome these issues, and to improve reprogramming efficiency, researchers sought to develop other methods for delivery of reprogramming factors. Adenoviruses are non-integrating, and therefore seemed like an excellent replacement for the retrovirus. Sure enough, derivation of iPSCs using an adenovirus was successful; however, reprogramming efficiency was very low, at ~0.0002% (Zhou and Freed 2009). A more efficient, non-integrating system was found in the Sendai virus (Fusaki et al. 2009; Seki et al. 2010). iPSCs could be made in 25 days from human fibroblasts or blood cells, with efficiencies of 1% and 0.1% respectively. Reprogramming factors were found to persist in the iPSCs for a number of passages, but were diluted to non-detectable levels over time, while pluripotency was maintained. The Sendai virus has since become the most widely used delivery system for reprogramming factors. GMP-grade Sendai virus systems, such as Cytotune (Lieu et al. 2013) have been developed and are now used by researchers worldwide to produce iPSCs using a standardised method.

A major advantage of iPSCs over ESCs is that they can be produced from easily accessible tissues of the human body. As iPSCs retain their genetic identity after reprogramming, this

presents a major opportunity for disease modelling (Figure 1.4). Non-invasive skin biopsies or blood samples can be taken from patients suffering from a disease, such as PD, and

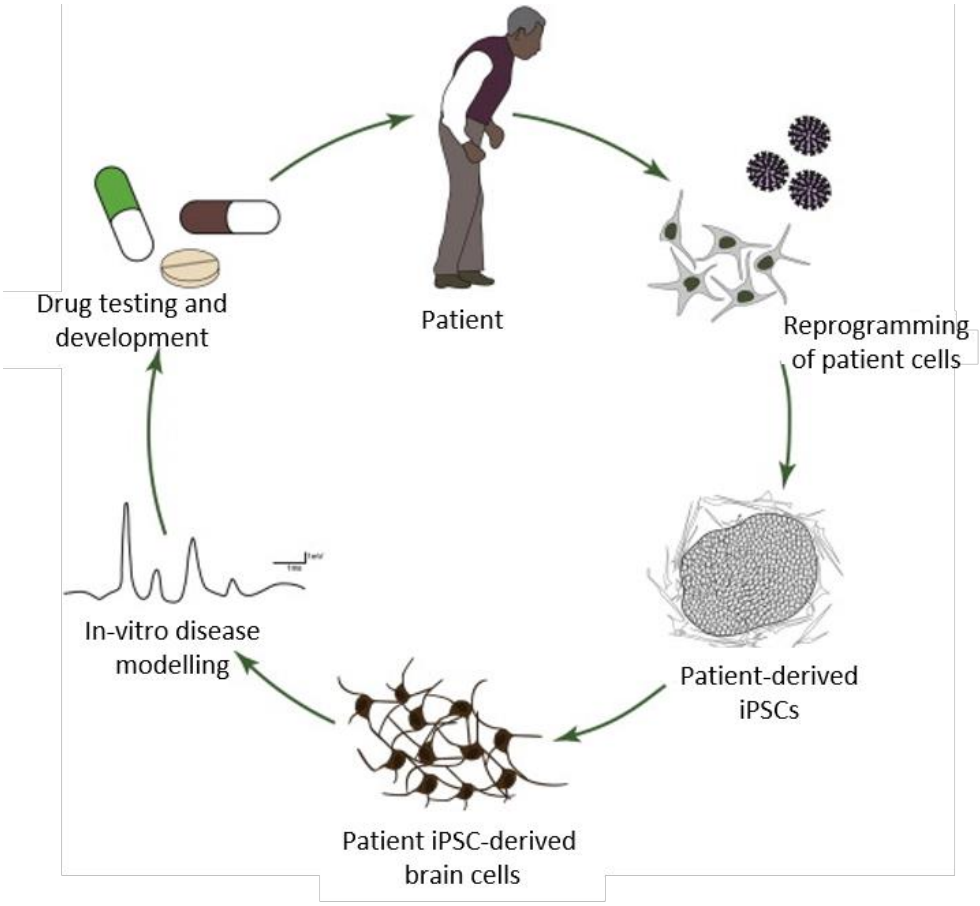

Figure 1.4. Modelling PD using iPSCs.
Schematic demonstrating the steps involved in modelling of PD using iPSCs, modified from Badger et al. (Badger et al. 2013). Clockwise from top: PD patients present to the clinic, they provide a skin biopsy, which is then cultured and reprogrammed into iPSCs. These are then differentiated into brain cells (e.g. astrocytes and neurons), which can be used to establish cellular disease phenotypes. Identified phenotypes can then be used for screening of potential drugs, and successful candidates can be further developed in clinical trials and then provided to patients as a treatment for the disease.

reprogrammed to produce iPSCs. These can then be differentiated into disease-relevant cell types for the study of disease mechanisms. For many diseases including PD, iPSCs provide access to cell types that were previously only available post-mortem, and allow for in-depth studies that could have never previously been realised. iPSCs are now widely used for the study of diseases caused by known genetic mutations. Furthermore, they provide the

opportunity for drug screening in human disease models that closely recapitulate disease phenotypes.

1.3. LRRK2 in Parkinson's disease

1.3.1. LRRK2 mutations and Parkinson's disease

As discussed in section 1.1.5, a minority of PD cases arise from genetic mutations, which are inherited in either autosomal recessive or autosomal dominant manners. Autosomal dominant PD mutations tend to result in disease phenotypes most similar to the sporadic disease. In particular, patients with *LRRK2* mutations exhibit disease progression that is indistinguishable from sporadic patients (Saiki et al. 2012).

The Park8 locus, where the *LRRK2* gene resides, was first identified in 2002 in a genome-wide analysis of a Japanese family with autosomal-dominant PD (Funayama et al. 2002). Two studies published simultaneously in 2004 subsequently identified the *LRRK2* gene as the location of disease-causing mutations in this locus (Paisain-Ruiz et al. 2004; Zimprich et al. 2004). These studies identified the Y1699C mutation in one British (Paisan-Ruiz et al. 2004) and one German-Canadian kindred (Zimprich et al. 2004), the R1441G mutation in four Basque kindreds (Paisan-Ruiz et al. 2004), and the R1441C mutation in a Western Nebraskan kindred (Zimprich et al. 2004). Subsequently, in 2005, the G2019S mutation was identified in multiple kindreds across North America and Europe (Hernandez et al. 2005; Kachergus et al. 2005), and the R1441H mutation was identified in a patient of European ancestry (Zabetian et al. 2005). Furthermore, the I2020T mutation was identified as the causative mutation in the original Park8 family (Funayama et al. 2005). In 2010, the N1437H mutation was identified for the first time, in a large Norwegian family (Aasly et al. 2010). All of these mutations exhibit a pattern of autosomal-dominant inheritance with varying levels of penetrance. Of the

confirmed mutations, G2019S is widely recognised as the most frequent (Dachsel and Farrer 2010), and its penetrance has been most well studied. Early publications estimated penetrance of the G2019S mutation at 80-100%; however, as more families carrying the mutation have been identified, this number has decreased and is now considered to be between 25-42.5% (Goldwurm et al. 2011; Lee et al. 2017).

In addition to the seven autosomal-dominant *LRRK2* mutations described above, two monogenic risk factors, R1628P and G2385R, have been identified (Ross et al. 2008; Di Fonzo et al. 2006). These risk factors both confer a two-fold increased risk for the development of PD. Furthermore, one *LRRK2* polymorphism, R1398H, has been associated with decreased risk of developing PD in Han Chinese cohorts (Chen et al. 2011). *LRRK2* mutations are now the most commonly identified monogenic cause of PD and cause a disease phenotype most similar to that found in patients with the sporadic disease (Saiki et al. 2012). For this reason, *LRRK2* is arguably the most suitable PD-associated gene to study to gain an understanding of the disease processes that may be occurring in a broader population of patients.

1.3.2. LRRK2 structure and function

The *LRRK*2 gene is located on chromosome 12 and consists of 51 exons; it codes for a 286 kDa protein, which contains a number of conserved domains (Figure 1.5). Working from the N-terminus these include an ankyrin repeat (ANK) followed by the leucine-rich repeat (LRR) for which the protein is named. There is then a GTPase Ras of complex proteins (ROC) domain, followed by a C-terminal of ROC (COR) domain, a serine/threonine kinase domain, and then at the C-terminus, a WD-40 domain (Lesage et al. 2007).

The two enzymatic domains of LRRK2 are intrinsically regulated in a highly complex manner. Biochemical studies where LRRK2 mutant proteins were overexpressed have demonstrated that GTP binding and hydrolysis, and LRRK2 dimerisation, are essential for kinase activity (Ito et al. 2007; Biosa et al. 2013; Sen et al. 2009). This kinase activity results in autophosphorylation of the protein at multiple residues, mutation of which result in decreased kinase activity and GTP binding (Webber et al. 2011). Furthermore, LRRK2 is capable of forming a dimer in solution, and this dimerisation has been shown to be dependent on the protein's capacity for kinase activity and GTP binding, but not GTP hydrolysis (Biosa et al. 2013). LRRK2 dimers demonstrate increased kinase and GTPase activity in comparison to monomers, and are thought to be enriched at cell membranes (Berger et al. 2010).

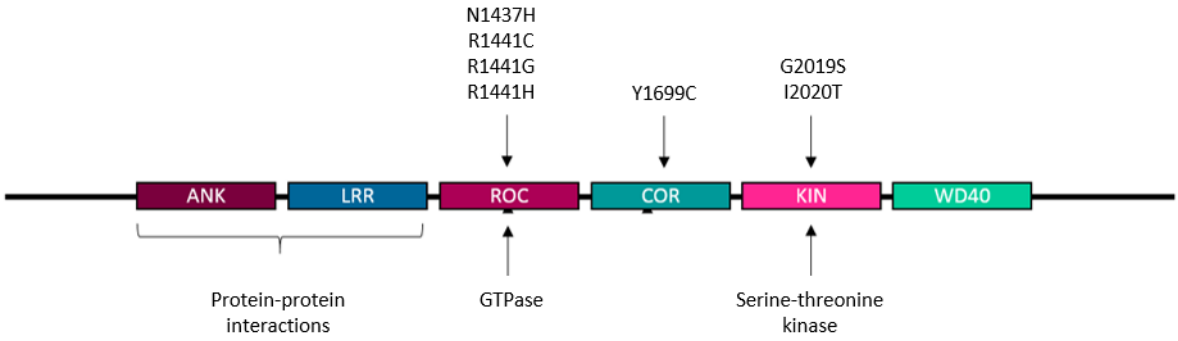

Figure 1.5. LRRK2 structure.
Schematic showing the domains of LRRK2 and their functions, including locations of PD pathogenic mutations, which have been identified in multiple kindreds by multiple research teams. Abbreviations: ANK: ankyrin repeat; LRR: leucine-rich repeat; ROC: ras of complex proteins; COR: C-terminal of ROC; KIN: kinase.

1.3.3. Effect of LRRK2 mutations on enzymatic activity

Seven monogenic *LRRK2* mutations have been identified as truly pathogenic in relation to PD, by their presence in multiple kindreds and identification by multiple research teams. All seven

cluster around the catalytic domains of the protein (Figure 1.5). Both the G2019S and I2020T mutations are located in the kinase domain, and have been reproducibly shown to increase kinase activity (Gloeckner et al. 2006; Anand et al. 2009; Biosa et al. 2013; Kamikawaji et al. 2013; Ray et al. 2014). Due to this finding, LRRK2 kinase inhibition is being widely explored as a potential treatment for PD (Chan and Tan 2017); however, there is no conclusive evidence that mutations outside of the kinase domain have the same effect on activity. Mutations in the ROC-COR GTPase domain, R1441C/G/H and Y1699C, have been shown to decrease GTP hydrolysis (Lewis et al. 2007; Li et al. 2007; Daniels et al. 2011; Liao et al. 2014), whereas the protective LRRK2 variant, R1398H, exhibits increased GTP hydrolysis (Nixon-Abell et al. 2016), suggesting that GTPase activity is just as important as kinase activity for normal LRRK2 function.

1.3.4. Cellular function of LRRK2

LRRK2 has been shown to contribute to a wide range of cellular functions including neurite growth, protein degradation, mitochondrial clearance, synaptic activity, and vesicle trafficking.

i) LRRK2 and the control of neurite growth

Neurite outgrowth is important for formation of complex neuronal networks during brain development. Many studies have shown that when overexpressed, the LRRK2-G2019S mutant results in reduced neurite outgrowth (Macleod et al. 2006; Gandhi et al. 2008; Parisiadou et al. 2009; Dachsel et al. 2010; Lin et al. 2010; Winner et al. 2011). However, when the mutation is expressed at physiological levels in rodent cells, this phenotype is not present (Daschel et al. 2010; Garcia-Miralles et al. 2015). It was therefore suggested that neurite outgrowth may only be impacted when mutant LRRK2 is present at high levels (Daschel et al.

2010). It has since been shown, however, that physiological levels of LRRK2-G2019S expression in patient iPSC-derived DA neurons result in neurite shortening (Sanchez-Danes et al. 2012a; Reinhardt et al. 2013; Su et al. 2013; Borgs et al. 2016), suggesting that this phenotype is a true effect of the mutation in human cells.

Neurite outgrowth phenotypes have been in part explained by the ability of LRRK2 to bind cytoskeletal proteins including Ezrin, Radixin, Moesin (ERM proteins) (Jaleel et al. 2007; Parisiadou et al. 2009), Tubulins (Gandhi et al. 2008, Law et al. 2014), and Microtubule-associated protein Tau (Tau) (Kawakami et al. 2012) (Figure 1.6), as well as P21-Activated Kinase 6 (PAK6) (Civiero et al. 2015), Vimentin (VIM), and Sec1 family domain-containing protein 1 (SCFD1) (Daschel et al. 2007). Furthermore, LRRK2 can phosphorylate ERM proteins and tubulin-associated Tau (Figure 1.6). Overexpression of LRRK2 mutants has been shown to disrupt its interaction with Tubulins (Law et al. 2014), leading to formation of microtubule-associated filamentous structures (Kett et al. 2012; Godena et al. 2014), and increased Tau and ERM protein phosphorylation (Parisiadou et al. 2009; Lin et al. 2010; Kawakami et al. 2012). The majority of these pathways have been uncovered either *in vitro*, or in overexpression systems, and are yet to be explored in models that express physiological levels of mutant LRRK2 protein.

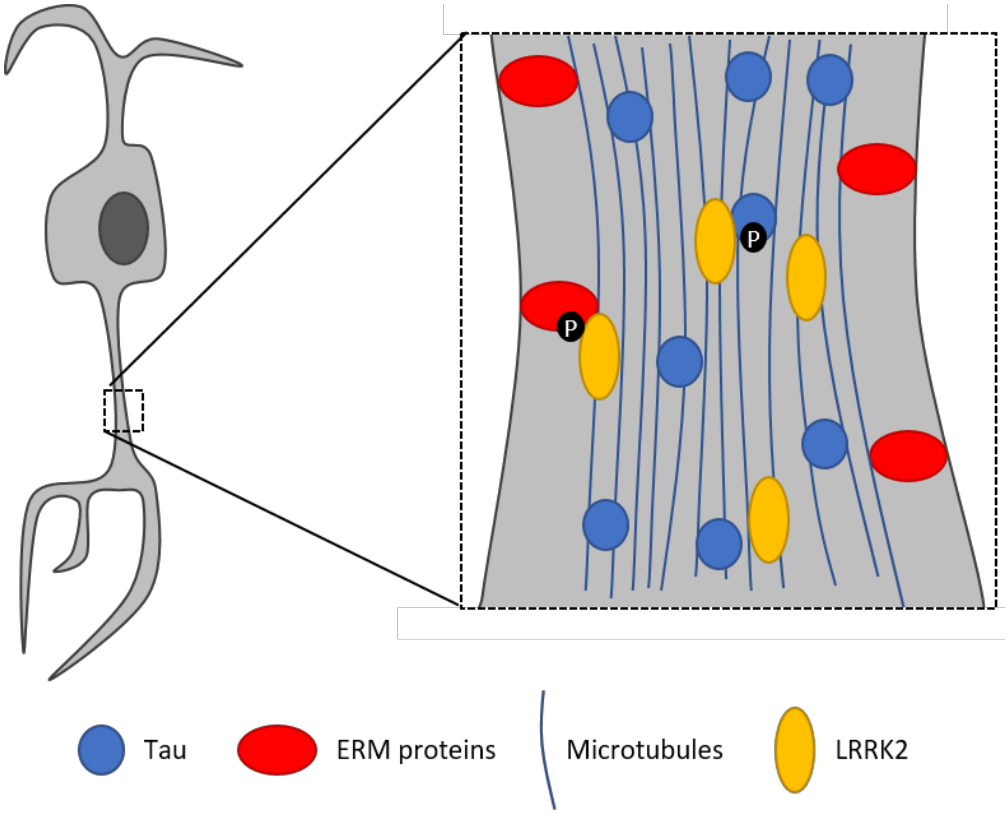

Figure 1.6. Interaction of LRRK2 with cytoskeletal proteins.
LRRK2 has been demonstrated to interact with ERM proteins, Tau, and microtubules, and to phosphorylate ERM proteins and Tau.

ii) LRRK2 and the autophagy-lysosome pathway

Autophagy is a process that cells use to degrade damaged or unnecessary components (De Duve 1963). It has been widely implicated in PD, with PD-causing mutations in *LRRK2*, *SNCA*, *GBA*, *ATP13A2*, *PINK*1, *PRKN*, and *PARK7*, having been implicated in its regulation (Zhang et al. 2014). This pathway is known to proceed via three mechanisms. The first, known as macroautophagy, involves the encapsulation of the components to be degraded into vesicles called autophagosomes, which then fuse with lysosomes to form autolysosomes, and enzymatically degrade their contents (De Duve 1963) (Figure 1.7A). The second, known as chaperone-mediated autophagy (CMA), involves direct chaperoning of proteins possessing a specific recognition sequence to the lysosome for degradation (Arias and Cuervo 2011)

(Figure 1.7B). A third mechanism, which has not yet been implicated in PD, is microautophagy (De Duve and Wattiaux 1966), whereby cellular components are degraded by direct lysosomal engulfment.

Although a wealth of evidence points towards a role for LRRK2 in autophagy, its precise involvement in this process is still not clear. There are contradictory reports regarding the nature of the effect of *LRRK2* mutations on macroautophagy. Many studies show that heterozygous *LRRK2* mutations, whether overexpressed or present at physiological levels, lead to increased autophagic content, as measured by immunostaining for Microtubule-Associated Proteins 1A/1B Light Chain 3B (LC3) or WD-repeat Protein Interacting with Phosphoinositides (WIPI) puncta, blotting for LC3 lipidation (LC3-II), or characterisation by electron microscopy (Plowey et al. 2008; Xiong et al. 2010; Ramonet et al. 2011; Sanchez-Danes et al. 2012a; Bravo-San Pedro et al. 2013; Cherra et al. 2013; Su et al. 2013; Grünewald et al. 2014; Saha et al. 2014; Yakhine-Diop et al. 2014). However, multiple other studies have reported no effect of LRRK2 mutations on basal autophagy (Herzig et al. 2011; Manzoni et al. 2013a; Orenstein et al. 2013; Yue et al. 2015). In addition to reports on autophagic vesicle content, it has been demonstrated that *LRRK2* mutations result in either enlarged, or increased numbers of lysosomes, along with increased levels of the lysosomal proteins Lysosomal-Associated Membrane Protein 1 (LAMP1) and/or 2 (LAMP2) (Orenstein et al. 2013; Su et al. 2013; Saha et al. 2014; Henry et al. 2015; Hockey et al. 2015).

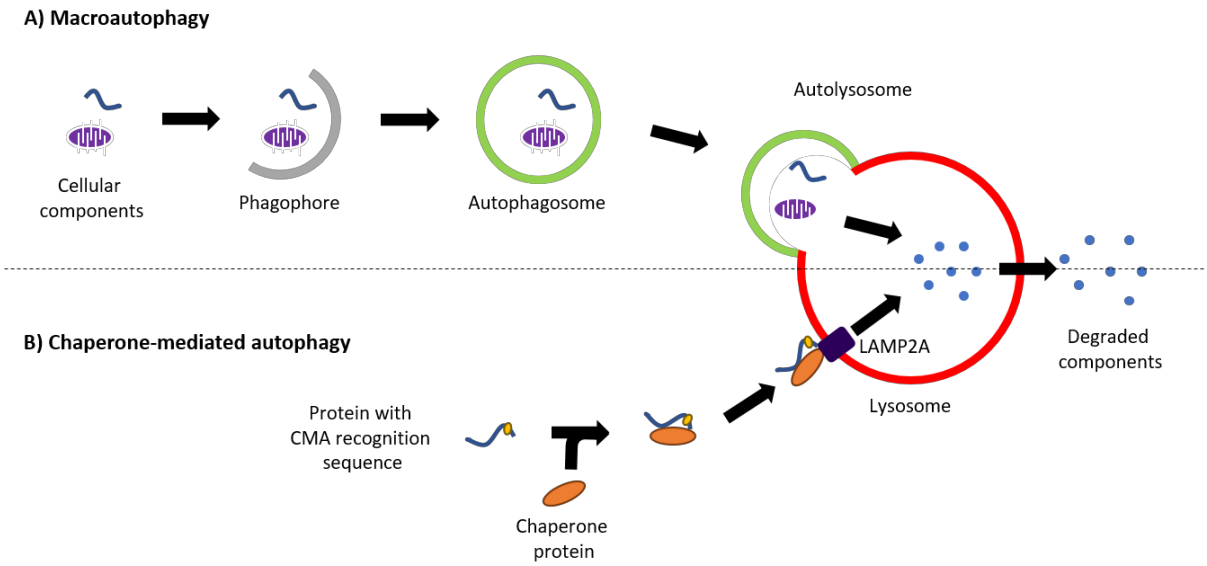

Figure 1.7. The autophagy pathway.
Degradation of cellular component can be achieved through autophagy. LRRK2 has been implicated in two of the autophagy pathways, A) macroautophagy, and B) chaperone-mediated autophagy. A) Macroautophagy involves the encapsulation of cellular components into a phagophore, which matures into an autophagosome. This then fuses with a lysosome, to form an autolysosome, which degrades the cellular components. B) Chaperone-mediated autophagy is a selective process for degradation of proteins that possess a specific consensus sequence. These proteins are bound by a chaperone protein and trafficked directly to the lysosome, where they are taken up via LAMP2A for degradation.

Complexities arise when it comes to interpreting cellular levels of autophagic puncta and proteins; it is very difficult to ascertain whether an increase in autophagic or lysosomal content is due to increased autophagy, with more vesicles being produced at a time, or inhibited autophagy, where vesicles remain in the cell for longer due to a blockage in the system. Some of the studies discussed have analysed cells in the presence and absence of autophagy inhibitors or activators to clarify the effects of LRRK2 in their models. Using this method, it has been shown that knockdown, or inhibition of LRRK2 results in increased autophagic vesicle formation (Manzoni et al. 2013b; Manzoni et al. 2016) and flux through the system (Alegre-Abarrategui et al. 2009; Manzoni et al. 2013b; Manzoni et al. 2016). However, a separate study found that LRRK2 kinase inhibition increased autophagic vesicle

production, but also resulted in a blockage of fusion with the lysosome (Saez-Atienzar et al. 2014). The LRRK2-G2019S mutation has been shown by two studies to increase autophagosome formation; however, one found that this was coupled with an increase in autophagic flux (Bravo san Pedro et al. 2013), whereas the other showed a decrease in autophagic flux (Sanchez-Danes et al. 2012a). A third study found that in LRRK2-G2019S patient fibroblasts, where basal autophagy was unaffected by the presence of the mutation, induction of autophagy in response to starvation was impaired (Manzoni et al. 2013a).

Although there are mixed reports regarding the effects of LRRK2 on the autophagy-lysosome pathway, a number of mechanisms for its interaction with the pathway have been described. LRRK2 has been suggested to affect autophagosome formation via an mTOR-independent, Beclin-1-mediated pathway (Manzoni et al. 2016). Other studies have found that LRRK2 interacts with the lysosome via NAADP receptors, namely Two-Pore Calcium Channel 2 (TPC2), and that LRRK2-mediated changes in lysosome number and protein levels could be reversed using TPC2 inhibitors, or TPC2 inactive mutants (Gomez-Suaga et al. 2012; Hockey et al. 2015). Orenstein et al. also demonstrated that a proportion of wildtype (WT) LRRK2 is degraded by CMA, but that the G2019S and R1441C mutations result in a low efficiency of chaperoning, and blockage at the lysosome (Orenstein et al. 2013). It has been shown that Ubiquitin Binding Protein P62/Sequestosome (P62), which binds to ubiquitin-tagged proteins and targets them to the autophagosome, binds LRRK2 to regulate its stability (Park et al. 2016). Furthermore, this study also demonstrated that the presence of LRRK2 reduces phosphorylation of P62, decreasing its affinity for ubiquitin-tagged proteins, which results in decreased protein degradation via macroautophagy (Park et al. 2016).

The LRRK2-G2019S mutation has also been shown to increase phosphorylation of the Mitogen Activated Protein Kinases (ERK1/2) (Bravo-San Pedro et al. 2013). Small-molecule inhibition of ERK1/2 using U0126 resulted in normalisation of autophagic/lysosomal content in two studies (Plowey et al. 2008; Bravo-San Pedro et al. 2013). Additionally, a study of iPSC-derived vmDA neurons carrying the LRRK2-G2019S mutation also demonstrated transcriptomic changes in the ERK pathway (Reinhardt et al. 2013). In this model, they found that the G2019S mutation resulted in increased levels of p-ERK1/2, although they did not investigate implications for autophagy. Further studies are needed to clarify how physiological levels of LRRK2 modulate autophagy, and what impact LRRK2 mutations have on this pathway.

iii) LRRK2, mitochondria, and mitophagy

Starting in 1979, a series of accidental exposures to the mitochondrial toxin MPTP were found to induce Parkinsonism in humans (Davis et al. 1979; Langston et al. 1983; Ballard et al. 1985). MPTP is metabolised to MPP+, which is specifically taken up into DA neurons via the dopamine transporter (DAT). Exposure resulted in DA neuron degeneration and permanent Parkinsonism in the affected individuals. Since this discovery, recessive PD-causing mutations have been found to occur in *PINK1* and *PRKN*, which have been widely demonstrated to play a role in mitophagy (Eiyama and Okamoto 2015). Furthermore, other PD-causing mutations in *LRRK2*, *SNCA*, and *PARK7* have also been implicated in mitochondrial dysfunction (Bose and Beal 2016).

Many studies have investigated the role of LRRK2 in mitochondrial function. LRRK2 mutations have been shown to affect mitochondrial content (Cherra et al. 2013; Su et al. 2013; Zhu et al 2013; Grunewald et al. 2014), fragmentation (Niu et al. 2012; Wang et al. 2012, Su et al. 2013; Grunewald et al. 2014; Saez-Atienzar et al. 2014), membrane potential (MMP) (Mortiboys et

al. 2010; Cherra et al. 2013; Grunewald et al. 2014; Hsieh CH et al. 2016) oxygen consumption (Cooper et al. 2012; Papkovskaia et al. 2012; Mortiboys et al. 2015), and to induce mitochondrial DNA (mtDNA) damage (Sanders et al. 2014) (Figure 1.8). In many cases, these changes were associated with perturbations in autophagy (Su et al. 2013; Cherra et al. 2013; Zhu et al. 2013; Grunewald et al. 2014; Hsieh et al. 2016), leading to the suggestion that LRRK2 plays a role in initiating mitochondrial degradation by autophagy (mitophagy). Studies provide mixed reports regarding the effects of LRRK2 mutations on mitochondrial function and mitophagy; the G2019S mutation has been demonstrated to both increase (Cherra et al. 2013; Su et al. 2013; Zhu et al. 2013) and decrease (Hsieh et al. 2016) levels of mitochondrial clearance via this process. Concurrent changes in autophagy and mitochondrial function in response to LRRK2 mutations may originate from autophagic dysfunction (see section 1.3.4.ii) or mitochondrial dysfunction. Autophagic dysfunction may result in increased reactive oxygen species production, which then leads to mitochondrial dysfunction and dysfunctional mitophagy, or mitochondrial dysfunction may lead to an overload of unhealthy mitochondria, which results in an overload of the autophagy pathway.

A number of mechanisms have been proposed regarding LRRK2's effects on mitochondria. Two studies have demonstrated that LRRK2 interacts with Dynamin-Like Protein 1 (DLP1), (Wang et al. 2012; Niu et al. 2012), which is important for mitochondrial fission. These studies also found increased DLP1 levels in the presence of LRRK2 mutations (Figure 1.8). However, a third study found no evidence of an interaction (Papkovskaia 2012). Another hypothesis is that LRRK2 mutations may exert their effect upon mitochondria by disturbing the mitochondrial electron transport chain. Mitochondrial Uncoupling Proteins 2 (UCP2) and 4 (UCP4) were found to be upregulated in cells expressing the LRRK2-G2019S mutation

(Papkovskaia et al. 2012; Grunewald et al. 2014) (Figure 1.8). These proteins promote uncoupling of the mitochondrial electron transport chain, and their increased expression may explain the increased proton leakage and decreased MMP that have been reported in multiple models. Furthermore, changes have been detected in the expression levels and activities of various mitochondrial electron chain complexes (Mortiboys et al. 2010; Mortiboys et al. 2015; Yue et al. 2015), suggesting that this system is perturbed by LRRK2 mutations.

A separate study utilising PD patient fibroblasts and iPSC-derived DA neurons has suggested that *LRRK2* mutations result in a delayed induction of mitophagy due to inhibition of LRRK2-mediated removal of Mitochondrial Rho GTPase 1 (MIRO1) from the surface of the mitochondria (Hsieh et al. 2016). MIRO1 anchors mitochondria to microtubules, and its removal is necessary for mitophagy to occur. Cells from patients with *PINK1* mutations or sporadic PD were found to exhibit the same impaired degradation of MIRO1 as the *LRRK2* mutant lines, suggesting that this could be a common pathogenic mechanism in PD.

A number of appealing mechanisms for LRRK2's involvement in mitochondrial health have been proposed; however, there are still conflicting reports regarding the consequences of *LRRK2* mutations for mitochondrial regulation. As such, further research is necessary to improve our understanding of this aspect of LRRK2 biology.

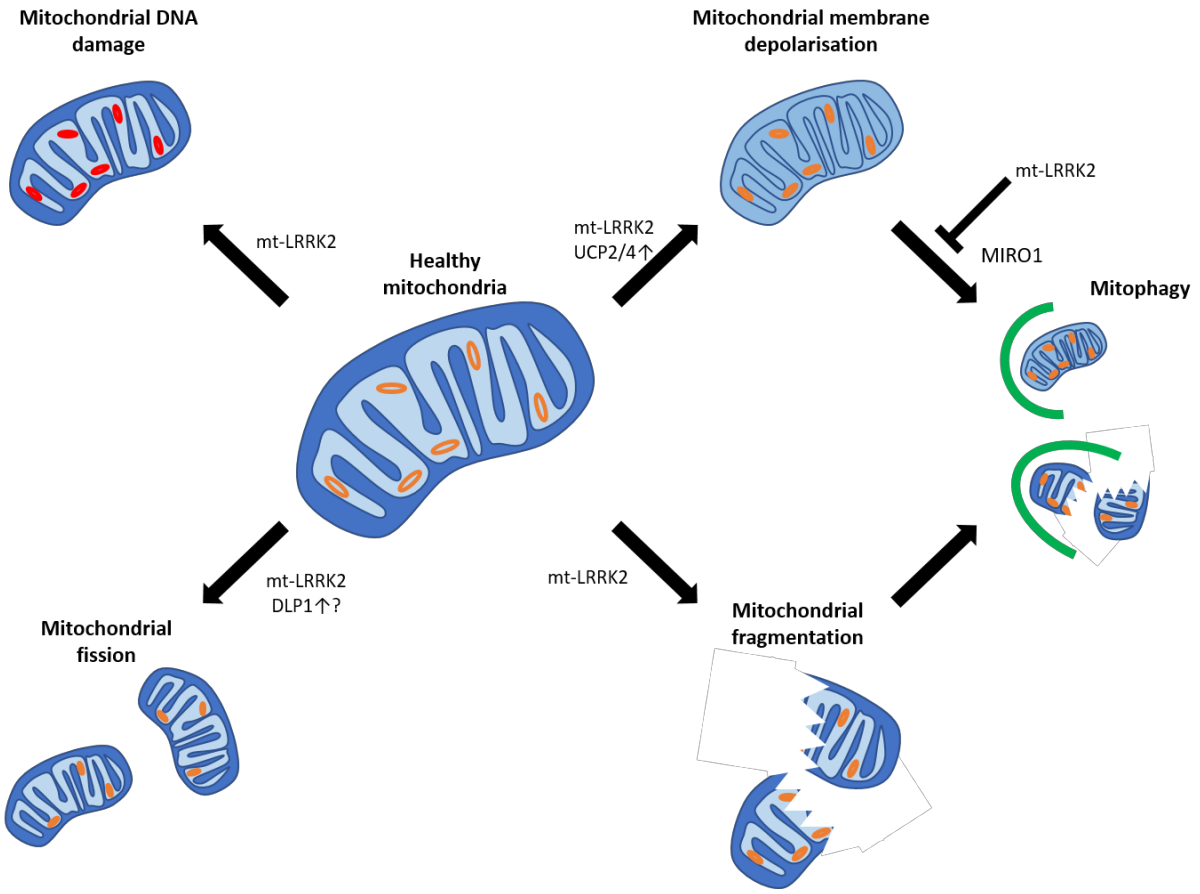

Figure 1.8. Effects of mutant LRRK2 on mitochondrial health.
LRRK2 mutant protein (mt-LRRK2) has been demonstrated to result in a number of mitochondrial phenotypes including mitochondrial DNA damage, excessive mitochondrial fission (potentially via increased DLP1), mitochondrial membrane depolarisation (via increased UCP2), and mitochondrial fragmentation. Furthermore, mt-LRRK2 has been demonstrated to inhibit MIRO1-mediated mitophagy in response to mitochondrial membrane depolarisation.

iv) LRRK2 at the synapse

PD models have brought attention to the role of synaptic dysfunction in the disease (Plowey and Chu 2011; Picconi et al. 2012). WT LRRK2 has been demonstrated to play a role in normal synaptic function; KO of LRRK2 in primary neuronal cultures has shown that the WT protein is involved in the control of action-potential firing rates, with the KO demonstrating slightly decreased inter-event intervals (Piccoli et al. 2011; Beccano-Kelly et al. 2014; Parisiadou et al. 2014). Action potential amplitude is also increased in LRRK2 KO models, suggesting that WT LRRK2 also controls this aspect of synaptic function (Picolli et al. 2011; Parisiadou et al. 2014).

LRRK2 mutations have been found to result in both glutamatergic and dopaminergic synaptic phenotypes. Expression of LRRK2-G2019S and -R1441C mutants leads to an increase in excitatory synaptic activity in mouse primary cortical (Plowey et al. 2014; Beccano-Kelly et al. 2014) and hippocampal (Maas et al. 2017) neuron cultures, as well as in striatal slice cultures taken from young mice (Matikainen-Ankney et al. 2016). Such excitatory phenotypes have been shown to lead to excitotoxicity via glutamate-mediated calcium entry through *N*-methyl-D-aspartate (NMDA) receptors and to result in cell death (Sattler et al. 1998; Koutsilieri and Riederer 2007). Dopaminergic phenotypes have been identified in aged animals in a number of studies; LRRK2 G2019S- and R1441C BAC-transgenic rats (Sloan et al. 2016), R1441G BAC-transgenic mice (Li et al. 2009), and G2019S-KI mice (Yue et al. 2015), all develop an age-related deficit in striatal dopamine release. Furthermore, I2020T-mutant iPSC-derived DA neuron cultures exhibited decreased dopamine release (Ohta et al. 2015). These changes all suggest that LRRK2 mutations interrupt the proper functioning of synaptic machinery.

In the search for a mechanistic explanation for these findings, studies have implicated LRRK2 in synaptic vesicle endocytosis (Picolli et al. 2011; Matta et al. 2012; Picolli et al. 2014; Arranz et al. 2015; Maas et al. 2017). Endophilin A, which plays a key role in this process, has been identified as a substrate of the *Drosophila* LRRK2 ortholog, Lrrk, under physiological conditions, and of human LRRK2 in the presence of both copies of *Drosophila* Lrrk, as well as *in vitro* (Matta et al. 2012; Arranz et al. 2015). Furthermore, both the LRRK2-G2019S mutation and *Drosophila* Lrrk loss-of-function mutants were shown to result in impaired synaptic-vesicle endocytosis, due to too much, or too little, phosphorylation of Endophilin A respectively. Lrrk2 KO mice exhibit a similar phenotype, suggesting that this process may be conserved amongst species (Arranz et al. 2015).

LRRK2 has also been shown to interact with a number of other synaptic proteins. Experiments using LRRK2 overexpression systems, or purified recombinant LRRK2 *in vitro*, have demonstrated interactions with proteins including Snapin (Yun et al. 2013), N-Ethylmaleimide-Sensitive Factor (NSF), Vesicle-Associated Membrane Protein 2 (VAMP2), Syntaxin-1A, Dynamin-1, and Mammalian Uncoordinated-18-1 (MUNC18-1) (Piccoli et al. 2011, Piccoli et al. 2014). Whether these interactions exist when LRRK2 is present at physiological expression levels is yet to be confirmed.

v) LRRK2 and vesicle trafficking

A common pathway that connects neurite growth, autophagy, mitophagy, and synaptic function, is vesicle trafficking (Tang and Edidin 2001; Sudhof 2004; Kern et al. 2015) (Figure 1.9). Multiple genetic mutations (in *LRRK2*, *SNCA*, Vacuolar Protein Sorting-Associated 35 (*VPS35*) and *DNAJC13*) and risk variants (in *GAK* and *RAB7L1*) identified in PD have been found to disrupt this pathway (Perrett et al. 2015). LRRK2 has been implicated in many different stages of vesicle trafficking. Firstly, as discussed in Section 1.3.4.iv, LRRK2 has been shown to regulate synaptic vesicle endocytosis via Endophilin A (Matta et al. 2012). Secondly, behavioural and pathological effects of LRRK2 overexpression in *Drosophila* can be modified by the overexpression of VPS35 (Macleod et al. 2013; Linhart et al. 2014), a component of the retromer complex, which mediates transport of cargo proteins from endosomes to the trans-golgi network (Bonifacino and Hurley 2008). Furthermore, when both proteins were overexpressed, LRRK2 was found to interact with VPS35 (Macleod et al. 2013). Thirdly, the ROC domain of LRRK2 was demonstrated to interact with Clathrin Light Chains (CLCs) (Schreij et al. 2015), which contribute to the clathrin coating of endocytic vesicles (Brodsky et al. 2001). Finally, LRRK2 has been shown to interact with multiple members of the Ras-Related

Protein (RAB) family, which consists of around 70 RAB proteins. These proteins are vitally important for the trafficking of vesicles within the cell (Stenmark 2009).

Evidence has been building that LRRK2 may play a key role in regulating RABs. Studies in a variety of models including patient samples, immortalised cell lines, and d*rosophila*, have demonstrated that LRRK2 colocalises with RAB7 in the late endosome (Higashi et al. 2009; Dodson et al. 2012; Gomez-Suaga et al. 2014). Furthermore, mutations in LRRK2 have been shown to result in reduced RAB7 expression, due to a delay in maturation of early endosomes (RAB5 expressing) to late endosomes (RAB7 expressing) (Gomez-Suaga et al. 2014). A number of studies in models where recombinant LRRK2 was used, or where the protein was overexpressed, have identified interactions between LRRK2 and RABs. These include interactions with RAB5B in early endosomes in HEK293 cells (Yun et al. 2015), RAB32 and RAB38 in late and recycling endosomes in yeast (Waschbüsch et al. 2014), and RAB7L1 in the autophagy/lysosome pathway in HEK293 cells and mouse brain lysates (Beilina et al. 2014). Whether these interactions exist at physiological expression levels in disease-relevant cell types is yet to be determined.

A recent study by Steger et al. conducted two parallel phosphoproteomics experiments, each with different methodologies, to find physiological LRRK2 substrates in MEFs (Steger et al. 2016). Only two proteins, LRRK2 itself and RAB10, were identified in both datasets. RAB10 was found to be phosphorylated at threonine 73 (T73), an amino acid that is highly conserved amongst RAB proteins. The T73 residue is located in the switch-II domain of the protein, which is essential for the interaction of RABs with other regulatory proteins (Pfeffer 2005). Eight of the 42 RABs possessing this conserved phosphorylation site were tested in an *in-vitro* kinase assay and were all phosphorylated by LRRK2 (Steger et al. 2016). In some family members,

threonine is substituted for a serine; it was found that RABs possessing a threonine residue (RAB1b, RAB8a, and RAB10) were more efficiently phosphorylated by LRRK2 than those possessing a serine residue (RAB5b, RAB7a, RAB7L1, RAB12, and RAB39b). Furthermore, LRRK2 pathogenic mutations were demonstrated to result in increased phosphorylation of RABs, disrupting their interaction with RAB GDP Dissociation Inhibitors α and β (GDI1 and GDI2). GDIs remove prenylated RABs from membranes and bind them in the cytosol (Pylypenko et al., 2003); impairment of this process could result in impaired vesicle trafficking, and may be a pathogenic mechanism of LRRK2 mutations.

Although Steger et al. found that other RABs were phosphorylated by LRRK2 *in vitro*, only RAB10 was reproducibly identified in their phosphoproteomics study in MEFs. They then went on to identify two RABs, RAB8 and RAB12, as LRRK2 kinase substrates in the brains of mice (Steger et al. 2016), and a second study has since identified RAB10 and RAB12 as LRRK2 kinase substrates in human peripheral blood mononuclear cells (PBMCs) (Thirstrup et al. 2017). It could therefore be the case that LRRK2 phosphorylates different RABs in different cellular contexts. This may go some way to explain the variation seen between model systems; however, more studies need to be conducted in models where LRRK2 is expressed at physiological levels in order to confirm this hypothesis.

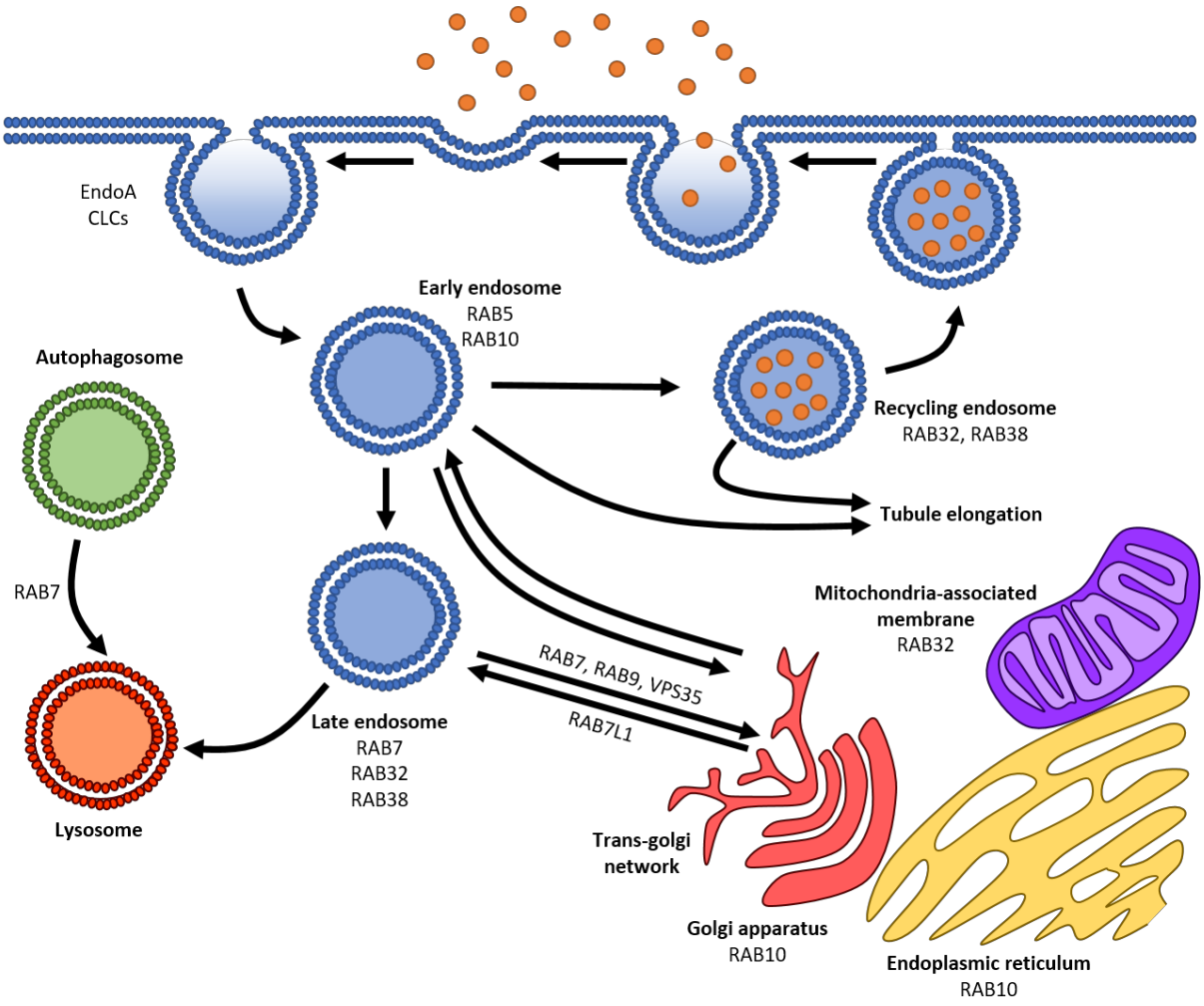

Figure 1.9. Interaction of LRRK2 with proteins involved in vesicle trafficking.
Schematic detailing vesicle trafficking pathways in the cell, noting only proteins that LRRK2 has been demonstrated to interact or colocalise with. Abbreviations: CLCs: Clathrin Light Chains, EndoA: Endophilin A.

vi) LRRK2 in iPSC-derived vmDA-neuron cultures

The development of iPSCs has provided a platform for studying LRRK2 in cell types that are specific to PD, and where human LRRK2 is expressed at physiological levels. To date, no studies of LRRK2 have been conducted in iPSC-derived astrocytes; however, multiple studies have been conducted in iPSC-DA and iPSC-vmDA neuron cultures. These have uncovered a variety of phenotypes.

One of the most consistent phenotypes across these studies is a reduction in neurite growth due to the presence of the G2019S mutation (Sanchez-Danes et al. 2012a; Reinhardt et al. 2013; Su et al. 2013; Borgs et al. 2016). This phenotype could be reversed either by ERK inhibition (Reinhardt et al. 2013), or DLP1 inhibition (Su et al. 2013), suggesting that LRRK2 may be involved in ERK signalling or mitochondria fission respectively. Perturbation of either of these pathways may put stress on the cell, resulting in the observed neurite phenotype. Further evidence of LRRK2's role in the cytoskeleton has been demonstrated in iPSC-DA neurons carrying the I2020T mutation, which exhibited increased Glycogen synthase kinase 3 beta (GSK3β)-mediated phosphorylation of the cytoskeletal protein Tau (Ohta et al. 2015).

Autophagy phenotypes were also found in some studies, but mechanisms were not investigated in great depth in the iPSC-DA neuron cultures. Increases in levels of the autophagic vesicle marker LC3-II were observed in the presence of the G2019S and I2020T mutants (Sanchez-Danes et al. 2012a; Ohta et al. 2015), and were associated with an increase in autophagosome number, a decrease in autolysosome number, and a decrease in autophagic flux (Sanchez-Danes et al. 2012a). Changes at the lysosome in the presence of the G2019S mutation have also been observed; one study found that LAMP2 levels were increased (Su et al. 2013), whereas another demonstrated increased colocalisation of α-Synuclein with LAMP2 (Orenstein et al. 2013).

A number of mitochondrial phenotypes have been described in iPSC-derived DA neuron cultures from patients with LRRK2 mutations. Multiple studies have found that LRRK2-mutant expressing iPSC-derived DA-neuron cultures undergo enhanced cell death in response to mitochondrial toxins and oxidative stressors (Nguyen et al. 2011; Cooper et al. 2012; Reinhardt et al. 2013; Ohta et al. 2015). Increased bidirectional mitochondrial shuttling along

axons has also been observed, and is suggestive of dysfunctional cytoskeletal trafficking of the mitochondria (Cooper et al. 2012). Additionally, decreases in mitochondrial length and mitochondrial membrane potential have been found (Cooper et al. 2012; Su et al. 2013), suggesting that mitochondrial health is affected. It has also been shown that mitophagy is impaired in cells expressing the G2019S and R1441C mutations (Hsieh et al. 2016) (see Section 1.3.4.iii). Furthermore, extensive mitochondria DNA damage has been detected in cells expressing the G2019S mutation (Sanders et al. 2014).

Only one study thus far has measured synaptic function in LRRK2-mutant iPSC-DA neuron cultures (Ohta et al. 2015). It was found that the I2020T mutation resulted in a decrease in neuronal dopamine release. This agrees with findings in aged animal models expressing the G2019S mutation (see Section 1.3.4.iv).

A key feature of PD is aggregation of α-Synuclein in Lewy bodies. Although no such aggregates have been found in iPSC-DA neuron cultures, changes in α-Synuclein levels have been detected. Five studies found increased α-Synuclein levels in mutant cultures, one of which demonstrated increased localisation of α-Synuclein to lysosomes in the presence of the G2019S mutation (Nguyen et al. 2011; Sanchez-Danes et al. 2012a; Orenstein et al. 2013; Reinhardt et al. 2013; López de Maturana et al. 2016).

Whole-transcriptome and -methylome analyses have been conducted to study the effects of LRRK2 mutations in iPSC-DA neuron cultures (Reinhardt et al. 2013; Fernández-Santiago et al. 2015; Sandor et al. 2017). These have revealed that the LRRK2-G2019S mutation results in changes in signalling downstream of ERK phosphorylation (Reinhardt et al. 2013), as well as aberrant DNA methylation that is specific to dopaminergic neurons (Fernández-Santiago et al. 2015).

The findings from iPSC-derived DA-neuron models to date demonstrate that a wide range of LRRK2-mutant phenotypes can be detected in these cultures, many of which support findings from other model systems. Early studies focussed on defining phenotypes in these cultures; however more recent work has begun to interrogate the mechanisms underlying these changes. Due to the wide range of phenotypes that have been identified, it is important that further studies are conducted to clarify the cellular effects of LRRK2 mutations. Although LRRK2 is a large multi-domain protein, it is unlikely to act directly upon so many different pathways. The phenotypes observed across studies may represent different manifestations of cellular dysfunction that stem from the effects of the LRRK2 mutations upon the same few pathways, but that are observed under different conditions or at different stages of pathogenesis in different models. It is important that more research be conducted to understand what pathways LRRK2 directly impacts upon to result in this vast array of observed phenotypes.

The majority of the studies described in this section utilise iPSC-neuron cultures that contain a low percentage of DA neurons (5-20%), and an even lower percentage of vmDA neurons (typically 2-10%). Many of the assays conducted take measurements from the whole culture, so it can be difficult to attribute phenotypes specifically to the neurons of interest. To combat this, future studies will need to use cultures that are more highly enriched for vmDA neurons. This will better enable the study of disease phenotypes that are specific to this cell type. Furthermore, it will also be important for researchers to derive other midbrain-specific cell types such as astrocytes from patient iPSCs. Such studies will improve our understanding of how LRRK2 mutations affect different cell types, and whether LRRK2-PD pathogenesis arises from vmDA neurons themselves, or from non-cell-autonomous effects.

1.4. Aims of this thesis

1. To optimise and validate protocols for the differentiation of ventral-midbrain dopaminergic (vmDA) neurons and midbrain-patterned (MP) astrocytes from human iPSCs.

2. To carry out hypothesis-driven, functional analysis of vmDA neurons and MP astrocytes derived from iPSCs from patients carrying the LRRK2-G2019S mutation, to identify disease phenotypes.

3. To take an unbiased approach, utilising proteomics and transcriptomics methods, to identify cellular pathways perturbed by the LRRK2-G2019S mutation in iPSC-derived vmDA neurons and MP astrocytes.

Chapter 2: Materials and methods

2.1. Cell culture

2.1.1. Maintenance of iPSC lines

Cell culture plates were coated for a minimum of 60 min at 37°C with Matrigel (Corning) diluted in KO DMEM (ThermoFisher Scientific). Each vial of iPSCs was thawed rapidly at 37°C, diluted 1:10 in DPBS -$CaCl_2$/-$MgCl_2$ (DPBS-/-), centrifuged at 400 xg for 5 min at room temperature, and resuspended in 2 mL mTesR1 medium (Stem Cell Technologies). Cells were then plated into one well of a Matrigel-coated 6-well plate, and cultured in a cell culture incubator at 37°C/5% CO_2/95% humidity. Cells were maintained as colonies in mTesR1 medium (Stem Cell Technologies) supplemented with Penicillin (100 U/mL)-Streptomycin (100 µg/mL) (1X PenStrep) (ThermoFisher Scientific) and passaged once confluent. To passage, cells were washed once with DPBS-/- (ThermoFisher Scientific), then once with 500 µM EDTA, and then incubated in 500 µM EDTA for 5 min at 37°C. EDTA was removed from the well, and colonies were resuspended in 2 mL mTesR1 medium and transferred to fresh wells.

2.1.2. The Fernandes protocol for differentiation of vmDA neurons

Differentiation of iPSCs was carried out as previously described (Fernandes et al. 2016), and as follows. Aggrewell 800 plates (Stem Cell Technologies) were prepared according to the manufacturer's instructions, and 1 mL mTesR1 medium (Stem Cell Technologies) supplemented with Y27632 (10 µM) added per well. iPSCs were washed 1x with DPBS-/-, then incubated with TrypLE express (ThermoFisher Scientific) for 5 min at 37°C to dissociate. Cells were transferred to a 15 mL tube containing DPBS-/-. An aliquot was taken from each cell line

for counting, then samples were centrifuged at 400 xg for 5 min. Cells were resuspended to a concentration of $4x10^6$ cells/mL and 1 mL of the suspension was added to each pre-prepared Aggrewell for embryoid body (EB) formation. Cultures were maintained in a cell culture incubator at 37°C/5% CO_2/95% humidity throughout the differentiation protocol. EBs were cultured according to the manufacturer's instructions in mTesR1 medium supplemented with 1X PenStrep and Y27632 (10 µM), and harvested after 4 days. Harvested EBs (~50 per well) were plated onto 6-well plates coated with Geltrex (ThermoFisher Scientific) in Neural induction medium (DMEM/F12 (ThermoFisher Scientific), 1X N2 supplement (ThermoFisher Scientific), 2 mM L-Glutamine (ThermoFisher Scientific), 1mg/mL BSA (Sigma), 1% v/v antibiotic-antimycotic (ThermoFisher Scientific)) supplemented with 10 µM Y26732 (Tocris), 100 nM LDN-193189 (Pfizer), 10 µM SB-431542 (Tocris), 500 ng/mL Recombinant Human Sonic Hedgehog/SHH C24II N-Terminus (SHH C24II) (R&D Systems), and 700 nM CHIR99021 (Tocris), at 0 DIV. Cells were maintained in this medium until 12 DIV, with medium changes every two days. At 12 DIV, medium was changes to neural induction medium supplemented with 10 µM Y26732, 20 ng/mL SHH C24II, 100 ng/mL Fibroblast growth factor 8a (FGF8a) (R&D Systems), 5 µg/mL Heparin (Sigma), 20 ng/mL Brain-Derived Neurotrophic Factor (BDNF) (Peprotech), and 200 µM ascorbic acid (Sigma). Cells were maintained in this medium for a further 8 days, with medium changes every two days. At 20 DIV, neural rosettes were manually dissected and plated onto Geltrex-coated plates and coverslips in neural induction medium supplemented with 10 µM Y26732, 20 ng/mL BDNF, 20 ng/mL Glial-Derived Neurotrophic Factor (GDNF) (Peprotech), 500 µM N6,2'-O-Dibutyryladenosine 3',5'-cyclic monophosphate sodium salt (db-cAMP) (Sigma), and 1 µg/mL Laminin (ThermoFisher Scientific). Cells were maintained for a further 15 days in this medium.

2.1.3. The Booth-Zambon protocol for differentiation of vmDA neurons

Differentiation of iPSCs was carried out as previously described (Kriks et al. 2011), with minor modifications, and as follows. Two days before the start of the differentiation, confluent iPSCs were washed once with DPBS-/- and then incubated with Tryple Express (ThermoFisher Scientific) for 5 min at 37°C to dissociate. Cells were then resuspended in DPBS-/- and centrifuged at 400 xg for 5 min to pellet. Supernatant was aspirated and cells were resuspended in mTesR1 medium supplemented with 10 µM Y26732. Cells were then plated as single cells on plates coated with 18 µg/mL Geltrex at $1.5x10^5$ cells/cm^2. Cultures were maintained in a cell culture incubator at 37°C/5% CO_2/95% humidity throughout the differentiation protocol. The next day the medium was replaced to remove Y26732. From 0 DIV cells were grown in KO DMEM KSR medium (KO DMEM, 15% knockout serum replacement, 2 mM L-Glutamine, 100 µM non-essential amino acids (all ThermoFisher Scientific), and 10 µM β-mercaptoethanol (Sigma)) which was switched in 25% increments every two days to NNB medium (Neurobasal, 0.5x N2 supplement, 0.5x B27 supplement without vitamin A, and 2mM-L-Glutamine (all ThermoFisher Scientific)) between 5-9 DIV, from 11 DIV cells were grown in NB medium (Neurobasal, 1x B27 supplement without vitamin A, 2 mM L-Glutamine (all ThermoFisher Scientific)). Medium was supplemented with the following factors: 100nM LDN-193189 at 0–11 DIV; 10 µM SB-431542 at 0–5 DIV; 100 ng/mL SHH C24II, 2 µM Purmorphamine (Millipore), and 100ng/mL FGF8a at 1–7 DIV; 3 µM CHIR99021 at 3–13 DIV; 20 ng/mL BDNF, 20 ng/mL GDNF, 1 ng/mL Transforming Growth Factor β3 (TGFβ3) (Peprotech), 10 µM DAPT (Abcam), 200 µM ascorbic acid, and 500 µM db-cAMP at 11–20 DIV. On DIV 20, cells were washed once with DPBS-/- then incubated with Accutase (ThermoFisher Scientific) at 37°C for 10 min, or until dissociated, then resuspended in NB medium. Cells were then centrifuged at 500 xg for 5 min to pellet. Supernatant was

removed and the cell pellet was resuspended in final medium (NB medium supplemented with 20 ng/mL BDNF, 20 ng/mL GDNF, 1 ng/mL TGFβ3 (Peprotech), 10 µM DAPT (Abcam), 200 µM ascorbic acid, 500 µM db-cAMP) supplemented with 10 µM Y26732. Cells were replated at various densities (150,000-500,000 cells/cm^2) depending on the experiment, onto plates or coverslips coated with Geltrex. On DIV 22 cells were treated with 1 µg/mL Mitomycin C (Sigma) for 60 min at 37°C to inactivate any proliferating cells. Cells were maintained for the desired culture duration with half media changes three times a week.

2.1.4. The Booth protocol for differentiation of MP astrocytes

Two days before the start of the differentiation, confluent iPSCs were washed once with DPBS-/- and then incubated with Tryple Express for 5 min at 37°C to dissociate. Cells were then resuspended in DPBS-/- and centrifuged at 400 xg for 5 min to pellet. Supernatant was aspirated and cells were resuspended in mTesR1 medium supplemented with 10 µM Y26732. Cells were then plated as single cells on plates coated with 18 µg/mL Geltrex at $1.5x10^5$ cells/cm^2. The next day the medium was replaced to remove Y26732. From 0 DIV cells were grown in KO DMEM KSR medium (KO DMEM, 15% knockout serum replacement, 2 mM L-Glutamine, 100 µM non-essential amino acids, and 10 µM β-mercaptoethanol) which was switched in 25% increments every two days to NNB medium (Neurobasal, 0.5x N2 supplement, 0.5x B27 supplement without vitamin A, 2mM-L-Glutamine) between 5-9 DIV, from 11 DIV cells were grown in NB medium (Neurobasal, 1x B27 supplement without vitamin A, 2 mM L-Glutamine). Medium was supplemented with the following factors: 100nM LDN-193189 at 0–11 DIV; 10 µM SB-431542 at 0–5 DIV; 100 ng/mL SHH C24II, 2 µM Purmorphamine, and 100ng/mL FGF8a at 1–7 DIV; 3 µM CHIR99021 at 3–13 DIV; 20 ng/mL BDNF, 20ng/mL GDNF, 1 ng/mL TGFβ3, 10 µM DAPT, 200 µM ascorbic acid, 500 µM db-cAMP at 11–20 DIV. On DIV 20, cells were washed once with DPBS-/- then incubated with Accutase

at 37°C for 10 min or until dissociated, then resuspended in NB medium. Supernatant was removed and the cell pellet resuspended in NSC-EL medium (NSC medium (Advanced DMEM/F12, 1x B27 supplement without vitamin A, 1X N2 supplement, 1x Glutamax (all ThermoFisher Scientific)) supplemented with 20 ng/mL Epidermal growth factor (EGF), 20 ng/mL Leukaemia inhibitory factor (LIF) (both Peprotech)) containing 10 μM Y26732. Cells were then plated at a range of densities (50,000, 100,000 and 200,000 cells/cm^2) on plates coated with 0.01% poly-ornithine (Sigma)/1 μg/mL Laminin/2 μg/mL Fibronectin (Sigma). Cells were maintained in NSC-EL medium with daily feeding until DIV 30, when they were switched into NSC-EFH medium (NSC medium supplemented with 20 ng/mL EGF, 20 ng/mL Fibroblast growth factor 2 (FGF2) (Peprotech) and 5 μg/mL Heparin). On DIV 34 cells were washed once with DPBS-/- then incubated with Accutase for 5 min at 37°C, or until dissociated. Cells were then resuspended in NSC medium and centrifuged at 400 xg for 5 min to pellet. Supernatant was removed and the pellet resuspended in NSC-EFH medium supplemented with 10 μM Y26732. Cells were seeded onto Geltrex coated wells at 50,000 cells/cm^2 and maintained in NSC-EFH medium. On DIV 41, cells were passaged again, this time selecting only condition that had grown most successfully for each cell line. Cells were then passaged in NSC-EFH every seven days until 90 DIV, each time seeding at 50,000 cells/cm^2 onto Geltrex-coated plates. At 90 DIV, cells were passaged and seeded for terminal differentiation. Optimal seeding density for terminal differentiation was determined individually for each cell line (Table 2.1). Cells were terminally differentiated in NSC medium for four or five weeks.

Table 2.1. Optimal plating density for MP-astrocyte progenitors at 90 DIV.

Cell line	Optimal plating density (cells/cm^2)
NHDF1	25,000
JR053-6	50,000
SFC840-3	25,000
JR036-1	18,000
MK144-7	50,000
SFC832-19	50,000
SFC855-6	50,000

2.1.5. Freezing of MP-astrocyte progenitors

MP astrocyte progenitors were derived as described in section 2.1.4. From 41–90 DIV, upon passaging, cells could be frozen for storage in liquid nitrogen. Cells were washed once with DPBS-/- then incubated with Accutase for 5 min at 37^{o}C, or until dissociated. Cells were then resuspended in NSC medium and centrifuged at 400 xg for 5 min to pellet. Supernatant was removed and the pellet resuspended in NSC medium supplemented with 10% DMSO, 20 ng/mL FGF2 and 10 µM Y26732. Cells were frozen at -80^{o}C using a CoolCell (Biocision) and transferred to liquid nitrogen after 24 hrs. A substantial frozen stock was made for each cell line at 90 DIV, to be used for future experiments. All experiments described are conducted from frozen stocks. Smaller stocks were also banked at 41, 69 and 83 DIV.

2.1.6. Multifactorial analysis of gliogenic factors for improving astrocyte differentiation

Cells were differentiated to midbrain patterned astrocytes until 41 DIV or 90 DIV as described in section 2.1.4, when cells were plated into 96-well plates and treated with combinations of CNTF, BMP2, CT-1, TGFβ3, and LIF (all Peprotech) at two concentrations (Table 2.2), in NSC medium. Cells were treated for a further 14 DIV, with medium and factor replacement every two days. Cells were then fixed and immunostained (see section 2.2.5) for GFAP (chicken, Abcam) and costained with DAPI. Cells were then imaged using an EVOS FL auto microscope (ThermoFisher Scientific). Four images were analysed per treatment for the presence of

GFAP-positive cells with tufted or star-like morphology. Quantification was carried out using the cell counter plugin on Fiji (Image J).

Table 2.2. Gliogenic factor concentrations for multifactorial analysis.

Growth factor	Concentration 1 (ng/mL)	Concentration 2 (ng/mL)
CNTF	10	100
BMP2	20	100
CT-1	20	100
TGFβ3	20	100
LIF	20	100

2.2. Molecular biology

2.2.1. RNA extraction

RNA extraction was carried out according to the manufacturer's instructions, using the RNeasy mini kit (QIAgen) for samples estimated to contain more than 500,000 cells or the RNeasy micro kit (QIAgen) for samples estimated to contain less than or equal to 500,000 cells. An on-column DNAse digest was included for both methods. RNA concentration was quantified using a NanoDrop 1000 spectrometer (ThermoScientific).

2.2.2. First-strand cDNA synthesis

First-strand cDNA was synthesised from RNA samples using SuperScript III reverse transcriptase (ThermoFisher Scientific) for experiments in Chapter 3, and SuperScript IV VILO Mastermix (ThermoFisher Scientific) for experiments in Chapter 5. Briefly, for SuperScript III, components 1–3 (Table 2.3) were combined and then incubated in a thermocycler at 65^{o}C for 5 min. Samples were then transferred to ice for 1 min before addition of components 4–7 (Table 2.4). Samples were mixed gently by pipetting, then incubated in a thermocycler at 50^{o}C for 60 min, then at 70^{o}C for 15 min. For SuperScript IV VILO mastermix, components (Table 2.4) were combined, then mixed gently by pipetting, and incubated in a thermocycler at 25^{o}C for 10 min, 50^{o}C for 10 min, then 85^{o}C for 5 min. Samples were diluted 5–10 fold in sterile, distilled H_2O, then stored at -20^{o}C.

Table 2.3. Components for cDNA synthesis using SuperScript III reverse transcriptase.

	Component	Final concentration or mass	Volume
1	Oligo$(dT)_{20}$	2.5 µM	1 µL
2	Total RNA	200-1000 ng	Up to 12 µL
3	Sterile, distilled H_2O	-	To 13 µL
4	5X First-strand buffer	1X	4 µL
5	DTT	5 µM	1 µL
6	RNAse OUT	40 Units	1 µL
7	SuperScript III reverse transcriptase	200 Units	1 µL
	Total		**20 µL**

Table 2.4. Components for cDNA synthesis using SuperScript IV VILO mastermix.

Component	Final concentration or mass	Volume
SuperScript IV VILO mastermix	1X	4 µL
Total RNA	200-1000 ng	Up to 16 µL
Sterile, distilled H_2O	-	To 20 µL
Total		**20 µL**

2.2.3. Real-time quantitative polymerase-chain reaction

Real-time quantitative polymerase-chain reaction (qPCR) was carried out using fast SYBR green mastermix (ThermoFisher Scientific) on a StepOnePlus machine (ThermoFisher Scientific). Components were combined in a 96-well PCR plate (Table 2.5), mixed gently by pipetting, and the plate sealed with an ultra-clear seal. The plate was centrifuged briefly, then placed into the thermocycler and cycled as described in Table 2.6. Threshold cycles (C_T), were calculated using StepOne software. $2^{-\Delta\Delta CT}$ values were calculated relative to reference genes (Chapter 3: B2M and SDHA; Chapter 5: B2M, SDHA, HPRT1, and MALAT1) in Microsoft Office Excel. All primers (Table 2.7) were tested before use using a cDNA standard curve to ensure they possessed an amplification efficiency between 80-120%.

Table 2.5. Components for qPCR.

Component	Final concentration or mass	Volume
Fast SYBR mastermix	1X	10 µL
Primer pair (F&R)	500 nM	1 µL
Diluted cDNA	4-20 ng	2-4 µL
Sterile, distilled H_2O	-	To 20 µL
Total		**20 µL**

Table 2.6. Cycling parameters for qPCR.

Step #	Step purpose	Temperature (°C)	Duration (s)	Cycles
1	Enzyme activation	95	20	1
2	Denaturation	95	3	40
3	Annealing, extension, & fluorescence read	60	30	

Table 2.7. Primers for qPCR.

Primer	Sequence
AQP4-F	AGCTTTGCTGAAGGCTTCTTT
AQP4-R	GGGAAATTGGGAAAACCATT
B2M-F	CCTGAATTGCTATGTGTCTGGGTTTC
B2M-R	CTCCATGATGCTGCTTACATGTCTCG
EPHA5-F	CTGGACGTGCCTTCTCCTGTG
EPHA5-R	CCCATGACAGTGCGTGAATCC
FOXA2-F	GTGAAGATGGAAGGGCACGA
FOXA2-R	CATGTTGCTCACGGAGGAGT
GFAP-F	CACCACGATGTTCCTCTTGA
GFAP-R	GTGCAGACCTTCTCCAACCT
GIRK2-F	GGCCAAGCTGACAGAATCCA
GIRK2-R	GCTTAGGCAACTTTGGCTGG
GLAST1-F	ACTACAGCTCGCATTCCCAT
GLAST1-R	TCCTTTCCTGGGGAACTTCT
GNAI1-F	AGGGCTATGGGGAGGTTGAA
GNAI1-R	CACAAAGAGTTGGCGTGCAT
HPRT1-F	GCCAGACTTTGTTGGATTTG
HPRT1-R	CTCTCATCTTAGGCTTTGTATTTTG
KRAS-F	CACAAAACAGGCTCAGGACTT
KRAS-R	GCATCATCAACACCCTGTCT
LMX1A-F	GCTCAGATCCCTTCCGACAG
LMX1A-R	GAGGTGTCGTCGCTATCCAG
MALAT1-F	GACGGAGGTTGAGATGAAGC
MALAT-R	ATTCGGGGCTCTGTAGTCCT
NANOG-F	GAGATGCCTCACACGGAGAC
NANOG-R	GGGTTGTTTGCCTTTGGGAC
NRP1-F	ACAGGTGATGACTTCCAGCTCA
NRP1-R	ATTTGATACCTGATTGTATGGTGCT
NURR1-F	CAAGGAACCCAAGAGAGTGG
NURR1-R	TGTGTGCAAAGGGTACGAAG
OCT4-F	GAGAACCGAGTGAGAGGCAACC
OCT4-R	CATAGTCGCTGCTTGATCGCTTG
PAX6-F	TGGTTGGTATCCGGGGACTT
PAX6-R	GGCCTCAATTTGCTCTTGGG
PITX3-F	AGAGGACGGTTCGCTGAAAA
PITX3-R	CCTCTGGAAGGTCGCCTCTA
RAB7A-F	CAATGCAGATATGGGACACAGC
RAB7A-R	TTGGGGGCAGTCACATCAAA
SDHA-F	TGGGAACAAGAGGGCATCTG
SDHA-R	CCACCACTGCATCAAATTCATG
SH3GL3-F	GTGGTGCTGAAGGAACTAAACT
SH3GL3-R	AGCTCTGGATTTGGCTGAAGA
TH-F	CGAGCTGTGAAGGTGTTTGA
TH-R	CACGAAGTACTCCAGGTGG
VMAT2-F	CAGCTCATCACCAACCCTTT
VMAT2-R	AAGGCATAGCTGCTGGAGAA

2.2.4. Genotyping of iPSC lines

Genomic DNA was extracted from iPSCs using Illustra Tissue and Cells Genomic Miniprep Kit (GE Healthcare) and quantified using a Nanodrop 1000 (ThermoScientific). Polymerase chain reaction (PCR) was carried out using AmpliTaq Gold DNA polymerase with primers specific for regions of the LRRK2 gene that contain the G2019S and R1441C mutations (Table 2.8). Components were combined (Table 2.9), mixed gently by pipetting, then briefly centrifuged. Samples were loaded into the thermocycler and cycling conducted as described in Table 2.10. SfcI (G2019S) or BstUI (R1441C) restriction enzymes (0.2 µL) were added to an aliquot of the relevant PCR product (10 µL), and incubated at 37°C for 90 min. Digestion products were analysed for the presence of mutations by agarose gel electrophoresis (2% agarose, 89 mM Tris-borate, 2 mM EDTA) run at 130 V for 30 min, then 140 V for 40 min in 89 mM Tris-borate, 2 mM EDTA.

Table 2.8. Primers for genotyping.

Primer	Sequence 5'–3'	Restriction enzyme	Expected bands
G2019S-F	TTTAAGGGACAAAGTGAGCAC	SfcI	G2019G: ~380bp + ~120bp G2019S: ~380bp + ~350bp + ~120bp
G2019S-R	ACTCTGTTTTCCTTTTGACTC		
R1441C-F	GGAGGACCCAATTGGGTGCGT	BstUI	R1441R: ~300bp + ~200bp R1441C: ~400bp + ~300bp + ~200bp
R1441C-R	ACGCTGTCTTCAGCCCACTTC		

Table 2.9. Components for PCR.

Component	Final concentration or mass	Volume
Buffer II	1X	10 µL
dNTPs	200 nM	1 µL
$MgCl_2$	1.5 mM	3 µL
AmpliTaq Gold DNA polymerase	1.25 Units	1 µL
Primer pair (F&R)	200 nM	1 µL
DNA	10 ng	4.5 µL
Sterile, distilled H_2O	-	32.25 µL
Total		**50 µL**

Table 2.10. Cycling parameters for PCR.

Step #	Step purpose	Temperature (°C)	Duration	Cycles
1	Enzyme activation	95	3 min	1
2	Denaturation	95	30 sec	40
3	Annealing	55	45 sec	
4	Extension	72	1 min	
5	Extension	72	7 min	1

2.2.5. Immunostaining

Cells were fixed in 4% paraformaldehyde (PFA) for 20 minutes at room temperature and then washed 3x with DPBS +$MgCl_2$/+$CaCl_2$ (DPBS+/+) (ThermoFisher Scientific). Cells were blocked for 60 min at room temperature in DPBS+/+/0.1% TritonX 100/10% serum, then incubated with primary antibodies (Table 2.11) in DPBS+/+/0.1% TritonX 100/1% serum for 90 min at room temperature. Cells were washed 3x with DPBS+/+ then incubated with Alexa Fluor secondary antibodies (Table 2.12) in DPBS+/+ /0.1% TritonX 100/1% serum for 60 min at room temperature. Cells were washed 1x with DPBS+/+ then incubated with 1 µg/mL DAPI (ThermoFisher Scientific) in DPBS+/+ for 10 min at room temperature, then washed 1x with DPBS+/+. Plates were wrapped in Parafilm (Sigma) and stored at 4°C in the dark. Coverslips were mounted onto microscope slides using Fluorsave reagent (Millipore), allowed to dry for at least 60 min at room temperature, and then stored at 4°C in the dark.

Table 2.11. Primary antibodies for immunostaining.

Protein	Antibody host species	Product code	Manufacturer	Dilution
α-Synuclein	Mouse	610786	BD Biosciences	1:250
CD44	Mouse	555476	BD Pharmigen	1:200
FOXA2	Goat	AF2400	R&D systems	1:250
GFAP	Rabbit	Z0334	Dako	1:500
GFAP	Chicken	Ab4674	Abcam	1:1000
GLAST1	Rabbit	NBP-20135	Novus Biologicals	1:200
LAMP1	Mouse	sc-20011	Santa Cruz	1:500
LAMP2A	Rabbit	ab18528	Abcam	1:200
LC3	Rabbit	CS2775	Cell Signalling	1:100
LMX1A	Rabbit	AB10533	Millipore	1:1000
MAP2	Rabbit	AB5622	Millipore	1:500
S100	Rabbit	Ab868	Abcam	1:500
TH	Rabbit	AB152	Millipore	1:500
TH	Mouse	sc-25269	Santa Cruz	1:200
TH	Goat	sc-7847	Santa Cruz	1:50
TUJ1	Chicken	ab107216	Abcam	1:500

Table 2.12. Secondary antibodies for immunostaining.

**Purchased from Jackson Laboratories. All other antibodies were purchased from ThermoFisher Scientific.*

Antibody host species	Antibody target species	Alexa Fluor wavelength	Product code	Dilution
Donkey	Rabbit	488	A-21206	1:1000
Donkey	Rabbit	555	A-31572	1:1000
Donkey	Rabbit	594	A-21207	1:1000
Donkey	Mouse	488	A-21202	1:1000
Donkey	Mouse	555	A-31570	1:1000
Donkey	Mouse	594	A-21203	1:1000
Donkey	Goat	647	A21447	1:1000
Donkey	Chicken	488	*703-454-155	1:500
Goat	Chicken	488	A-11039	1:1000

2.2.6. Western blotting

Cells were lysed in RIPA buffer +/+ (50 mM Tris-Cl pH 8.0, 150mM NaCl, 1% NP-40, 1% sodium deoxycholate, 0.1% SDS, 1X complete mini, EDTA-free protease inhibitors (Roche) and 1X PhosSTOP phosphatase inhibitors (Roche)). Lysates were snap frozen on dry ice and then stored at -80^{o}C. Lysates were then thawed on ice, followed by centrifugation at 14,000 xg for

10 min to remove any cell debris. Supernatant was transferred to a new tube and an aliquot taken for protein quantification using a BCA assay (Section 2.2.7). Lysates were then combined 4:1 with Laemmli buffer (1 M Tris-Cl pH 6.8, 10% SDS, 50% glycerol, 2.9 M 2-mercaptoethanol, 0.25% (w/v) bromophenol blue). Samples were loaded onto 4-15% Criterion-TGX, or mini-protean-TGX gels (BioRad) and electrophoresis conducted in running buffer (25 mM Tris, 192 mM Glycine, 0.1% SDS) for 50 min at 150 V. BLUeye prestained protein marker (Geneflow) was run alongside samples for estimation of protein band sizes. Proteins were transferred to a PVDF membrane using a Trans-Blot Turbo (BioRad). Membranes were blocked in Tris-buffered saline (0.2 M Tris pH 7.5, 1.37 M NaCl) (TBS)/0.1% Tween/5% milk for 60 min at room temperature and then incubated with primary antibodies (Table 2.13) overnight (or for 36 hrs in the case of antibodies against LRRK2) in TBS/0.1% Tween/5% milk. Membranes were washed 3x 10 min in TBS/0.1% Tween, then incubated with secondary antibodies (Table 2.14) in TBS/0.1% Tween/5% milk for 60 min at room temperature. Membranes were washed 3x 10 min in TBS/0.1% Tween and then developed using Immobilon Western Chemiluminescent HRP substrate (Millipore), and visualised on a Chemidoc (BioRad). Band densitometry was measured using Image Lab software (BioRad). Proteins of interest were quantified relative to β-actin.

Table 2.13. Primary antibodies for Western blotting.

Protein	Antibody host species	Product code	Manufacturer	Dilution
AADC	Rabbit	AB1569	Millipore	1:1000
α-Synuclein	Rabbit	ab138501	Abcam	1:5000
β-actin (HRP-conjugated)	Mouse	ab49900	Abcam	1:20000
DAT	Rabbit	DAT13-A	Alpha Diagnostics	1:500
Dynamin-1	Rabbit	ab52611	Abcam	1:1000
Endophilin I-III	Rabbit	sc-30101	Santa Cruz	1:1000
EPHA5	Mouse	sc-517242	Santa Cruz	1:200
FYN	Mouse	610163	BD Biosciences	1:250
GIRK2	Rabbit	APC-006	Alomone labs	1:500
GNAI1	Mouse	sc-13533	Santa Cruz	1:1000
LAMP1	Mouse	sc-20011	Santa Cruz	1:500
LAMP2	Rabbit	ab37024	Abcam	1:500
LAMP2A	Rabbit	ab18528	Abcam	1:200
LC3	Rabbit	CS2775	Cell Signalling	1:100
LRRK2	Mouse	73-253	Antibodies Incorporated	1:50
NRP1	Mouse	sc-5307	Santa Cruz	1:500
RAB5B	Rabbit	ab72907	Abcam	1:200
RAB7A	Rabbit	ab137029	Abcam	1:1000
Tau	Mouse	ab80579	Abcam	1:2000
TH	Rabbit	AB152	Millipore	1:500

Table 2.14. HRP-conjugated secondary antibodies for Western blotting.

Antibody host species	Antibody target species	Product code	Manufacturer	Dilution
Goat	Rabbit	170-6515	BioRad	1:5000
Goat	Mouse	170-6516	BioRad	1:5000

2.2.7. BCA assay

Bicinchoninic acid solution was combined 49:1 with 4% Copper(II) Sulfate Pentahydrate Solution to make BCA solution. Protein samples were diluted five- and ten-fold and 5 µL added to a well of a 96-well plate. 150 µL BCA solution was added to each well and incubated at 37^{o}C for 30 min. Absorbance was read at 562 nm and the concentration of protein calculated from a bovine serum albumin standard curve.

2.2.8. Immunohistochemistry

Formalin-fixed, paraffin-embedded, 5 μm thick, coronal sections through the mouse SNc, were provided mounted on glass slides by Dr Nora Bengoa-Vergniory (University of Oxford). Sections were processed, then immunostained as follows. Before and after each incubation step for dewaxing and rehydration, slides were dipped in and out of the solution five times. Firstly, sections were dewaxed; slides were incubated for in xylenes for 2 min, then in HistoClear (National Diagnositics) for 2 min. Sections were then rehydrated for 2 min in 100% ethanol, followed by 2 min in 95% ethanol, 2 min in 70% ethanol, and finally, incubated in running reverse-osmosis (RO) water for 5 min. Sections were then incubated for 15 min in 10% H_2O_2 in Phopshate-buffered saline (PBS) (Sigma) to quench endogenous peroxidases, then incubated in running RO water for 5 min. Antigen retrieval was performed by submerging sections in 1X citrate buffer (pH 6.0) (Abcam) and by microwaving on full power for 4 min, then 4x 1.5 min, with a 5 min incubation at room temperature between each, and a final incubation on ice for 20 min. Sections were then incubated in running RO water for 5 min. Prior to immunostaining, a circle was drawn around each section using a pap pen. Sections were then washed 2x 5min in TBS/0.05% Tween, then blocked for 1 hr at room temperature in TBS/1M glycine/10% NDS/0.1% Triton. Sections were incubated with primary antibodies against GFAP (rabbit, DAKO, 1:1000) and FOXA2 (goat, R&D systems, 1:100) in blocking solution overnight at 4^{o}C, then washed 4x 5 min in TBS/0.05% Tween. Secondary antibodies (alexafluor-680 Donkey-anti-rabbit, and alexafluor-594 donkey-anti-goat 594, ThermoFisher Scientific) were added in blocking solution for 60 min at room temperature in the dark. DAPI (1ug/mL) was then added in TBS for 5 min at room temperature in the dark. Sections were then washed 4x 5min in TBS/0.05% Tween in the dark, then mounted with coverslips using

Fluorsave reagent (EMD Millipore). Slides were incubated at room temperature, in the dark, for a minimum of 60 min, for Fluorsave reagent to solidify, then were stored at 4^{o}C.

2.3. Phenotypic assays

2.3.1. Quantification of floorplate progenitor percentages

VmDA-neuron cultures were cultured for 11 DIV and then fixed and immunostained with antibodies against LMX1A (rabbit, Millipore) and FOXA2 (goat, R&D systems), and costained with DAPI. Images were acquired using an EVOS FL auto fluorescent microscope (ThermoFisher Scientific). Quantification of was carried out on three images per cell line, using a pipeline designed on CellProfiler (Carpenter et al. 2006).

2.3.2. Quantification of vmDA-neuron percentages

VmDA-neuron cultures, plated at 300,000–500,000 cells/cm^2 at 20 DIV, were cultured until 35 DIV then fixed and immunostained with antibodies against TH (rabbit, Millipore), Tuj1 (Chapter 3: mouse, Covance; or Chapter 4&5: chicken, Abcam), and FOXA2 (goat, R&D systems), and costained with DAPI. Images were acquired using an EVOS FL auto fluorescent microscope (ThermoFisher Scientific), or a Phenix Opera fluorescent, confocal microscope (Perkin Elmer). Maximum projections were produced for images acquired on the confocal microscope. Quantification of was carried out on three images per cell line, per differentiation, using the Cell Counter plugin on Fiji (Image J).

2.3.2. Quantification of MP-astrocyte percentages

MP-astrocyte cultures were cultured for 118 or 125 DIV and then fixed and immunostained with an antibody against GFAP (rabbit, Dako; or chicken, Abcam), and costained with DAPI. Images were acquired using an EVOS FL auto fluorescent microscope (ThermoFisher Scientific), or a Phenix Opera fluorescent, confocal microscope (Perkin Elmer). Maximum projections were produced for images acquired on the confocal microscope. Quantification

of was carried out on at least three images per cell line, per differentiation, using the Cell Counter plugin on Fiji (Image J), or using a pipeline in Harmony software (Perkin Elmer).

2.3.3. Quantification of α-Synuclein-positive cells and α-Synuclein puncta

VmDA-neuron cultures, plated at 300,000–500,000 cells/cm^2 at 20 DIV, were cultured until 35 DIV then fixed and immunostained with antibodies against TH (rabbit, Millipore) and α-Synuclein (mouse, BD Biosciences), and costained with DAPI. Images were acquired using an EVOS FL auto fluorescent microscope (ThermoFisher Scientific), or a Phenix Opera fluorescent, confocal microscope (Perkin Elmer). Maximum projections were produced for images acquired on the confocal microscope. Quantification of α-Synuclein/TH double-positive cells was carried out on 25 cells per image, from three images per cell line, per differentiation, using the Cell Counter plugin on Fiji (Image J). Quantification of α-Synuclein puncta was conducted using a pipeline in Harmony software (Perkin Elmer).

2.3.4. Quantification of autophagy puncta

VmDA neurons, plated at 300,000–500,000 cells/cm^2 at 20 DIV, were cultured until 35 or 76 DIV, then fixed and immunostained with antibodies against LC3 (rabbit, Cell Signalling), LAMP1 (mouse. Santa Cruz), and TH (goat, Santa Cruz), or LAMP2A (rabbit, Abcam) and TH (mouse, Santa Cruz), and costained with DAPI. MP-astrocytes were cultured for 125 DIV, then fixed and immunostained with antibodies against LC3 (rabbit, Cell Signalling), LAMP1 (mouse. Santa Cruz), and GFAP (chicken, Abcam). Images were acquired using an EVOS FL auto fluorescent microscope (ThermoFisher Scientific), or a Phenix Opera fluorescent, confocal microscope (Perkin Elmer). Maximum projections were produced for images acquired on the confocal microscope. Puncta number and size were quantified within individual TH-positive vmDA neurons, and in GFAP-positive regions of images, using pipelines in CellProfiler

software (Carpenter et al. 2006). Puncta number and size across whole images were quantified using a pipeline in Harmony software (Perkin Elmer).

2.3.5. Quantification of neurite growth using semi-automated Sholl analysis

VmDA-neurons, plated at 150,000 cells/cm^2 at 20 DIV, were matured on glass coverslips until 28 DIV, then fixed and immunostained for TH (mouse, Santa Cruz) and MAP2 (rabbit, Millipore), and costained for DAPI. Images were captured using an EVOS FL auto fluorescent microscope. Semi-automated Sholl analysis of neurites was conducted on TH/MAP2 double positive cells using the FastSholl script (Gutierrez and Davies 2007) in MatLab (MathWorks).

2.3.6. Dopamine content analysis

VmDA-neuron cultures, plated at 500,000 cells/cm^2 at 20 DIV, were cultured until 35 DIV, then were harvested for dopamine analysis. In the dark, cells were removed from the well by scraping in 1 mL DPBS-/-, 900 µL were transferred to an opaque 1.5 mL tube for HPLC analysis, and the remaining 100 µL were transferred to a clear 1.5 mL tube for protein quantification. Scraped cells were centrifuged at 500 xg for 5 min to pellet, supernatant was then removed. Pellets in clear tubes were resuspended in RIPA buffer and their protein content was quantified using a BCA assay. Pellets in opaque tubes were resuspended in 150 µL 0.1% perchloric acid and incubated at room temperature for 5 min to lyse. Lysates were snap-frozen and stored at -80^oC until HPLC analysis was conducted. Upon thawing, lysates were applied to a 0.2µm nylon filter (VWR) and centrifuged at 14,000 xg for 10 min to homogenise. Samples (50 µL) were injected on to an isocratic HPLC system and separated using a 250 mm Microsorb C18 reverse-phase column (Agilent), and a mobile phase consisting of methanol (13 % v/v), NaH_2PO_4 (120 mM), EDTA (0.8 mM) and sodium octane sulfonate (3.2 mM) at pH 3.27, with a fixed flow rate of 1 mL/min. Samples were quantified using a LC-4B

electrochemical detector and a carbon working electrode held at +0.7 V vs an Ag/AgCl reference electrode. Dopamine content was quantified relative to freshly prepared dopamine standards and normalised to protein content as determined by BCA assay.

2.3.7. Analysis of mitochondrial membrane potential using TMRM

VmDA neurons, plated at 150,000 cells/cm^2 at 20 DIV, were matured in 35 mm dishes with glass coverslip bottoms until 35-41 DIV. Each day, one dish of cells from each line was analysed. Cells were washed 2x with Tyrode's buffer and then loaded with 25 nM TMRM in 1.8 mL Tyrode's buffer for a minimum of 30 min at 37^{o}C/5% CO_2/95% humidity in a cell culture incubator. Cells were then imaged in the Texas Red channel using an epifluorescence microscope (Nikon) every 10 sec for 2 min before addition of 200 µL CCCP (100 µM) in Tyrode's buffer. Cells were imaged every 10 sec for a further 8 min after addition of CCCP. Data was analysed using Image J. ΔFluorescence was calculated by subtracting the average fluorescence intensity of the cell in the last minute of imaging from the average fluorescence intensity of the cell in the minute before CCCP addition.

2.3.8. Analysis of mitochondrial and glycolytic respiration

VmDA-neuron cultures plated at 500,000 cells/cm^2 at 20 DIV, and MP-astrocyte cultures, plated at line-dependent densities, were grown in specialised XF96 plates for analysis on the Seahorse Analyser (Agilent) until 37 and 125 DIV respectively. On the day of analysis, cells were prepared as following the manufacturer's guidelines. Briefly, medium was changed into Seahorse XF medium containing D-Glucose (10 mM), L-Glutamine (2 mM), and sodium pyruvate (1 mM) at pH 7.4, and incubated at 37^{o}C for 60 min. The plate was then transferred to the Seahorse XF analyser and the oxygen consumption rate (OCR) and extracellular acidification rate (ECAR) measured every three minutes. Three readings were taken under

basal conditions (1), followed by three readings after addition of each of the following compounds: 1 µM oligomycin (2), 0.5 µM Carbonyl cyanide-4-(trifluoromethoxy)phenylhydrazone (FCCP) (3), 0.5 µM rotenone in combination with 0.5 µM antimycin A (4), and 50 mM 2-deoxyglucose (2-DG) (5). Following analysis, medium was removed from the cells and 45 µL RIPA buffer added per well to facilitate cell lysis. A BCA assay was then carried out in duplicate using 20 µL of lysate per reaction. The protein content for each well was calculated and Seahorse XF96 data was averaged across the three readings following each treatment and normalised to the average protein content for each cell line. Mitochondrial respiration parameters were derived from the analysis of OCR data, and glycolytic respiration parameters were derived from the analysis of ECAR data (Table 2.15)

Table 2.15: Derivation of respiration parameters from normalised Seahorse XF96 data.

Calculations were performed on OCR and ECAR data recorded under basal conditions (1) and after treatment with oligomycin (2), FCCP (3), rotenone & antimycin A (4), and 2-deoxyglucose (2-DG) (5).

Respiration parameter	Calculation
Mitochondrial proton leakage	OCR 2-4
Mitochondrial maximal capacity	OCR 3-4
Mitochondrial ATP production	OCR 1-2
Mitochondrial spare capacity	OCR 3-1
Mitochondrial basal respiration	OCR 1-4
Basal glycolysis	ECAR 1-5
Maximal glycolysis	ECAR 4-5
Glycolytic reserve	ECAR 2-1

2.3.9. Analysis of protein degradation using a pulse-chase assay

At 125 DIV, MP-astrocyte cultures in 12-well plates were washed 3x with DPBS+/+, then incubated with ^{14}C-Valine (925 pM, 250 nCi/mL) in 500 µL NSC medium for 48 hrs at 37^{o}C/5% CO_2/95% humidity. Cells were then washed 3x with NSC medium containing 2 mM ^{12}C-Valine, then incubated in NSC medium containing 2 mM ^{12}C-Valine for 24 hrs at 37^{o}C/5% CO_2/95% humidity. Cells were then treated with MG132 (10 µM), Chloroquine (20 µM), or vehicle, in

NSC containing ^{12}C-Valine for a further 24 hrs. Medium (500 µL) was transferred to a 1.5 mL tube containing an equal volume of 20% trichloroacetic acid and centrifuged at 17,000 xg for 10 min. Supernatant was transferred to scintillation vials. Cells were lysed in 200 µL NaOH (0.1 M), 5 µL lysate per sample was taken for protein quantification by BCA assay, and the remainder of each sample was transferred to individual scintillation vials. 3mL Optiphase Supermix (Perkin Elmer) scintillation fluid was added to each scintillation vial, which was capped and inverted to mix before analysis using a Tri-Carb 2800 TR liquid scintillation counter (Perkin Elmer). Data was normalised to protein content as calculated using a BCA assay. Percentage protein degradation in 24 hrs was calculated by dividing the total radioactive counts per minute (CPM) from the medium by the total CPM from the cell lysate, then multiplying by 100.

2.3.10. ^{3}H-Glutamate uptake assay

At 125 DIV, MP-astrocyte cultures in 12-well plates were washed 3x with DPBS+/+ and then incubated with 50 nM L-[3,4-^{3}H]-Glutamic Acid in 135 mM NaCl, 3.1 mM KCl, 1.2 mM $CaCl_2$, 1.2 mM $MgSO_4$, 0.5 mM KH_2PO_4, and 2.0 mM glucose, adjusted to pH 7.4, for 10 min. Sodium-independent uptake was measured by incubating cells under the same conditions, substituting 135 mM choline chloride for sodium chloride. The uptake assay was stopped by the addition of 500 µM cold ^{1}H-Glutamic Acid (Sigma). Supernatant was removed, cells were washed 2x DPBS+/+, and then lysed in 200 µL NaOH (0.1 M). 5 µL lysate per sample was taken for protein quantification by BCA assay, and the remainder of each sample was transferred to individual scintillation vials. 3mL Optiphase Supermix (Perkin Elmer) scintillation fluid was added to each scintillation vial, which were capped and then inverted before analysis using a Tri-Carb 2800 TR liquid scintillation counter (Perkin Elmer). Data was normalised to protein content as calculated using a BCA assay.

2.3.11. Analysis of astrocyte proliferation/migration using a scratch assay

MP-astrocyte cultures were grown until 125 DIV in 96-well plates. A scratch was applied through the centre of the well, and medium replaced. Bright field images were captured at 37^{o}C/5% CO_2 every 2 hrs for 42 hrs using a Phenix Opera (Perkin Elmer). Cell coverage of the well over time was measured using a pipeline in Harmony software (Perkin Elmer).

2.3.12. Analysis of neurite regrowth using a scratch assay

VmDA-neuron cultures were grown until 33 DIV in 96-well plates. A scratch was applied through the centre of the well, and medium replaced. Bright field images were captured 24 hrs for 7 days using a Phenix Opera (Perkin Elmer). Cell coverage of the well over time was measured using a pipeline in Harmony software (Perkin Elmer).

2.3.13. Analysis of α-Synuclein and Tau content in medium

At 34 DIV, fresh vmDA-neuron medium was added to vmDA-neuron cultures, 48 hrs later medium was transferred to a 1.5 mL tube. Samples were centrifuged at 500 xg for 5 min, supernatant transferred to a new 1.5 mL tube, and then snap frozen on dry ice, then stored at -80^{o}C until analysis. Samples were thawed by and analysed for α-Synuclein and Tau protein levels using highly sensitive immunoassays (Meso Scale Discovery) according to the manufacturer's instructions; these assays were conducted by Drs Siv Vingill and Brent Ryan (University of Oxford).

2.3.14. Electrophysiological recording from dopaminergic neurons

Electrophysiological analysis was conducted by Emma Whiteley (University of Oxford) as follows: vmDA-neuron cultures, matured on glass coverslips for 52–72 DIV were recorded from by whole-cell patch clamp electrophysiology using a potassium internal bathed in an isotonic aCSF external solution bubbled with carbogen (95% O_2/5% CO_2) to maintain pH 7.3.

The passive membrane properties were noted including resting membrane potential, capacitance, and membrane resistance. For measurement of active currents (K^+/Na^+) the cells were held at -70 mV in voltage clamp mode and a steps protocol was applied from -90 mV to +30 mV in 10 mV increments, each step had a 400 ms duration. To observe action potentials the cell was held in current clamp mode at -70 mV and a steps protocol was applied, injecting current in 5 pA increments from -20 pA to +35 pA, for 400 ms duration. After recording, cells were injected with biotin to enable identification via immunostaining. Following electrophysiological analysis, cells were fixed. I then carried out immunostaining with an antibody against TH (rabbit, Millipore) and an AlexaFluor-488 streptavidin conjugate (ThermoFisher Scientific), to detect biotin injected neurons.

2.4. General statistical methods

Statistical analysis of data was performed in GraphPad Prism. Where data from multiple differentiations are displayed, the mean for each line across the differentiations was used. Statistical comparisons across genotypes were performed on these values. Student's T-Test was used for the comparison of two groups, and a one-way ANOVA was used for analysis of three or more groups with one variable. A two-way ANOVA was used for analysis of two or more groups with two or more variables. The Mann-Whitney test was used where data were obtained from only one cell line, or when the variance of the groups to be compared was not equal.

2.5. Transcriptomics and proteomics

2.5.1. Cell culture for transcriptomics and proteomics analysis

VmDA neurons, plated at 500,000 cells/cm^2 at 20 DIV, were cultured until 35 or 56 DIV. MP astrocytes, plated at line-dependent densities, were cultured until 125 DIV. For transcriptomics and proteomics analyses, samples were harvested as described in sections 2.5.2 and 2.5.3 respectively. For phosphoproteomics analysis, cells were treated with mLi-2 (25 nM), PF-475 (100 nM), or DMSO, for 90 min before harvesting as described in section 2.5.3.

2.5.2. RNA-seq methodology for transcriptomics analysis

RNA extraction was conducted as described in section 2.2.1. RNA was quantified using a Nanodrop 1000, and RNA integrity number (RIN) assessed using the RNA 6000 Pico Kit on a Bioanalyzer (Agilent). All RNA used for analysis conformed to a RIN of 8.8 or higher. RNA samples were frozen at -80^{o}C and shipped to Biogen Inc.

Library preparation, clustering, and sequencing was carried out by Norm Allaire (Biogen Inc.) as follows. 500 ng of high quality RNA was used as starting for poly-A library construction. Briefly, automated poly-A library construction was completing using TruSeq Stranded mRNA sample Preparation kit (Illumina) according to manufacturer's recommendations, using an Arrayplex automated liquid handler (Beckman Coulter). Individual libraries were quality controlled for size distribution and concentration using a LabChip GX and KAPA library quantification kit (Kapa Biosystems) according to the manufacturer's recommendations. Pooled libraries were clustered on a cBot (Illumina) using HiSeq PE Cluster kit V4 (Illumina) and sequenced on a HiSeq 2500 Sequencing system (Illumina) using HiSeq SBS kit v4 (Illumina) with 50/50 paired end sequencing at a read depth of approximately 30 million fragments in

high output mode. Sequencing run quality control parameters were uploaded to BaseSpace (Illumina) and reviewed. Completed runs were considered high quality if >85% of bases above Q30 and Cluster Pass Filter >85%.

2.5.3. Cell lysis for proteomics and phosphoproteomics analysis

Cells were lysed in 200 µL of denaturing urea lysis buffer (9M urea, 0.1 M Tris HCl pH 8.5, 2 mM EDTA, 1X PhosStop (Roche), phosphatase inhibitor cocktail 2 (1:100; Sigma) and cocktail 3 (1:100; Sigma)). Lysates were frozen at -80^{o}C and shipped to Biogen Inc. The following steps were conducted by Dr Jeff Martin (Biogen Inc.). Lysates were thawed and sonicated using a Covaris E220 focused-ultrasonicator for two 30 sec treatments at 50 W, 15% duty factor, 200 cycles per burst followed by a 30 second treatment at 75 W, 15% duty factor, 200 cycles per burst. Lysates were clarified by centrifugation at 21,000 xg for 5 min, and protein concentrations of the clarified lysates were measured by BCA assay.

2.5.4. Sample preparation for proteomics analysis

Samples were prepared for proteomics analysis by Dr Jeff Martin (Biogen Inc.) as follows. 150 µg of cell lysate was reduced and alkylated with 10 mM tris(2-carboxyethyl)phosphine (TCEP) and 30 mM iodoacetamide respectively. Samples were diluted 10-fold with 50mM Tris HCl (pH 8.0) prior to their overnight digestion with LysC and trypsin at 1:100 enzyme-to-protein ratio at 37^{o}C. Digested samples were acidified with trifluoroacetic acid to a final concentration of 1%, and centrifuged at 21,000 xg. Samples were desalted on C18 SepPak columns (Waters) and dried down using a speedvac. Desalted peptides were labelled with TMT 10-plex reagents (ThermoFisher Scientific). Specifically, for each 150 µg peptide sample, peptides were dissolved in 150 µL of 0.2 M triethylammonium bicarbonate (TEAB) (pH 8.5) solution, and labelling reagent was added in 20 µL of anhydrous acetonitrile. After 60 min incubation, 6 µL

of 5% hydroxylamine in 0.2 M TEAB was added to quench the unreacted TMT reagents. Trifluoroacetic acid was added to a final concentration of 1% and the TMT labelled peptides were mixed (10 x 60 µg) then dried down to remove acetonitrile. Samples were then reconstituted in 550 µL of 5% acetonitrile, 5% formic acid and loaded on a 4.6mm x 250mm column Extend-C18 column (Agilent), and separated on an Agilent 1200 Series HPLC instrument using basic reversed-phase chromatography. Solvent A (5% acetonitrile, 5 mM ammonium bicarbonate, pH 8.0) with increasing concentration of solvent B (90% acetonitrile, 5 mM ammonium bicarbonate, pH 8.0) were used to separate peptides. The fractions were pooled in a checkerboard manner, dried down, desalted by an Empore C18 stage tip, and re-suspended in 0.1% formic acid for LC-MS/MS analysis.

2.5.5. Sample preparation for phosphoproteomics analysis

Samples were prepared for phosphoproteomics analysis by Dr Jeff Martin (Biogen Inc.) as follows. 175 µg of cell lysate was reduced and alkylated with 10 mM TCEP and 30 mM iodoacetamide respectively. Samples were diluted 10-fold with 50mM Tris HCl (pH 8.0) prior to their overnight digestion with LysC and trypsin at 1:100 enzyme-to-protein ratio at 37^{o}C. Digested samples were acidified with trifluoroacetic acid to a final concentration of 1%, and centrifuged at 21,000 xg. Samples were desalted on C18 SepPak (Waters) columns and dried down using a speedvac. Desalted peptides were labelled with TMT 10-plex reagents (ThermoFisher Scientific). Specifically, for each 175 µg peptide sample, peptides were dissolved in 0.2 M TEAB (pH 8.5) solution and labelling reagent was added in 40 µL of anhydrous acetonitrile. After 60 min incubation, 6 µL of 5% hydroxylamine in 0.2 M TEAB was added to quench the unreacted TMT reagents. Trifluoroacetic acid was added to a final concentration of 1% and the TMT labelled peptides were mixed, then dried down to remove the acetonitrile.

TMT labelled peptides were desalted on C18 SepPak columns (Waters) and were subsequently enriched for phosphopeptides using immobilized metal affinity chromatography (IMAC). Ni-NTA agarose beads (QIAgen) were stripped with 100 mM EDTA (pH 7.5), then charged with 0.1 M FeCl3 in 0.1 M acetic acid for 60 min. For each TMT set, peptides in 80% acetonitrile/0.1% trifluoroacetic acid were incubated with 500 µg of the IMAC beads for 60 min at room temperature. After incubation, beads were collected on a magnetic rack, washed with 80% acetonitrile, 0.1% trifluoroacetic acid, and eluted with 3x 100 µL of 50 mM sodium phosphate. Elutions were acidified, dried, reconstituted in 1% trifluoroacetic acid, and desalted on C18 stagetips (Empore). Phosphopeptides were fractionated on a 2.1mm x 100mm column Extend-C18 column (Agilent) on a 1200 Series HPLC instrument (Agilent) using basic reversed-phase chromatography. Solvent A (5% acetonitrile, 5 mM ammonium bicarbonate, pH 8.0) with increasing concentration of solvent B (90% acetonitrile, 5 mM ammonium bicarbonate, pH 8.0) were used to separate peptides. Eluted peptides were pooled into six fractions plus the flow through, dried down, desalted on C18 stage tips (Empore) and re-suspended in 0.1% trifluoroacetic acid for LC-MS/MS analysis.

2.5.6. LC-MS/MS analysis for proteomics and phosphoproteomics

LC-MS/MS analysis of samples for proteomics and phosphoproteomics was conducted by Dr Jeff Martin (Biogen Inc.) as follows. LC-MS/MS analysis was performed using a QExactive HF mass spectrometer (ThermoFisher Scientific) coupled to an EASY-nLC 1000 system (ThermoFisher Scientific) using a 75 µm by 50 cm EASY-Spray analytical column (Thermo Fisher Scientific) at 50˚C. Solvent A (0.1% formic acid) with increasing concentration of solvent B (80% acetonitrile, 0.1% formic acid) was used to separate peptides at a flow rate of 275 nL/min. The QExactive HF mass spectrometer was set to acquire in a data-dependent mode (Top10). Full scans were acquired at 60,000 resolution at 200 m/z, with a target of $3x10^6$

ions with a maximum injection time of 20 ms. For MS^2, a target value of 1 x106 with a maximum injection time of 120 ms was used. MS^2 higher-energy collision dissociation (HCD) fragmentation was performed using a normalized collision energy (NCE) of 33%, and a resolution of 60,000 at 200 m/z to be able to resolve the TMT signals.

MaxQuant version 1.5.3.30 for total proteomics and 1.6.0.1 for phosphoproteomics were used to process MS data. The false discovery rate (FDR) was set at <0.01, enzyme was set to trypsin, and miss cleavages was set at <2. The Human UniProt FASTA database (March 2015) was used for peptide identification, with cysteine carbamidomethylation as a fixed modification and N-acetylation, oxidation of methionine for total proteomics, and the addition of phosphorylation of Ser, Thr, Tyr residue (PhosphoSTY) for phosphoproteomics, as variable modifications. TMT quantification was performed by MaxQuant, using correction factors supplied with TMT reagents, reporter mass tolerance set to 0.01 Da, and a parent ion fraction (PIF) filter at 0.75.

2.5.7. Bioinformatics analysis of transcriptomics data

Bioinformatics analysis of transcriptomics data was conducted by Dr Kejie Li (Biogen Inc.) as follows. Sequencing reads were aligned to reference genome (hg38) using OSA aligner (OmicSoft Sequence Aligner (Hu et al. 2012). Quality control for the sequence alignment involved the analysis of sequence quality, GC content, and 5'-3' gene body coverage. Aligned reads were then counted against gene model annotation (gencode v23) to obtain expression values by using RSEM (Li and Dewey 2011). DESeq2 (Love et al. 2014) was used for gene expression normalization. The regularised log transformation function in DESeq2 was used to transform the count data to the log2 scale, minimising differences between samples for rows with small counts (transcripts with low expression), and normalising to library size. These

values were used to obtain clustering and PCA results for biological QC and downstream differential analysis. DESeq2 generalized linear model (GLM) was used for differential analysis. Transcripts with >0.5 Fragments per Kilobase of transcript per Million mapped reads (FPKM) were considered to be robustly detected. Differentially expressed gene (DEG) signature was defined by using the following criteria: FPKM>0.5, false-discovery-rate (FDR)-adjusted *p*-value<0.05 and absolute fold change (FC)>1.5.

2.5.8. Bioinformatics analysis of proteomics data

Bioinformatics analysis of proteomics data was conducted by Dr Benbo Gao (Biogen Inc.) as follows. Protein lists exported from MaxQuant software (Max Planck Insititute of Biochemistry) were used for statistical analysis. The data normalisation, principal component analysis (PCA), and statistical analysis of proteomics data were performed using R programming language (www.r-project.org), version 3.4.0. The raw data were normalised to the median intensity of all proteins within the TMT 10-plex set. The normalised intensity for each protein was then transformed to a relative ratio by dividing by the mean normalised intensity of the protein across the TMT 10-plex set. The LIMMA package (Ritchie et al. 2015) was used for statistical analysis of differential abundance. The *p*-values were adjusted for multiple comparisons using the Benjamini and Hochberg method (Benjamini and Hochberg 1995); a protein was considered significantly different between groups if it had a FDR-adjusted *p*-value<0.05.

2.5.9. Combined bioinformatics analysis of proteomics and transcriptomics data for dual omics analysis

Bioinformatics analysis of proteomics and transcriptomics data was conducted by Dr Benbo Gao (Biogen Inc.) as follows. Proteomics data was multiplied by 1.4 to compensate for TMT-

10plex labelling compression. Transcriptomics and proteomics datasets from 35 and 56 DIV for vmDA-neuron cultures were combined to produce integrated FC and adjusted *p*-values. Briefly, if a protein was significantly differentially expressed at 35 DIV, then 35 DIV protein data was used; if not, and the protein was significantly differentially expressed at 56 DIV, then 56 DIV protein data was used. If the protein was not significantly differentially expressed at either time point, and the gene was significantly differentially expressed at 35 DIV, then 35 DIV gene data was used. If this also wasn't significant, but significantly different gene expression was seen at 56 DIV, then the 56 DIV gene data was used. Enrichment analyses of gene ontology (GO) terms and KEGG pathways were performed on this integrated dataset by applying Ensemble of Gene Set Enrichment Analyses (EGSEA) (Alhamdoosh et al. 2017) and utilizing all differentially expressed proteins/genes with $p<0.05$ and a FC>1.5 in either direction as input. Significant pathways with adjusted *p*-value<0.05 were reported.

2.5.10. Bioinformatics analysis of phosphoproteomics data

Bioinformatics analysis of phosphoproteomics data was conducted by Dr Benbo Gao (Biogen Inc.) as follows. Phosphorylation site lists exported from the MaxQuant software (Max Planck Insititute of Biochemistry) were used for statistical analysis. Only phosphorylation sites that were quantified in at least 3 out of the 4 replicate experiments were used. The data normalisation, principal component analysis (PCA), and statistical analysis of phosphoproteomics data were performed using R programming language (www.r-project.org), version 3.4.0. The raw data were normalised to the median intensity of all phosphoproteins within the TMT 10-plex set. The normalised intensity for each phosphoprotein was then transformed to a relative ratio by dividing by the mean normalised intensity of the phosphoprotein across the TMT 10-plex set. The LIMMA package (Ritchie et al. 2015) was used for statistical analysis of differential abundance. The *p*-values were

adjusted for multiple comparisons using the Benjamini and Hochberg method (Benjamini and Hochberg 1995); a phosphopeptide was considered significantly different between groups if it had an adjusted *p*-value<0.05. Phosphopeptides that exhibited differential abundances between untreated and LRRK2-inhibitor treated cultures were taken forward for downstream analysis. An ANOVA was conducted to identify phosphopeptides that were significantly modulated in the same direction by both LRRK2 inhibitors in the WT and G2019S lines, and that were not significantly modulated in the same direction by both inhibitors in the KO line. A cut-off of $p<0.001$ was used to identify differentially phosporylated phosphopeptides.

Chapter 3: Optimisation and validation of protocols for the differentiation of iPSCs to ventral-midbrain dopaminergic neurons and midbrain-patterned astrocytes

3.1. Introduction

To achieve the goal of modelling LRRK2 mutation-mediated Parkinson's disease (PD) in iPSC-derived cultures, it is necessary to differentiate iPSCs into the specific neuron and astrocyte subtypes implicated in the disease. As discussed in Section 1.1.3, there are different subtypes of dopaminergic neurons and astrocytes, and only certain types are implicated in PD. Of particular interest are the ventral midbrain dopaminergic (vmDA) neurons of the SNc, which degenerate in PD, and the midbrain astrocytes that surround them. Years of research by developmental biologists have provided a wealth of knowledge about how these cell types develop in the embryo. Careful studies have detailed the precise timings of expression of the transcription factors and growth factors needed for their development, and this knowledge has aided the generation of protocols to produce these specific cell types from iPSCs. This introduction details the field's understanding of how vmDA neurons and midbrain-patterned (MP) astrocytes develop *in vivo* and the differentiation protocols that have been developed to produce vmDA neurons and astrocytes to date.

3.1.1 Embryonic development of vmDA neurons

In the early stages of development, the cells of the embryo differentiate into the three germ layers—endoderm, mesoderm, and ectoderm (Kiecker et al. 2016). Neural specification of ectodermal tissue is induced by the underlying mesoderm, which secretes inhibitors of the Bone Morphogenic Protein (BMP) and Activin pathways (Lamb et al. 1993; Hemmati-

Brivanlou et al. 1994), resulting in dual-SMAD inhibition. This process is followed by neural tube formation, and in response to signals from the underlying mesoderm, a region known as the floor plate develops along the ventral midline of the neural tube (Wilson et al. 2005). A rostral-caudal axis is induced along the neural tube and expression of Orthodentical Homeobox 2 (OTX2) in the forebrain and midbrain, and Gastrulation Brain Homeobox 2 (GBX2) in the hindbrain dictates the positioning of the isthmus organiser at the midbrain-hindbrain boundary (Rhinn and Brand 2001). Wingless-Type MMTV Integration Site Family Member 1 (WNT1) is expressed in the midbrain (Davis and Joyner 1988), Fibroblast Growth Factor 8 (FGF8) is secreted by the isthmus organiser (Rhinn and Brand 2001), and Sonic Hedgehog (SHH) is expressed by the floorplate (Hynes et al. 1995). Ventral midbrain DA (vmDA) neuron progenitors (NPs) then arise from the floorplate where these signals intersect.

Expression of SHH in the floorplate activates expression of Lim Homeobox Transcription Factor 1 Alpha (LMX1A), a transcription factor that is essential for vmDA neuron formation (Andersson et al. 2006). LMX1A then induces expression of Msh Homeobox 1 (MSX1), which in turn induces Neurogenin 2 (NGN2) expression, resulting in neural differentiation (Andersson et al. 2006). LMX1A is co-expressed with Lim Homeobox Transcription Factor 1 Beta (LMX1B) in ventral-midbrain neural progenitors (NPs); LMX1B can partially compensate for LMX1A loss of function, and both are important for the proliferation of vmDA NPs and their subsequent differentiation into vmDA neurons (Yan et al. 2011). Expression of SHH also induces GLI1 expression, which in turn activates expression of another key floorplate marker, Forkhead Box Protein A2 (FOXA2) (Hynes et al. 1997). FOXA2 and LMX1A are both essential for the proper development of vmDA neurons in the midbrain, and continue to be expressed in these cells once they mature (Ferri et al. 2007; Yan et al. 2011).

In addition to its importance for the formation of the vmDA NPs, WNT signalling plays a role in their proliferation and differentiation to vmDA neurons (Hegarty et al. 2013). WNT1 in particular is essential for maintaining expression of Engrailed homeobox 1 (EN1) (Danielian and McMahon 1996; McGrew et al. 1999), which is important for vmDA neuron specification and maintenance (Simon et al. 2001).

As vmDA neurons become post-mitotic and mature, they begin to express Nuclear Receptor Related-1 (NURR1) and Pituitary Homeobox 3 (PITX3). NURR1 is important for the expression of proteins involved in the dopamine synthesis pathway, including Tyrosine Hydroxylase (TH), DOPA Decarboxylase (AADC), Vesicular Monoamine Transporter 2 (VMAT2), and Dopamine Transporter (DAT) (Castillo et al. 1998). This function of NURR1 is specific to vmDA neurons, as the protein is not required in hypothalamic, olfactory or lower-brainstem DA neurons (Castillo et al. 1998). PITX3 is thought to regulate expression of TH and Brain Derived Neurotrophic Factor (BDNF) in vmDA neurons (Maxwell et al. 2005; Peng et al. 2011). Survival of DA neurons in the adult brain has been shown to be maintained by the presence of neurotrophic factors such as BDNF (Hyman et al. 1991) and GDNF (Lin et al. 1993), as well as Transforming Growth Factor Beta 2/3 (TGFβ2/3) (Poulsen et al. 1994). PITX3 expression may therefore be important for the maintenance of both vmDA neuron machinery and cell survival.

3.1.2. Embryonic development of midbrain astrocytes

During development, the same NPs can give rise to both neurons and astrocytes. As described in Section 3.1.1, neurogenesis is known to occur in restricted domains that have been patterned in a way that results in the production of specific neuronal subtypes. Although the development of astrocytes from individual brain regions has not been delineated,

astrogenesis occurs following neurogenesis; as such, it follows that astrocytes produced in each domain will also develop from these restricted progenitors, giving rise to anatomically distinct classes of astrocytes (Hochstim et al. 2008; Tsai et al. 2012). Although this is considered to be the case, little characterisation of the development of such subtypes has been conducted.

Following neurogenesis, NPs undergo a process known as the gliogenic switch, whereby they convert to glial progenitors (GPs). This switch is time dependent, and occurs after numerous rounds of progenitor self-renewal (Shen et al. 2006). Epidermal Growth Factor (EGF) and Fibroblast Growth Factor (FGF) signalling are essential for the maintenance of these proliferating NPs (Kitchens et al. 1994; Tropepe et al. 1999), and also for the production of astrocytes during development (Kornblum et al. 1998; Sibilia et al. 1998; Kang and Song 2010).

It has been demonstrated that once formed, cortical neurons release Cardiotrophin-1 (CT-1), a member of the Interleukin 6 (IL6) family, which also includes Leukaemia Inhibitory Factor (LIF), and Ciliary Neurotrophic Factor (CNTF) (Barnabe-Heider et al. 2005). These molecules have been shown to activate the gp130-JAK-STAT pathway, to promote gliogenesis (Bonni et al. 1997; Ochiai et al. 2001; Barnabe-Heider et al. 2005). Additionally, new-born neurons have been shown to express Notch ligands that enable them to contribute to activation of the gliogenic switch in local notch-expressing NPs (Namihira et al. 2009). Members of the Transforming Growth Factor Beta (TGFβ)/BMP superfamily have also been demonstrated to play a role in astrocyte differentiation. When applied to NPs, BMPs promote neurogenesis; however, when applied to GPs in the presence of LIF, they promote gliogenesis via a SMAD–p300–CREB-binding-protein–STAT complex (Mabie et al. 1999; Nakashima et al. 1999). Furthermore, expression of TGFβ1, either from surrounding neurons or in GPs themselves,

has been shown to promote astrocyte maturation (De Sampaio e Spohr et al. 2002; Stipursky and Gomes 2007). It is not known whether the signalling pathways that lead to terminal astrocyte differentiation are conserved in all brain regions, and no specific markers of midbrain astrocytes have been identified. Nevertheless, terminally differentiated astrocytes are characterised by their expression of Glial Fibrillary Acid Protein (GFAP), a cytoskeletal protein (Bignami et al. 1972; Chiu et al. 1981); Aquaporin 4 (AQP4), a water channel involved in blood-brain barrier function (Nielsen et al. 1997; Nico et al. 2001); Glutamate-Aspartate Transporter 1 (GLAST1), which takes up glutamate from the extracellular space (Arriza et al. 1994; Lehre et al. 1995); and S100 Calcium Binding Protein B (S100B), which is expressed in a subset of mature astrocytes (Raponi et al. 2007).

3.1.3. Protocols for the differentiation of iPSCs into vmDA neurons

Early protocols for vmDA neuron differentiation from human pluripotent stem cells (hPSCs) employed the use of embryoid bodies, or differentiation of cells on stromal or astrocytic feeders in the presence of SHH alone or in combination with FGF8 (Perrier et al. 2004; Zeng et al. 2004; Park et al. 2005; Roy et al. 2006). Although these protocols produced reasonable yields of functional DA neurons (Perrier et al., 19–40%; Zeng et al., not quantified; Park et al., 12.5%; Roy et al., 13.4%) they did not demonstrate midbrain specification as denoted by expression of the floor-plate transcription factors FOXA2 and LMX1A. In 2009, a protocol utilising forced expression of LMX1A via lentiviral transduction following patterning of neural progenitors with SHH and FGF8 was developed for mESCs (Friling et al. 2009). This protocol was then adapted for use in hESCs and iPSCs by the research team of Belmonte and was successful in producing DA neurons, a subset of which expressed vmDA neuron markers including LMX1B, NURR1 and PITX3 (Sanchez-Danes et al. 2012b).

Two protocols that used small molecules and growth factors to promote differentiation of hPSCs to a vmDA fate were subsequently published in 2011 and 2012 by the research teams of Studer (Kriks et al. 2011) and Parmar (Kirkeby et al. 2012) respectively. The Kriks protocol from the Studer laboratory begins with a monolayer of human embryonic stem cells (hESCs), whereas the Kirkeby protocol from the Parmar laboratory starts with embryoid bodies. Both protocols involve precise patterning of the cells by dual-SMAD inhibition, activation of SHH and FGF8 signalling, and—the key component that was missing in previous protocols—activation of WNT signalling via Glycogen Synthase Kinase 3 Beta (GSK3β) inhibition. Both protocols demonstrated production of high yields of FOXA2/LMX1A double-positive floorplate progenitors by 11 DIV (Kriks ~60%, Kirkeby ~80%). Additionally, the Kriks publication demonstrated that after maintenance of their cultures in the presence of neurotrophic factors for a further 39 days, 75% of the cells were positive for TH, and 80% were positive for FOXA2. The Kriks protocol was further optimised in a second paper from the group (Miller, JD. 2013), which introduced a treatment with the anti-mitotic agent mitomycin C to remove proliferating background cells, resulting in more consistent purity of the cultures. From here on, reference to the 'Modified Kriks' protocol includes the addition of this step. Following publication of these protocols, the Wade-Martins laboratory published the Hartfield protocol (Hartfield et al. 2014), and the Fernandes protocol (Fernandes et al. 2016). Both of these protocols involve attachment of embryoid bodies to a Geltrex-coated culture surface, followed by midbrain patterning using dual-SMAD inhibition, activation of SHH and FGF8 signalling, and inhibition of GSK3β. Neural rosettes are then manually selected, expanded, and matured to produce cultures containing around 40-50% Beta-III Tubullin (TUJ1)-positive neurons and 10-20% TH-positive neurons, with expression of FOXA2 demonstrated but not quantified (Hartfield et al 2014; Fernandes et al. 2016).

3.1.4. Protocols for the differentiation of iPSCs into MP astrocytes

At the beginning of this study, no protocols were available for the specific production of MP astrocytes; however, a number of protocols for the derivation of other types of astrocyte had been published. These all start from either non-specific NPs to make generic astrocytes (Emdad et al. 2012; Juopperi et al. 2012; Shaltouki et al. 2013; Chen et al. 2014), motor neuron/spinal-cord NPs to make spinal-cord astrocytes (Serio et al. 2013; Roybon et al. 2013), or broadly defined forebrain/midbrain and hindbrain/spinal cord NPs to make corresponding forebrain/midbrain and hindbrain/spinal-cord astrocytes (Krencik and Zhang 2011). A common theme amongst these protocols is the induction of a proliferative state, using various combinations of EGF, FGF2, LIF, BMP4, and Fetal Bovine Serum (FBS) to induce NPs to self-renew until they undergo a temporally controlled switch to GPs. Final maturation of GPs then involves either continued growth in EGF/FGF2 with FBS (Roybon et al. 2013), or in maturation medium containing either CNTF with or without FBS (Emdad et al. 2012; Krencik and Zhang 2011; Serio et al 2013), or Heregulin, Insulin-Like Growth Factor 1 (IGF1) and Activin A (Shaltouki et al. 2013). All of these protocols demonstrated production of a high yield of astrocytes (55% to >95%), as measured by quantification of immunostaining for GFAP-positive cells.

3.2. Aims of this chapter

1. To describe and discuss the identification, optimisation, and validation of a protocol for the differentiation of **vmDA neurons**.
2. To describe and discuss the development, optimisation, and validation of a protocol for the differentiation of **MP astrocytes**.

3.3. Results I: Differentiation of vmDA neurons from iPSCs

3.3.1. iPSC lines for differentiation

iPSC lines were provided by Jane Vowles and Sally Cowley at the James Martin Stem Cell Facility, Sir William Dunn School of Pathology, University of Oxford. All lines were karyotypically normal, and determined to be pluripotent using the Pluritest gene array. A mixture of WT and LRRK2-G2019S mutant iPSC lines were used for the development and characterisation of protocols in this chapter (Sections 3.3-3.5) (Table 3.1).

Table 3.1. iPSC lines used in this chapter.
Confirmatory genotyping of lines can be found in Appendix (i).

#	Cell line	Age/Sex	LRRK2 Genotype	Reprogramming method	Figures included in
1	NHDF1	44/F	WT	Retrovirus	1.2, 1.5, 1.6, 1.7, 1.8, 1.15, 1.17
2	JR053-6	68/M	WT	Retrovirus	1.5, 1.7, 1.11, 1.12, 1.14, 1.15, 1.17, 1.18
3	SFC840-3	67/F	WT	Cytotune (Sendai virus)	1.3
4	SFC840-6	67/F	WT	Cytotune (Sendai virus)	1.5
5	JR036-1	49/M	LRRK2 G2019S	Retrovirus	1.3, 1.5, 1.7, 1.8, 1.10, 1.11, 1.12, 1.13, 1.14, 1.15, 1.17, 1.18
6	MK144-7	57/F	LRRK2 G2019S	Retrovirus	1.5, 1.7
7	MK002-4	72/F	LRRK2 G2019S	Retrovirus	1.3
8	SFC832-19	77/F	LRRK2 G2019S	Cytotune (Sendai virus)	1.15, 1.17

3.3.2. Identification of protocols for the differentiation of vmDA neurons from iPSCs

When this study began, the Wade-Martins laboratory was producing vmDA neurons from iPSC-derived embryoid bodies using the Fernandes protocol (Figure 3.1A). A disadvantage of using embryoid bodies for patterning is that a proportion of the cells are already committed to the mesoderm and endoderm fates, so are not capable of producing neurons. As such, this protocol produces a mixed culture containing 40-50% TUJ1-positive neurons and 10-20% TH-

positive DA neurons, a proportion of which are vmDA neurons. A further disadvantage of this protocol is the necessity for the manual dissection of neural rosettes, which does not allow for counting of cells, making it near impossible to plate the same number of cells per well. This step results in variable cultures, and means that the protocol is not scalable for large experiments.

Other protocols from the literature were considered to assess their suitability as a replacement for the Fernandes protocol (Table 3.2). A number of parameters were taken into consideration: the percentage of vmDA neurons produced and the time taken to produce them, whether the protocol involved formation of embryoid bodies or the use of a monolayer of cells, whether feeder cells were needed, the type of passaging method, and the method of induction. The Modified Kriks protocol (Figure 3.1B) was selected due to the fact that it involves patterning of a monolayer of hESCs/iPSCs in combination with enzymatic dissociation steps, which theoretically make this protocol more scalable and reproducible. Furthermore, it promised the highest yield of vmDA neurons, and included a selection step to remove unwanted proliferating progenitor cells (Section 3.1.3). Table 3.3 outlines the functional role of each small molecule or growth factor used for derivation of vmDA neurons from iPSCs using the Modified Kriks and the Fernandes protocols.

Table 3.2. Comparison of protocols for the differentiation of iPSCs to vmDA neurons.

Protocol	Percentage DA neurons (vmDA neurons)	Time to produce DA neurons	Starting cell type	Extracellular matrix (ECM) or feeder cells (FC)	Passaging method	Method of induction
Fernandes	10-20% (Present, not quantified)	35 days	iPSC-derived Embryoid bodies	ECM: Geltrex	Manual dissection	Small molecule
Kriks	75% by day 50 (~75%)	25 days	hESC monolayer	ECM: Matrigel then combination of poly-L-ornithine, laminin and fibronectin	Enzymatic	Small molecule
Modified Kriks	75% expected by day 50 (~75% expected)	25 days	hESC /iPSC monolayer	ECM: Matrigel then combination of poly-L-ornithine, laminin and fibronectin	Enzymatic	Small molecule
Kirkeby	Present, not quantified (Present, not quantified)	42 days	hESC-derived Embryoid bodies	ECM: Combination of poly-L-ornithine, laminin and fibronectin	Enzymatic	Small molecule
Sanchez-Danes	41% (Present, not quantified)	34 days	hESC/iPSC-derived Embryoid bodies	FC: PA6 for final stage	Mechanical dissociation with pipette	Combination of small molecules and use of LMX1A overexpressing stable lines

Table 3.3. Functional role of growth factors and small molecules for the differentiation of vmDA neurons from iPSCs.

Growth factor/ small molecule name	Abbreviation	Function in differentiation protocol
Y27632	Ri	Inhibition of Rho-associated, coiled-coil containing protein kinase (ROCK), to prevent induction of apoptosis of iPSCs (Watanabe et al. 2007).
LDN-193189	LDN	Induction of neural fate via inhibition of Bone Morphogenic Protein (BMP) receptors to prevent phosphorylation of Mothers against decapentaplegic homolog (SMAD) 1/5/8 proteins (Surmacz et al. 2012).
SB-431542	SB	Induction of neural fate via inhibition of Transforming Growth Factor beta (TGFβ) receptors to prevent phosphorylation of SMAD 2/3 proteins (DaCosta Byfield et al. 2004; Smith et al. 2008).
CHIR99021	CHIR	Necessary for floorplate cell patterning, promotes proliferation and differentiation of floorplate progenitors to vmDA neurons, through activation of WNT signalling via GSK3β inhibition (Kriks et al. 2011).
Sonic Hedgehog C24II N-terminal fragment	SHH	Necessary for floorplate patterning and vmDA neuron specification (Andersson et al. 2006).
Purmorphamine	-	A small molecule SHH agonist, that boosts SHH signalling in the culture to further promote floorplate patterning (Kriks, et al. 2011).
Fibroblast Growth Factor-8a	FGF8a	Necessary for floorplate patterning (Rhinn and Brand 2001).
Heparin	-	Promotes DA neuron differentiation (Yamazoe et al. 2006)
Brain-derived neurotrophic factor	BDNF	Neurotrophic factor that promotes survival of vmDA neurons (Hyman et al. 1991).
Glial-derived neurotrophic factor	GDNF	Neurotrophic factor that promotes survival of vmDA neurons (Lin et al. 1993).
Transforming growth factor beta 3	TGFβ3	Neurotrophic factor that promotes survival of vmDA neurons (Poulsen et al. 1994).
DAPT	-	Inhibits progenitor proliferation and promotes neuronal differentiation through notch inhibition by targeting γ-Secretase (Ogura et al. 2013).
Ascorbic acid	AA	Promotes differentiation of progenitors to DA neurons (Yan et al. 2001).
N^6,2′-O-Dibutyryladenosine 3′,5′-cyclic monophosphate	db-cAMP	Promotes differentiation and maturation of DA neurons (Mena et al. 1995).

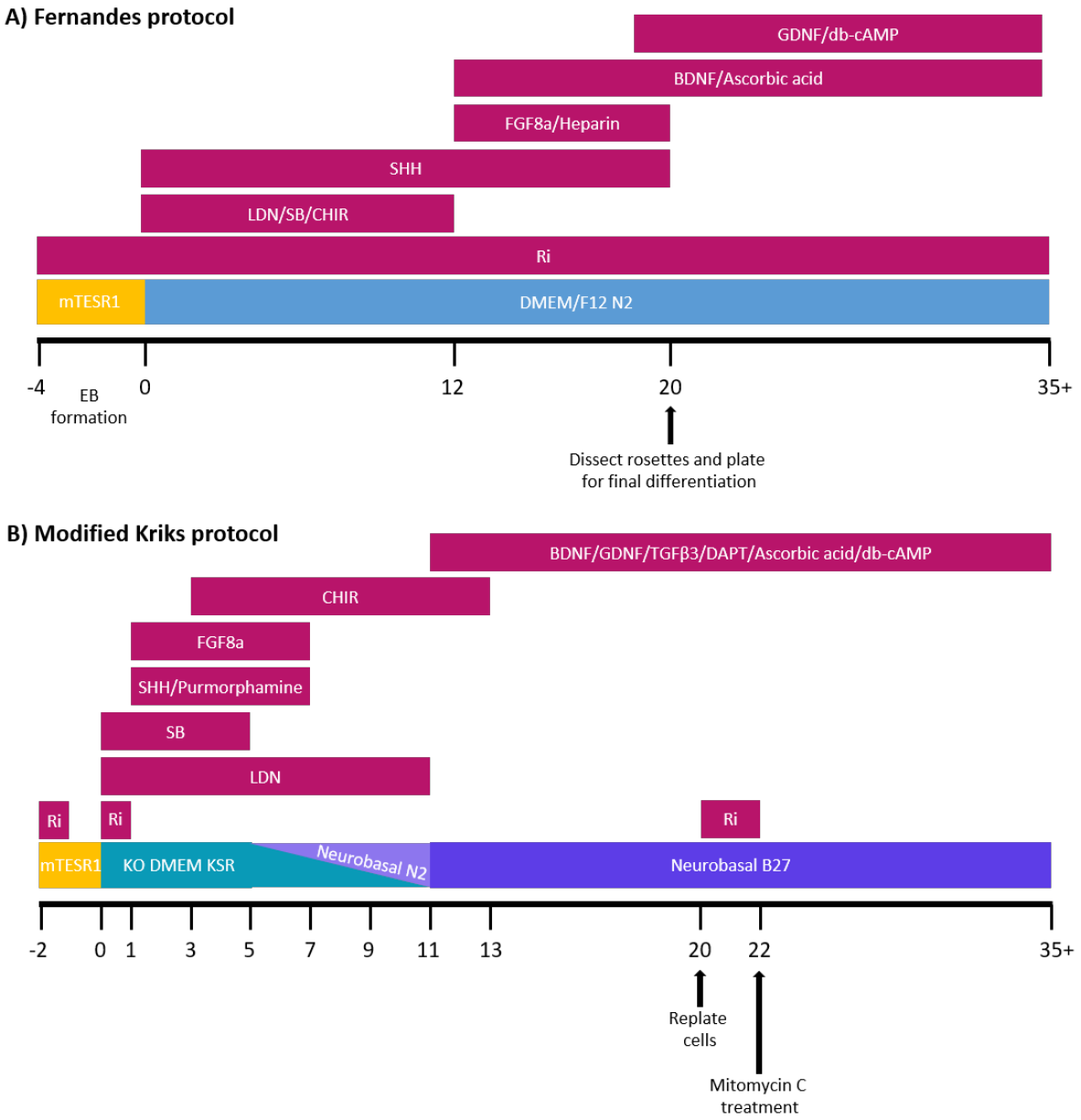

Figure 3.1. iPSC-derived vmDA-neuron differentiation protocol schematics.

Schematics showing A) the Fernandes protocol and B) the Modified Kriks protocol for differentiation of vmDA neurons. Numbers denote days in vitro (DIV). iPSCs are plated at A) -4 DIV for embryoid body formation or B) -2 DIV as a monolayer. Neural induction is initiated at 0 DIV in both cases. Abbreviations: Y27632 (Ri); LDN-193189 (LDN); SB-431542 (SB); CHIR99021 (CHIR); Sonic Hedgehog C24II N-terminal fragment (SHH); Fibroblast Growth Factor-8a (FGF8a); Brain-derived neurotrophic factor (BDNF); Glial-derived neurotrophic factor (GDNF); N^6,2'-O-Dibutyryladenosine 3',5'-cyclic monophosphate (db-cAMP).

3.3.3. Optimisation of the Modified Kriks protocol for use with feeder-free iPSCs

The Modified Kriks protocol was originally developed using hESCs and iPSCs that had been cultured on MEFs, then transferred into feeder-free conditions for differentiation. It was not known whether the conditions used in the original publication would be directly applicable to differentiation of iPSCs that had undergone long-term culture in feeder-free conditions. Therefore, careful optimisation of the modified Modified Kriks protocol was conducted. The optimisation discussed in this section (Section 3.3.3) was completed in collaboration with Federico Zambon (University of Oxford).

Firstly, the initial iPSC plating density was assessed. The density used in the Kriks protocol is 3.5-4.0x10^4 cells/cm^2; however, the publication also dictates that cells must be >70% confluent when patterning begins. In order to achieve this confluency within two days of plating using feeder-free iPSCs, a seeding density of 1.25-1.50x10^5 cells/cm^2 was necessary. Secondly, it was noticed that as the cells were patterned, they became very dense and began to peel off the culture plates. Two factors were found to be crucial in alleviating this issue. Firstly, the extracellular matrix used to adhere the cells to the plates was changed from Matrigel to Geltrex, which resulted in better adherence. Secondly, it was noted that whilst the cell culture medium was changed every two days, it was becoming acidic very rapidly. To combat this, the volume of medium used was increased from two to four millilitres per six-well, and an additional half media change conducted on the intervening days. Finally, the extracellular matrix (poly-L-ornithine, laminin and fibronectin) used for the neuronal maturation stage in the original protocol did not result in strong enough adherence of the cells, which had the propensity to peel off the culture dish. It was found that coating of wells with Geltrex resulted in better adherence of the cultures (Figure 3.2). This optimised version

of the Modified Kriks protocol is referred to as the Booth-Zambon protocol from here onwards (Figure 3.3).

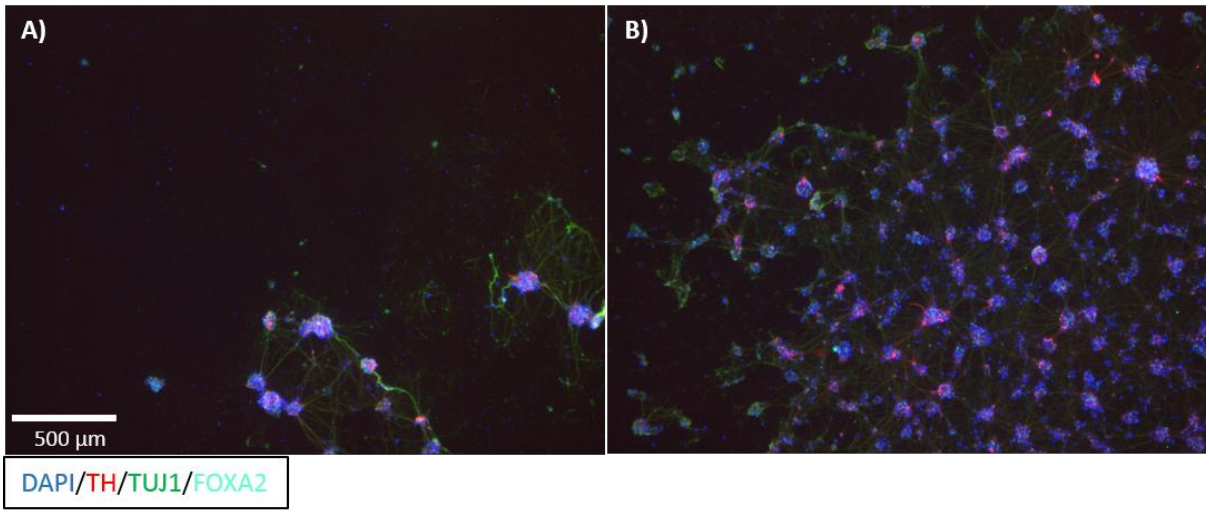

Figure 3.2. Comparison of extracellular matrices for culture of iPSC-derived vmDA neurons during the Modified Kriks protocol.
vmDA neuron cultures derived using the modified Kriks protocol were grown on A) poly-L-ornithine with laminin and fibronectin, or B) Geltrex, from 20 DIV. Cells were fixed at 35 DIV and immunostained for TH (red), TUJ1 (green) and FOXA2 (cyan), and co-stained with DAPI (blue).

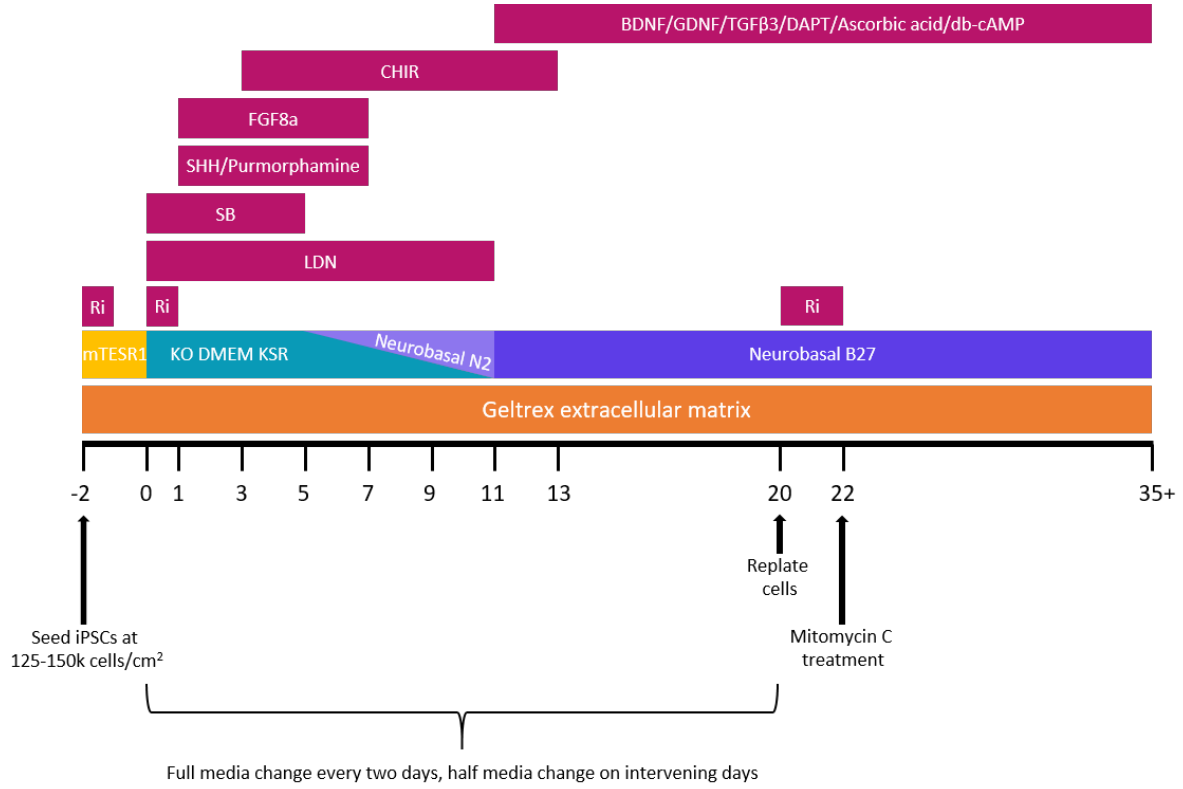

Figure 3.3. The Booth-Zambon protocol for derivation of vmDA neurons from iPSCs.
Schematic showing the Booth-Zambon protocol and indicating key points of optimisation. iPSCs are plated at -2 DIV as a monolayer on Geltrex extracellular matrix. Neural induction is initiated at 0 DIV, with media changes every two days from 1 DIV, and half media changes on intervening days. After 20 DIV, cells are replated onto Geltrex extracellular matrix, and matured in medium containing growth factors. Abbreviations: Y27632 (Ri); LDN193189 (LDN); SB431542 (SB); CHIR99021 (CHIR); Sonic Hedgehog C24II N-terminal fragment (SHH); Fibroblast Growth Factor-8a (FGF8a); Brain-derived neurotrophic factor (BDNF); Glial-derived neurotrophic factor (GDNF); N^6,2'-O-Dibutyryladenosine 3',5'-cyclic monophosphate (db-cAMP).

3.3.4. Comparison of the Booth-Zambon and Fernandes protocols for differentiation of iPSCs to vmDA neurons

Once the Booth-Zambon protocol had been optimised, differentiation of three iPSC lines was conducted in parallel using this and the Fernandes protocols, to compare their ability to produce TH-positive cells. It was found that the Booth-Zambon protocol consistently produced a higher proportion of TH positive cells, as assessed by immunostaining and western blotting for TH (Figure 3.4A-C). Additionally, expression of LRRK2 was assessed to ensure that the cultures resulting from these protocols would be suitable for studying the functional impact of LRRK2 mutations. As LRRK2 is expressed in many cell types, and is present at relatively low levels in DA neurons, it was not known what effect the change in culture composition would have on LRRK2 expression. Western blot analysis demonstrated that there was no significant difference in expression of LRRK2 between the two protocols (Figure 3.4B, D). As such, due to its higher yield of TH-positive cells, the Booth-Zambon protocol was chosen as the protocol for producing vmDA neuron cultures for the duration of this study.

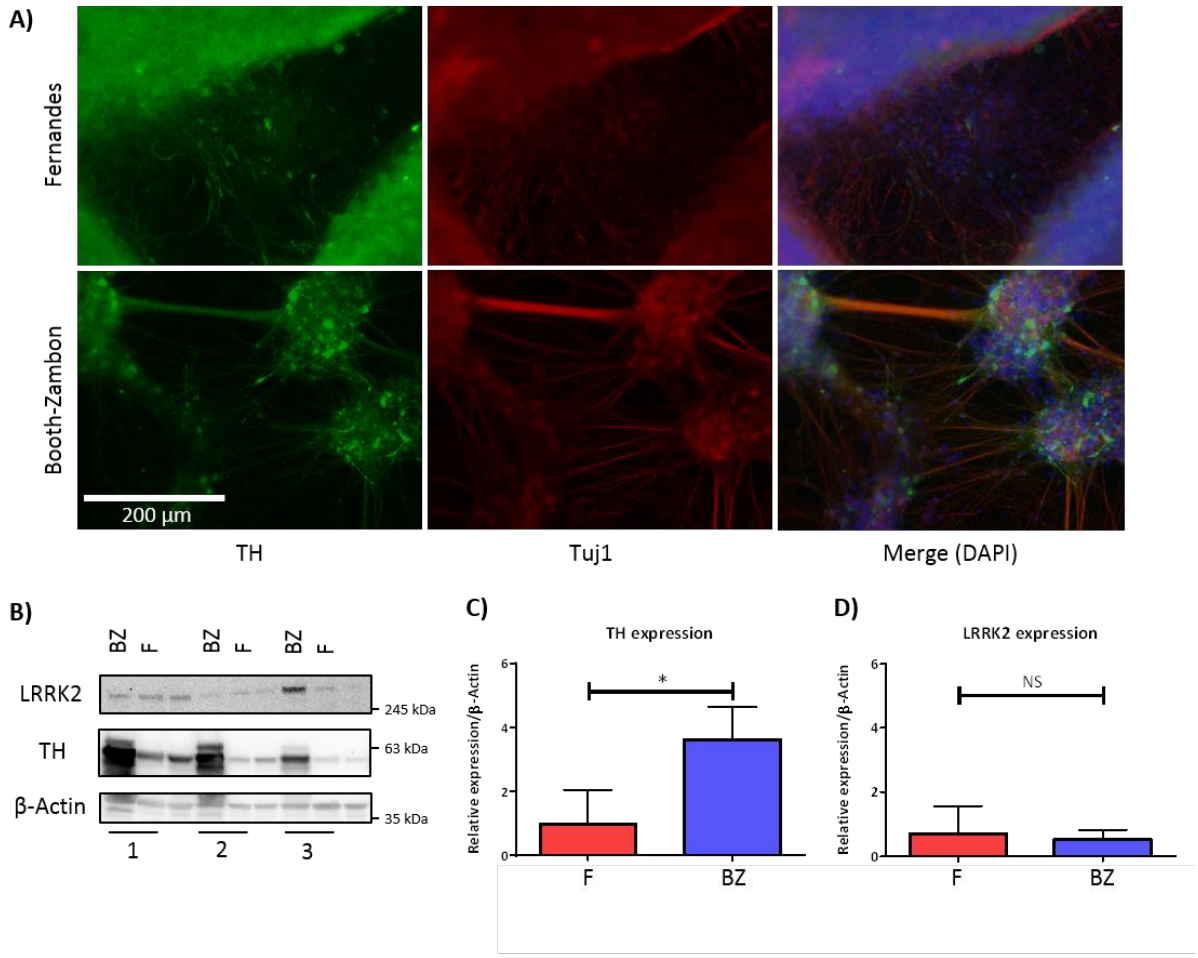

Figure 3.4. Analysis of culture composition in vmDA-neuron cultures derived from iPSCs using the Fernandes and Booth-Zambon protocols.

*A) Immunostaining of vmDA neurons differentiated using the Fernandes and Booth-Zambon protocols at 35 DIV for TH (green), TUJ1 (red) and DAPI (blue). B) Western blot images demonstrating expression of TH and LRRK2 in vmDA neurons differentiated from three independent iPSC lines (1-3) using the Fernandes (F) and Booth-Zambon (BZ) protocols. Analysis of C) TH and D) LRRK2 protein levels as measured by western blot in B). (Graphs show average of three lines, from one differentiation, mean ± SD, Student's T-Test *p<0.05, NS = not significant).*

3.3.5. Characterisation of vmDA neurons differentiated from iPSCs using the Booth-Zambon protocol

Four iPSC lines were differentiated into vmDA neurons following the Booth-Zambon protocol and a full molecular characterisation was conducted. Immunostaining for LMX1A and FOXA2 was carried out at 11 DIV to confirm derivation of neurons through the floorplate lineage (Figure 3.5A, C). Immunostaining for the vmDA neuron markers TH and FOXA2, as well as the pan-neuronal marker TUJ1, was carried out at 35 DIV to assess the percentage of vmDA

neurons in the cultures (Figure 3.5B, D). On average, 80% of the cells were found to be positive for Tuj1, with 31% identified as DA neurons by staining for TH, and >80% of the cells positive for FOXA2. In addition to immunostaining, real-time qPCR analysis was also carried out for these markers as well as the more mature vmDA neuronal markers PITX3, G Protein-Activated Inward Rectifier Potassium Channel 2 (GIRK2), NURR1 and VMAT2 (Figure 3.5E). Furthermore, Federico Zambon conducted western blot analysis confirming the presence of the DA markers TH, DAT, VMAT2, AADC and GIRK2 in the cultures (Figure 3.5F).

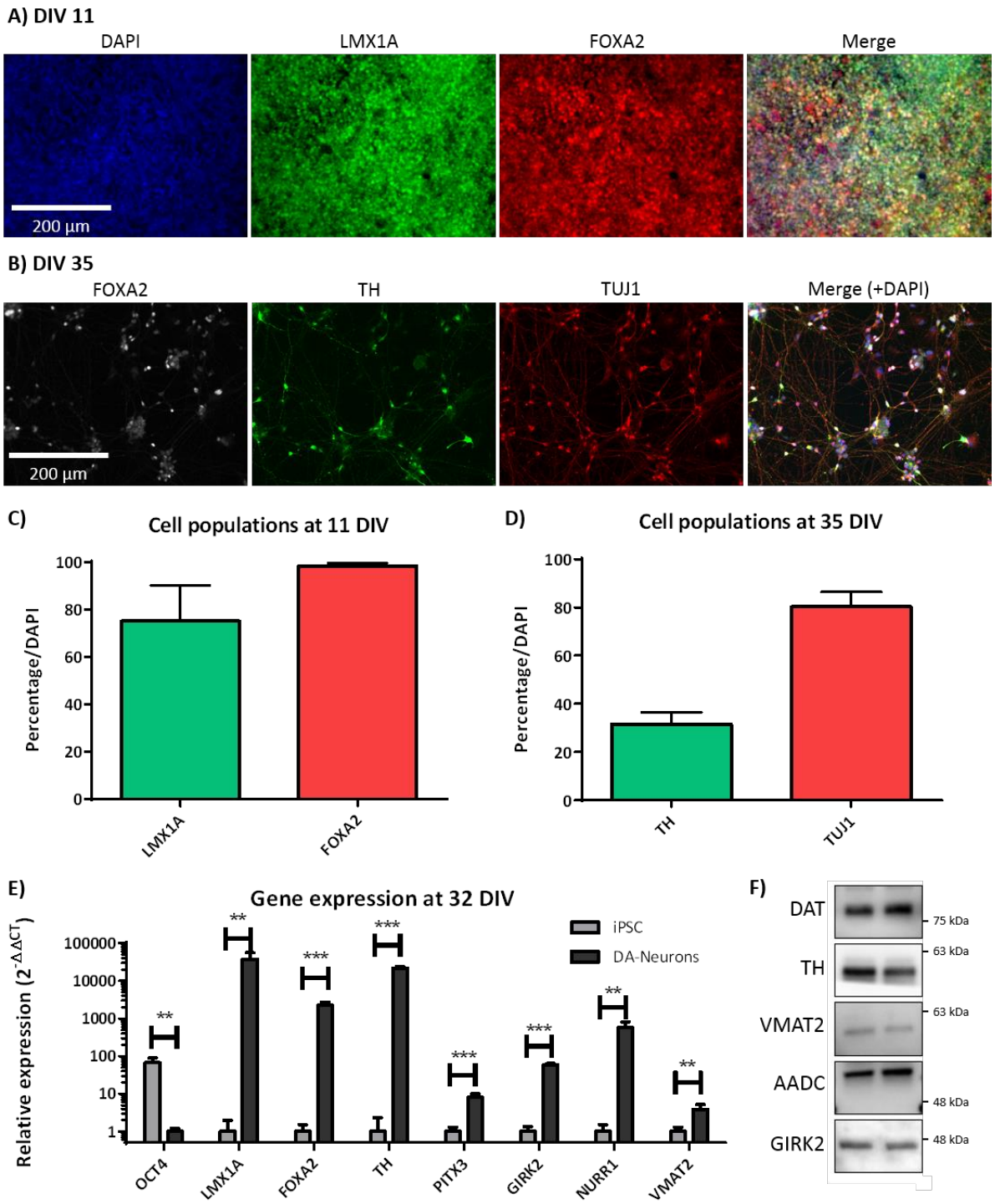

Figure 3.5. Characterisation of iPSC-derived vmDA-neuronal cultures generated using the Booth-Zambon protocol.

*Representative immunostained images of cells differentiated using the Booth-Zambon protocol at A) 11 DIV, and B) 35 DIV, and analysis of cell populations at each of these timepoints C) and D). E) Shows gene expression analysis of the pluripotency marker OCT4, as well as the vmDA neuron markers LMX1A, FOXA2, TH, PITX3, GIRK2, NURR1, and VMAT2. F) Shows western blots for for TH, DAT, VMAT2, AADC and GIRK2 in iPSC-derived vmDA neuron cultures from one control line (NHDF1), conducted by Federico Zambon. (All graphs show average of four lines, from one differentiation, mean ± SD. Student's T-Test **p<0.01, ***p<0.001)).*

Treatment with neurotrophic factors including BDNF and GDNF results in protective effects in a number of PD models, and GDNF is currently being explored as a therapy for PD (Migliore et al. 2014; Tereshchenko et al. 2014; Hernandez-Chan et al. 2015; Nam et al. 2015; Razgado-Hernandez et al. 2015). Before further characterisation was conducted, it was considered that maintaining iPSC-derived vmDA neuron cultures in the neurotrophic environment used thus far in the Booth-Zambon protocol could mask disease phenotypes that might otherwise arise. Therefore, the necessity for the addition of growth factors in the culture medium during the final stage of differentiation was reassessed. Three conditions for withdrawal of growth factors were tested; cells were plated at 20 DIV either into base medium (Neurobasal, B27 without vitamin A, L-glutamine), or into complete final medium (Neurobasal, B27 without vitamin A, L-glutamine, BDNF, GDNF, TGFβ3, DAPT, AA, db-cAMP), which was replaced with base medium after two or seven days. These conditions were compared to maintaining final medium throughout the 14-day period (Figure 3.6). It was found that withdrawal of growth factors at all stages tested resulted in cultures that appeared healthy and neuronal, but that were devoid of any neurons expressing the DA neuron marker TH (Figure 3.6). It was therefore concluded that the inclusion of growth factors was essential for the maintenance of vmDA-neuronal cultures.

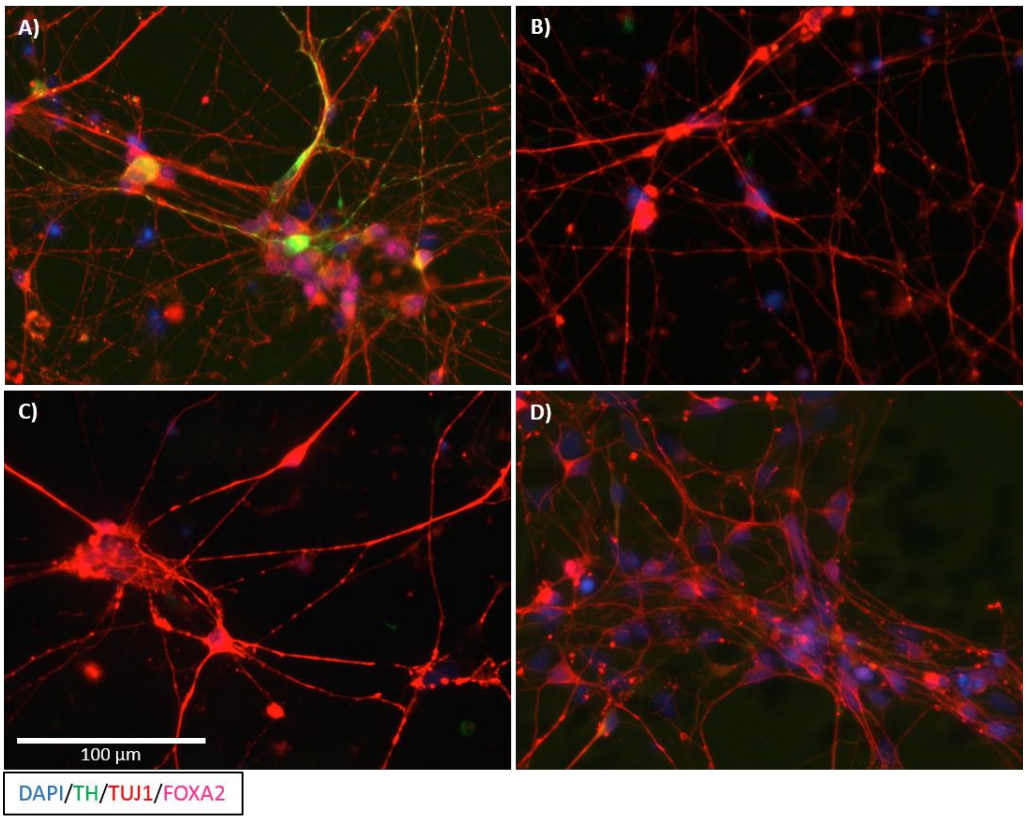

Figure 3.6. Effect of withdrawal of growth factors from iPSC-derived vmDA-neuron cell culture medium.
Cells were differentiated as described until A) 35 DIV, B) 27 DIV, C) 22 DIV and D) 20 DIV at which point growth factors were withdrawn. Cells were fixed at 35 DIV then immunostained for TH (green), TUJ1 (red) and FOXA2 (pink), and co-stained with DAPI (blue) to assess their identity.

To determine whether the cells produced using the Booth-Zambon protocol displayed functional properties of DA neurons, their ability to produce dopamine and to fire action potentials was assessed. HPLC analysis of dopamine content demonstrated that the cells possessed functional dopamine synthesis machinery by 35 DIV (Figure 3.7).

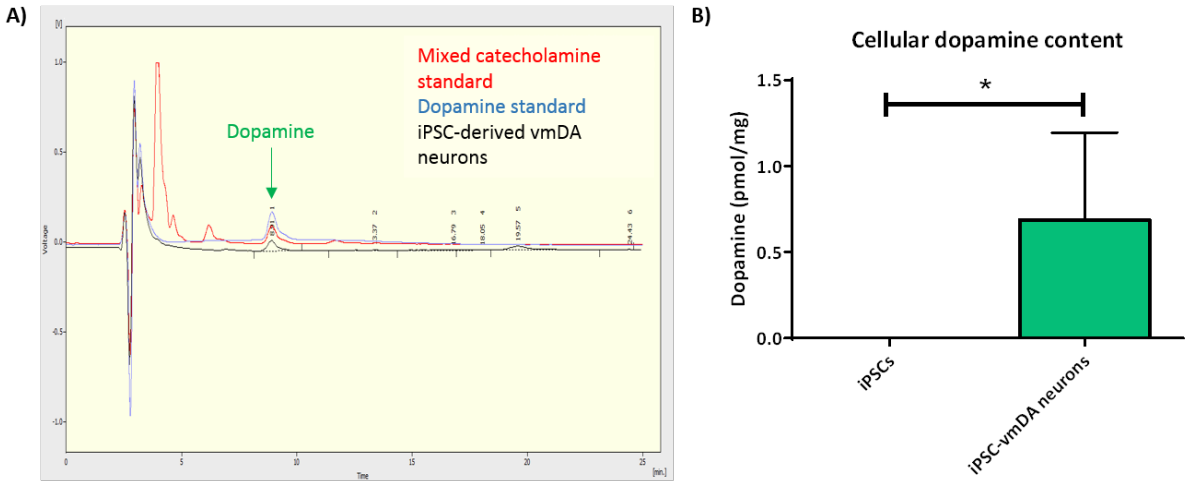

Figure 3.7. Dopamine content of iPSC-derived vmDA-neuron cultures.
*A) Example HPLC trace demonstrating the presence of dopamine in vmDA neurons derived using the optimised Booth-Zambon protocol. Traces show mixed catecholamine standard (red), dopamine standard (blue) and example iPSC-derived vmDA neuron sample (black). B) Quantification of dopamine levels in iPSCs and iPSC-derived vmDA neurons. (Graph shows average of four lines, from one differentiation, mean ± SD, Mann-Whitney test *p<0.05).*

Electrophysiological analysis was conducted on cells from one representative control line (NHDF1) by Emma Whiteley (University of Oxford). Seventeen cells, at 52 DIV and 72 DIV, were assessed using whole cell patch clamp and all were capable of firing multiple action potentials (Figure 3.8A). Of these cells, three were filled with biotin and then immunostained for TH and biotin (Figure 3.8B). One biotin-labelled cell remained after immunostaining and was positive for TH, indicating that at least a proportion of the cells analysed were DA neurons. Several electrophysiological properties of the cells were examined, including their resting membrane potentials, which were found to be around -60mV (Figure 3.8C), similar to those seen in *ex-vivo* vmDA neurons in mouse brain slices (Gambardella, C. 2012). These results demonstrate that vmDA neuron cultures produced using the Booth-Zambon protocol synthesise dopamine and exhibit electrophysiological properties of mature neurons. These characteristics indicate that they are an excellent model of *bona-fide* vmDA neurons, and

should be suitable for studying the role of LRRK2 in early PD mechanisms. The Booth-Zambon protocol is used from here onwards to produce vmDA neurons.

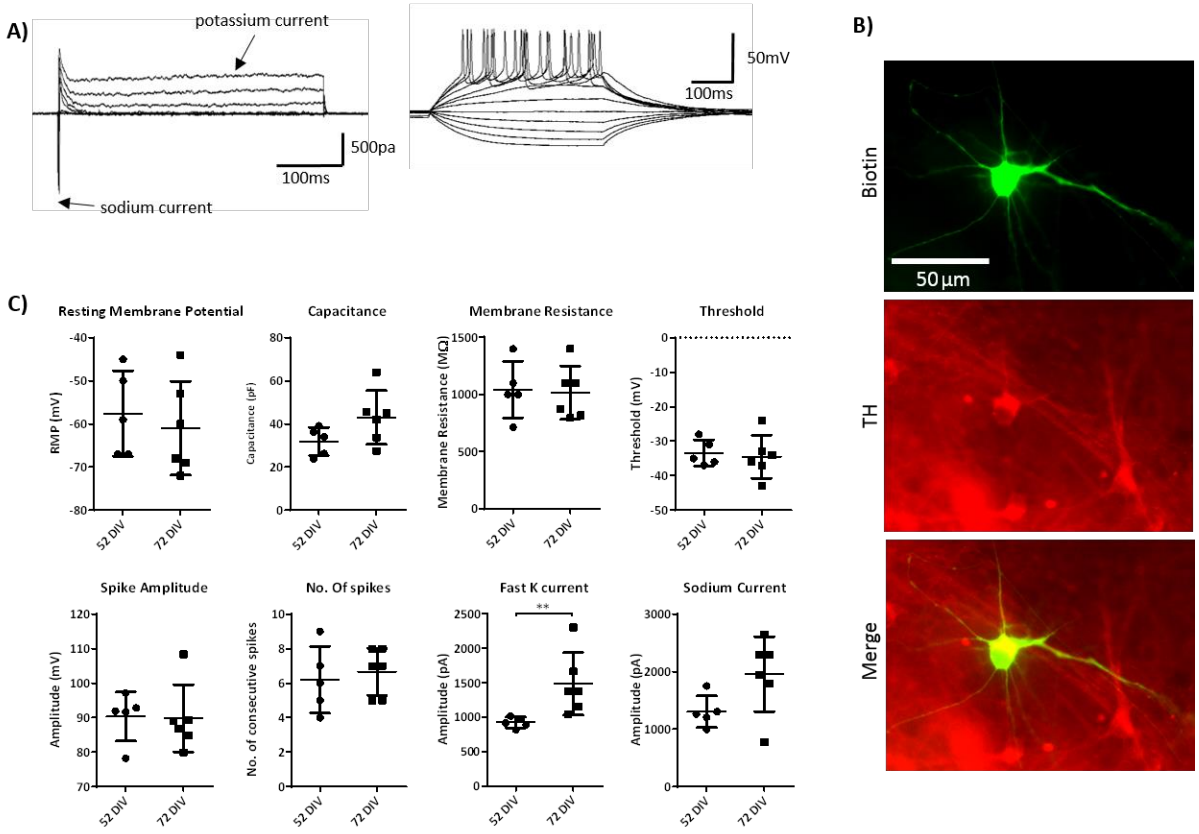

Figure 3.8. Electrophysiological analysis of iPSC-derived vmDA-neuron cultures.
*A) Electrophysiological analysis performed by Emma Whiteley, using whole-cell patch clamp, demonstrated that iPSC-derived vmDA neurons differentiated from one representative iPSC line (NHDF1) are capable of producing sodium and potassium currents, and firing multiple action potentials. B) Biotin was injected into cells through the electrode following the recording, cells were then fixed and immunostained for biotin (green) and TH (red). C) During recording, intrinsic membrane properties of the cells were measured. (Graphs show mean ± SD, Mann-Whitney Test ** p<0.005).*

3.4. Results II: Differentiation of MP astrocytes from iPSCs

3.4.1. Development of a protocol to produce MP astrocytes from iPSCs

Although it is considered that astrocytes arise from regionally patterned glial progenitors (GPs) within the brain, no specific markers of midbrain astrocytes have been identified. As such, the aim here was to develop a protocol to produce astrocytes from midbrain-patterned (MP) progenitors, referred to as MP astrocytes. A collaborator from the Cowley research group, Dr Federica Rinaldi (University of Oxford), had successfully modified the Serio protocol (Serio et al. 2013) for derivation of cortical astrocytes from monolayer cultures (Rinaldi et al. unpublished). For this reason, the Rinaldi protocol was chosen as a starting point for deriving MP astrocytes (Figure 3.9).

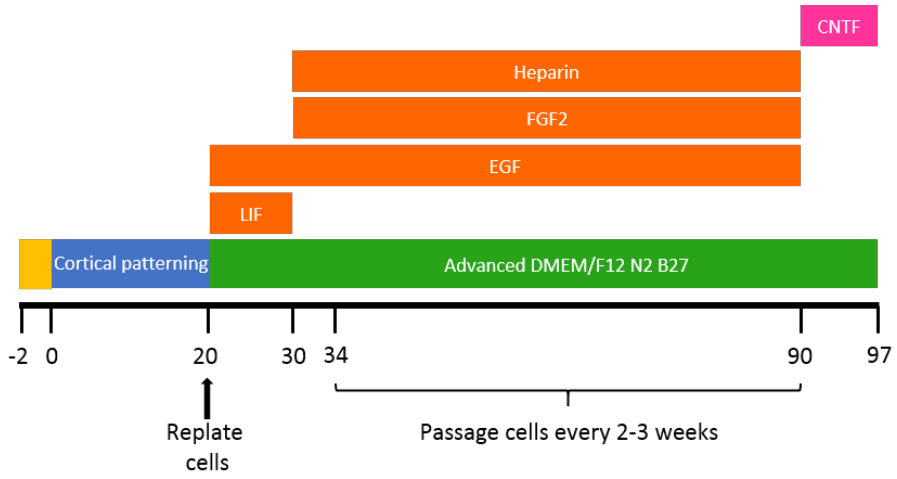

Figure 3.9. The Rinaldi protocol for differentiation of iPSCs to cortical astrocytes.
Numbers denote days in vitro (DIV). iPSCs are plated as a monolayer at -2 DIV. Neural induction is initiated at DIV 0 in both cases. Induction of neural progenitors to a glial fate is initiated from 20 DIV. Cultures are maintained in a proliferative environment until 90 DIV, when they are treated with the gliogenic factor CNTF. Abbreviations: Leukaemia inhibitory factor (LIF); Epidermal growth factor (EGF); Fibroblast growth factor-2 (FGF2); Ciliary neurotrophic factor (CNTF).

An important step for developing a protocol for the specific production of MP astrocytes, rather than cortical astrocytes, was to replace the cortical patterning in the Rinaldi protocol

with the midbrain patterning employed in the Booth-Zambon protocol for the production of vmDA neurons. In order to successfully culture midbrain progenitors for the derivation of astrocytes, it was necessary to grow them to a point at which proliferation could be maintained. Midbrain-patterned cells differentiated using the Booth-Zambon protocol are replated at 20 DIV, so it was known that they would survive replating at this stage. However, there was a concern that the cells would have shifted too far towards a neuronal fate by this timepoint. It was known that cells adopt a floorplate identity by 11 DIV, but are not yet neuronal; however, their capacity to survive replating was unknown. Therefore, both of these timepoints were assessed for development of the MP astrocyte differentiation protocol. iPSCs were patterned following the Booth-Zambon protocol until 11 DIV and 20 DIV (Figure 3.10), at which point they were dissociated and replated at a range of densities in media containing EGF and LIF, as detailed in the Rinaldi protocol. Cells that were replated at 11 DIV failed to proliferate and eventually died (data not shown), whereas cells replated at 20 DIV successfully expanded in culture.

Table 3.4. Functional role of growth factors for the differentiation of MP astrocytes from iPSCs.

Growth factor/ small molecule name	**Abbreviation**	**Function in differentiation protocol**
Leukaemia inhibitory factor	LIF	Induction of progenitor proliferation (Sanalkumar et al. 2010).
Epidermal growth factor	EGF	Induction of glial progenitor fate and maintenance of progenitor proliferation (Sanalkumar et al. 2010).
Fibroblast growth factor	FGF2	Maintenance of progenitor proliferation (Tropepe et al. 1999).
Heparin	-	Maintenance of progenitor proliferation (Kelly et al. 2005).
Ciliary neurotrophic factor	CNTF	Promotion of astrocyte differentiation (Bonni et al. 1997).

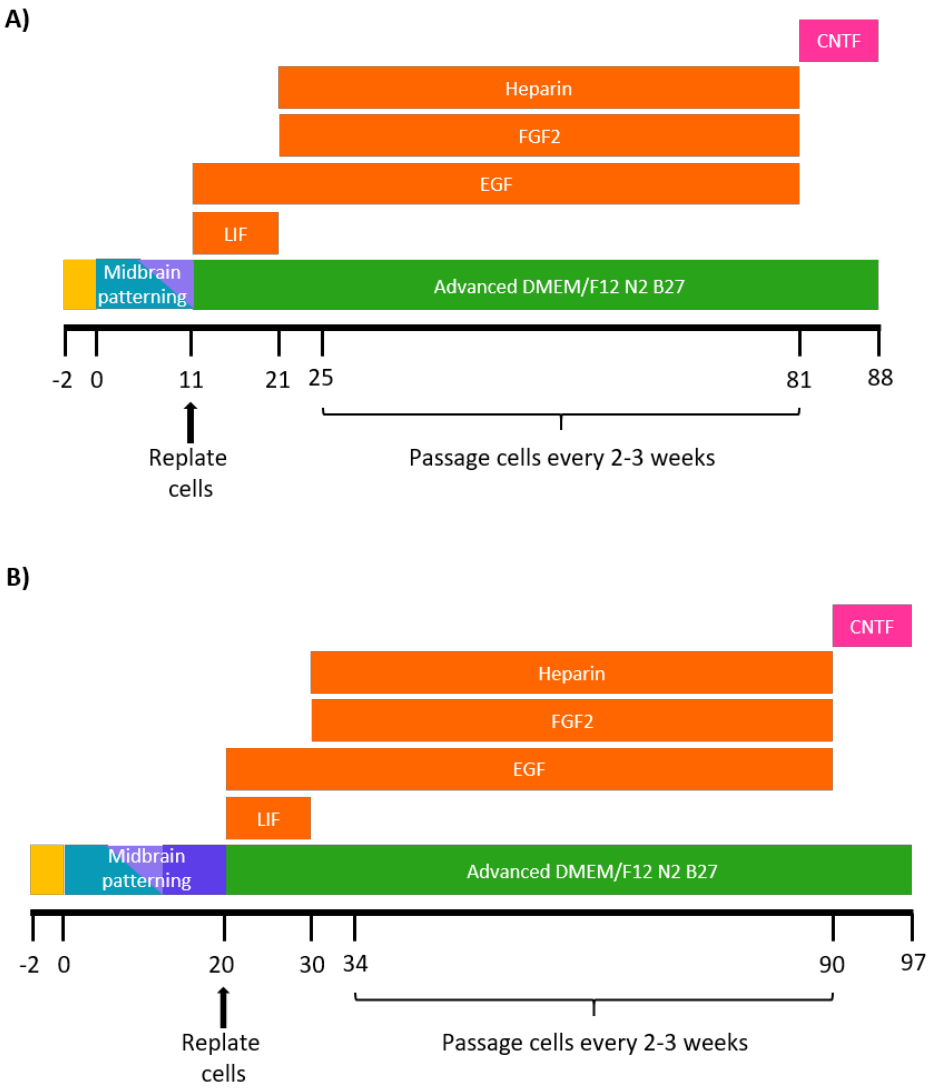

Figure 3.10. Proposed midbrain-patterned astrocyte derivation protocols.
Cells were patterned towards a midbrain progenitor fate for A) 11 DIV or B) 20 DIV as described for the Booth-Zambon protocol for derivation of vmDA neurons. Cells were then replated and grown as described in the Rinaldi protocol.

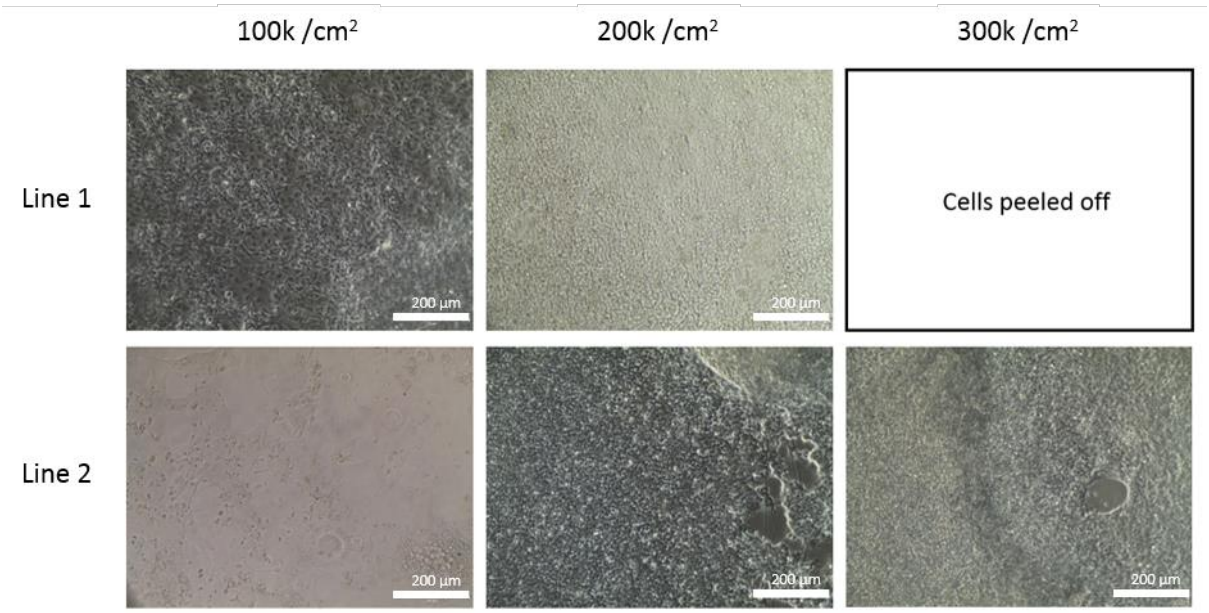

Figure 3.11. Culture of iPSC-derived MP-glial progenitors to 34 DIV.
Phase-contrast images of cells replated at 20 DIV, and successfully maintained in culture until 34 DIV during the MP astrocyte differentiation protocol. Figure shows three cell densities (100-300k cells/cm^2) for two cell lines.

The cells replated at 20 DIV were then maintained successfully as described in the Rinaldi protocol (Figure 3.11, Table 3.4). Briefly, they were grown in EGF and LIF until 30 DIV, then in EGF, FGF2 and Heparin to enable further expansion. Cultures from all surviving densities were then passaged on 34 DIV and assessed for morphology (densely packed, small cells) and survival at 41 DIV. It was found that the optimal replating density varied for each line. Cells proliferated more rapidly than was described in the Rindaldi protocol; therefore, optimal cultures were passaged every seven days until 90 DIV, when they were plated at a range of densities into medium containing CNTF, and maintained for a further seven days. Again, optimal seeding densities varied for each line. At 97 DIV, GFAP positive cells were identified by immunostaining; however, the yield was low, and their morphologies were not representative of the star-like or tufted morphologies expected of astrocytes (Figure 3.12A).

Extending the period of treatment with CNTF from seven to fourteen days improved yield but resulted in no change in morphology (Figure 3.12B).

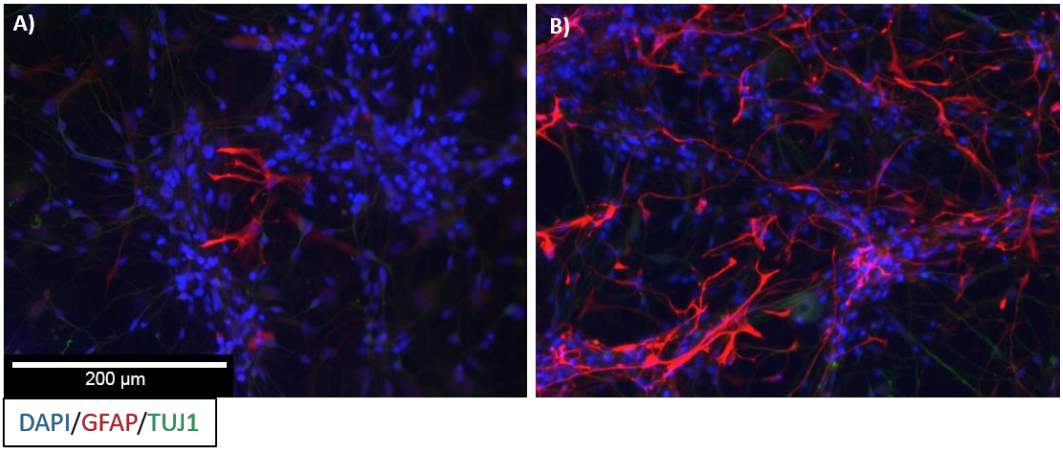

Figure 3.12. Effect of CNTF incubation duration on yield of GFAP-positive cells.
MP astrocytes from two iPSC lines were cultured as described in Figure 3.10B until 90 DIV, then treated with CNTF for A) 7 days and B) 14 days (representative images). Cells were then fixed and immunostained for the astrocyte marker GFAP (red) and the neuronal marker TUJ1 (green), and co-stained with the nuclear dye DAPI (blue).

In an effort to produce GFAP-positive cells exhibiting astrocyte morphology, the effects of various gliogenic molecules from the literature were assessed. A screen involving all possible combinations of CNTF, BMP2, CT1, LIF, and TGFβ1, at two different concentrations, was initiated at 90 DIV for 14 days (Figure 3.13A, C). Additionally, the screen was replicated starting at 41 DIV to determine whether derivation of astrocytes was possible at an earlier timepoint (Figure 3.13B). In total, 192 conditions were tested. 96-well plates containing all 192 combinations of the growth factors (two plates per timepoint) were prepared using an ECHO liquid handler. Cells were grown in NSC medium, which was replenished every two days. For each media change, growth factor plates were reconstituted with NSC medium (Advanced DMEM/F12, N2, B27 without vitamin A, Glutamax), which was then transferred to the cell culture plates. At the end of the screen, cells were fixed and immunostained for GFAP.

Differentiation to astrocytes was quantified by counting GFAP-positive cells with astrocyte morphology (star-like cell bodies, rather than long neuritic processes). In the screen initiated at 41 DIV, no condition was found to induce successful differentiation of the progenitors to astrocytes (data not shown). The screen initiated at 90 DIV identified that under the conditions used, all factors tested inhibited astrocyte differentiation, and that the best condition for differentiation was NSC medium alone (Figure 3.13D). This condition still only yielded around 4% astrocytes in the culture after 14 days. This result was unexpected, as all of the factors tested in the screen have been previously demonstrated to promote astrocyte differentiation. However, the studies that this evidence was derived from were not performed in midbrain cells; therefore, this result may suggest that astrocytes in different brain regions mature in response to different, region-specific molecular signals.

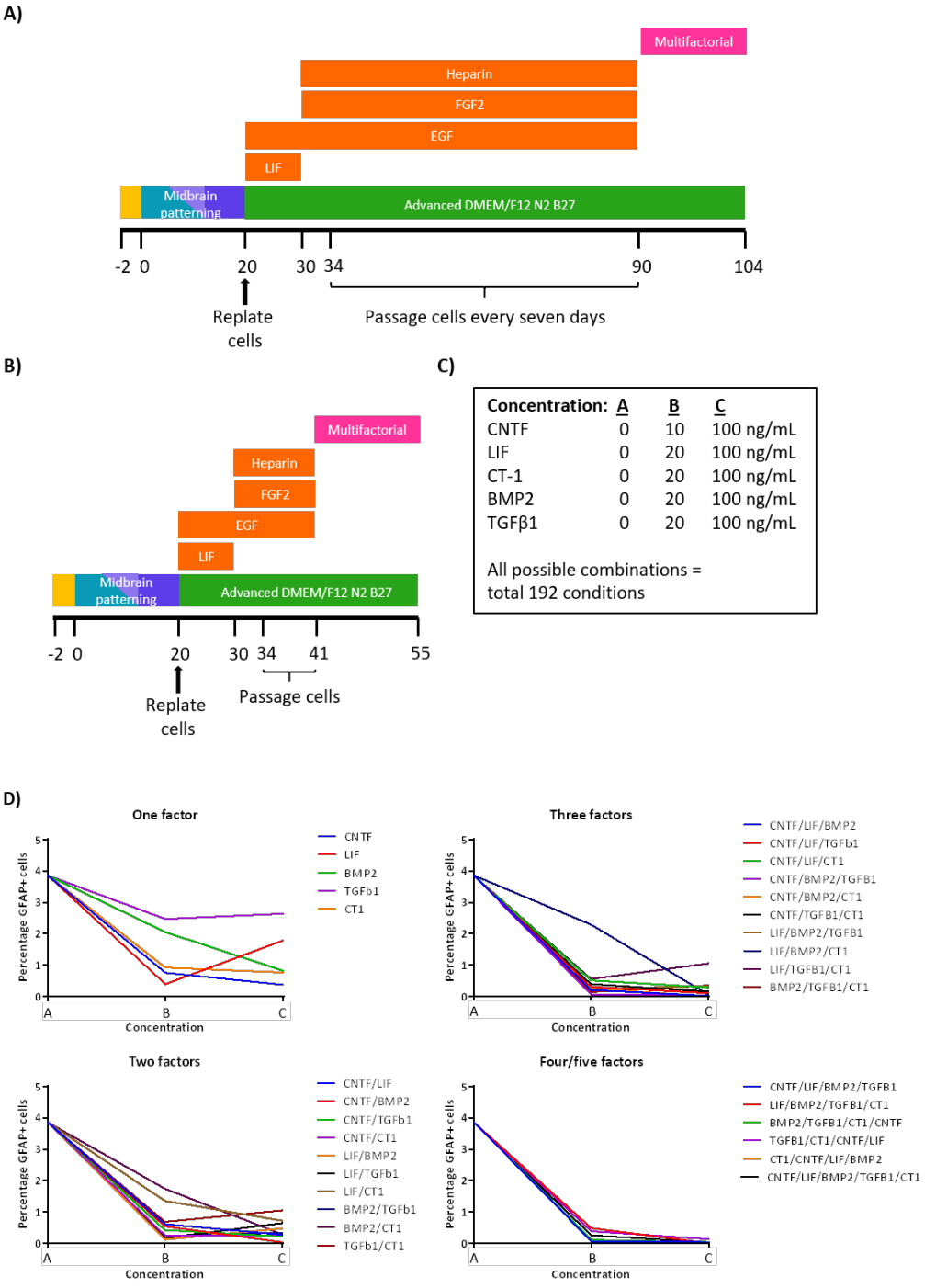

Figure 3.13. Multifactorial experiment design and results.

Cells were cultured for 90 DIV or 41 DIV then treated with combinations of growth factors in NSC medium for 14 days. Cells were then fixed and immunostained for the astrocyte marker GFAP. Figure shows schematics detailing the multifactorial experiments starting at A) 90 DIV and B) 41 DIV, C) the growth factors used in the experiment and their concentrations, and D) The percentage of GFAP-positive cells that exhibited astrocyte morphology was analysed. Abbreviations: Ciliary neurotrophic factor (CNTF); Leukaemia inhibitory factor (LIF); Cardiotrophin-1 (CT-1); Bone morphogenic protein-2 (BMP2); Transforming growth factor beta-1 (TGFβ1).

An experiment was conducted to determine whether maintenance of these cultures for longer periods of time in NSC medium would result in higher astrocyte yield. Cultures derived from two iPSC lines were plated at a range of densities at 90 DIV and maintained until 118 DIV. The optimal plating density for successful differentiation was, again, line dependent. However, it was found that the extended differentiation period resulted in an increased yield of GFAP-positive astrocytes, averaging 48% of the culture (at optimal density), these cells also expressed S100B, GLAST1, and the astrocyte cell surface marker CD44 (Alfei et al. 1999) (Figure 3.14A). Additionally, cells displayed the star-shape morphology characteristic of astrocytes. This protocol is used to generate MP astrocytes from here onwards, and is referred to as the Booth protocol (Figure 3.14B).

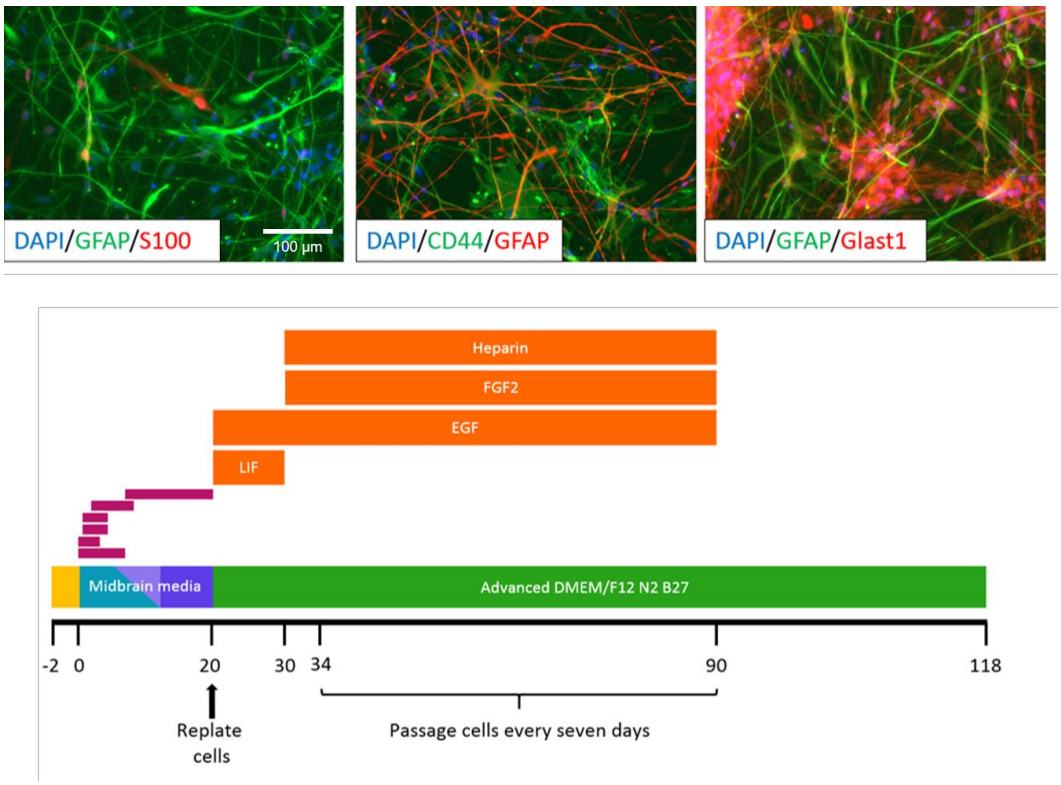

Figure 3.14. The Booth protocol for production of MP astrocytes.
A) Schematic detailing the final protocol for differentiation of iPSCs to MP astrocytes. iPSCs are plated as a monolayer at -2 DIV and midbrain patterning induced from 0 DIV. Cultures are maintained in a proliferative environment until 90 DIV, when they are replated into NSC medium for maturation until 118 DIV. B) Cells were fixed at 118 DIV and immunostained for the astrocyte markers GFAP, S100, CD44, and GLAST1 (representative images). Abbreviations: Leukaemia inhibitory factor (LIF); Epidermal growth factor (EGF); Fibroblast growth factor-2 (FGF2).

3.4.2. Characterisation of MP astrocytes derived using the Booth protocol

To characterise the MP astrocytes, real-time qPCR analysis was conducted on samples collected from four individual iPSC lines throughout the differentiation time course (Figure 3.15). These data showed that differentiation of the cells results in downregulation of the pluripotency markers Octamer-binding transcription factor 4 (*OCT4*) and Nanog Homeobox (*NANOG)* by 20 DIV. They also demonstrate that the cells proceed through the floorplate lineage, as denoted by expression of *FOXA2* and *LMX1A* at 20 DIV, as is expected for midbrain cells of the SNc (Lin et al. 2009). *FOXA2* and *LMX1A* expression was then lost by 30 DIV. The pan-neuronal transcription marker Paired box protein PAX6 (*PAX6)*, which is expressed in TH-negative cells in the developing midbrain, is expressed transiently at 30 DIV (Duan et al. 2013). From 90 DIV, expression of the astrocytic glutamate transporter *SLC1A3* (GLAST1) is switched on, with levels increasing 5-fold by 118 DIV. Finally, at 118 DIV, the astrocyte cytoskeletal marker *GFAP* and the astrocyte specific water channel *AQP4* are also present.

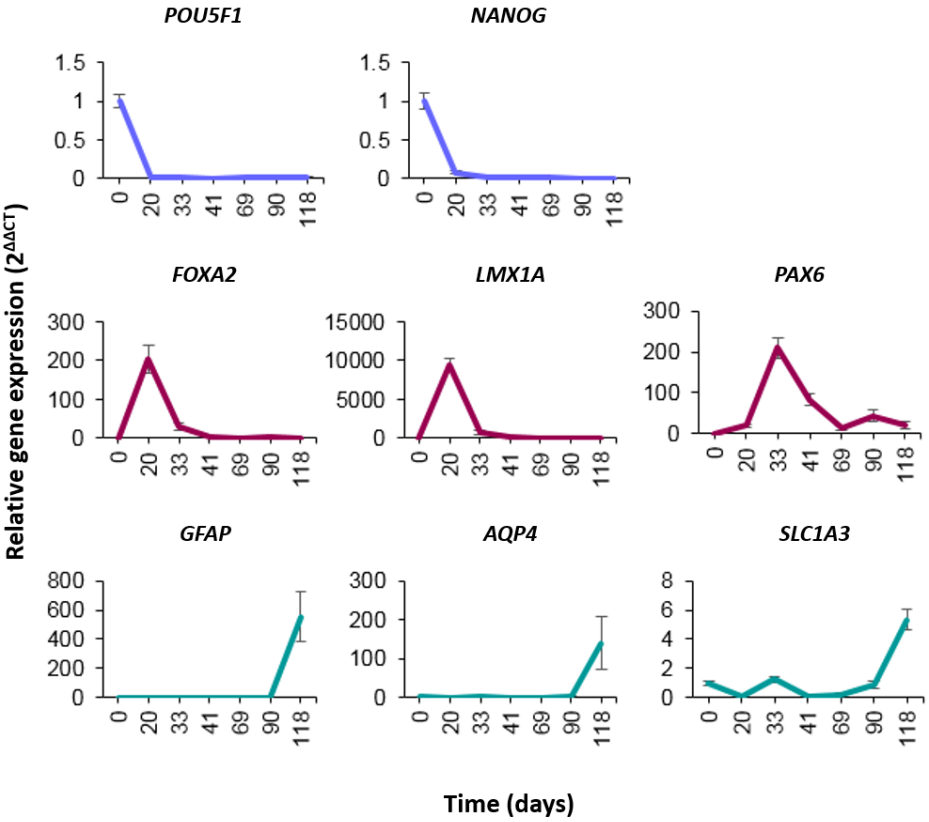

Figure 3.15. Gene expression analysis during differentiation of iPSCs to MP astrocytes.
Cells were harvested throughout the differentiation protocol, and analysed using qPCR for expression of pluripotency markers (POU5F1, NANOG), midbrain and neuronal transcription factors (FOXA2, LMX1A and PAX6) and astrocyte markers (GFAP, AQP4 and SLC1A3). (Graphs show average of four lines, from one differentiaton, mean ± SEM).

The presence of these markers confirms the successful derivation of astrocytes from MP progenitors. One thing that remained unclear was whether MP astrocytes should retain expression of the floorplate transcription factor FOXA2; the MP astrocytes derived using this protocol do not stain positive for the FOXA2 protein (data not shown). Immunostaining of nigral sections from three-month-old mice was conducted to establish whether FOXA2 is present in GFAP-positive astrocytes in the SNc. It was found that all astrocytes assessed were devoid of FOXA2 expression (Figure 3.16). Although this has never been shown previously, it is an unsurprising result. As discussed in Section 3.1.1, FOXA2 expression is important for

vmDA neuron differentiation and maintenance. It is likely that continued expression would inhibit astrocyte differentiation in favour of the vmDA neuronal lineage; therefore, it is probable that expression is switched off after midbrain patterning, to allow differentiation of progenitors to astrocytes.

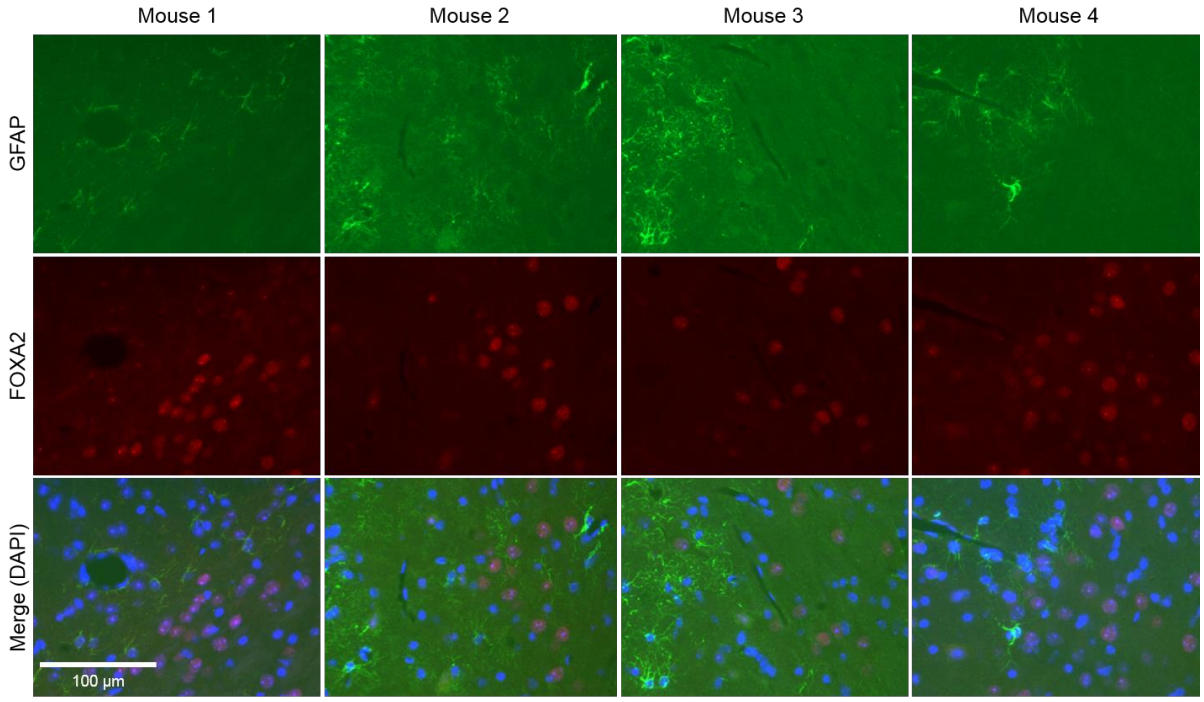

Figure 3.16. FOXA2 and GFAP staining in the mouse SNc.
Nigral sections from three-month-old mice were immunostained for the astrocyte marker GFAP (green) and the floorplate transcription factor FOXA2 (red), and co-stained with DAPI (blue). Images show a lack of costaining of cells for FOXA2 and GFAP.

In addition to the molecular characterisation described above, it was important to determine whether the MP astrocytes were functional. In vivo, astrocytes take up glutamate in a sodium-dependent manner through their glutamate transporters (Schousboe et al. 1977). This process was therefore tested by incubating MP astrocytes with L-[3,4-^{3}H]-Glutamic acid for 10 minutes in the presence or absence of sodium, and measuring the glutamate content of the cells. All lines tested demonstrated the specific uptake of glutamate in the presence of

sodium, indicating expression of functional glutamate transporters at the cell surface (Figure 3.17).

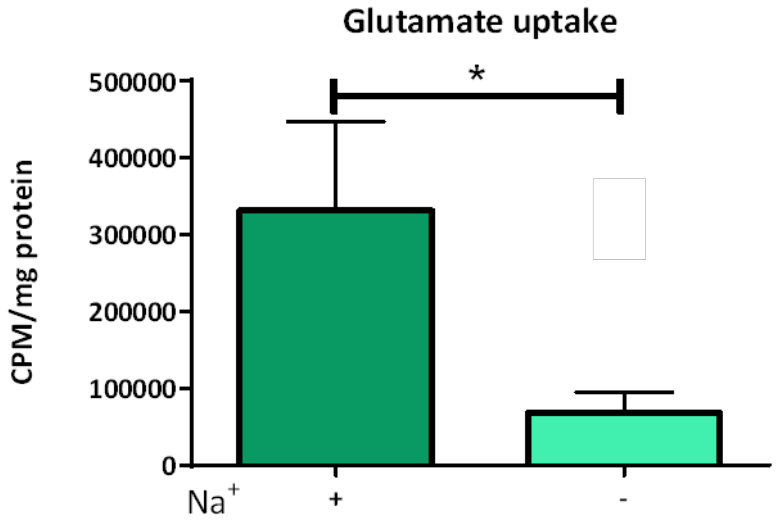

Figure 3.17. Glutamate uptake in MP astrocytes.
*Specific uptake of glutamate through glutamate transporters was assessed by measuring the ability of cells to take up tritiated glutamate in the presence and absence of sodium (Na^+). Counts per minute (CPM) were normalised to cell protein content. (Graph shows average of four lines, from one differentiation, mean ± SD, Student's T-Test * $p<0.05$).*

3.5. Results III: LRRK2 protein levels in iPSC-derived vmDA neurons and MP astrocytes

Data from the literature suggest that LRRK2 expression is similar in isolated human cortical astrocytes and neurons (Zhang et al. 2016); however, this comparison has not been made in the midbrain, or in iPSC-derived cultures. Therefore, western blot analysis of LRRK2 levels was conducted in vmDA neurons and MP astrocytes derived from two iPSC lines (Figure 3.18). LRRK2 levels were found to be over nine-fold higher in MP astrocyte cultures than in vmDA neuron cultures. This expression pattern has been demonstrated previously at the RNA level in mouse cortical astrocytes and neurons (Zhang et al. 2014), but not in human cells. It is not known what implications this finding may have, as few studies have been conducted on LRRK2 in astrocytes.

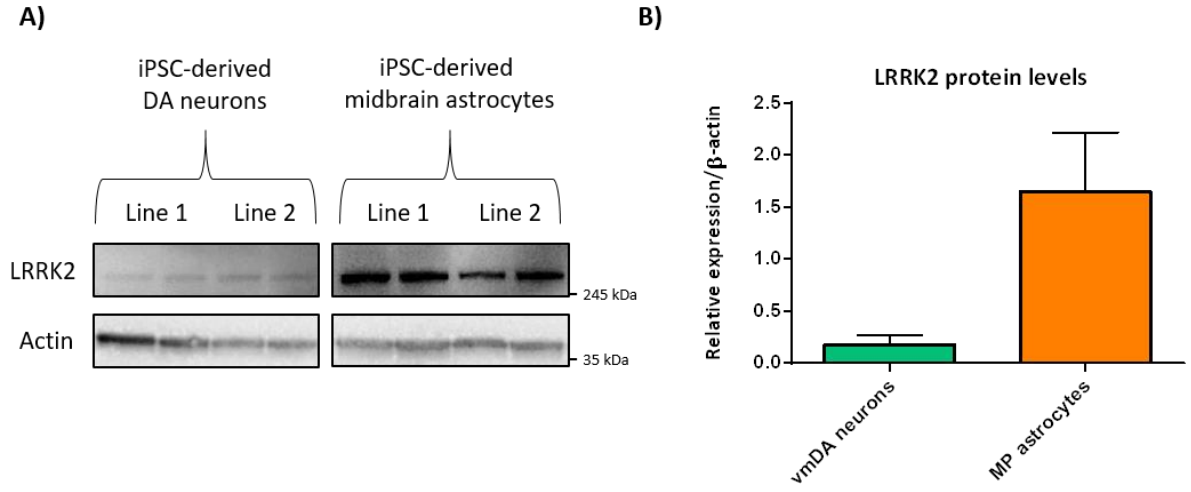

Figure 3.18. Comparison of LRRK2 expression levels in iPSC-derived vmDA neurons and MP astrocytes.
A) LRRK2 expression in vmDA neurons and midbrain patterned astrocytes derived from the same iPSC lines was measured by western blot. B) Quantification of LRRK2 expression, normalised it β-Actin as measured in A. (Graph shows average of two lines, from one differentiation, mean ± SD).

3.6. Alternative protocols

During the course of this study, the Holmqvist protocol for the derivation of MP astrocytes was published by the Roybon research group (Holmqvist et al. 2015). This publication demonstrated the production of cultures containing 100% GFAP-positive midbrain patterned astrocytes, a percentage of which also expressed S100, GLAST1, and CD44. The Kirkeby method for midbrain patterning (Kirkeby et al. 2012) was used in the Holmqvist protocol to derive floorplate progenitors, which were then expanded and differentiated following a modified version of Roybon's previously published protocol for astrocyte differentiation (Roybon et al. 2013). Cells were differentiated until 130 DIV, and high variability in astrocyte yield (1-80%) between cell lines was noted. To overcome this, clonal iPSC lines, stably expressing TagRFP-reporter driven by the ABC1D domain of the GFAP promoter were used for differentiation, enabling purification of GFAP-positive astrocytes using flow cytometry, and resulting in reproducible, pure astrocyte cultures (Holmqvist et al. 2015). Glutamate uptake was not assessed; however, functional characterisation was performed by measuring the release of pro-inflammatory cytokines in response to IL-1β.

A key advantage of the Holmqvist protocol over the MP astrocytes produced using the Booth protocol is the use of a GFAP reporter for enrichment of the cultures. However; this reporter could be used in combination with the Booth protocol in the future, to produce highly enriched, functional astrocyte cultures.

3.7. Discussion and conclusions

The aim of this chapter was to develop protocols for the differentiation of iPSCs to PD-relevant cell types—vmDA neurons and MP astrocytes—to facilitate the study of LRRK2 mutations in PD pathogenesis. To this end, a previously published protocol for the differentiation of vmDA neurons has been fully optimised for use with iPSCs under feeder-free conditions. This optimised Booth-Zambon protocol produces a reasonable yield of floorplate-derived neurons, with vmDA neurons accounting for 31% of the culture by 35 DIV. This percentage is lower than was expected from the original Kriks protocol, which claims a 75% yield of vmDA neurons (quantified at 50 DIV); however, the yield was still considerably higher than in cultures produced using the Fernandes protocol. The difference in yield between the Booth-Zambon and the Kriks protocols may be due to the use here of iPSCs rather than hESCs, as it has previously been demonstrated that hESCs have a higher differentiation capacity than iPSCs (Hu et al. 2010), or potentially because of cell counts being conducted at an earlier timepoint. Nevertheless, the protocol was found to be reproducible and scalable. Characterisation of the cultures indicated that they contain functional vmDA neurons, which produce dopamine and are capable of firing action potentials reminiscent of those seen in primary slice cultures.

When the work described here was started, no published protocols for the derivation of MP astrocytes existed; therefore, the Rinaldi protocol for derivation of cortical astrocytes was adapted for their production. Modification of this protocol resulted in a culture containing 48% GFAP-positive MP astrocytes by 118 DIV, which also expressed the astrocyte markers S100, GLAST1, AQP4 and CD44. Characterisation of the cells demonstrated their ability to take up glutamate in a sodium-dependent manner, suggesting that these cultures are representative of functional astrocytes.

These differentiation protocols were developed to facilitate the analysis of LRRK2 mutations in cell types that are relevant to PD; as such, it was essential that LRRK2 be expressed in the resulting cells. Western blot analysis confirmed that both the vmDA neurons and the MP astrocytes described here express LRRK2. Interestingly, LRRK2 levels were found to be higher in the MP astrocytes than the vmDA neurons. This expression pattern has been demonstrated previously at the RNA level in mouse cortical astrocytes and neurons (Zhang et al. 2014); however, expression levels were found to be the same in human cortical astrocytes and neurons (Zhang et al. 2016). This difference in LRRK2 protein levels in midbrain cells may point to a specific function for LRRK2 in astrocytes in this region, and gives credence to their study in this thesis.

Chapter 4: Hypothesis-driven phenotypic analysis of the LRRK2-G2019S mutation in iPSC-derived vmDA neurons and MP astrocytes

4.1. Introduction

In Chapter 3, high-yield protocols were developed for the robust differentiation of ventral-midbrain dopaminergic (vmDA) neurons and midbrain-patterned (MP) astrocytes from iPSCs, to enable the study of LRRK2 mutations in disease-relevant cell types. In order to investigate the mechanisms by which LRRK2 mutations exert their pathogenic effects, we sought to identify cellular phenotypes in these cell types. As described in Section 1.3.4, LRRK2 has been implicated in a wide range of cellular functions, many of which have been demonstrated to be perturbed by the G2019S mutation. A number of studies have already characterised the LRRK2-G2019S mutation in iPSC-derived cultures containing vmDA neurons (Section 1.3.4.vi); however, due to the relatively small number of studies conducted thus far, and variations between vmDA-neuron percentages, no consensus has been reached regarding the effects of the mutation on this cell type. Furthermore, although LRRK2 is expressed in astrocytes (Zhang et al. 2016), no studies using iPSC-derived astrocytes have characterised the effects of LRRK2 mutations on their function.

4.2. Aims of this chapter

1. To analyse the effects of the LRRK2-G2019S mutation on the cellular function of iPSC-derived **vmDA neurons** using a hypothesis-driven approach.
2. To analyse the effects of the LRRK2-G2019S mutation on the cellular function of iPSC-derived **MP astrocytes** using a hypothesis-driven approach.

4.3. Results I: Hypothesis-driven phenotyping of vmDA-neuron cultures expressing the LRRK2-G2019S mutation

4.3.1. Differentiation of LRRK2 patient iPSC lines to vmDA neurons

To get a clear understanding of the effects of the LRRK2-G2019S mutation across a range of genetic backgrounds, iPSCs derived from four healthy control individuals (all of whom were unrelated), and five individuals carrying the G2019S mutation (all unrelated apart from one sibling pair), were used (Table 4.1). The differentiation capacity of iPSC lines can be variable; therefore, it was important to characterise the ability of these lines to produce vmDA neurons before proceeding with phenotyping experiments. To do this, cells were differentiated using the Booth-Zambon protocol (Section 3.3.3) for 35 DIV and then fixed and immunostained for markers of vmDA neurons. The composition of the cultures was found to be consistent across lines and across multiple differentiations (Figure 4.1A-E). 32.7 ± 4.3% of the cells in the cultures expressed the dopaminergic marker TH (Figure 4.1B), 98.2 ± 1.3% expressed the pan-neuronal marker TUJ1 (Figure 4.1C), and 83.7 ± 5.9% expressed the floorplate transcription factor FOXA2 (Figure 4.1D). Consistent with the results from the protocol optimisation in Chapter 3, 30.0 ± 4.0% of the cells (91.6 ± 2.9% of all DA neurons) expressed all three markers and were therefore identified as vmDA neurons (Figure 4.1E).

To further confirm the dopaminergic phenotype of the cultures, cell lysates were prepared and analysed for cellular dopamine content by HPLC. All lines produced dopamine at comparable levels, and there was no difference in dopamine content between the LRRK2-G2019S expressing

lines and controls (Figure 4.2). This finding confirms that the dopamine synthesis pathway is active in these cultures, and is not affected by the presence of the LRRK2-G2019S mutation.

Table 4.1. iPSC lines used for differentiation to vmDA neurons.
Siblings are denoted with an asterisk. Confirmatory genotyping of lines can be found in Appendix (i).

#	Cell line	Age/Sex	LRRK2 Genotype	Reprogramming method
1	NHDF1	44/F	WT	Retrovirus
2	JR053-6	68/M	WT	Retrovirus
3	SFC840-6	67/F	WT	Cytotune (Sendai virus)
4	SFC856-4	78/F	WT	Cytotune (Sendai virus)
5	JR036-1*	49/M	G2019S	Retrovirus
6	MK144-7*	57/F	G2019S	Retrovirus
7	MK002-4	72/F	G2019S	Retrovirus
8	SFC832-19	77/F	G2019S	Cytotune (Sendai virus)
9	SFC855-6	57/M	G2019S	Cytotune (Sendai virus)

LRRK2 mutations have been previously demonstrated to have an impact upon a number of cellular functions and pathways (Section 1.3.4). The iPSC-derived vmDA-neuron cultures characterised here were used to investigate the effects of the LRRK2-G2019S mutation upon LRRK2 protein expression, neurite length, autophagic function, mitochondrial health, and glycolysis. For a number of these studies, identification of vmDA neurons by immunostaining was necessary. As the majority (91.6 ± 2.9%) of DA neurons were identified as vmDA neurons in the cultures, the DA-neuron marker TH was used alone to identify these cells.

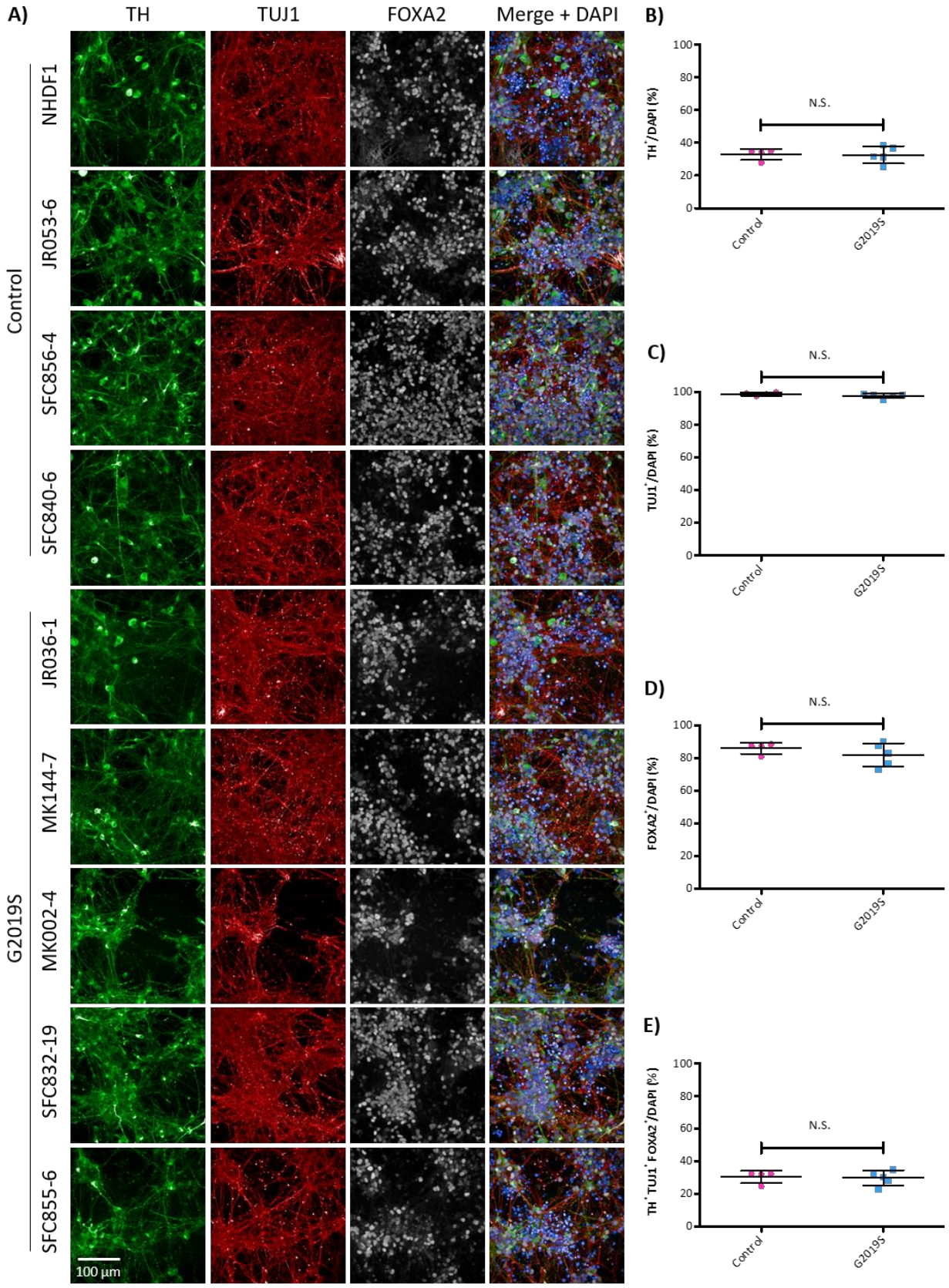
A)
TH
TUJ1
FOXA2
Merge + DAPI
Control
NHDF1
JR053-6
SFC856-4
SFC840-6
G2019S
JR036-1
MK144-7
MK002-4
SFC832-19
SFC855-6
100 µm
B)
TH+/DAPI (%)
N.S.
Control
G2019S
C)
TUJ1+/DAPI (%)
N.S.
Control
G2019S
D)
FOXA2+/DAPI (%)
N.S.
Control
G2019S
E)
TH+TUJ1+FOXA2+/DAPI (%)
N.S.
Control
G2019S

Figure 4.1. (Previous page) Differentiation of iPSCs from healthy controls and LRRK2-G2019S patients to vmDA neurons.

iPSCs were differentiated for 35 DIV, then fixed and immunostained for markers of vmDA neurons. A) Example images of cells immunostained for TH (green), TUJ1 (red), FOXA2 (white) and costained for DAPI (blue). B-E) Quantification of cells that were positive for B) TH, C) TUJ1, D) FOXA2, and E) TH, TUJ1, and FOXA2, from three independent differentiations. (Graphs show mean ± SD. Significance was assessed using Student's T-test. N.S. = not significant).

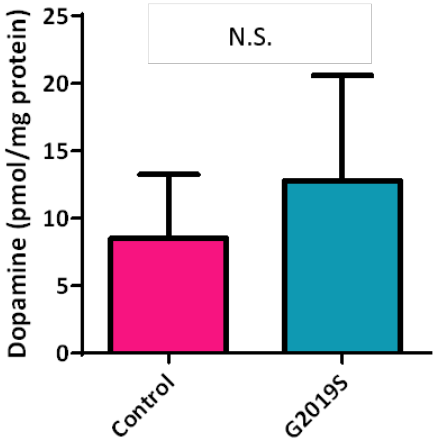

Figure 4.2. Intracellular dopamine content of iPSC-derived vmDA-neuron cultures.

Cells were cultured until 35 DIV, then lysed and analysed for dopamine using HPLC. (Graph shows mean ± SD from three controls and five G2019S lines, from two independent differentiations. Significance was assessed using Student's T-test. N.S. = not significant).

4.3.2. LRRK2 protein levels in iPSC-derived vmDA-neuron cultures

Western blot analysis was conducted to examine whether LRRK2 protein levels are affected by the G2019S mutation in iPSC-derived vmDA-neuron cultures. In rodent primary cultures, it has previously been demonstrated that LRRK2 protein levels increase with neuronal maturation (Beccano-Kelly et al. 2014). Therefore, protein levels were analysed by Western blotting at two timepoints during the differentiation (35 DIV and 56 DIV) to determine whether LRRK2 levels also increased upon maturation of iPSC-derived vmDA-neuron cultures. All lines expressed LRRK2,

and, as has been previously described in the literature (Miklossy et al. 2006; Berger et al. 2010; Melrose et al. 2010), LRRK2 was detected as two bands on the Western blot. Both bands were quantified together, and it was found that the LRRK2-G2019S mutation did not affect protein levels, and LRRK2 expression did not increase upon maturation (Figure 4.3).

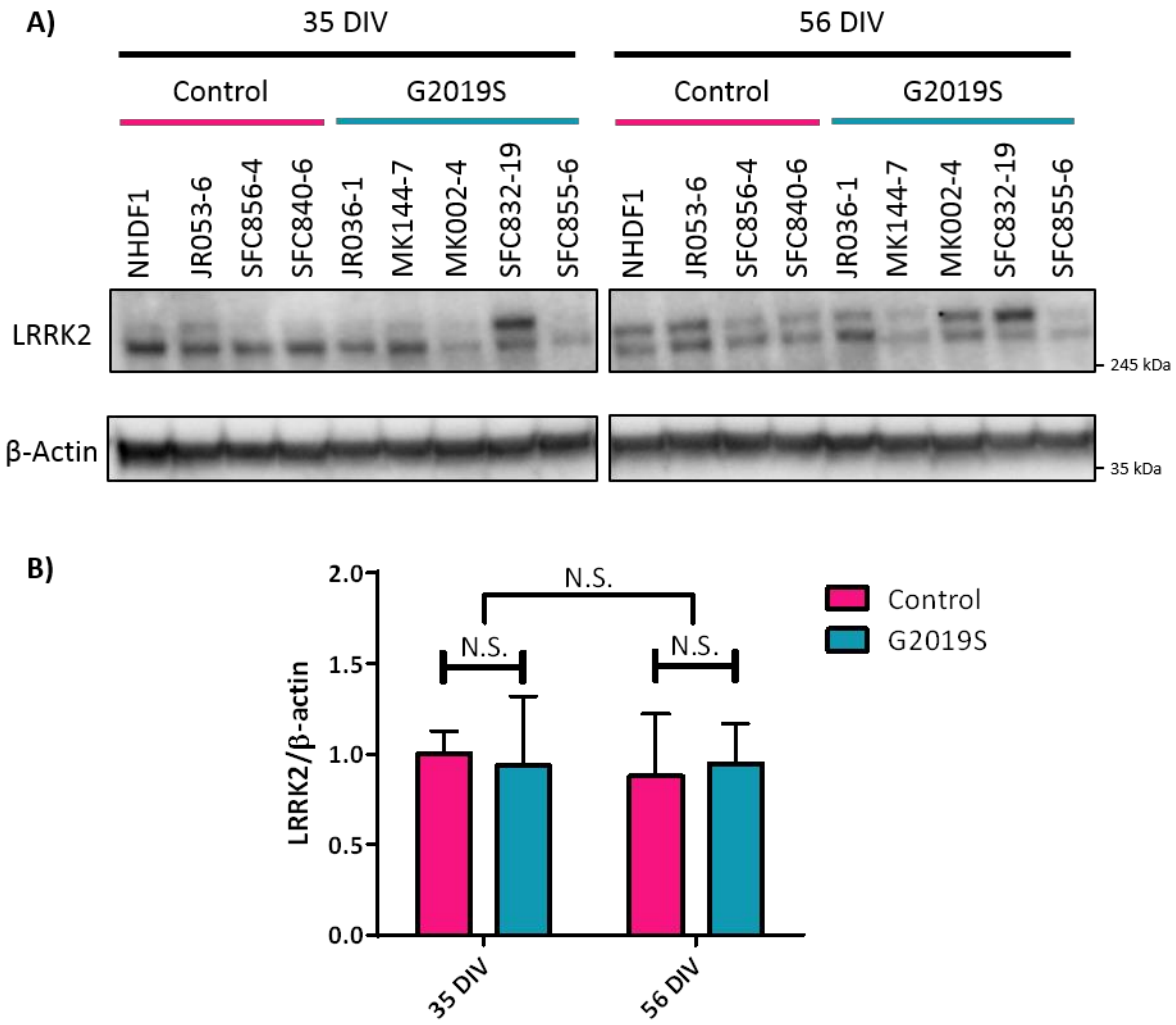

Figure 4.3. LRRK2 protein levels in iPSC-derived vmDA-neuron cultures.
Western blot analysis of LRRK2 protein levels was conducted at 35 and 56 DIV. A) Example images of western blots for LRRK2 and β-Actin. B) Quantification of LRRK2 protein levels (both bands) relative to β-actin, and normalised to controls at 35 DIV. (Graph shows mean ± SD from four controls and five G2019S lines, from three independent differentiations. Significance was assessed using a two-way ANOVA. N.S. = not significant).

4.3.3. Analysis of neurite outgrowth in iPSC-derived vmDA-neuron cultures

A commonly identified neuronal phenotype resulting from expression of the LRRK2-G2019S mutation is decreased neurite outgrowth (Section 1.3.4.i). Sholl analysis is commonly used to assess characteristics of neurites, including their number, length, and complexity (Sholl 1953; Sholl 1956). In order to assess neurite outgrowth in the iPSC-derived vmDA-neuron cultures, progenitor cells (20 DIV) were plated at a low density to enable visualisation of individual neurons. They were matured for a further eight days, until 28 DIV; long enough to allow for neurite growth, but not so long as to allow complex entanglement of neurites. Cells were then fixed and immunostained for TH, to identify vmDA neurons, as well as Microtubule-associated Protein 2 (MAP2), to identify neurites (Figure 4.4A). Semi-automated Sholl analysis (Gutierrez and Davies 2007) was then conducted; no significant differences were found between the number of neurites, and their complexity, and length were also unchanged (Figure 4.4B–D).

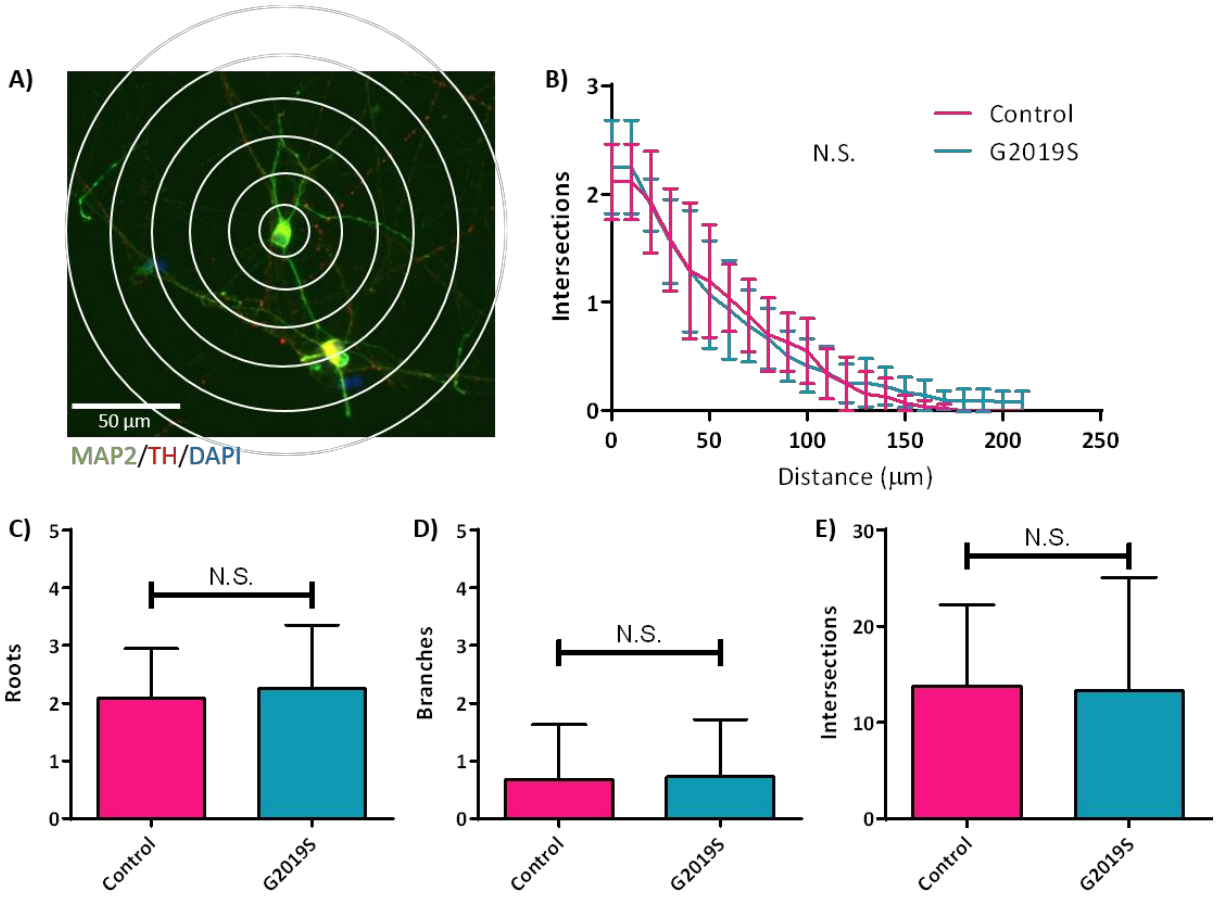

Figure 4.4. Analysis of neurites in vmDA-neuron cultures.

Cells were differentiated to 28 DIV, then fixed and immunostained, then analysed using Sholl analysis. A) Example image of a cell immunostained for MAP2 (green) and TH (red), and costained for DAPI (blue), overlaid with Sholl rings. B-E) Sholl analysis was conducted and B) the Sholl profile, C) neurite number, D) neurite complexity, and E) neurite length assessed. (Graphs show mean ± SD from three controls and four G2019S lines, 15–27 cells per line, from one differentiation. Significance was assessed using B) a two-way ANOVA and C-E) Student's T-test. N.S. = not significant).

4.3.4. Analysis of autophagic function in iPSC-derived vmDA-neuron cultures

LRRK2 has been widely implicated in autophagy; however, no consensus has been reached about its precise role in this pathway (Section 1.3.4.ii). Western blot analysis of proteins that are involved in this pathway can provide insight into the levels of autophagy that are occurring in cells. LC3 is a protein that is involved in the formation of autophagic vesicles, in its unlipidated

state (LC3-I), it is freely present in the cytoplasm; however, upon lipidation to LC3-II, it is recruited to the membrane of autophagosomes, where it remains until degradation following lysosomal fusion. Western blot analysis of the levels of LC3-II, and LAMP1 (an essential lysosomal protein), was conducted in vmDA-neuron cultures at 35 DIV (Figure 4.5). The levels of these proteins were not affected by the presence of the LRRK2-G2019S mutation.

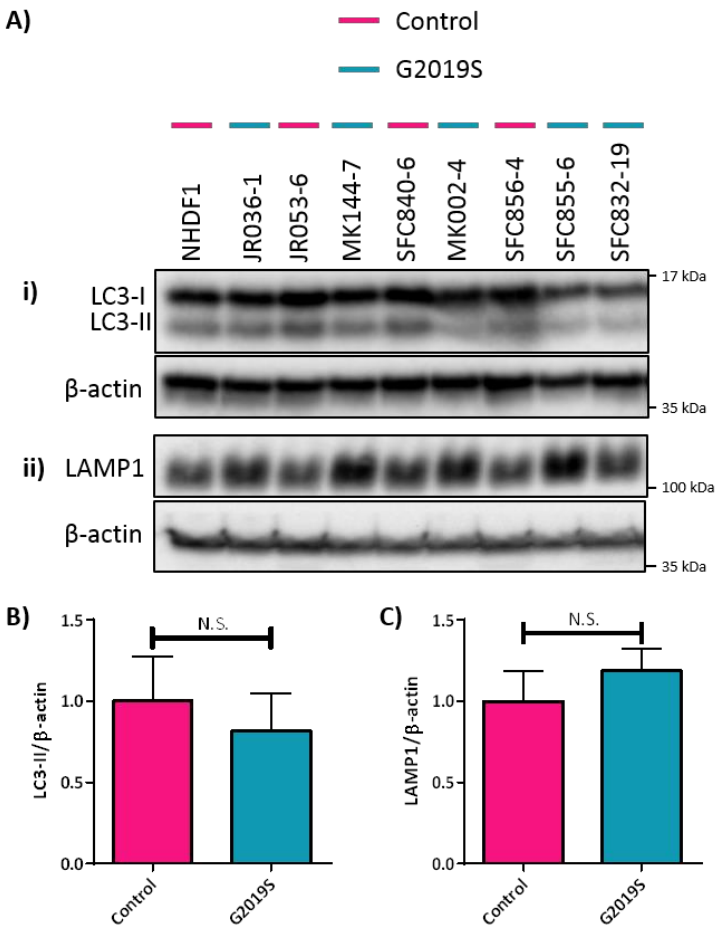

Figure 4.5. Autophagy protein levels in iPSC-derived vmDA-neuron cultures.
Western blot analysis of LC3-II and LAMP1 protein levels was conducted at 35 DIV. A) Example images of western blots for LC3, LAMP1, and corresponding β-Actin. Quantification of B) LC3-II and C) LAMP1 protein levels relative to β-Actin. (Graphs show mean ± SD from four controls and five G2019S lines, from three independent differentiations. Significance was assessed using Student's T-test. N.S. = not significant).

Although the levels of LC3 and LAMP1 were not changed in these cultures, there remained the possibility that their localisation could be disrupted. One study has previously demonstrated LRRK2-G2019S-mediated changes in autophagic vesicle content by immunostaining in iPSC-derived neurons using LC3 and LAMP1 costaining; however, changes were only detected in cultures that had been matured for 75 days (Sanchez-Danes et al. 2012b). In an attempt to replicate the findings of the Sanchez-Danes paper, iPSC-derived vmDA-neurons were matured for 35 DIV and 76 DIV, then immunostained for LC3 and LAMP1 in combination with TH, to allow identification of vmDA neurons within the cultures. The number of LC3 and LAMP1 puncta in each vmDA neuron was quantified, and colocalization of the puncta was analysed to provide counts for autophagosomes (LC3 alone), lysosomes (LAMP1 alone), and autolysosomes (colocalization of LC3 and LAMP1) (Figure 4.6). No changes in autophagic vesicle content were detected at either time point. These findings, in combination with the results of the LC3-II and LAMP1 Western blots that were conducted on samples at 35 DIV, suggest that macroautophagy is not affected by the LRRK2-G2019S mutation in these cultures.

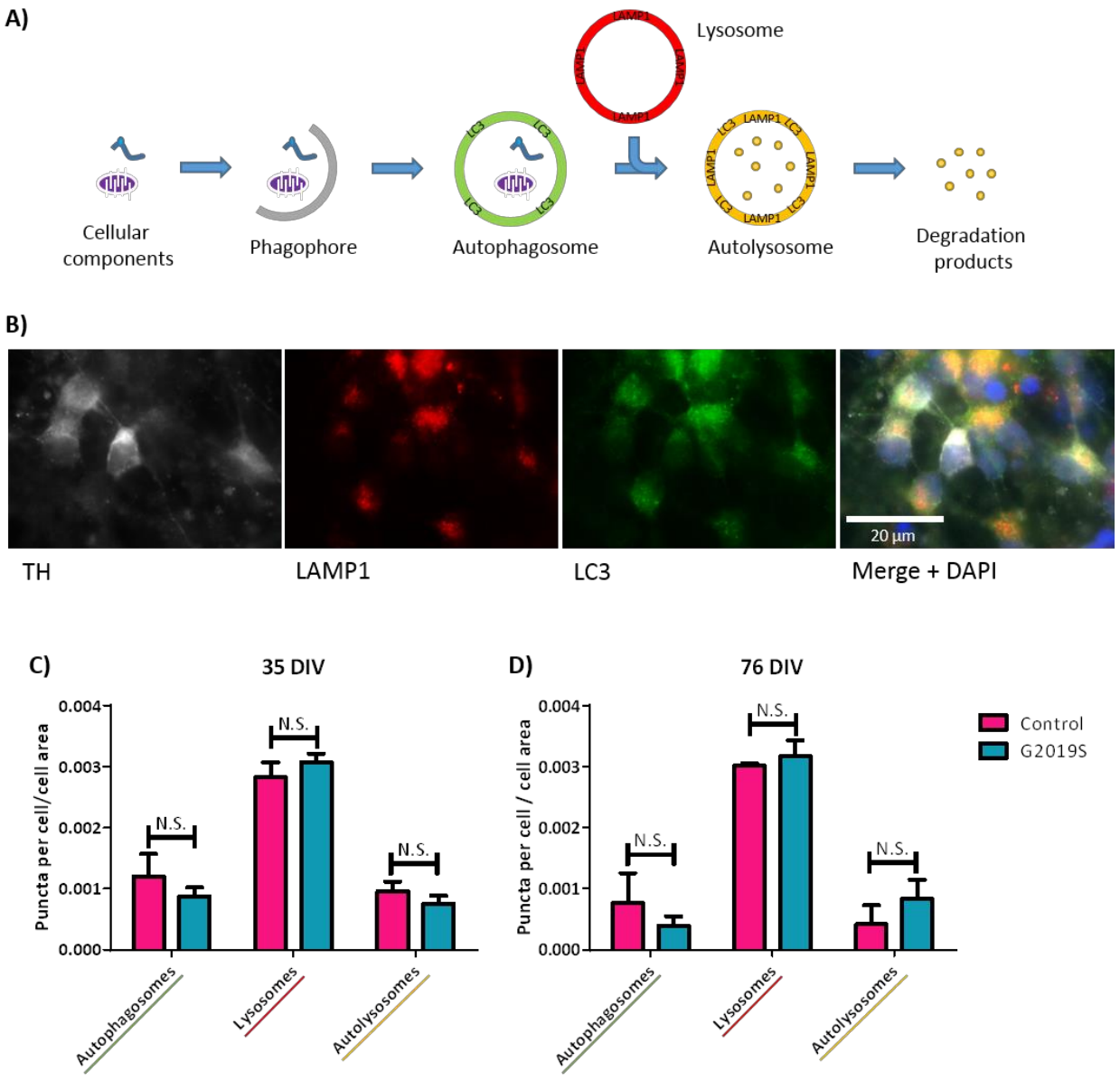

Figure 4.6. Autophagic vesicle analysis in vmDA-neuron cultures.

A) Schematic of the autophagy process; LC3 marks the autophagosome, LAMP1 marks the lysosome, and both are present after fusion of these vesicles to form the autolysosome. B) Example images of cells at 35 DIV, immunostained for TH (white), LAMP1 (red), LC3 (green), and costained for DAPI (blue). Quantification of autophagic vesicles in cultures at C) 35 DIV, D) 76 DIV. (Graphs show mean ± SD from three controls and five G2019S lines, 22–35 cells per line from C) one differentiation, D) two independent differentiations. Significance was assessed using Student's T-test. N.S. = not significant).

4.3.5. Analysis of mitochondrial function in iPSC-derived vmDA-neuron cultures

A number of studies have found that LRRK2 mutations result in mitochondrial dysfunction (Section 1.3.4.iii). The ability of mitochondria to produce ATP is reliant on their mitochondrial membrane potential (MMP), which is maintained by the mitochondrial respiratory complexes (Mitchell 1961). Depolarisation of the MMP is indicative of mitochondrial dysfunction. MMP can be measured using a number of mitochondrial dyes, including tetramethylrhodamine methyl ester (TMRM). TMRM is a lipophilic cation that is accumulated in mitochondria in a manner that is dependent on, and proportional to their MMP (Scaduto and Grotyohann 1999).

To investigate whether the LRRK2-G2019S mutation resulted in decreased MMP in iPSC-derived vmDA-neurons, progenitor cells (20 DIV) were plated at a low density on glass coverslips to enable visualisation of individual neurons. TMRM analysis of MMP was conducted over a period of six days, between 35–41 DIV. Carbonyl cyanide m-chlorophenyl hydrazone (CCCP), a protonophore, which disrupts the mitochondrial proton gradient (Heytler and Prichard 1962), was added to the cells during imaging to induce complete MMP depolarisation. The average MMP for each cell was calculated by subtracting the fluorescence after depolarisation from the fluorescence in the first two minutes of imaging. Cells carrying the LRRK2-G2019S mutation exhibited MMPs that were comparable with controls (Figure 4.7), indicating that this aspect of mitochondrial function is not affected by the mutation in these cultures.

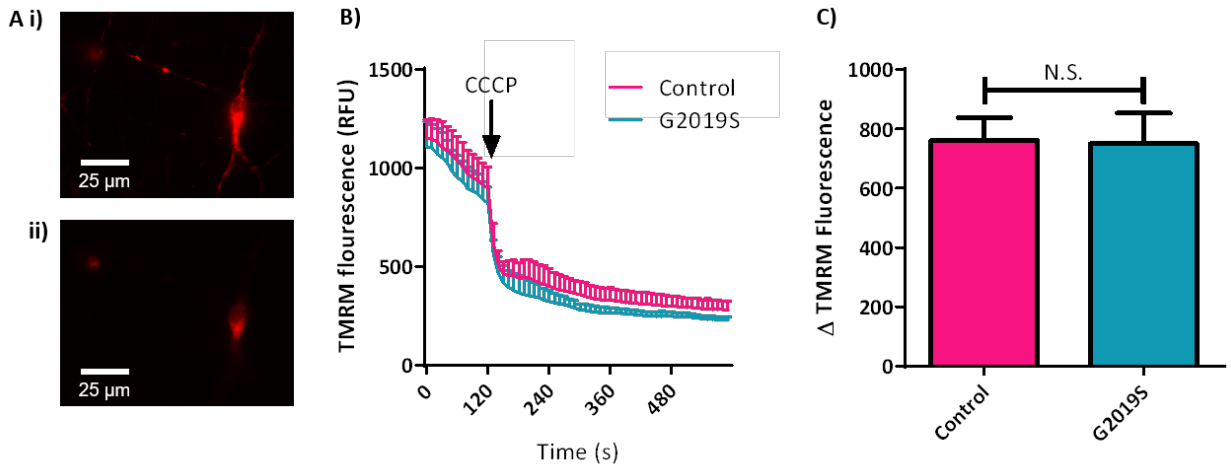

Figure 4.7. Analysis of mitochondrial membrane potential in vmDA-neuron cultures.
Live cells were loaded with TMRM and imaged using fluorescence microscopy for ten minutes, with addition of CCCP (10 µM) after two minutes. A) Example images of a neuron loaded with TMRM i) before and ii) after CCCP addition. B) TMRM fluorescence over time. C) Quantification of MMP (ΔTMRM fluorescence). (Graphs show mean ± SD from three controls and four G2019S lines, 12–24 cells per line, from one differentiation. Significance was assessed using Student's T-test. N.S. = not significant).

As no changes in MMP were detected, a more sensitive assay of mitochondrial function was sought. Mitochondrial oxygen consumption can be measured using a Seahorse metabolic analyser, which detects oxygen using a solid-state sensor. Sequential addition of a series of mitochondrial respiratory chain complex inhibitors during oxygen consumption analysis enables the analysis of mitochondrial respiration (Figure 4.8).

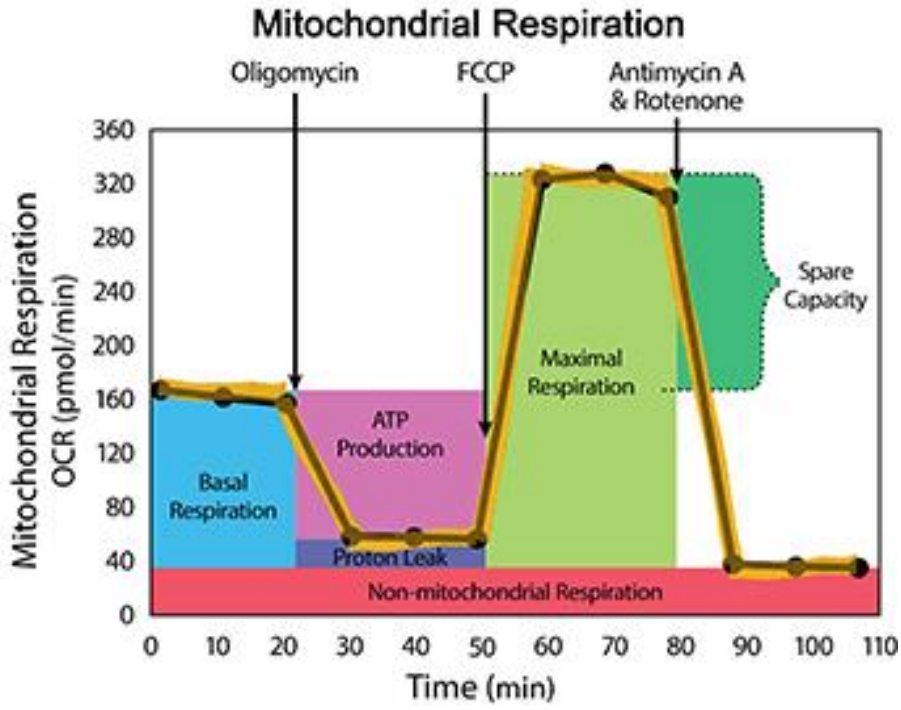

Figure 4.8. Protocol for measurement of mitochondrial respiration.

Schematic detailing the Seahorse Mito Stress test protocol. The oxygen consumption rate (OCR) is measured over time. Initially, OCR is measured in the absence of inhibitors, following this, oligomycin, which inhibits ATP synthase (complex V) is added. Carbonyl cyanide 4-(trifluoromethoxy)phenylhydrazone (FCCP), a protonophore with the same mode of action as CCCP, is then added, resulting in depolarisation of the mitochondrial membrane and decoupling of mitochondrial oxygen consumption from ATP synthesis. Finally, a combination of Antimycin A and Rotenone are added to inhibit oxygen consumption by mitochondrial complexes I and III respectively. ATP production can be calculated by subtracting the oxygen consumption rate (OCR) after oligomycin addition from the OCR before oligomycin addition. Maximal respiration can be calculated by subtracting OCR after addition of antimycin A/rotenone from OCR after addition of FCCP. Spare capacity can be calculated by subtracting OCR before addition of inhibitors, from OCR after addition of FCCP. Basal respiration and proton leak can be calculated by subtracting OCR after Antimycin A/Rotenone treatment from OCR before addition of any inhibitors, and OCR after oligomycin addition respectively. Figure produced by Agilent Technologies, Inc.

To assess whether the LRRK2-G2019S mutation exerts an effect on mitochondrial respiration, iPSC-derived vmDA-neurons were cultured until 37 DIV, then analysed using the Seahorse metabolic analyser. Mitochondrial respiration was not affected by the presence of the G2019S

mutation (Figure 4.9), confirming the findings from the TMRM assay, and suggesting that the mitochondria in these cells are healthy.

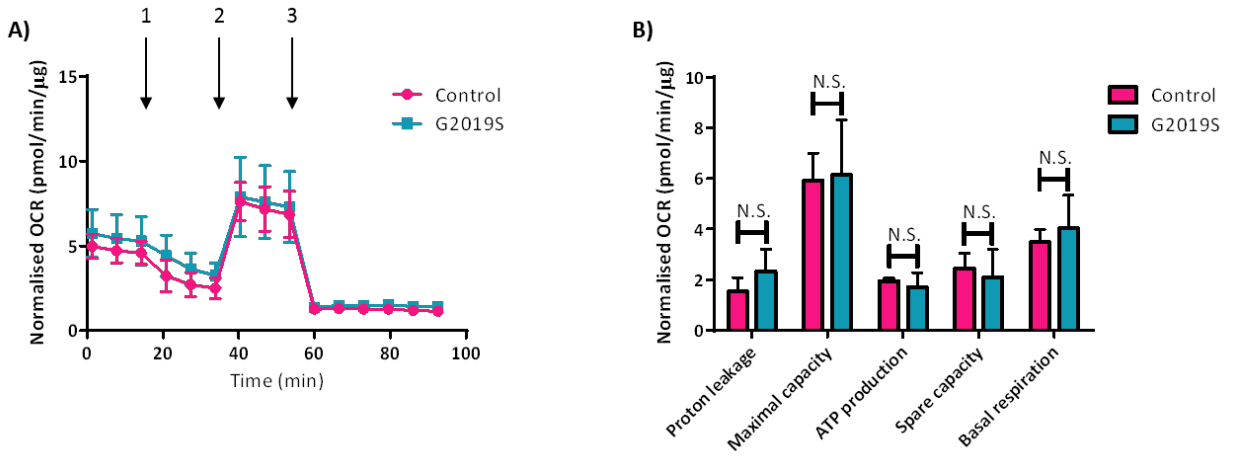

Figure 4.9. Analysis of mitochondrial respiration in iPSC-derived vmDA-neuron cultures.
Cells were cultured until 37 DIV then analysed using the Seahorse metabolic analyser, all data was normalised to cellular protein content, which was calculated using a bicinchoninic acid (BCA) assay. A) Oxygen consumption rate (OCR) over time, following addition of mitochondrial inhibitors 1) oligomycin, 2) FCCP, 3) antimycin A and rotenone. B) Quantification of mitochondrial respiration parameters. (Graphs show mean ± SD from three controls and five G2019S lines, from two independent differentiations. Significance was assessed using Student's T-test. N.S. = not significant).

4.3.6. Analysis of glycolytic function in iPSC-derived vmDA-neuron cultures

No studies to date have functionally investigated glycolytic respiration in cells carrying LRRK2 mutations; however, a transcriptomic study in the brains of transgenic LRRK2-G2019S mice has identified this pathway as significantly perturbed (Nikonova et al. 2012). As well as the OCR, the Seahorse metabolic analyser can simultaneously measure the extracellular acidification rate (ECAR), a measurement of glycolytic respiration. Therefore, glycolytic function was also analysed in these cultures. Following addition of mitochondrial inhibitors as described in Figure 4.8, 2-deoxyglucose (2DG), which competitively inhibits the phosphorylation of glucose by hexokinase,

was added to the cells to inhibit glycolysis (Figure 4.10A). Basal glycolysis levels were calculated by subtracting the ECAR after addition of 2DG, from the ECAR before addition of oligomycin (Figure 4.10B). Maximal glycolysis was calculated by subtracting the ECAR after 2DG addition, from the ECAR after oligomycin addition (Figure 4.10B). The glycolytic reserve was calculated by subtracting the ECAR before oligomycin addition, from the ECAR after oligomycin addition (Figure 4.10B). No changes in glycolytic respiration were detected in the cells expressing the G2019S mutation when compared to controls. These results, in combination with the results from the mitochondrial oxygen consumption assay (Section 4.3.5), suggest that cellular respiration is normal in iPSC-derived vmDA-neuron cultures expressing the LRRK2-G2019S mutation.

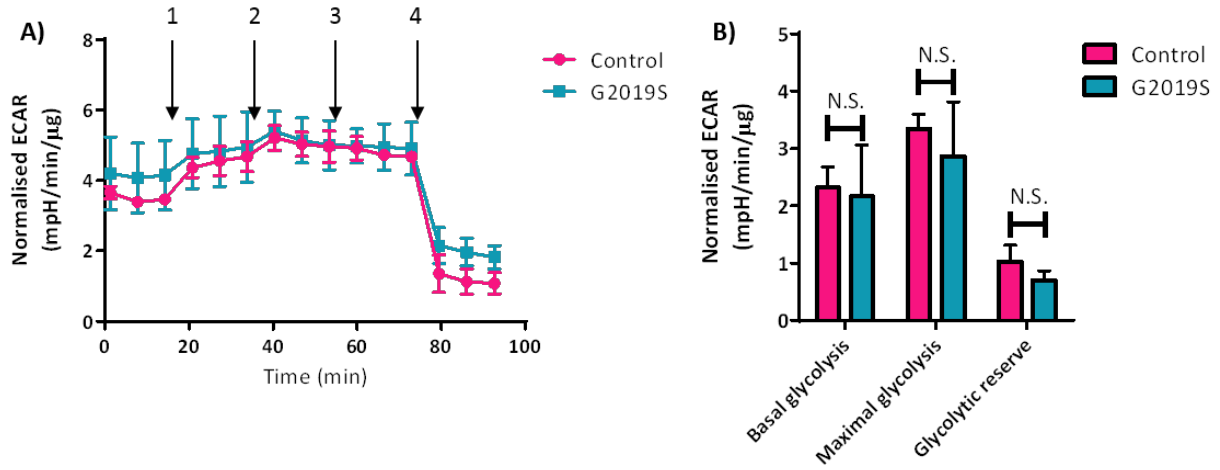

Figure 4.10. Analysis of glycolytic respiration in iPSC-derived vmDA-neuron cultures.
Cells were cultured until 37 DIV then analysed using the Seahorse metabolic analyser, all data was normalised to cellular protein content. A) Extracellular acidification rate (ECAR) over time, following addition of mitochondrial inhibitors 1) oligomycin, 2) FCCP, 3) antimycin A and rotenone, and 4) the glycolysis inhibitor 2-deoxyglucose. B) Quantification of glycolytic respiration parameters. (Graphs show mean ± SD from three controls and five G2019S lines, from two independent differentiations. Significance was assessed using Student's T-test. N.S. = not significant).

4.4. Results II: Hypothesis-driven phenotyping of MP-astrocyte cultures expressing the LRRK2-G2019S mutation

4.4.1. Differentiation of LRRK2 patient iPSC lines to MP astrocytes

Following the investigation of LRRK2 mutation-mediated phenotypes in vmDA-neuron cultures, experiments were conducted to study the effect of the LRRK2-G2019S mutation in MP-astrocyte cultures. iPSCs from four healthy control individuals (all of whom were unrelated), and five individuals carrying the LRRK2-G2019S mutation (all unrelated apart from one sibling pair), were differentiated to MP astrocytes following the Booth protocol, as described in Section 3.4.1. Single clones were used for all individuals apart from SFC840, where two clones were differentiated. These ten iPSC lines included the same nine lines used to make vmDA neurons in Section 4.3, plus the additional clone for SFC840 (Table 4.2). As the differentiation capacity of iPSC lines can be variable, it was important to characterise the ability of these lines to produce MP-astrocytes before proceeding with phenotyping experiments. Seven (three controls, four patients) of the ten lines survived until 90 DIV of the differentiation (Table 4.2), at which point cells were plated at a range of densities for maturation as described in Section 3.4.1. Upon completion of the Booth differentiation protocol after 118 DIV, four of seven lines produced successful MP astrocyte cultures; however, three lines produced sparse cultures, or low yields of GFAP-positive astrocytes (Figure 4.11).

Table 4.2. iPSC lines used for differentiation to MP astrocytes.

Siblings are denoted with an asterisk. Confirmatory genotyping of lines can be found in Appendix (i).

#	Cell line	Age/Sex	LRRK2 Genotype	Reprogramming method	Survived to 90 DIV?
1	NHDF1	44/F	WT	Retrovirus	Yes
2	JR053-6	68/M	WT	Retrovirus	Yes
3	SFC840-3	67/F	WT	Cytotune (Sendai virus)	Yes
4	SFC840-6	67/F	WT	Cytotune (Sendai virus)	No
5	SFC856-4	78/F	WT	Cytotune (Sendai virus)	No
6	JR036-1*	49/M	G2019S	Retrovirus	Yes
7	MK144-7*	57/F	G2019S	Retrovirus	Yes
8	MK002-4	72/F	G2019S	Retrovirus	No
9	SFC832-19	77/F	G2019S	Cytotune (Sendai virus)	Yes
10	SFC855-6	57/M	G2019S	Cytotune (Sendai virus)	Yes

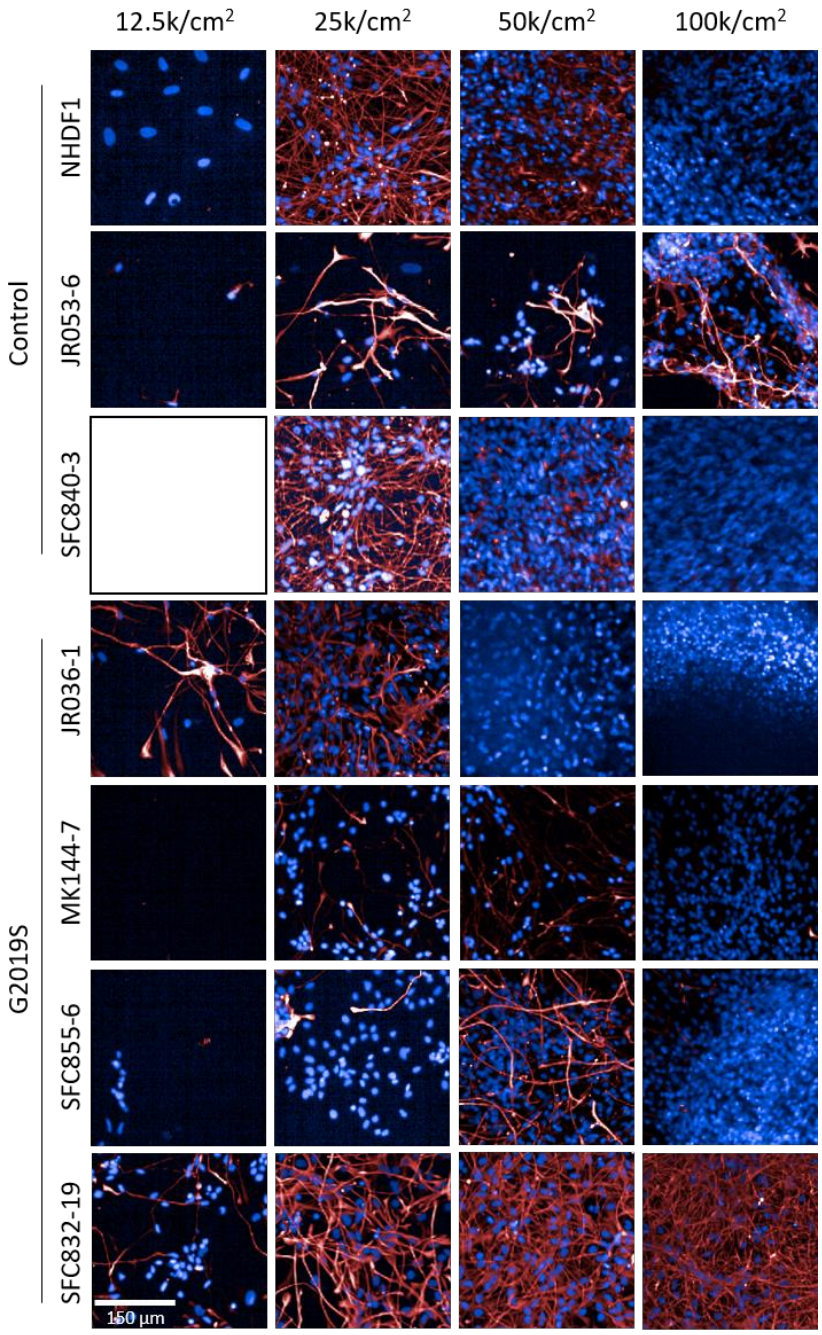

Figure 4.11. Differentiation of iPSCs from healthy controls and LRRK2-G2019S patients to MP-astrocyte cultures, at 118 DIV. *iPSCs were differentiated to MP astrocytes; for the final four weeks of the protocol, cells were plated at a range of densities. Samples at 12.5k/cm^2 density for SFC840-3 were not available for immunostaining. After 118 DIV cells were fixed and immunostained for the astrocyte marker GFAP (red) and costained for DAPI (blue).*

During optimisation of the differentiation protocol, it was demonstrated that maturing iPSC-derived MP-astrocyte cultures until 118 DIV, rather than 104 DIV, improved the yield of GFAP-positive MP astrocytes (Section 3.4.1). Therefore, it was hypothesised that maturation of the cultures further past 118 DIV might improve MP-astrocyte yield. To test this hypothesis, cells were matured for a further week, until 125 DIV. This approach was successful, and after 125 DIV, all seven lines produced reasonable yields of MP astrocytes (Figure 4.12). For all lines, apart from JR036-1, an optimal density was selected from those tested (Figure 4.12A, asterisks). For JR036-1, a density of 18,000 cells/cm^2 was selected—midway between two of the tested densities. For optimal densities, the yield of astrocytes was quantified by calculating the percentage of GFAP-positive cells in the culture (Figure 4.12B). Astrocyte yield was somewhat variable between lines; however, this was not found to correlate with the plating density used (Figure 4.12C). From here onwards, MP astrocytes were derived using the 125 DIV version of the Booth protocol, and the optimal densities determined in Figure 4.12.

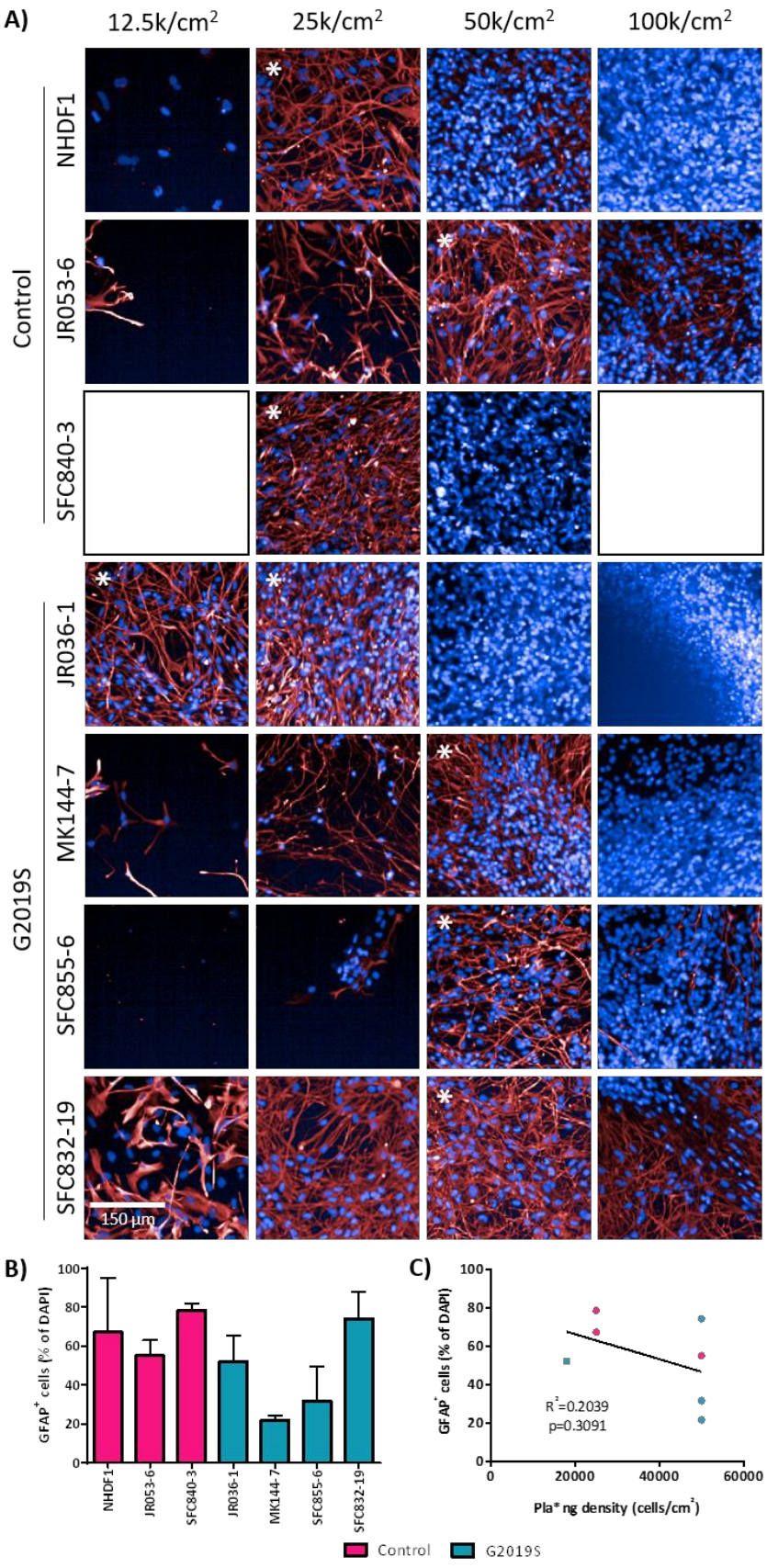

Figure 4.12. Differentiation of iPSCs from healthy controls and LRRK2-G2019S patients to MP-astrocyte cultures, at 125 DIV.

iPSCs were differentiated to MP astrocytes; for the final five weeks of the protocol, cells were plated at a range of densities (12.5k, 25k, 50k, and 100k cells/cm^2). Samples at 12.5k/cm^2 and 100k cells/cm^2 densities for SFC840-3 were not available for immunostaining. A) After 125 DIV cells were fixed and immunostained for the astrocyte marker GFAP (red) and costained for DAPI (blue). Optimal densities for each line are denoted with an asterisk. B) The percentage of GFAP-positive MP astrocytes was quantified from the optimal density for each line. (Graph shows mean ± SD, from two independent differentiations).

4.4.2. LRRK2 protein levels in iPSC-derived MP-astrocyte cultures

Western blot analysis was conducted to examine whether LRRK2 protein levels are affected by the G2019S mutation in iPSC-derived MP-astrocyte cultures. Cells were differentiated to 125 DIV, then harvested. All lines expressed LRRK2, and there was no effect of the mutation on protein levels (Figure 4.13).

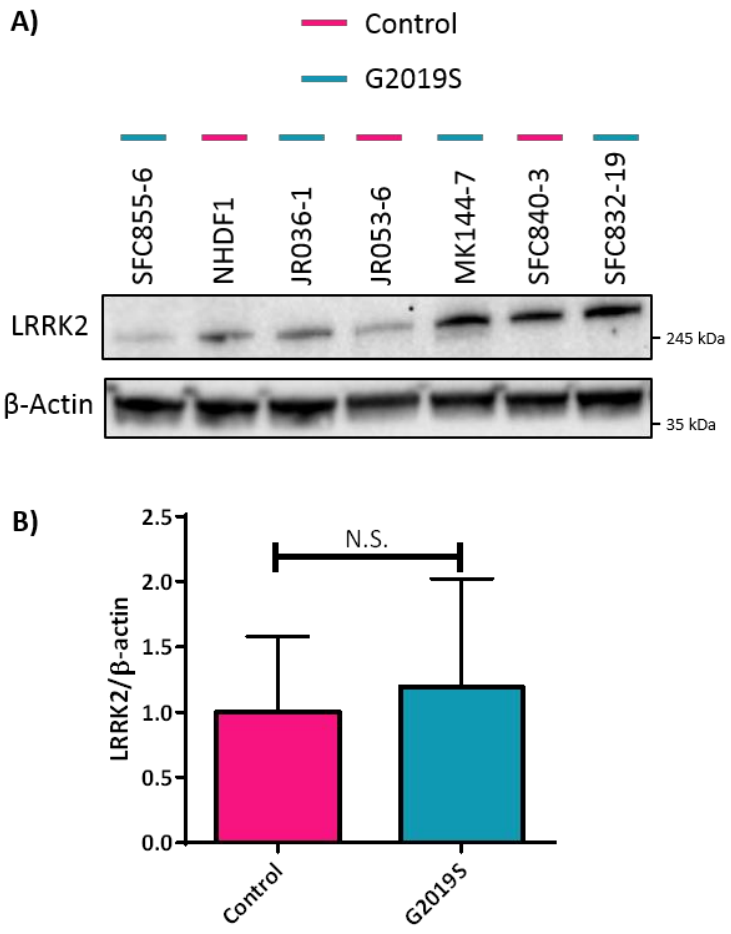

Figure 4.13. LRRK2 protein levels in iPSC-derived MP-astrocyte cultures.
Western blot analysis of LRRK2 protein levels was conducted at 125 DIV. A) Images of western blots for LRRK2 and β-Actin. B) Quantification of LRRK2 protein levels relative to β-Actin. (Graph shows mean ± SD from three controls and four G2019S lines, from one differentiation. Significance was assessed using Student's T-test. N.S. = not significant).

4.4.3. Analysis of autophagic function in iPSC-derived MP-astrocyte cultures

No studies to date have investigated the role of LRRK2 in iPSC-derived astrocytes, and only two studies have investigated the role of LRRK2 mutations in astrocytes of any kind. These studies both used primary rodent astrocytes to demonstrate a role for LRRK2 in the autophagy/lysosome pathway (Manzoni et al. 2013b; Henry et al. 2015). To determine whether this pathway is perturbed in iPSC-derived MP astrocytes, autophagic content of the cells was assessed. Western blotting demonstrated a small but significant decrease in LC3-II levels (Figure 4.14A, B), and no significant difference in LAMP1 levels (Figure 4.14A, C) in cells expressing the LRRK2-G2019S mutation. These findings suggested that there may be a decrease in autophagic content in these cells. To further investigate this possibility, immunostaining for LC3-II, LAMP1, and the astrocyte marker GFAP was conducted (Figure 4.15). LC3 and LAMP1 puncta were assessed in GFAP-positive regions of the cultures. Surprisingly, the number of autophagosomes, lysosomes, and autolysosomes detected in the cultures were not affected by the presence of the G2019S mutation.

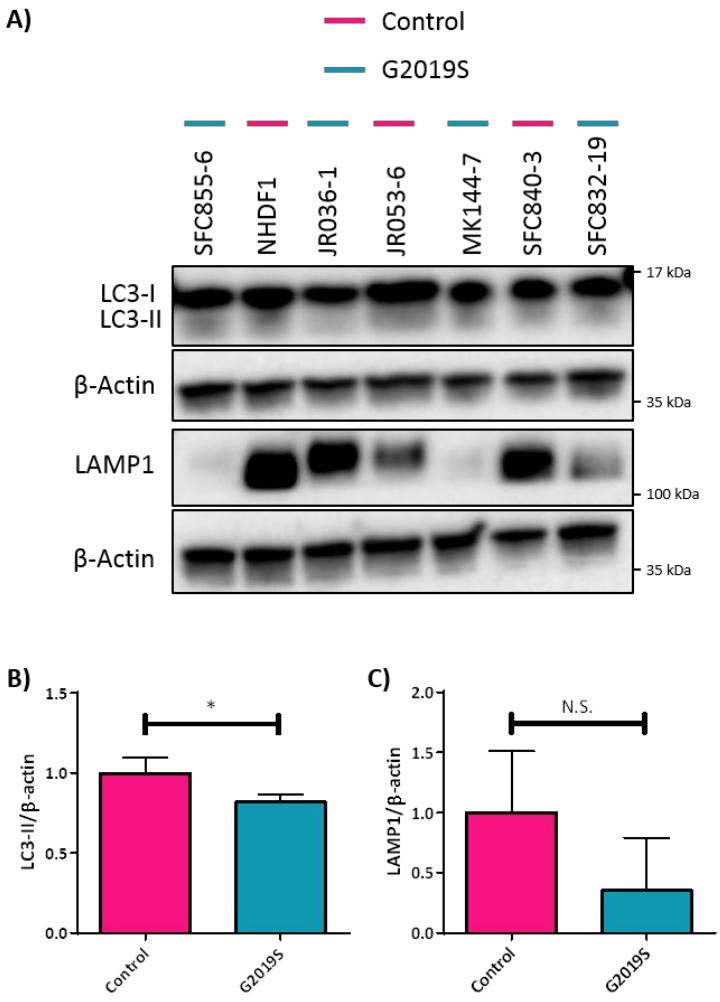

Figure 4.14. Autophagy protein levels in iPSC-derived MP-astrocyte cultures.

Western blot analysis of LC3-II and LAMP1 protein levels was conducted at 125 DIV. A) Images of western blots for LC3, LAMP1, and corresponding β-actin. Quantification of B) LC3-II and C) LAMP1 protein levels relative to β-actin, and normalised to the average of the controls. (Graphs show mean ± SD from four controls and five G2019S lines, from one differentiation. Significance was assessed using Student's T-test. N.S. = not significant).

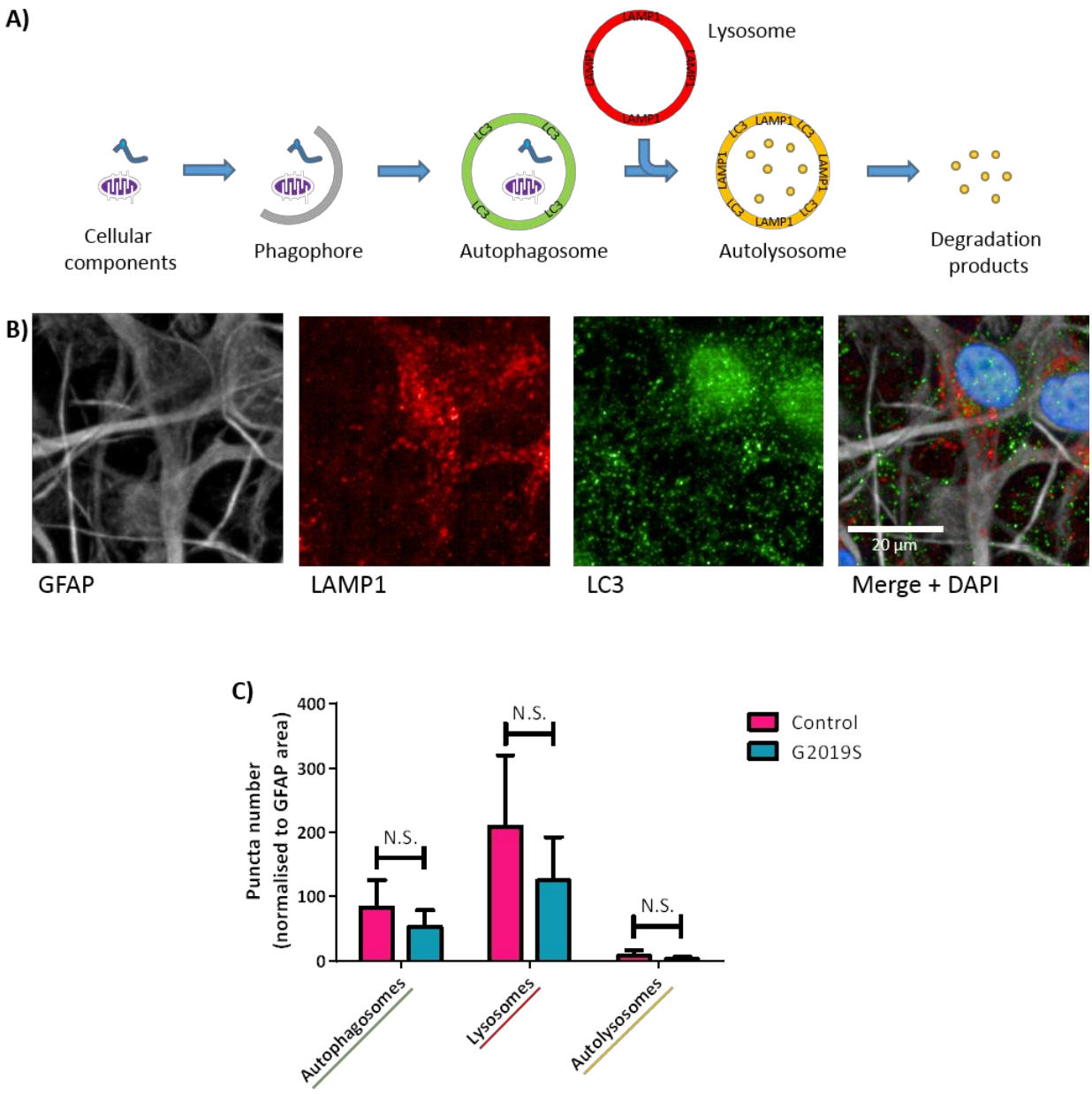

Figure 4.15. Autophagic vesicle analysis in iPSC-derived MP-astrocyte cultures.

A) Schematic of the macroautophagy process; LC3 marks the autophagosome, LAMP1 marks the lysosome, and both are present after fusion of these vesicles to form the autolysosome. B) Example images of cells at 125 DIV, immunostained for GFAP (white), LAMP1 (red), LC3 (green), and costained for DAPI (blue). C) Quantification of autophagic vesicles. (Graph shows mean ± SD from three controls and four G2019S lines, from one differentiation. Significance was assessed using Student's T-test. N.S. = not significant).

To directly measure protein degradation by autophagy, a radioactive pulse-chase assay can be used (Gronostajski and Pardee 1984). This involves the measurement of radiolabelled amino acids that are released from cells during protein degradation. The use of proteasome and autophagy inhibitors allows for the analysis of proteins that are degraded through each of these pathways. This assay requires a large number of cells, and was not conducted on the iPSC-derived vmDA-neuron cultures as their production at large scales is costly. However, as the MP-astrocyte differentiation protocol is relatively inexpensive and includes multiple expansion steps, a large number of cells can easily be produced. Therefore, enough cells were available to conduct this assay and to determine whether protein degradation was disrupted in the G2019S MP-astrocytes. Cells were pulsed with radiolabelled valine, then chased with medium containing non-radiolabelled valine. Degradation of long-lived proteins via autophagy and the ubiquitin-proteasome was assessed after 24 hrs. The total percentage of degraded radiolabelled valine was found to be ~16% in both LRRK2-G2019S and control cells (Figure 4.16). Addition of the proteasome inhibitor MG132 demonstrated that a large proportion of degradation occurred via this pathway, whereas inhibition with the autophagy inhibitor chloroquine, had a much smaller effect. No differential effects were observed between genotypes.

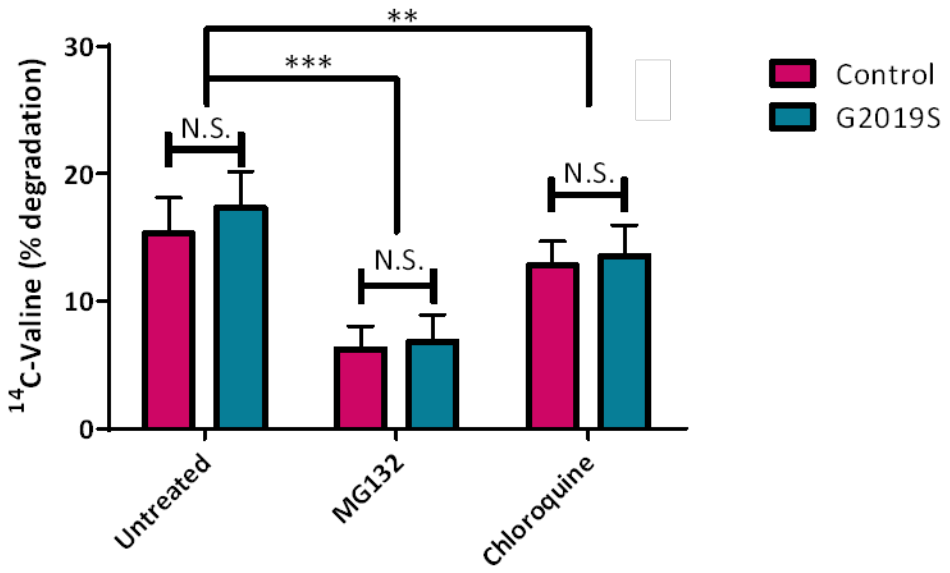

Figure 4.16. Protein degradation analysis in iPSC-derived MP-astrocyte cultures.
*Cells were pulsed with ^{14}C-valine for 48 hours, then chased with cold medium containing ^{12}C-Valine for 24 hours. Protein degradation was then assessed over a period of 24 hrs in the presence or absence of MG132 (10 µM) and Chloroquine (20 µM). (Graph shows mean ± SD from three controls and four G2019S lines, from two independent differentiations. Significance was assessed using a two-way ANOVA. **p<0.01, ***p<0.001, N.S. = not significant).*

4.4.4. Analysis of mitochondrial function in iPSC-derived MP-astrocyte cultures

To determine whether the LRRK2-G2019S mutation results in mitochondrial dysfunction in iPSC-derived MP-astrocyte cultures, their mitochondrial respiration was analysed using the Seahorse metabolic analyser as previously explained in Section 4.3.5. Consistent with the findings in the iPSC-derived vmDA-neuron cultures, mitochondrial respiration occurred at the same rate in G2019S MP-astrocyte cultures as in controls (Figure 4.17).

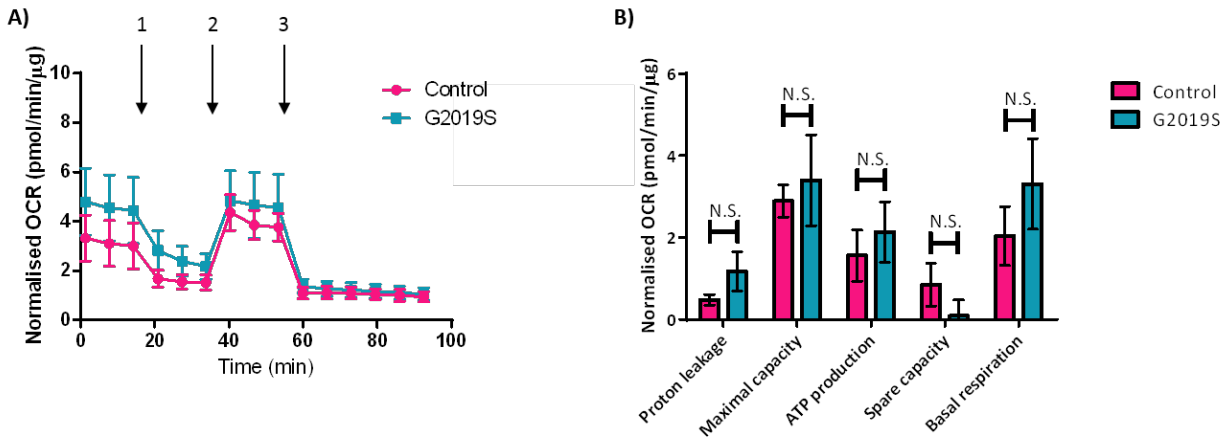

Figure 17. Analysis of mitochondrial respiration in iPSC-derived MP-astrocyte cultures.
Cells were cultured until 125 DIV then analysed using the Seahorse metabolic analyser, all data was normalised to cellular protein content, which was calculated using a bicinchoninic acid (BCA) assay. A) Oxygen consumption rate (OCR) over time, following addition of mitochondrial inhibitors 1) oligomycin, 2) FCCP, 3) antimycin A and rotenone. B) Quantification of mitochondrial respiration parameters. (Graphs show mean ± SD from three controls and four G2019S lines, from two independent differentiations. Significance was assessed using Student's T-test. N.S. = not significant).

4.4.5. Analysis of glycolytic function in iPSC-derived MP-astrocyte cultures

To further characterise cellular respiration in LRRK2-G2019S MP-astrocyte cultures, their glycolytic function was measured using the Seahorse metabolic analyser as previously described in Section 4.3.5. As was the case for iPSC-derived vmDA-neuron cultures, MP-astrocyte cultures expressing the LRRK2-G2019S mutation did not exhibit any changes in glycolytic function when compared to controls (Figure 4.18).

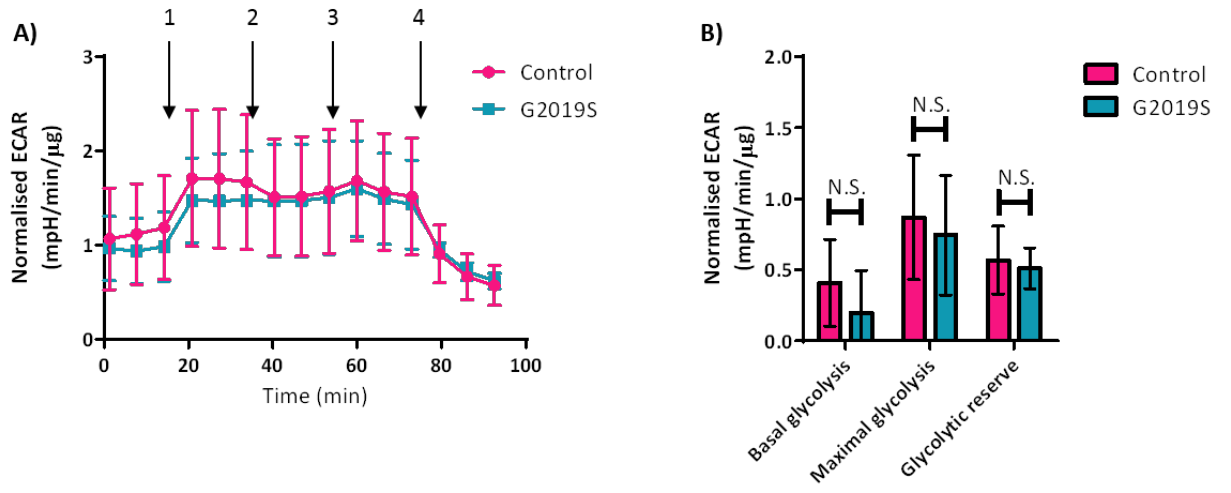

Figure 4.18. Analysis of mitochondrial respiration in iPSC-derived MP-astrocyte cultures.
Cells were cultured until 125 DIV then analysed using the Seahorse metabolic analyser, all data was normalised to cellular protein content. A) Extracellular acidification rate (ECAR) over time, following addition of mitochondrial inhibitors 1) oligomycin, 2) FCCP, 3) antimycin A and rotenone, and 4) the glycolysis inhibitor 2-deoxyglucose. B) Quantification of glycolytic respiration parameters. (Graphs show mean ± SD from three controls and five G2019S lines, from two independent differentiations. Significance was assessed using Student's T-test. N.S. = not significant).

4.4.6. Analysis of glutamate uptake by iPSC-derived MP-astrocyte cultures

In vivo, astrocytes take up glutamate in a sodium-dependent manner through their glutamate transporters (Schousboe et al. 1977). Other proteins that are implicated in PD pathogenesis have been shown to influence glutamate uptake; deficiency of DJ-1 and astrocyte-specific overexpression of α-Synuclein both result in impaired glutamate uptake in astrocyte cultures (Kim et al. 2016; Gu et al. 2010). In Chapter 3 (Figure 3.17), it was demonstrated that iPSC-derived MP-astrocytes could take up glutamate. To determine whether this uptake is disrupted by the LRRK2-G2019S mutation, a glutamate uptake assay was performed in patient and control lines (Figure 4.19). There was no difference in capacity for glutamate uptake between the two groups.

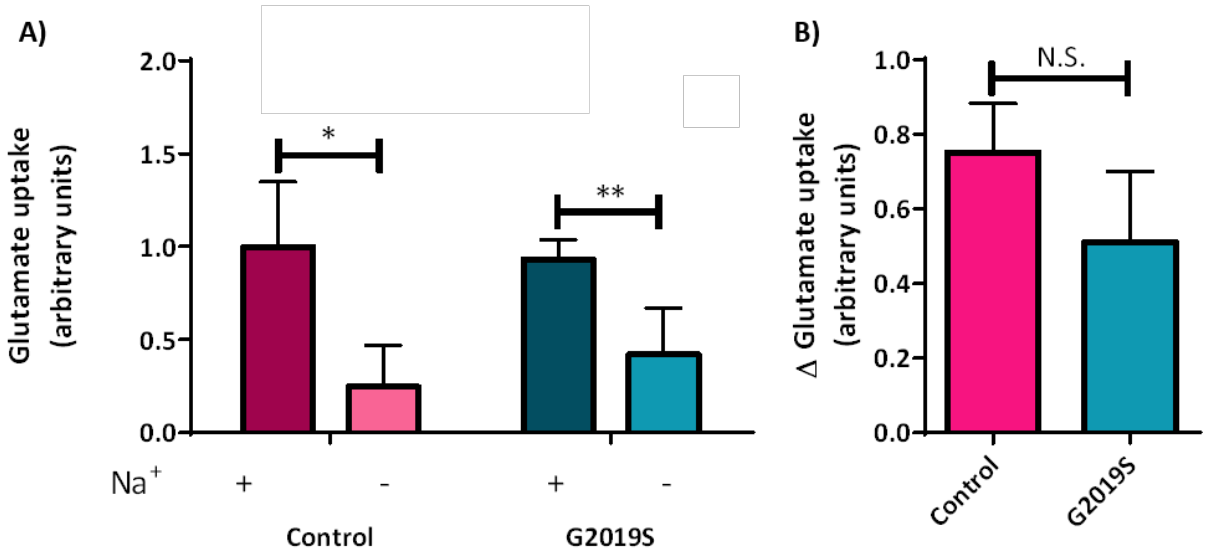

Figure 4.19. Glutamate uptake in iPSC-derived MP-astrocyte cultures.

*A) Specific uptake of glutamate through glutamate transporters was assessed by measuring the ability of cells to take up tritiated glutamate in the presence and absence of sodium (Na^+). Counts per minute (CPM) were normalised to cell protein content. B) Delta (Δ) was calculated as the difference in uptake in the presence and absence of Na^+. (Graphs show mean ± SD from three controls and four G2019S lines, from two independent differentiations. Significance was assessed using A) a two-way ANOVA, and B) Student's T-Test **p<0.01, N.S. = not significant).*

4.4.7. Analysis of cell proliferation and migration iPSC-derived MP-astrocyte cultures

KO of PD-linked genes *Prkn* and *Pink1* each result in decreased proliferation of astrocytes (Choi, et al. 2013; Solano et al. 2006). To determine whether LRRK2 plays a role in astrocyte proliferation, a scratch was applied to cultures, and the ability of the cells to proliferate and migrate into the resulting wound was monitored for 43 hours (Figure 4.20). The area covered by cells was quantified throughout the time course. There was no significant difference in response to the scratch between control and LRRK2-G2019S lines.

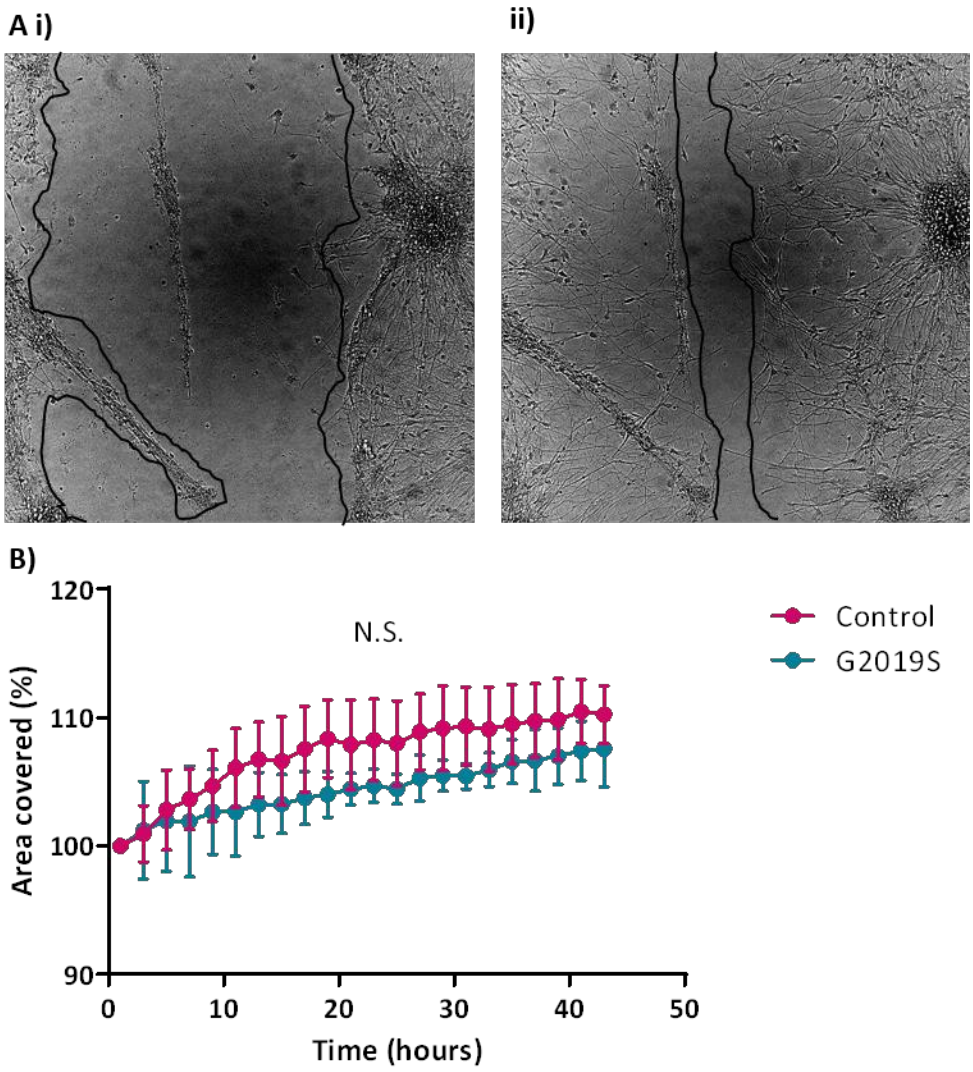

Figure 4.20. Proliferation and migration of iPSC-derived MP-astrocyte cultures.
Proliferation and migration of MP-astrocytes were measured by applying a scratch to the cultures and then monitoring cell growth into the space. A) Example images of cells i) 1 hr and ii) 42 hrs after application of the scratch, with the border of the scratch marked with a black line. B) Cell coverage over time, normalised to coverage 1 hr after application of the scratch. (Graph shows mean ± SD from three controls and four G2019S lines, from two independent differentiations. Significance was assessed using a two-way ANOVA, N.S. = not significant).

4.5. Discussion and conclusions

In this chapter, a hypothesis-driven approach was taken to investigate the effect of the pathogenic LRRK2-G2019S mutation on cellular functions in iPSC-derived vmDA neurons and, for the first time, MP astrocytes. Pathways that LRRK2 has previously been implicated in were investigated, with the aim of identifying disease phenotypes for further interrogation. Previous studies in iPSC-derived vmDA neurons expressing the LRRK2-G2019S mutation have demonstrated neurite shortening, changes in autophagy, and mitochondrial dysfunction (Section 1.3.4.vi). However, in this study, cells expressing the G2019S mutation did not exhibit phenotypes in any of these pathways when compared to cells from healthy LRRK2-WT controls.

There are a number of possible reasons that might explain why cellular phenotypes differ between these previous studies in vmDA neurons and the work described here. One key issue is differences in culture conditions between studies. The cultures used in this study are more highly enriched for neuronal cells and contain a higher percentage of vmDA neurons (~25-30%) than other studies (~2-10%). Therefore, it is possible that phenotypes seen in other systems may have resulted from other cells within the culture, which are not present in the model used here, or from the influence of those other cells upon the vmDA neurons. Differences in the density of cultures and the timepoints at which analyses were performed may also play a role. Furthermore, the use of different protocols for differentiation, and the growth medium that the cells are maintained in, may affect maturity of the cultures and predispose them to reveal certain phenotypes.

In the case of neurite outgrowth, there is evidence to suggest that neurite shortening in neurons expressing the LRRK2-G2019S mutation is affected by neuronal maturity and the substrate on which cells are grown (Sepulveda et al. 2013; Borgs et al. 2016). It is therefore possible that modification of the assay parameters used in Section 4.3.3 might reveal a phenotype.

Although LRRK2 has been widely implicated in autophagy, only one study has demonstrated altered LC3-II levels and autophagic vesicle content in iPSC-derived vmDA cultures expressing the LRRK2-G2019S mutation (Sanchez-Danes et al. 2012a). A further study also showed changes in lysosomal content (Orenstein et al. 2013). The cultures used in both studies were differentiated from iPSCs by overexpression of LMX1A, and grown on WT mouse astrocytes and contained a low percentage of vmDA neurons (~10%). Changes in autophagic vesicle content in vmDA neurons were only detected in aged cells (75 DIV) (Sanchez-Danes et al. 2012a). In the experiments described in this chapter, no phenotype was detected in vmDA neurons at either 35 DIV or 76 DIV (Section 4.3.4), suggesting that the maturity of the cultures does not impact on the development of this phenotype in our model. Furthermore, only a small reduction in LC3-II levels, but no change in autophagic vesicle content, was detected in MP astrocytes (Section 4.4.3). The discrepancy between the results presented here, and the work produced by Sanchez-Danes et al., may be due to an interaction between the vmDA neurons and the WT mouse astrocytes in their study. Alternatively, the differentiation protocol used in their study may give rise to cultures that represent a later stage of PD pathogenesis than the cultures used here.

A handful of studies have demonstrated mitochondrial phenotypes in iPSC-derived DA and iPSC-derived vmDA-neuron cultures expressing the G2019S mutation (Section 1.3.4.vi). One of these

studies showed increased cell death in response to mitochondrial toxins in LRRK2-G2019S expressing cultures when compared to controls (Reinhardt et al. 2013), another found increased mitochondrial DNA-damage (Sanders et al. 2014), and a third demonstrated that mitophagy was impaired (Hsieh et al. 2016). Mitochondrial respiration has been found to be dysfunctional in iPSC-derived DA-neuron cultures that are homozygous for the LRRK2-G2019S mutation (Cooper et al. 2012); however, this has not been demonstrated for the heterozygous mutation. In this chapter, it has been demonstrated that heterozygous LRRK2-G2019S mutation does not result in dysfunctional mitochondrial respiration in iPSC-derived vmDA-neuron or MP-astrocyte cultures, at least under the culture conditions used here. These results suggest that there may be a dosage effect associated with perturbation of mitochondrial function by the LRRK2-G2019S mutation. In addition to analysis of mitochondrial respiration, glycolytic respiration was also investigated in these cultures. This is the first study to functionally assess the effect of any LRRK2 mutation upon glycolysis, and it was found that the G2019S mutation had no effect on this cellular process.

This study is the first to investigate the effects of the LRRK2-G2019S mutation in iPSC-derived astrocytes of any kind. Assays that were used to investigate the effects of LRRK2 upon macroautophagy and cellular respiration in iPSC-derived vmDA-neuron cultures were replicated in MP astrocytes, to determine whether LRRK2 has a differential effect on these pathways in different cell types. No alteration of these pathways was detected; therefore, further investigation was carried out into astrocyte-specific functions. The ability of the MP-astrocytes to take up glutamate (Section 4.4.6) and to proliferate (Section 4.4.7) was assessed, as these functions have been demonstrated to be modulated by other proteins that are involved in PD pathogenesis (Kim et al. 2016; Gu et al. 2010). However, no changes in these functions could be

detected. During the course of this study, transcriptomic analysis of these cells was conducted (presented in Chapter 5, section 5.5). The results of this analysis showed that in the two female LRRK2-G2019S lines, the second X-chromosome was reactivated. X-chromosome reactivation has previously been shown to affect cellular phenotypes (Mekhoubad et al. 2012); therefore, these MP astrocyte cultures may not be suitable for identifying disease phenotypes. As such, it is difficult to draw any conclusions regarding the effect of the LRRK2-G2019S mutation on these cells.

The Park8 locus, where the *LRRK2* gene resides, was identified in 2002 (Funayama et al. 2002). Mutations in the *LRRK2* gene were subsequently identified in 2004 (Paisan-Ruiz et al. 2004; Zimprich et al. 2004), and since then the LRRK2 protein has been implicated in a wide range of cellular processes. This chapter set out to confirm and expand upon existing hypotheses around LRRK2 function, using culture conditions that yielded a high percentage of vmDA neurons and MP astrocytes. A selection of cellular functions were interrogated; however, the data described here show that neither vmDA neurons, nor MP astrocytes, grown under the conditions described, exhibit any LRRK2-G2019S mediated changes in these functions. This might suggest that these cell types are not involved in the pathogenesis of PD; however, this hypothesis, especially in the case of vmDA neurons, would be contrary to all that is known about the disease, and to what has been previously published in the literature. Rather, the findings described here suggest that emergence of mutant LRRK2 phenotypes may be highly dependent upon culture composition and conditions. It is possible that the cultures used in this study may be representative of an early disease state, where overt functional phenotypes have not yet developed. Only selected aspects of specific cellular pathways were chosen for analysis, and not all possibilities were assessed.

Furthermore, the assays performed in this chapter provide readouts on cellular functions that may be perturbed due to downstream, rather than direct, effects of the LRRK2-G2019S mutation. The results of this chapter demonstrate that a hypothesis-driven approach may limit identification of disease phenotypes. It may therefore be the case, that other, unbiased analyses would be more useful for identifying the pathogenic effects of disease mutations.

Chapter 5: Proteomic and transcriptomic analysis of iPSC-derived vmDA neurons and MP astrocytes carrying the LRRK2-G2019S mutation

5.1. Introduction

In Chapter 4, hypothesis-driven analysis of iPSC-derived vmDA-neuron and MP-astrocyte cultures harbouring the LRRK2-G2019S mutation was conducted with the aim of identifying disease phenotypes. This approach proved unsuccessful, as no phenotypes could be identified. Following these findings, it was considered that the identification of phenotypic changes in iPSC-derived cultures might be highly dependent upon culture and assay conditions. In order to reduce the impact of such effects on any further analysis, an unbiased approach for identifying disease phenotypes was sought. A combination of proteomic and transcriptomic analysis was chosen to provide a detailed understanding of the effects of the LRRK2-G2019S mutation on iPSC-derived vmDA-neuron and MP-astrocyte cultures. In addition to this, a phosphoproteomics analysis was designed to identify LRRK2 kinase substrates in iPSC-derived vmDA-neuron cultures.

5.1.1. Proteomic analysis methodologies

Quantitative, proteomic analysis can be conducted using mass spectrometry, and provides information about thousands of proteins in one sample. Mass spectrometry is most successful when used to identify the sequences of peptides that are around 20 amino acids in length (Steen and Mann 2004). To achieve such results, complex protein samples are first digested to peptides. These are then injected onto a reverse-phase, high-performance liquid-chromatography (LC) column, which separates them by hydrophobicity, before loading onto the mass spectrometer. In the mass spectrometer, peptides are ionized, and the mass to charge ratio (m/z) of each

peptide identified (MS^1). Fragmentation of the analysed peptides is then conducted, and further information regarding the peptide sequences is then acquired from a second mass spectrometry analysis (MS^2). This technique is referred to as LC-MS/MS.

Technical variation between mass spectrometry runs means that quantitation of samples without normalisation to an internal control can be difficult. To overcome this, samples can be labelled and then combined for mass spectrometry analysis, enabling the direct comparison of protein levels in one run. To conduct a meaningful comparison of iPSC-derived cell cultures from LRRK2-G2019S patient and control lines, it was necessary to quantitatively analyse a total of seven to nine samples. A number of labelling options were considered for this analysis. Stable isotope labelling by amino-acids in cell culture (SILAC) can be used to introduce heavy-labelled amino acids into samples (Ong et al. 2002). This technique was discounted for use with these iPSC-derived cultures, as it would be necessary to grow the cells in SILAC medium for long periods of time throughout the differentiations, which would be extremely costly.

Multiple techniques exist for labelling samples after they are digested to peptides. Early examples include techniques such as ICAT (Gygi et al. 1999) or dimethyl labelling (Hsu et al. 2003), which result in slightly different m/z for each sample, therefore allowing for the ratiometric comparison of protein levels. However, the number of comparisons that can be made using these techniques is limited. Quantitative comparison of multiple samples can be achieved using isobaric labelling techniques (Thompson et al. 2003; Ross et al. 2004; Dayon et al. 2008). These involve the labelling of fragmented peptides from each sample with a different tag. The tags each have the same overall mass and consist of three regions: a mass reporter—which differs in mass for each tag, a

mass normaliser, and an amine reactive group (Figure 5.1A). During identification of peptides in MS^1, identical peptides from multiplexed samples exhibit the same m/z, resulting in a single peak, and higher sensitivity than other labelling techniques such as ICAT and dimethyl labelling (Bakalarski and Kirkpatrick 2016). Upon fragmentation, the mass reporter is cleaved from each tag, and detected in MS^2, providing quantification of the level of peptide present in each multiplexed sample. Furthermore, up to ten samples can be multiplexed using tandem-mass tag (TMT)-10plex labels (Figure 5.1B), making it highly suitable for the comparison of iPSC-derived cultures from multiple lines.

In addition to providing information about the levels of proteins in a sample, LC-MS/MS analysis can be used to identify post-translational modifications, such as phosphorylation. In order to enrich for phosphopeptides, samples are commonly passed through an Immobilized Metal-Ion Affinity Chromatography (IMAC) column, or a Metal Oxide Affinity Chromatography (MOAC) column before analysis (von Stechow et al. 2015). Multiplexing of samples using techniques such as TMT-10plex labelling is especially useful for identification of post-translational modifications, as it allows for the pooling of labelled samples before phosphopeptide enrichment. This minimises variability across samples, and means that less starting material is needed per sample.

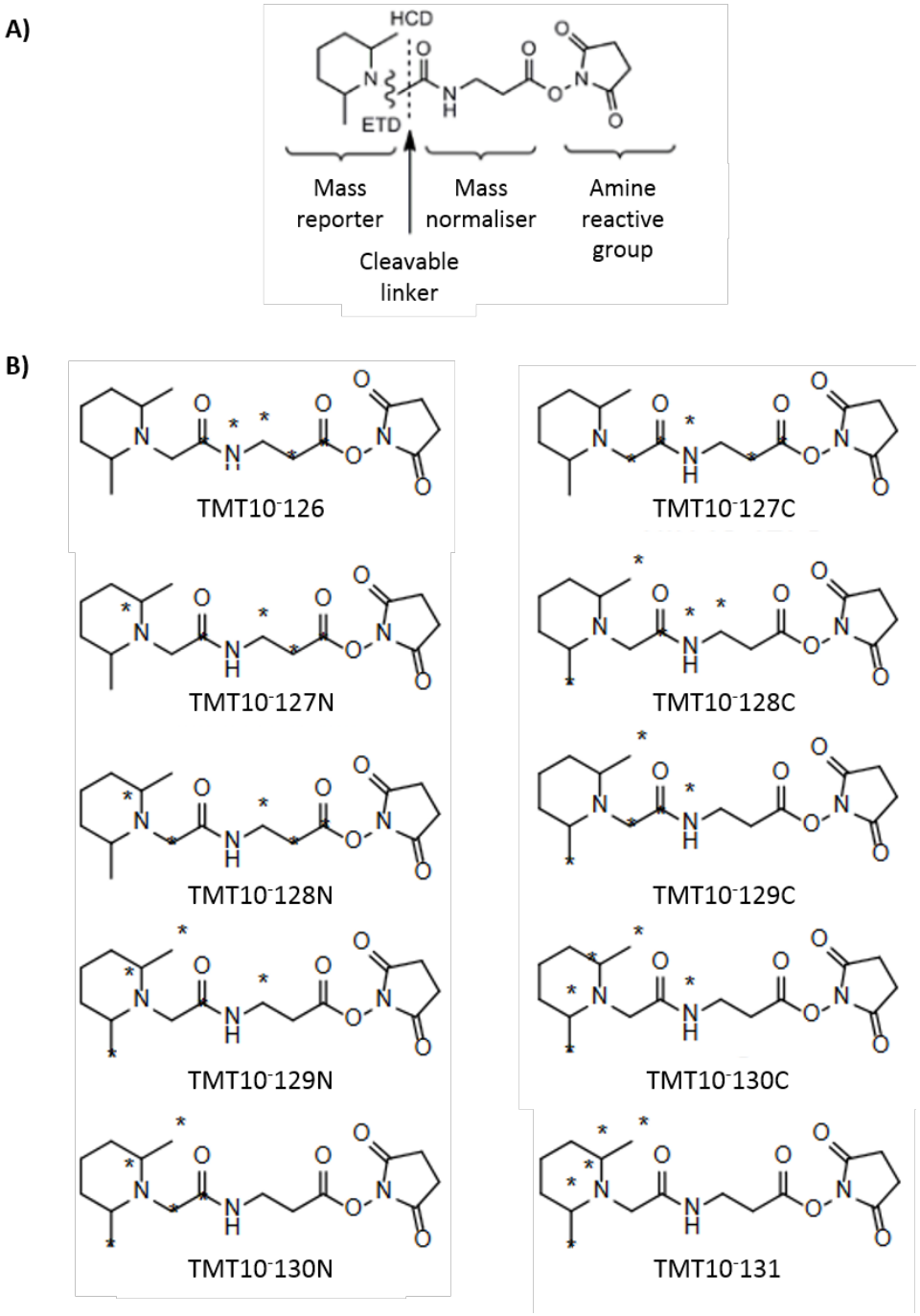

Figure 5.1. TMT tag structure.

A) TMT-10plex tags each have the same mass and consist of three regions: a mass reporter, a mass normaliser, and an amine reactive group. During MS^1, the tagged peptides are all read as the same mass; however, upon fragmentation by higher-energy collision dissociation (HCD) or electron transfer dissociation (ETD), the mass reporter is cleaved. The reporter is read during MS^2, to provide quantification of the amount of peptide from each sample. B) TMT-10plex reagent structures and isotope positions (*).

5.1.2. Transcriptomic analysis methodologies

RNA sequencing (RNA-seq) using next-generation sequencing (NGS) is the current gold-standard method for transcriptomic analysis. Although a number of NGS methodologies have been developed, the most widely used was developed by Solexa (now Illumina) (Bentley et al. 2008). This technique involves fragmentation of total cellular RNA to sequences of up to 300 bases in length, followed by reverse transcription of RNA to cDNA, and then second strand synthesis. Double-stranded fragments are then labelled with sequencing adaptors, amplified, and annealed to the sequencing flow cell. Isothermal bridging amplification is then conducted to create clusters of identical sequences. “Sequencing by synthesis” is then used to extend fragments one base at a time, using unextendible fluorescent DNA bases. Fluorescence wavelength and intensity is measured at each cluster, to determine which DNA base is present, then the fluorescent bases are chemically converted to regular, extendible bases. The process is repeated for each subsequent base. This technique is quantitative, and allows for the analysis and comparison of large numbers of samples. It is therefore highly suited for transcriptomic analysis of iPSC-derived cell cultures from multiple lines.

5.2. Aims of this chapter

1. To describe and discuss the proteomic and transcriptomic changes in iPSC-derived **vmDA-neuron cultures** that carry the LRRK2-G2019S mutation.
2. To describe and discuss proteomic and transcriptomic changes in iPSC-derived **MP-astrocyte cultures** that carry the LRRK2-G2019S mutation.
3. To describe and discuss the identification of LRRK2 substrates iPSC-derived **vmDA-neuron cultures** using LRRK2 inhibitors in combination with phosphoproteomics analysis.

5.3. Collaboration and confidentiality statement

All of the work in this chapter was conducted in collaboration with employees of Biogen Inc. The contents of this chapter are confidential.

I conducted all iPSC differentiations to vmDA neurons and MP astrocytes, and compound treatments of these cells and of primary neuronal cultures. I performed cell lysis for proteomics and phosphoproteomics analyses, and lysis, RNA extractions, and RNA quantification and RNA integrity analysis on samples for transcriptomics analysis.

Peptide/phosphopeptide enrichment, TMT-labelling, and LC-MS/MS analysis of samples for the proteomics and phosphoproteomics analyses were conducted by Dr Jeff Martin. Library preparation and RNA-seq runs for transcriptomics analysis were conducted by Norm Allaire. Bioinformatics analysis was conducted by Drs Benbo Gao and Kejie Li. Data interpretation was performed in a collaborative manner.

Following analysis of the proteomics, phosphoproteomics, and transcriptomics analyses, I conducted further iPSC differentiations for follow up analyses. I performed all analyses of these samples unless otherwise stated.

5.4. Results I: Proteomics and transcriptomics analysis of iPSC-derived vmDA-neuron cultures expressing the LRRK2-G2019S mutation

5.4.1. Identification of pathways perturbed by the LRRK2-G2019S mutation

To understand the effects of the LRRK2-G2019S mutation upon the transcriptome and proteome of iPSC-derived vmDA-neuron cultures, cells from the four control and five patient lines described in Chapter 4 (Table 4.1) were used. iPSCs were differentiated to vmDA-neuron cultures using the Booth-Zambon protocol and then harvested for proteomic analysis by LC-MS/MS and transcriptomic analysis by RNA-seq. In order to identify cellular pathways that were robustly perturbed by the LRRK2-G2019S mutation, each cell line was harvested for analysis at both 35 DIV and 56 DIV. To enable multiplex analysis by LC-MS/MS, samples were labelled using TMT-10plex tags to create TMT sets for each timepoint.

A total of 10502 proteins and 16893 genes were detected in the 35 DIV samples, and 10501 proteins and 18146 genes were detected in the 56 DIV samples. To assess the variance in the resulting data sets, principal component analysis (PCA) was conducted for LC-MS/MS and RNA-seq data (Figure 5.2). The resulting PCA plots both demonstrated separation of the genotypes using a combination of principal component 1 (PC1) and principal component 2 (PC2). Further investigation revealed that 2331 proteins and 2238 genes at 35 DIV, and 1439 proteins and 2572 genes at 56 DIV, were significantly differentially expressed (false-discovery adjusted (FDR) $p<0.05$, and fold change (FC)>1.5) (Figure 5.3A). Given that data from lines expressing the LRRK2-G2019S mutation clustered separately from the controls at the protein and gene levels at both timepoints, the data were combined into a single omics dataset for further analysis (this

combined dataset is referred to as the dual omics dataset from here onwards). This dual omics dataset was analysed using the Ensemble of Gene Set Enrichment Analyses (EGSEA) (Alhamdoosh et al. 2016), to reveal cellular pathways that were perturbed across all conditions (Figure 5.3B, Appendix (ii)).

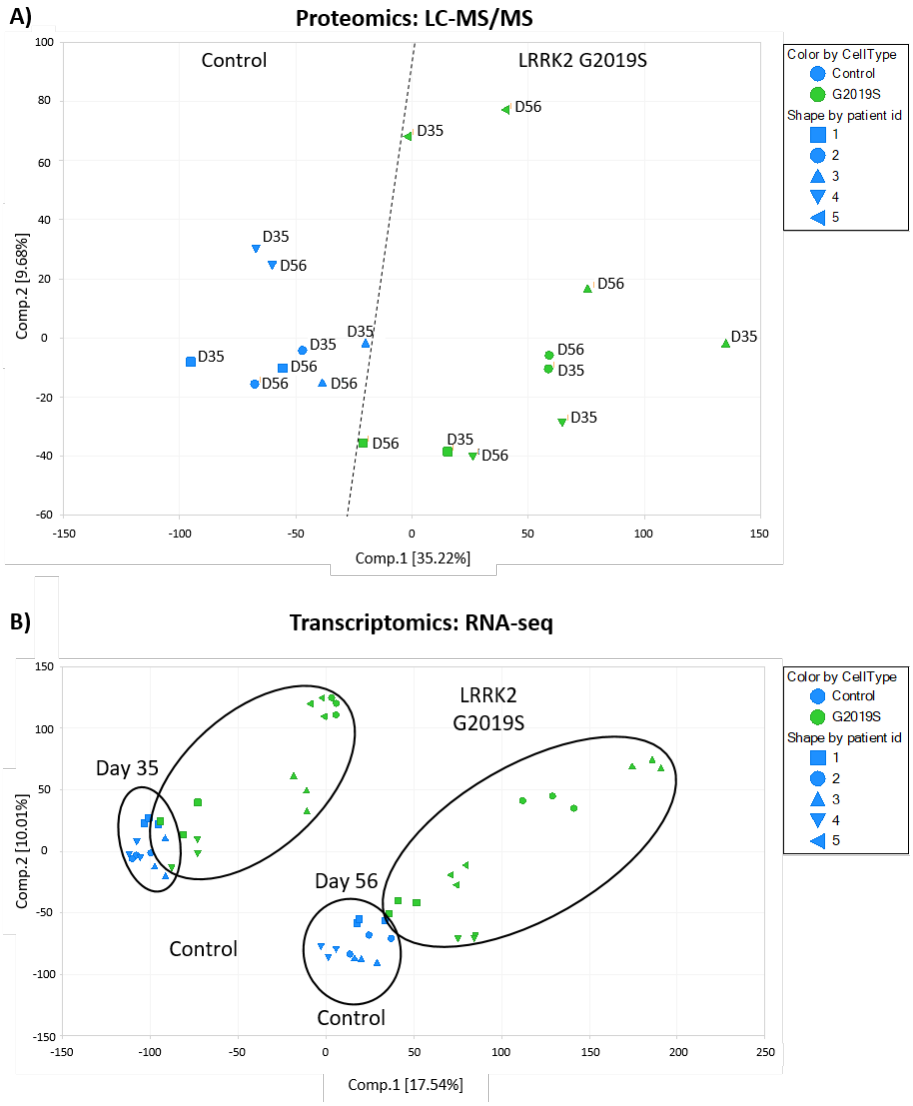

Figure 5.2. Principal component analysis of proteomics and transcriptomics data from iPSC-derived vmDA-neuron cultures.

Principal component analysis of A) proteomics data, and B) transcriptomics data, demonstrating separate clustering of LRRK2-G2019S cultures from controls at 35 and 56 DIV. PCA plots created by Dr Kejie Li.

A)

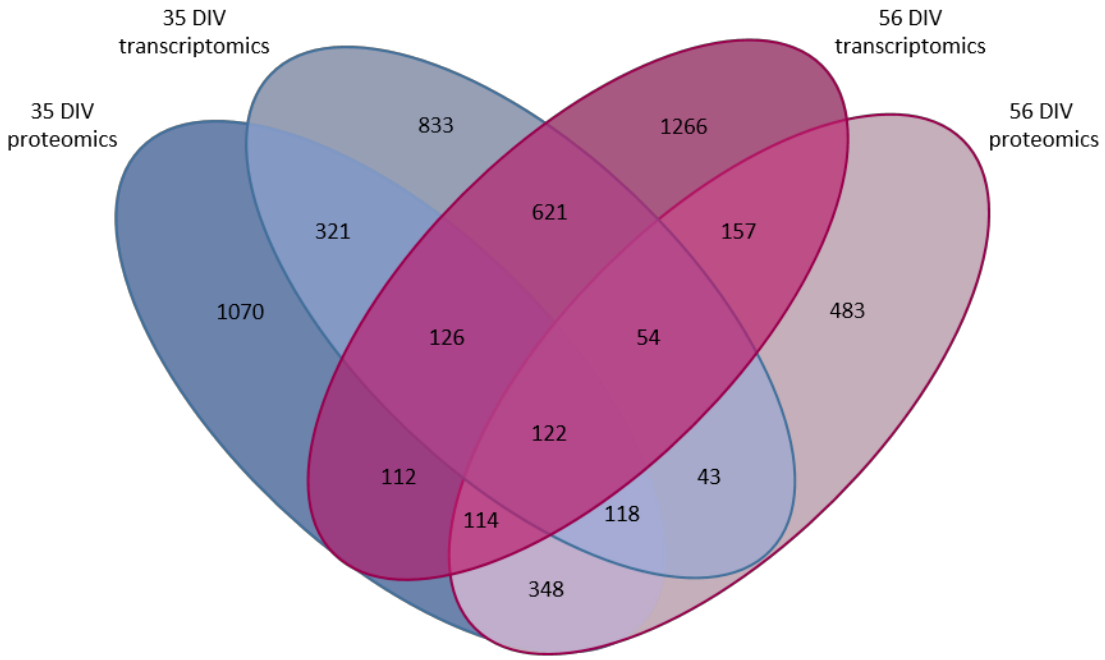

B)

EGSEA pathway	Adjusted *p*-value	Average FC	Direction
hsa04144 Endocytosis	8.85E-09	1.43	Down
hsa04360 Axon guidance	8.85E-09	1.42	Down
hsa05100 Bacterial invasion of epithelial cells	1.51E-07	1.43	Down
hsa03010 Ribosome	1.85E-07	1.20	Up
hsa04062 Chemokine signaling pathway	2.06E-05	1.45	Down
hsa04530 Tight junction	2.06E-05	1.48	Down
hsa04660 T cell receptor signaling pathway	2.06E-05	1.51	Down
hsa04728 Dopaminergic synapse	2.06E-05	1.42	Down
hsa05161 Hepatitis B	2.06E-05	1.47	Down
hsa04261 Adrenergic signaling in cardiomyocytes	2.65E-05	1.45	Down

Figure 5.3. Identification of differentially expressed proteins and genes, and the cellular pathways that they contribute to.

A) Venn diagram showing the number of overlapping genes/proteins that were differentially expressed between the control and G2019S genotypes in each experiment: blue, 35 DIV proteomics; light blue, 35 DIV transcriptomics; pink, 56 DIV transcriptomics; light pink, 56 DIV proteomics. B) Top ten most significantly differentially expressed pathways as identified by EGSEA analysis of the integrated omics dataset. p-values were adjusted for false-discovery rate. FC=fold change. Direction refers to the predicted direction of change of the pathway, down=downregulation of pathway, up=upregulation of pathway. A complete list of significant pathways can be found in Appendix (ii).

Differentially expressed pathways were considered for further follow-up. The pathways that were found to be the most significantly disrupted by the LRRK2-G2019S mutation were endocytosis and axon guidance, both of which were predicted to be downregulated in the presence of the mutation. These were selected for further experimental validation.

5.4.2. Experimental paradigm for confirmation of findings from the dual omics study

To determine whether selected genes/proteins were differentially expressed across multiple differentiations, two further differentiations of the same nine iPSC lines (four controls, five LRRK2-G2019S lines) were conducted. Furthermore, two lines expressing the pathogenic LRRK2-R1441C mutation were also differentiated (Table 5.1, Figure 5.4). These samples and the remainder of those used for the dual omics experiment were used to determine whether the selected genes/proteins were differentially expressed across multiple differentiations, and whether these changes were conserved in the presence of other LRRK2 mutations.

Table 5.1. LRRK2-R1441C iPSC lines for differentiation to vmDA neurons.
Confirmatory genotyping of lines can be found in Appendix (i).

#	Cell line	Age/Sex	LRRK2 Genotype	Reprogramming method
1	SFC869-4	56/F	R1441C	Cytotune (Sendai virus)
2	SFC870-5	32/M	R1441C	Cytotune (Sendai virus)

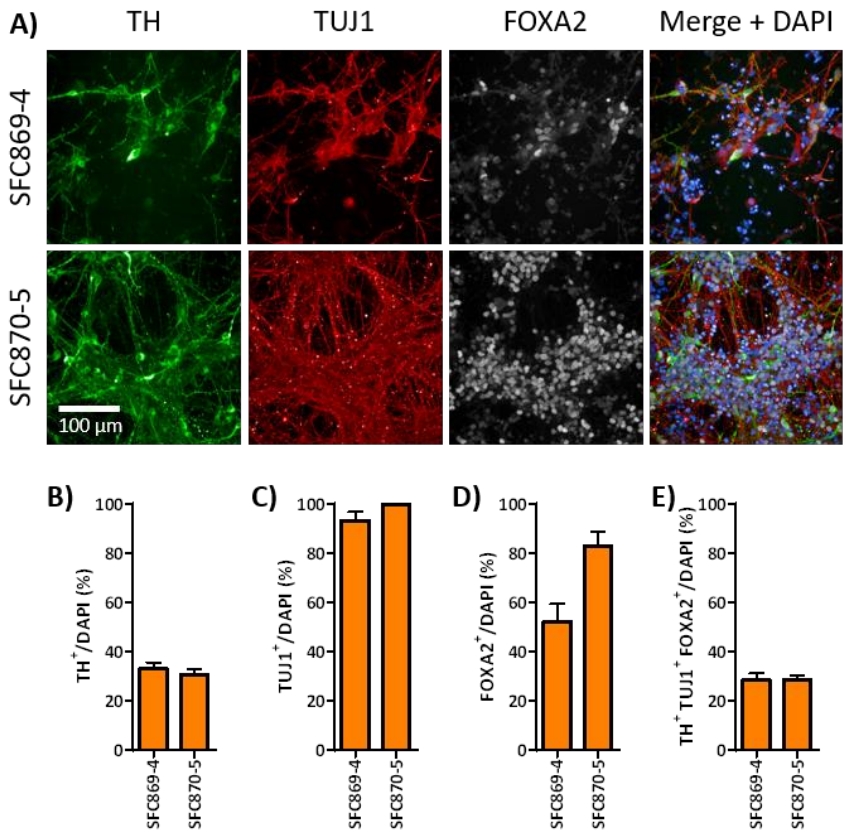

Figure 5.4. Differentiation of LRRK2-R1441C iPSC lines to vmDA neurons.
Two iPSC lines carrying the LRRK2-R1441C mutation were differentiated to vmDA neurons. A) Cells were fixed after 35 DIV and immunostained for TH (green), TUJ1 (red), FOXA2 (white), and costained with DAPI (blue). B-E) Quantification of cells that were positive for B) TH, C) TUJ1, D) FOXA2, and E) TH, TUJ1, and FOXA2, from two independent differentiations. (Graphs show mean ± SD).

5.4.3. Perturbation of the endocytic pathway in LRRK2-mutant iPSC-derived vmDA-neuron cultures

Differentially expressed genes/proteins that contributed to endocytosis were assessed (Table 5.2 and Figure 5.5). *CAV1* (Caveolin I), which was upregulated, and *SH3GL3* (Endophilin III), which was downregulated, were chosen for further validation as they demonstrated a significant change in expression across multiple conditions (protein and/or RNA at 35 and/or 56 DIV), and antibodies were readily available. Western blots were conducted to test antibodies for these two proteins. A pan-Endophilin I-III antibody successfully detected a band of the correct size; however, detection of Caveolin I was not successful (data not shown). Three further genes/proteins—*DNM1*/Dynamin-1, *RAB7A*/RAB7A, and *RAB5B*/RAB5B—were therefore selected for analysis (Table 5.3). These were known to be involved in the endocytic pathway and were differentially expressed in the omics dataset, but did not meet the stringent cut-offs of fold change>1.5 and adjusted $p<0.05$. These were selected as they have previously been shown implicated in LRRK2 cellular function (Higashi et al. 2009; Dodson et al. 2012; Gomez-Suaga et al. 2014; Piccoli et al. 2014; Yun et al. 2015), and could be detected by Western blot in the samples. Additionally, real-time qPCR primers were successfully validated for *SH3GL3* and *RAB7A* gene expression analysis (data not shown).

Table 5.2. Differentially expressed genes/proteins in the endocytosis pathway.
A total of 34 genes/proteins that are involved in endocytosis were differentially expressed, with an integrated fold change(FC)>1.5 and adjusted p-value<0.05. FC and p-values for proteomics (Ptx) and transcriptomics (Rseq) at 35 DIV (D35) and 56 DIV (D56) are shown. NA denotes conditions where the gene/protein was not detected. Those highlighted in blue were selected for further validation.

Gene name	Integrated FC	Integrated adjusted p-value	Ptx D35 FC	Ptx D35 adjusted p-value	Ptx D56 FC	Ptx D56 adjusted p-value	Rseq D35 FC	Rseq D35 adjusted p-value	Rseq D56 FC	Rseq D56 adjusted p-value
CAV3	5.38	6.13E-04	NA	NA	NA	NA	NA	NA	5.38	6.13E-04
FGFR3	4.08	7.03E-05	NA	NA	NA	NA	4.08	7.03E-05	3.29	4.16E-04
CBLC	4.03	4.56E-04	NA	NA	NA	NA	4.03	4.56E-04	2.88	3.70E-03
FLT1	3.44	6.40E-03	NA	NA	NA	NA	3.44	6.40E-03	0.71	5.29E-01
ERBB3	3.34	1.45E-03	NA	NA	NA	NA	3.34	1.45E-03	1.66	2.26E-01
DNM2	2.69	1.62E-02	2.03	1.62E-02	1.73	7.02E-02	1.22	5.74E-02	1.33	2.67E-03
CHMP4C	2.67	5.21E-03	NA	NA	NA	NA	2.67	5.21E-03	3.41	8.40E-05
CAV2	2.54	3.85E-02	NA	NA	NA	NA	2.09	1.10E-01	2.54	3.85E-02
ADRB1	2.24	1.87E-02	NA	NA	NA	NA	2.24	1.87E-02	0.38	2.33E-03
ARAP2	2.19	1.59E-02	NA	NA	NA	NA	2.19	1.59E-02	1.46	2.89E-01
IL2RG	2.18	4.02E-02	NA	NA	NA	NA	2.18	4.02E-02	1.71	1.77E-01
TGFBR2	2.18	2.66E-02	NA	NA	NA	NA	2.18	2.66E-02	1.71	1.40E-01
TFRC	2.09	4.14E-02	1.27	2.57E-01	1.69	4.14E-02	1.62	7.54E-02	3.05	2.39E-06
PSD4	1.94	1.48E-02	NA	NA	NA	NA	1.94	1.48E-02	2.65	4.73E-05
MET	1.86	1.28E-02	1.56	1.28E-02	1.18	2.88E-01	2.22	3.46E-03	2.33	6.38E-04
SNX5	1.81	6.25E-03	1.53	6.25E-03	1.26	4.94E-02	1.78	7.12E-03	1.61	2.16E-02
ARRB1	1.79	1.13E-02	1.52	1.13E-02	1.73	5.84E-03	0.69	5.21E-02	0.80	2.94E-01
LDLRAP1	1.73	1.51E-02	1.48	1.51E-02	1.22	1.49E-01	2.18	5.16E-02	1.87	1.32E-01
HLA-E	1.55	8.72E-03	1.36	8.72E-03	1.00	1.00E+00	2.03	4.65E-02	1.92	6.96E-02
CAV1	1.51	1.78E-02	1.34	1.78E-02	1.37	1.99E-02	2.86	3.45E-02	2.49	6.38E-02
MVB12A	1.50	1.58E-02	1.34	1.58E-02	1.16	1.66E-01	1.20	7.61E-02	1.00	9.92E-01
EPN2	0.67	3.90E-02	0.75	3.90E-02	0.92	4.02E-01	0.87	1.15E-01	0.91	3.54E-01
AGAP3	0.66	1.69E-02	0.74	1.69E-02	0.84	1.39E-01	0.82	8.99E-02	0.83	1.38E-01
IQSEC3	0.65	1.21E-02	0.74	1.21E-02	0.84	1.25E-01	0.65	5.57E-02	0.83	4.88E-01
DNM3	0.63	1.31E-02	0.72	1.31E-02	0.78	5.57E-02	0.60	5.46E-02	0.77	4.01E-01
AMPH	0.63	2.17E-02	0.72	2.17E-02	0.82	1.66E-01	0.77	1.06E-01	0.85	3.95E-01
GRK5	0.60	9.04E-03	0.70	9.04E-03	0.80	6.94E-02	0.84	4.14E-01	1.06	8.32E-01
DNAJC6	0.58	1.39E-02	0.68	1.39E-02	0.86	3.28E-01	0.61	4.30E-02	0.80	4.56E-01
KIF5A	0.57	2.38E-02	0.67	2.38E-02	0.79	1.83E-01	0.67	9.62E-02	0.77	3.64E-01
PSD2	0.55	8.91E-03	0.66	8.91E-03	0.80	1.12E-01	0.62	1.25E-02	0.72	8.45E-02
SH3GL3	0.54	1.16E-02	0.64	1.16E-02	0.71	4.72E-02	0.59	3.29E-02	0.68	1.34E-01
FGFR4	0.51	2.42E-02	NA	NA	NA	NA	0.99	9.78E-01	0.51	2.42E-02
TGFB3	0.49	4.26E-03	1.00	1.00E+00	0.60	4.26E-03	1.96	4.66E-02	2.39	5.72E-03
HLA-B	0.08	4.87E-02	0.69	6.85E-02	0.17	4.87E-02	1.64	1.05E-01	1.38	3.51E-01

Table 5.3. Additional genes/proteins from the endocytic pathway for further analysis.

Gene	Integrated FC	Integrated adjusted p-value	Ptx D35 FC	Ptx D35 adjusted p-value	Ptx D56 FC	Ptx D56 adjusted p-value	Rseq D35 FC	Rseq D35 adjusted p-value	Rseq D56 FC	Rseq D56 adjusted p-value
RAB7A	0.86	6.27E-02	0.90	6.27E-02	0.88	5.38E-02	0.89	3.79E-02	0.85	3.52E-03
RAB5B	0.78	1.63E-02	0.83	1.63E-02	0.87	5.66E-02	0.85	4.38E-02	0.97	7.66E-01
DNM1	0.68	7.86E-03	0.76	7.86E-03	0.82	7.19E-02	0.71	1.58E-01	0.79	4.08E-01

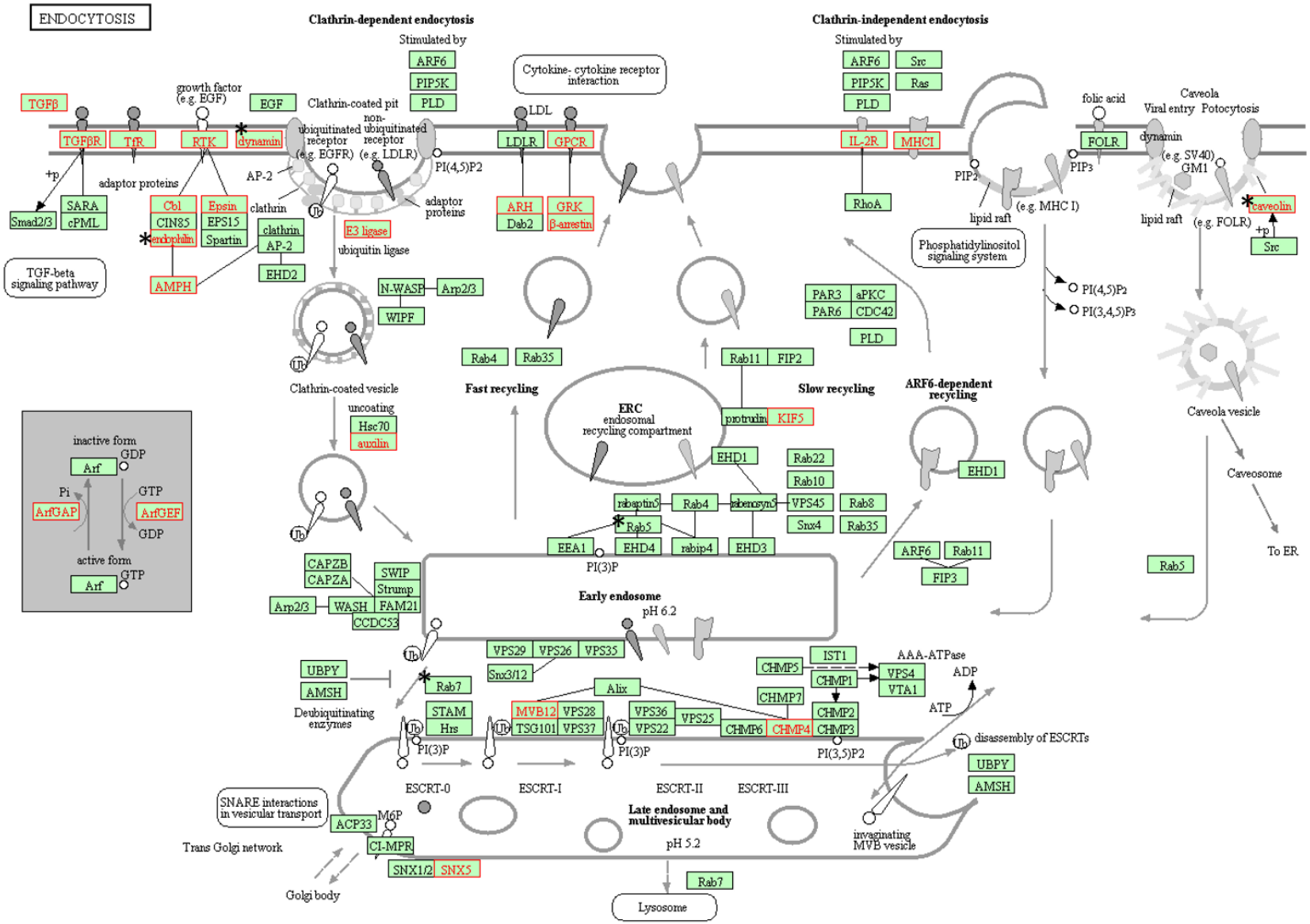

Figure 5.5. Differentially expressed genes/proteins in the endocytosis pathway.

Schematic detailing the genes/proteins involved in the endocytosis pathway. Genes/proteins that were differentially expressed ($p<0.05$, $FC>1.5$) in LRRK2-G2019S expressing vmDA-neuron cultures are highlighted in red. Those chosen for follow up are marked with an asterisk. Schematic created using Kyoto Encyclopaedia of Genes and Genomes (KEGG) pathway database.

Endophilin I-III and Dynamin proteins are involved in clathrin-dependent synaptic vesicle endocytosis, whereas RAB5B localises to the early endosome, and RAB7A localises to the late endosome (Figure 5.4). Endophilin I-III levels were found to be significantly decreased in both the G2019S and R1441C lines at 35 DIV (Figure 5.6A, B), and there was also a trend towards a decrease in gene expression (*SH3GL3*) at this timepoint (Figure 5.6C). At 56 DIV, Endophilin I-III protein levels and *SH3GL3* gene expression were decreased in both the G2019S and R1441C lines, but significance was only reached for the R1441C mutation (Figure 5.6A-C). RAB7A protein levels were decreased in both LRRK2-mutant genotypes at 35 DIV and 56 DIV, reaching significance for the R1441C mutation at both timepoints, and for the G2019S mutation at 56 DIV (Figure 5.6A, B). Gene expression was similarly reduced by the mutations, but only reached significance for the R1441C mutation at 35 DIV (Figure 5.6C). Although present at both timepoints, the decrease in RAB5B and Dynamin-1 protein levels only reached significance at 56 DIV (Figure 5.6A, B), for the R1441C mutation and the G2019S mutation respectively. Of the proteins and genes selected for this validation process, the majority demonstrated a reproducible, statistically-significant change in response to the presence of mutant LRRK2. Furthermore, the direction of change in all cases was consistent with the findings of the proteomics and transcriptomics experiment.

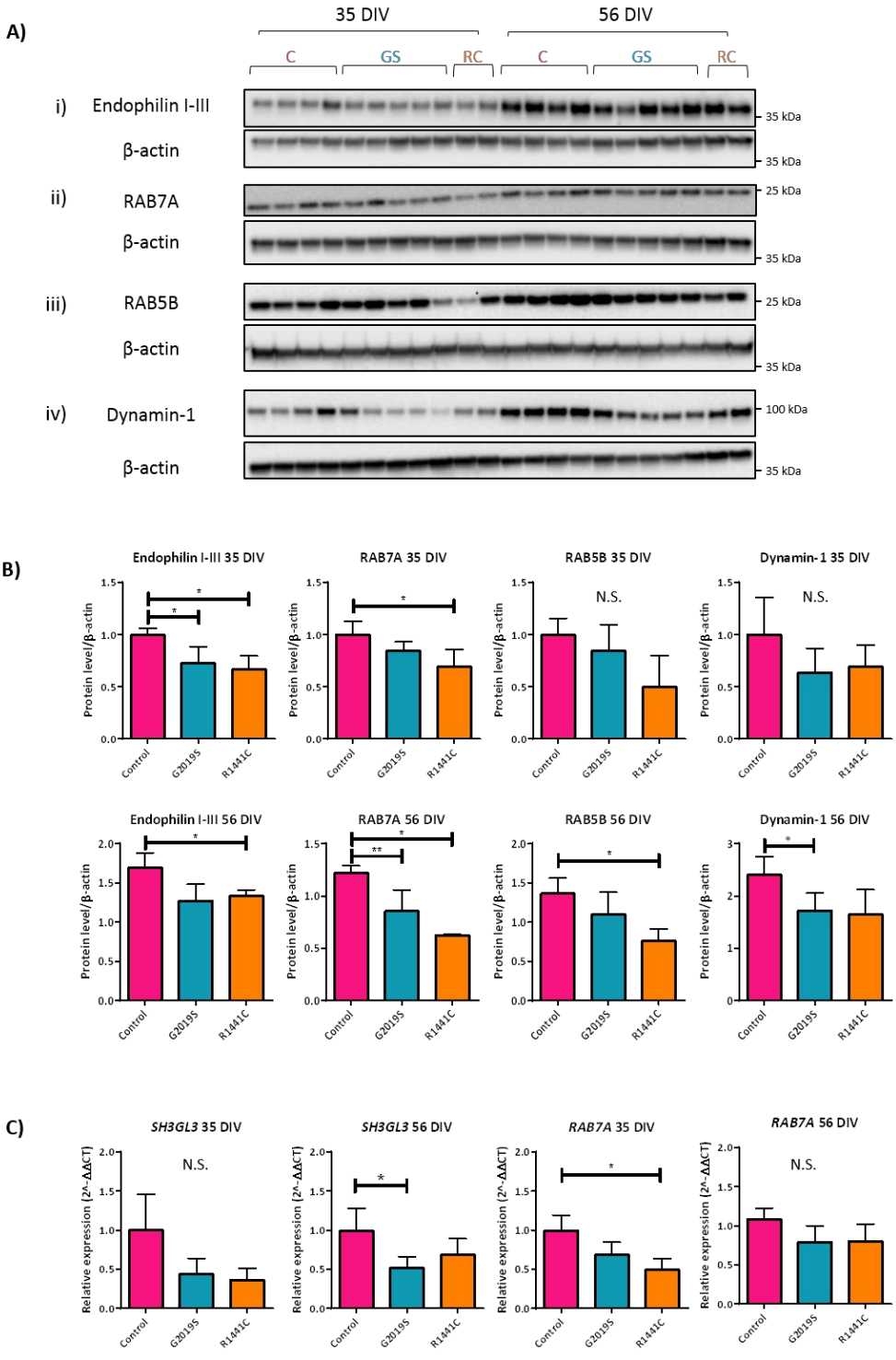

Figure 5.6. Validation of endocytosis gene/protein expression changes.
*A) Example western blots for proteins of interest. B) Quantification of Western blots. C) Real-time qPCR analysis. (Graphs show mean ± SD from four controls and five G2019S lines from three independent differentiations, and two R1441C lines from two independent differentiations. Significance was assessed using a one-way ANOVA *p<0.05, **p<0.01, N.S. = not significant).*

5.4.4. Perturbation of the axon-guidance pathway in LRRK2-mutant iPSC-derived vmDA-neuron cultures

Differentially expressed genes/proteins that were involved in axon guidance were investigated (Table 5.4 and Figure 5.7). KRAS proto-oncogene GTPase (*KRAS*/K-RAS), FYN proto-oncogene (*FYN*/FYN), G Protein Subunit Alpha I1 (*GNAI1*/GNAI1), Neuropilin 1 (*NRP1*/NRP1), and Ephrin type-A receptor 5 (*EPHA5*/EPHA5) were chosen for further validation, as they all demonstrated a significant reduction in expression under multiple conditions (protein and/or RNA at 35 and/or 56 DIV), and antibodies were readily available. Western blots were conducted to test antibodies for these proteins. Suitable antibodies were identified for all proteins aside from K-RAS (data not shown). Furthermore, suitable real-time qPCR primers were successfully validated for *KRAS*, *GNAI1*, *NRP1*, and *EPHA5* (data not shown).

Table 5.4. Differentially expressed genes/proteins in the axon guidance pathway.
A total of 35 genes/proteins that are involved in axon guidance were differentially expressed, with an integrated fold change (FC)>1.5 and adjusted p-value<0.05. FC and p-values for proteomics (Ptx) and transcriptomics (Rseq) at 35 DIV (D35) and 56 DIV (D56) are shown. NA denotes conditions where the gene/protein was not detected. Those highlighted in blue were selected for further validation.

Gene name	Integrated FC	Integrated adjusted p-value	Ptx D35 FC	Ptx D35 adjusted p-value	Ptx D56 FC	Ptx D56 adjusted p-value	Rseq D35 FC	Rseq D35 adjusted p-value	Rseq D56 FC	Rseq D56 adjusted p-value
RHOD	3.17	1.43E-03	NA	NA	NA	NA	1.81	1.39E-01	3.17	1.43E-03
EFNA1	2.23	2.81E-03	NA	NA	NA	NA	2.23	2.81E-03	1.46	1.93E-01
EFNA4	2.15	1.12E-02	NA	NA	NA	NA	2.15	1.12E-02	1.74	7.13E-02
EPHA1	2.08	2.62E-02	NA	NA	NA	NA	2.08	2.62E-02	2.89	2.93E-04
ROBO3	1.95	3.68E-02	NA	NA	NA	NA	1.95	3.68E-02	0.79	5.57E-01
MET	1.86	1.28E-02	1.56	1.28E-02	1.18	2.88E-01	2.22	3.46E-03	2.33	6.38E-04
NTN4	1.85	3.95E-02	NA	NA	NA	NA	1.85	3.95E-02	0.92	8.61E-01
SEMA3A	1.50	1.65E-02	1.34	1.65E-02	1.16	1.70E-01	1.09	5.17E-01	1.37	7.00E-03
KRAS	0.66	9.96E-03	0.75	9.96E-03	0.77	1.88E-02	0.70	3.73E-02	0.82	2.91E-01
PPP3CC	0.66	2.08E-02	0.74	2.08E-02	0.82	1.36E-01	0.75	3.50E-02	0.85	2.73E-01
PPP3CB	0.65	9.33E-03	0.74	9.33E-03	0.84	7.10E-02	0.76	3.57E-02	0.85	2.66E-01
SEMA6D	0.64	2.85E-02	0.73	2.85E-02	0.80	1.49E-01	0.71	1.02E-01	0.77	2.69E-01
FYN	0.64	1.27E-02	0.73	1.27E-02	0.80	4.97E-02	0.83	7.34E-02	0.83	8.10E-02
SLIT1	0.64	2.23E-02	0.73	2.23E-02	0.79	9.39E-02	0.71	9.01E-02	0.69	7.93E-02
EFNA3	0.64	2.85E-02	0.72	2.85E-02	0.79	1.10E-01	0.80	2.94E-01	0.72	1.10E-01
UNC5C	0.64	3.49E-02	0.72	3.49E-02	0.74	7.18E-02	0.72	2.84E-01	0.83	6.41E-01
ABLIM2	0.63	2.11E-02	0.72	2.11E-02	0.85	2.34E-01	0.81	3.63E-01	0.82	4.61E-01
EPHB2	0.61	3.73E-02	0.71	3.73E-02	0.77	1.27E-01	0.93	6.83E-01	0.84	3.43E-01
SEMA4G	0.61	1.10E-02	0.70	1.10E-02	0.86	1.82E-01	0.77	2.02E-01	0.82	4.01E-01
DPYSL2	0.60	1.19E-02	0.70	1.19E-02	0.77	5.02E-02	0.59	1.45E-02	0.74	1.98E-01
EPHA3	0.60	4.62E-02	0.70	4.62E-02	0.83	3.14E-01	0.85	5.98E-01	1.06	8.81E-01
ROBO1	0.59	3.37E-02	0.69	3.37E-02	0.87	4.08E-01	0.81	2.20E-01	1.11	6.38E-01
DPYSL5	0.57	8.91E-03	0.67	8.91E-03	0.76	4.37E-02	0.63	3.55E-02	0.73	1.76E-01
EPHB1	0.57	2.71E-02	0.67	2.71E-02	0.67	3.88E-02	0.64	1.40E-01	0.62	1.19E-01
SEMA4D	0.57	4.19E-02	0.67	4.19E-02	0.85	4.05E-01	0.90	5.99E-01	0.76	1.58E-01
EPHA4	0.55	1.27E-03	0.86	5.49E-02	0.65	1.27E-03	0.83	2.44E-01	0.66	4.77E-03
ABLIM1	0.55	7.18E-03	0.65	7.18E-03	0.85	1.67E-01	0.83	1.25E-01	0.95	7.39E-01
RAC3	0.53	1.35E-02	0.64	1.35E-02	0.80	1.64E-01	0.62	2.19E-02	0.74	1.69E-01
ABLIM3	0.52	1.35E-02	0.63	1.35E-02	0.87	4.59E-01	0.64	5.26E-02	0.76	2.81E-01
ROBO2	0.52	1.27E-02	0.63	1.27E-02	0.71	3.37E-02	0.66	1.70E-01	0.70	2.78E-01
GNAI1	0.50	6.95E-03	0.61	6.95E-03	0.70	2.53E-02	0.61	1.13E-02	0.75	1.79E-01
NTNG1	0.48	9.47E-03	0.59	9.47E-03	0.73	6.54E-02	0.57	1.46E-02	0.64	5.16E-02
L1CAM	0.48	1.78E-02	0.59	1.78E-02	0.75	1.62E-01	0.67	7.30E-02	0.74	2.36E-01
NRP1	0.48	7.38E-03	0.59	7.38E-03	0.77	9.22E-02	0.65	2.69E-03	0.78	1.06E-01
EPHA5	0.43	3.07E-02	0.54	3.07E-02	0.54	4.20E-02	0.44	1.67E-02	0.48	2.78E-02

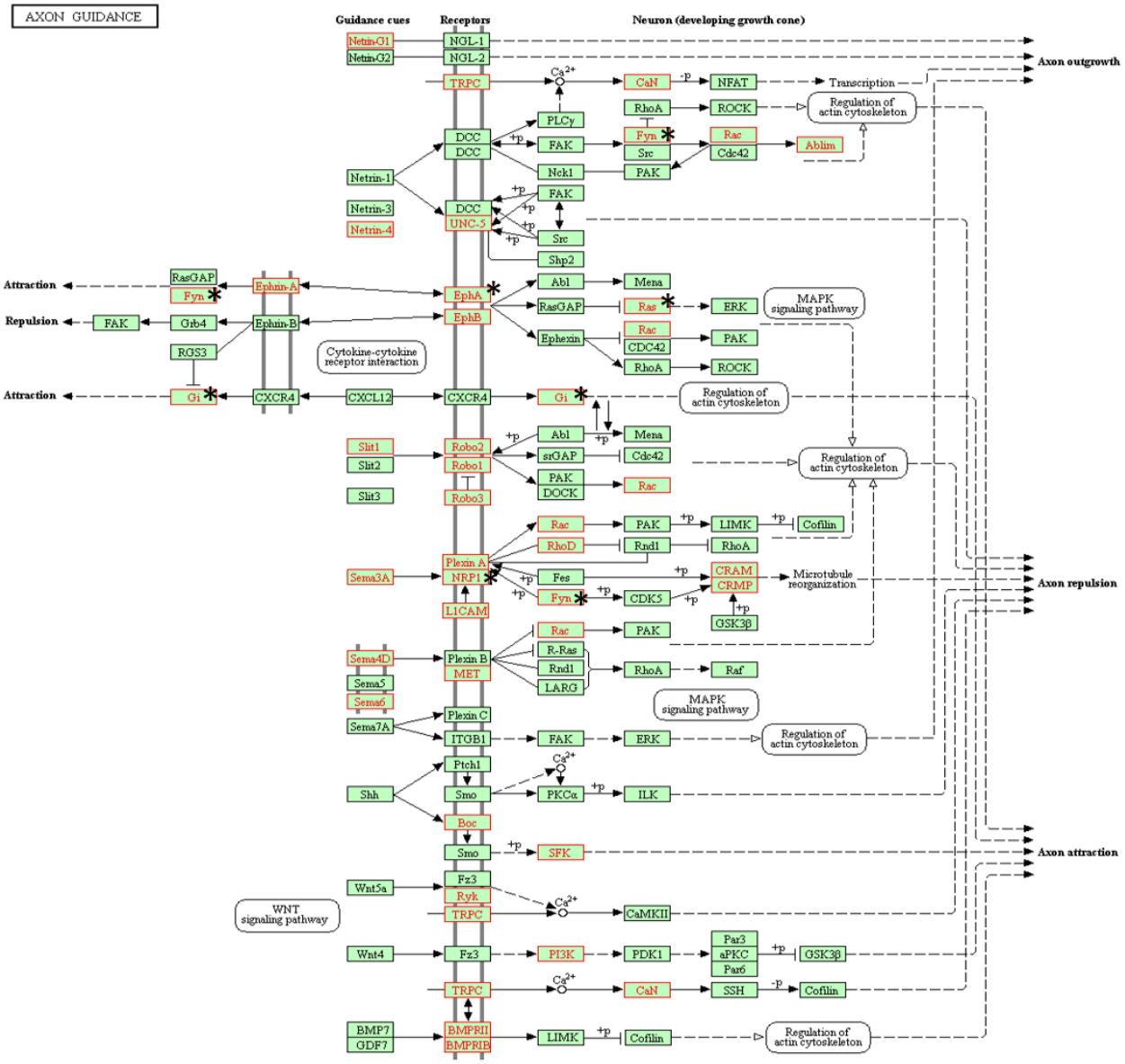

Figure 5.7. Differentially expressed genes/proteins in the axon guidance pathway.
Schematic detailing the genes/proteins involved in the axon guidance pathway. Genes/proteins that were differentially expressed ($p<0.05$, FC>1.5) in LRRK2-G2019S expressing vmDA-neuron cultures are highlighted in red. Those chosen for follow up are marked with an asterisk. Schematic created using the KEGG pathway database.

Of all the proteins assessed, only GNAI1 levels were significantly changed in the presence of LRRK2 mutations, and only at 56 DIV (Figure 5.8A, B). Blotting for all other proteins showed a trend towards a decrease in levels in the G2019S genotype, consistent with the findings of the omics study (Figure 5.8A, B). At the gene expression level, a greater number of statistically significant changes were detected. *NRP1*, *GNAI1*, and *EPHA5* were all significantly downregulated in the presence of the G2019S and the R1441C mutations at 35 DIV (Figure 5.8C). *KRAS* was also downregulated at this timepoint, although only reached significance for the R1441C mutation (Figure 5.8C). At 56 DIV, only downregulation of EPHA5 persisted; whereas, other gene expression changes were no longer detectable (Figure 5.8C).

In Chapter 4 (section 4.3.3), the assessment of neurite growth was assessed using Sholl analysis; however, no effect of the G2019S mutation was seen in this assay. As discussed in Section 4.5, there are several reasons why a difference between genotypes may not have been detected using this assay. As the results of the dual omics analysis clearly demonstrated that the axon guidance pathway is downregulated in these cells, a different approach was taken to functionally assess this pathway. Rather than investigating neurite growth in immature vmDA-neuron progenitors, a neurite regrowth assay was performed. Cells were allowed to mature until 34 DIV, at which point a scratch was applied to the centre of the cultures. Cells were then imaged every 24 hours for seven days, to measure neurite regrowth into the scratch (Figure 5.9). Regrowth was impaired in both the G2019S and R1441C lines in comparison to controls.

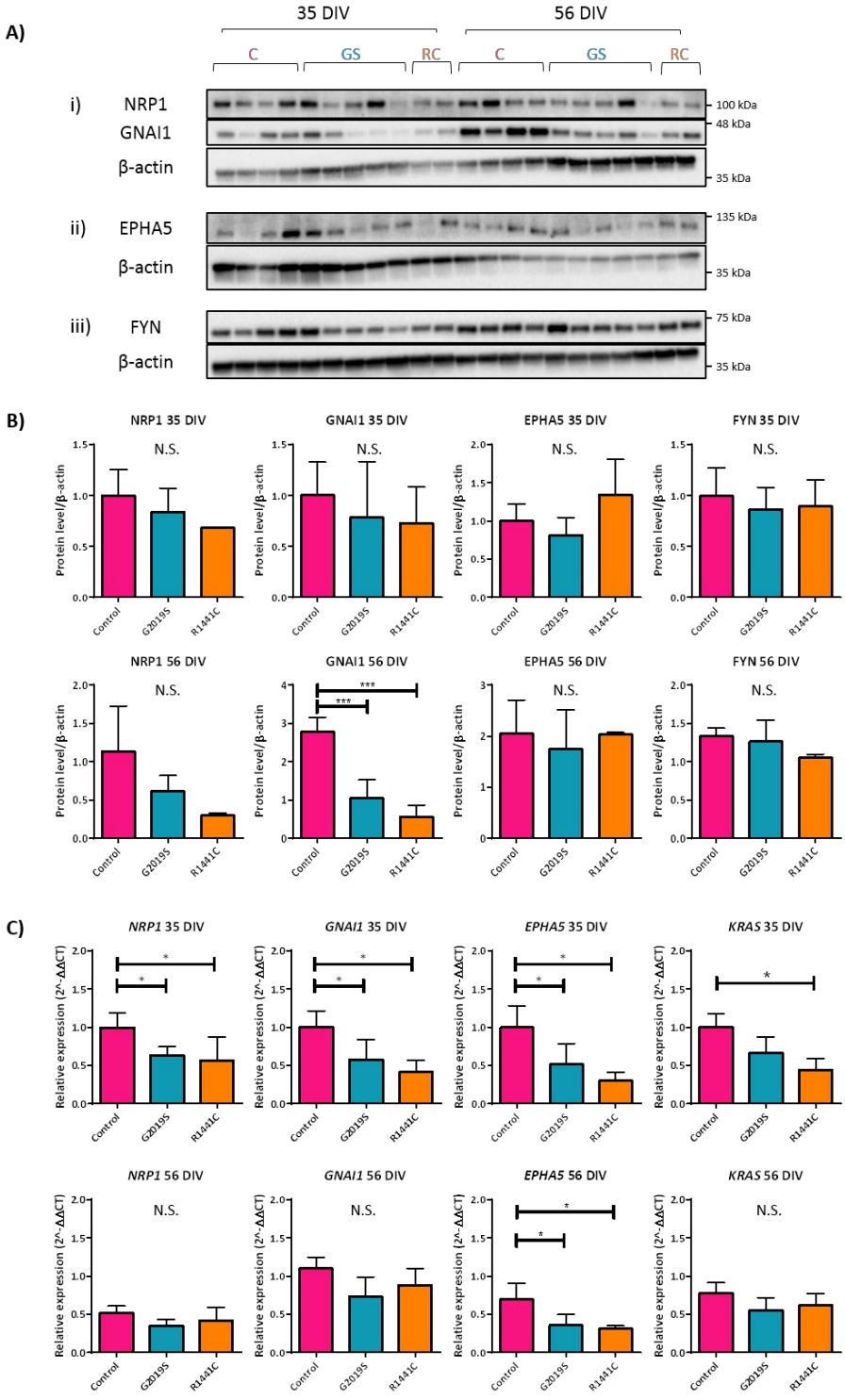

Figure 5.8. Validation of axon guidance gene/protein expression changes.

*A) Example western blots for proteins of interest. B) Quantification of Western blots. C) Real-time qPCR analysis. (Graphs show mean ± SD from four controls and five G2019S lines from three independent differentiations, and two R1441C lines from two independent differentiations. Significance was assessed using a one-way ANOVA *p<0.05, ***p<0.001, N.S. = not significant).*

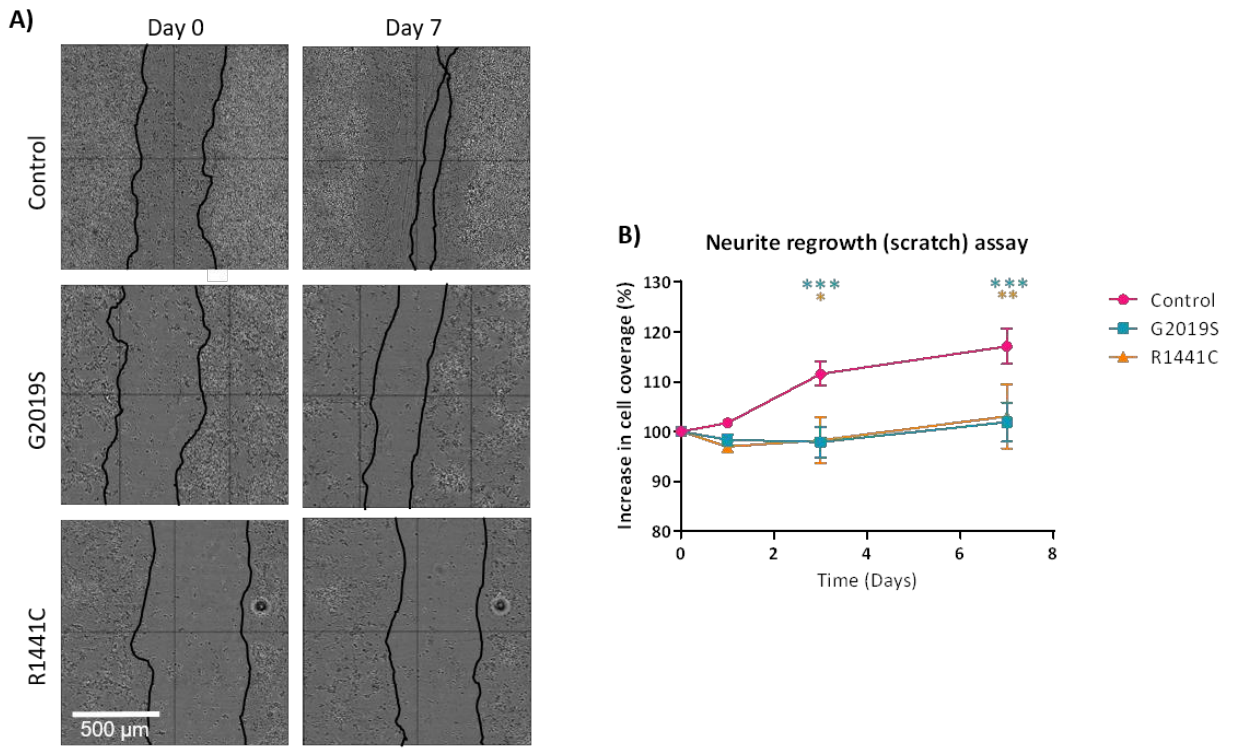

Figure 5.9. Neurite regrowth iPSC-derived vmDA-neuron cultures.
*A scratch was applied to cell cultures and regrowth of neurites was assessed over a period of seven days. A) Example bright-field images of cultures at days 0 and 7 of the assay; black lines denote the edge of the scratch. B) Graph shows quantification of regrowth, which is impaired in the G2019S and R1441C lines. (Graph shows mean ± SD from three controls, four G2019S, and two R1441C lines, from two independent differentiations. Significance was assessed using a two-way ANOVA *p<0.05, **p<0.01, ***p<0.001).*

5.4.5. Dysregulation of LAMP2, but not macroautophagy in LRRK2-mutant iPSC-derived vmDA-neuron cultures

In addition to the pathway-wide changes in endocytosis and axon guidance, a significant increase in levels of the lysosomal marker LAMP2, but not LAMP1, were noted in the dual omics experiment. This was of interest as in Chapter 4, levels of the lysosomal marker LAMP1 were assessed in cells expressing the LRRK2-G2019S mutation, and no changes were detected (Section 4.3.4). The decision was made to further investigate these changes in LAMP2. Western blot analysis was therefore conducted to assess LAMP2 protein levels in control and G2019S vmDA-

neuron cultures across three differentiations, as well as R1441C vmDA-neuron cultures across two differentiations (Figure 5.10). The upregulation of LAMP2 levels was confirmed at 35 DIV (Figure 5.10B, C). There are three splice variants of LAMP2; LAMP2A, LAMP2B and LAMP2C. Biologically, a change in LAMP2 levels in the absence of changed LAMP1 levels could arise from either upregulation or blockage of chaperone-mediated autophagy. LAMP2A is the splice variant that has been implicated in this pathway (Cuervo and Dice 2000), therefore western blotting for LAMP2A was conducted to determine whether its levels were also significantly upregulated in the presence of LRRK2 mutations (Figure 5.10B, C). LAMP2A was increased by both LRRK2 mutations at 35 DIV, but only reached significance for the R1441C lines. To determine whether this upregulation of LAMP2A translated into a change in the number of LAMP2A puncta present in cells, immunostaining was conducted at 35 DIV (Figure 5.10D). A significant upregulation of LAMP2A puncta number was detected in LRRK2 mutant lines when all cells in the culture were considered (Figure 5.10E). When only DA neurons (TH-positive cells) were assessed, a trend towards an increase was also detected; however, this did not reach significance. A small but statistically significant increase in LAMP2A puncta size was also detected across all cells. These results suggest that changes in LAMP2A levels may contribute to the upregulation of LAMP2 seen in this study, but as changes for LAMP2A are not as significant as those for LAMP2, other splice variants may also contribute.

A)

Gene	Integrated FC	Integrated adjusted p-value	Ptx D35 FC	Ptx D35 adjusted p-value	Ptx D56 FC	Ptx D56 adjusted p-value	Rseq D35 FC	Rseq D35 adjusted p-value	Rseq D56 FC	Rseq D56 adjusted p-value
LAMP1	1.41	5.14E-02	1.28	5.14E-02	1.25	9.93E-02	1.22	1.98E-01	1.28	1.16E-01
LAMP2	1.48	2.37E-02	1.32	2.37E-02	1.32	3.18E-02	1.28	9.47E-03	1.19	7.96E-02

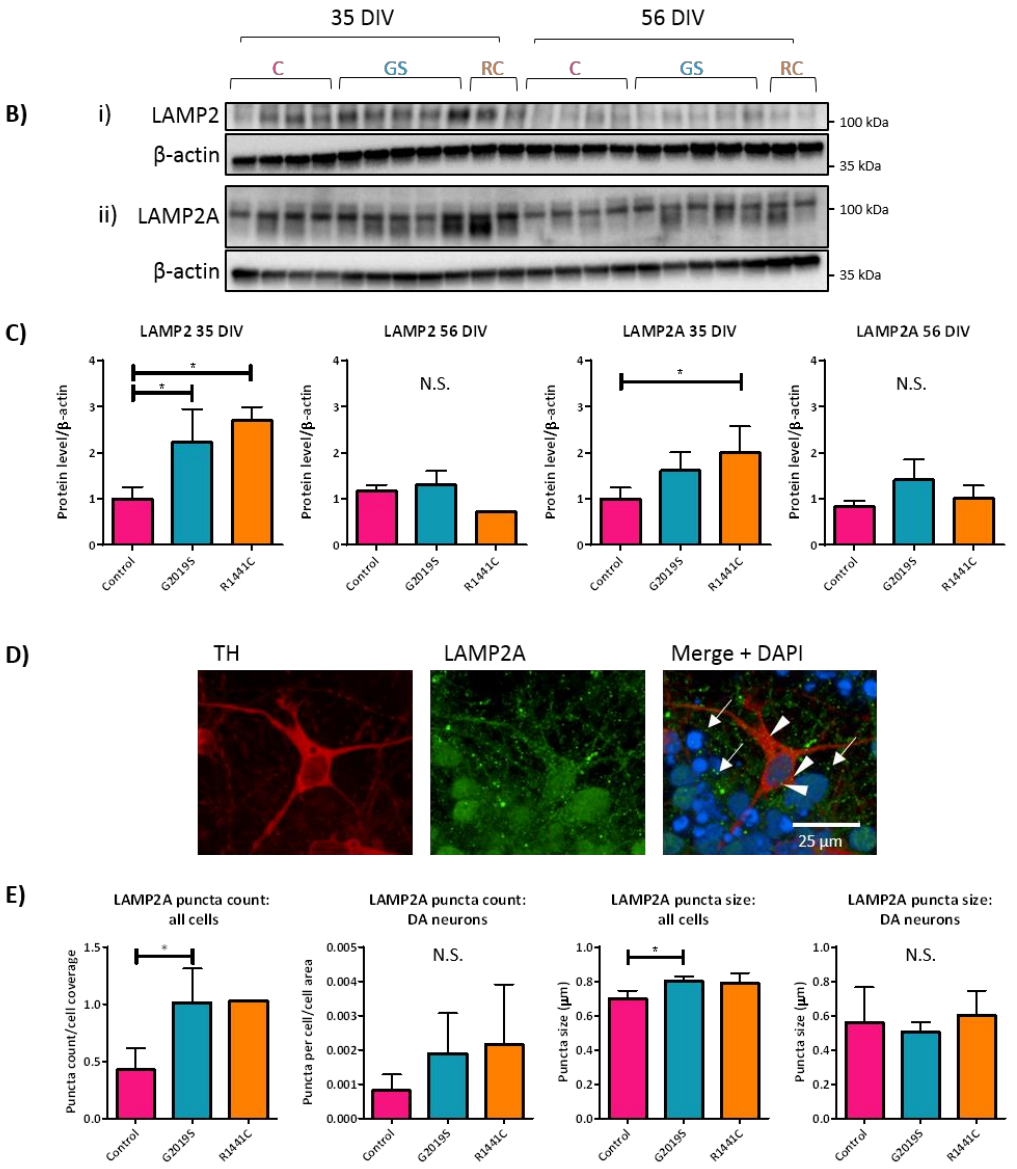

Figure 5.10. LAMP2 and LAMP2a levels in iPSC-derived vmDA-neuron cultures.
*A) Gene expression and protein level changes of LAMP1 and LAMP2 in the omics study. B) Example images of LAMP2 and LAMP2A Western blots. C) Quantification of Western blots (Graphs show mean ± SD from four controls and five G2019S lines from three independent differentiations, and two R1441C lines from two independent differentiations. D) Example images of cultures stained for TH and LAMP2A at 35 DIV. Arrows with tails indicate LAMP2A puncta in non-DA cells, triangles indicate LAMP2A puncta in TH-positive DA neurons. E) Quantification of LAMP2A puncta number and size across the whole culture, or specifically in TH-positive DA neurons (Graphs show mean ± SD from four controls, five G2019S, and two R1441C lines, from one differentiation) (Significance was assessed using a one-way ANOVA *p<0.05, N.S.=not significant.)*

5.4.6. Downregulation of α-Synuclein and Tau in LRRK2-mutant iPSC-derived vmDA-neuron cultures

Levels of proteins that have been shown to play a role in PD pathogenesis were assessed in the dual omics dataset. It was found that α-Synuclein and Tau were both significantly downregulated in the presence of the G2019S mutation at 35 DIV (Figure 5.11A). To determine whether these changes were reproducible, Western blot analysis was conducted in control and G2019S vmDA-neuron cultures across three differentiations, as well as R1441C vmDA-neuron cultures across two differentiations (Figure 5.11B, C). Significant downregulation of both proteins in cultures expressing the G2019S mutation at 35 DIV but not 56 DIV was confirmed. Furthermore, the proteins were also decreased in R1441C cultures at 35 DIV, although only α-Synuclein reached significance. These findings were unexpected, especially for α-Synuclein, as this protein is known to accumulate in PD. If α-Synuclein were accumulating into aggregates, it may not be detected in the LC-MS/MS experiment. To determine whether this was the case, cultures were immunostained for α-Synuclein and the number of α-Synuclein puncta, and cells with an α-Synuclein-positive cytoplasm were assessed (Figure 5.11D, E). No change was detected in either of these parameters. Another possible reason for decrease α-Synuclein and Tau levels could be that the proteins are being secreted into the media. Therefore, a high-sensitivity immunoassay from Meso Scale Discovery (conducted by Dr Siv Vingill and Dr Brent Ryan) was used to detect these proteins in cell culture medium from cultures expressing the G2019S mutation at 36 DIV (Figure 5.11F); however, no changes in secretion were detected.

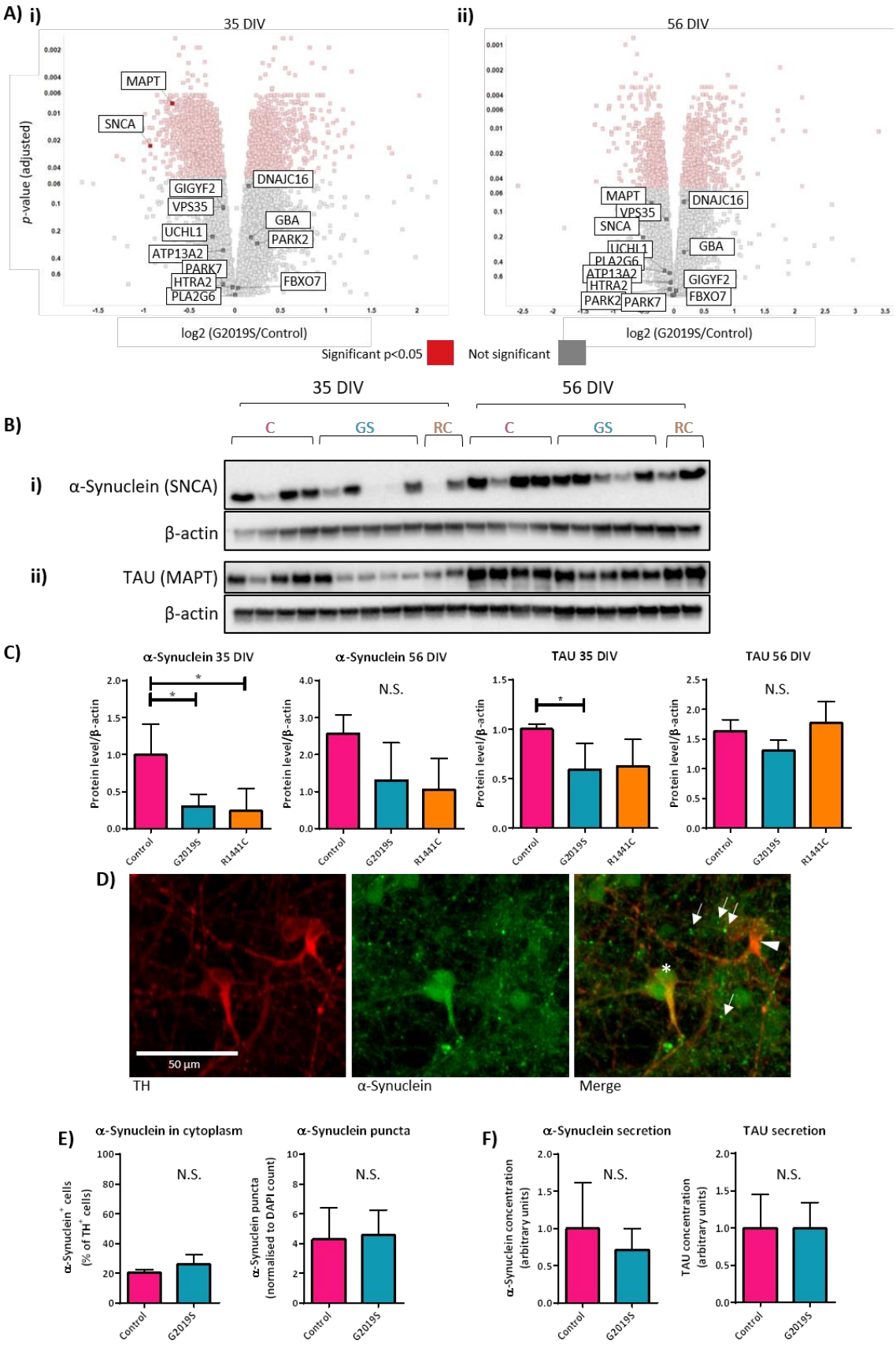
A) i)
35 DIV
MAPT
SNCA
GIGYF2
VPS35
UCHL1
ATP13A2
PARK7
HTRA2
PLA2G6
DNAJC16
GBA
PARK2
FBXO7
p-value (adjusted)
log2 (G2019S/Control)
ii)
56 DIV
MAPT
VPS35
SNCA
UCHL1
PLA2G6
ATP13A2
HTRA2
PARK2
PARK7
DNAJC16
GBA
GIGYF2
FBXO7
log2 (G2019S/Control)
Significant p<0.05
Not significant
B)
35 DIV
56 DIV
C
GS
RC
C
GS
RC
i)
α-Synuclein (SNCA)
β-actin
ii)
TAU (MAPT)
β-actin
C)
α-Synuclein 35 DIV
α-Synuclein 56 DIV
TAU 35 DIV
TAU 56 DIV
Protein level/β-actin
N.S.
Control
G2019S
R1441C
D)
50 µm
TH
α-Synuclein
Merge
E)
α-Synuclein in cytoplasm
α-Synuclein puncta
α-Synuclein+ cells (% of TH+ cells)
α-Synuclein puncta (normalised to DAPI count)
N.S.
Control
G2019S
F)
α-Synuclein secretion
TAU secretion
α-Synuclein concentration (arbitrary units)
TAU concentration (arbitrary units)
N.S.
Control
G2019S

Figure 5.11. (Previous page) α-Synuclein and Tau levels in iPSC-derived vmDA-neuron cultures.
*A) Volcano plots (made by Drs Jeff Martin and Benbo Gao) showing α-Synuclein (SNCA) and Tau (MAPT) protein levels at i) 35 DIV, and ii) 56 DIV in the proteomics study. B) Example images of α-Synuclein and TAU Western blots. C) Quantification of Western blots (Graphs show mean ± SD from four controls and five G2019S lines from three independent differentiations, and two R1441C lines from two independent differentiations. Significance was assessed using a one-way ANOVA. *p<0.05, N.S. = not significant). D) Immunostaining at 35 DIV for TH (red) and α-Synuclein (green); asterisk indicates a TH^+/α-$Synuclein^+$ cell, triangle indicates a TH^+/α-$Synuclein^-$ cell, arrows indicate α-Synuclein puncta. E) Quantification of TH/α-Synuclein colocalization and of α-Synuclein puncta. (Graphs show mean ± SD from four control and five G2019S lines from three independent differentiations, significance was assessed using Student's T-test. N.S. = not significant). F) Secretion of α-Synuclein and Tau from iPSC-derived vmDA-neuron cultures into the cell culture media was quantified (assay run by Drs Siv Vingill and Brent Ryan). (Graph show mean ± SD from three controls and five G2019S lines from one differentiation, significance was assessed using Student's T-test. N.S. = not significant).*

5.5. Results II: Proteomic and transcriptomic analysis of iPSC-derived MP-astrocyte cultures expressing the LRRK2-G2019S mutation

To understand the effects of the LRRK2-G2019S mutation upon the transcriptome and proteome of iPSC-derived MP-astrocyte cultures, cells from the three control and four patient lines described in Chapter 4 (Table 4.2) were used. iPSCs were differentiated to MP astrocytes using the Booth protocol and then harvested 125 DIV for proteomic analysis by LC-MS/MS and transcriptomic analysis by RNA-seq. To enable multiplex analysis by LC-MS/MS, samples were labelled using seven of the TMT-10plex tags.

PCA of LC-MS/MS and RNA-seq data did not demonstrate separation of genotypes in either the proteomics or transcriptomics dataset using PC1 and PC2 (Figure 5.12). Rather, both data sets separated by sex. Furthermore, no proteins were found to be differentially expressed between genotypes, although 2212 genes were differentially expressed (adjusted $p<0.05$, FC>1.5). Further investigation of the transcriptomics data revealed that the two female LRRK2-G2019S lines exhibited unexpectedly low expression of X-inactive specific transcript (XIST) (Figure 5.13). The XIST transcript is usually highly expressed in females, in order to maintain inactivation of one of

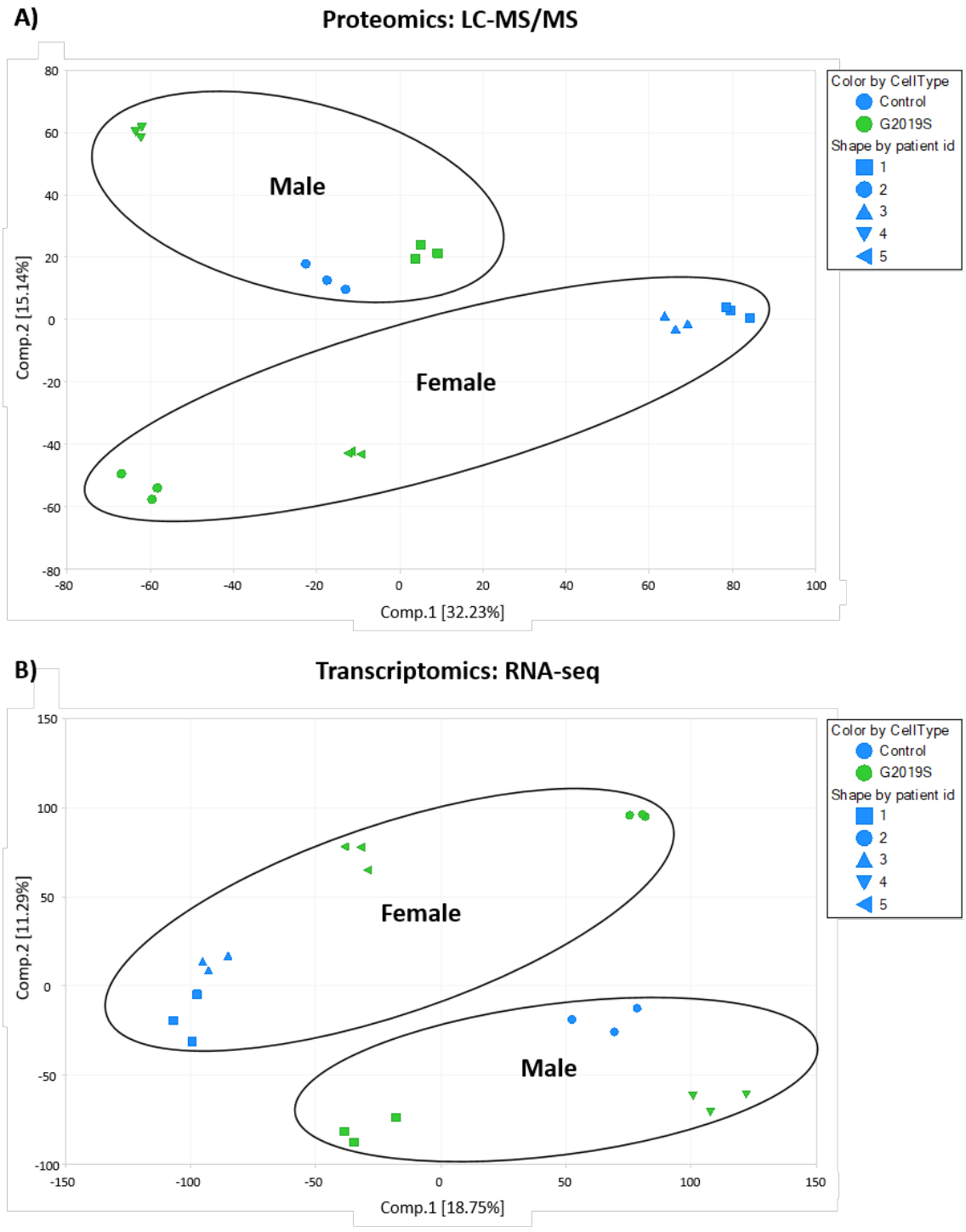

Figure 5.12. Principal component analysis of LRRK2-G2019S expressing, and control iPSC-derived MP-astrocyte cultures.

Principal component analysis of A) Proteomics data, and B) Transcriptomics data, demonstrates separation of samples by sex rather than genotype. PCA plots created by Dr Kejie Li.

the two X-chromosomes (Penny et al. 1996). Low expression is consistent with reactivation of the second X-chromosome. X-chromosome reactivation has been previously described as a stochastic event that can occur during stem cell culture, and has been demonstrated to affect disease phenotypes (Mekhoubad et al. 2012). Because of this, and the fact that no proteins were differentially expressed in these cultures, no further follow-up was conducted for this study. Such a phenomenon was not found in the dual omics study of iPSC-derived vmDA-neuron cultures (Section 5.4).

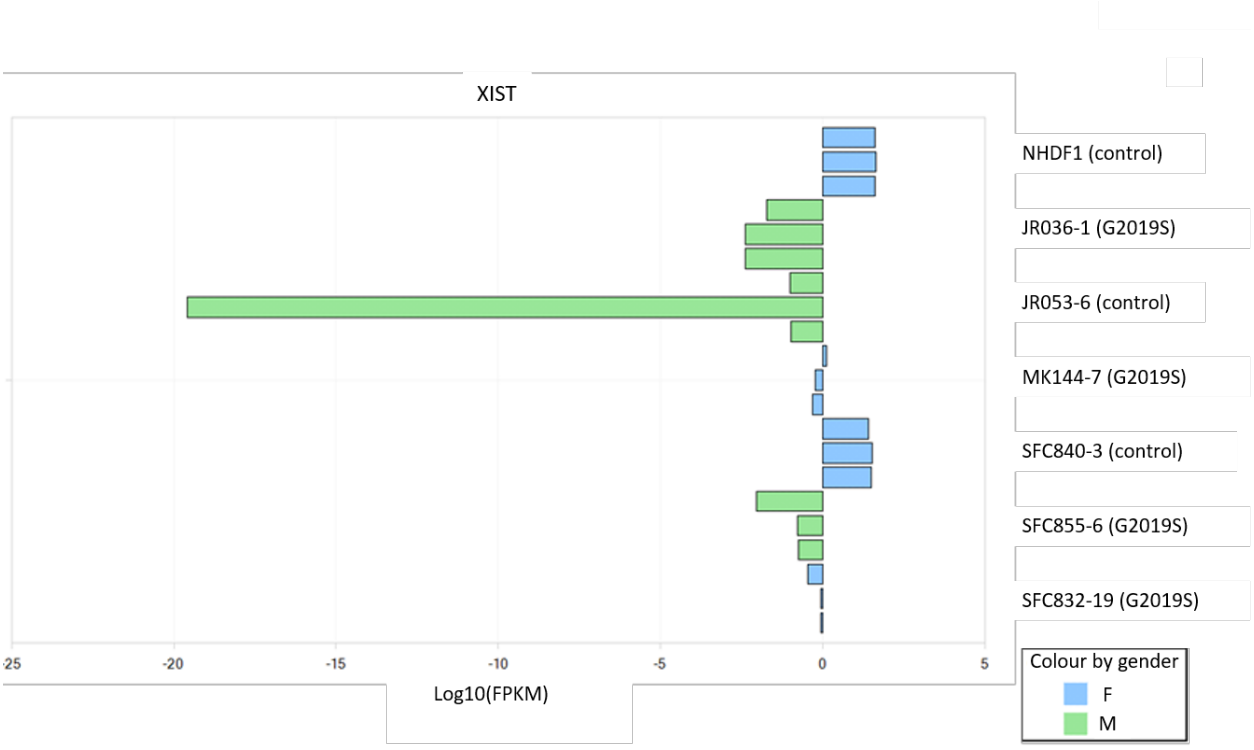

Figure 5.13. XIST expression in iPSC-derived MP-astrocyte cultures.
Graph shows XIST RNA expression in iPSC-derived MP-astrocyte cultures (three samples per line). Samples are categorised by the sex of the donor, female (blue) or male (green). Expression is reduced in the two female LRRK2-G2019S lines. FPKM=Fragments Per Kilobase of transcript per Million mapped reads. Graph created by Dr Kejie Li.

5.6. Results III: Identification of LRRK2 substrates in iPSC-derived vmDA neurons using LRRK2 inhibitors and phosphoproteomic analysis

5.6.1. Identification and optimisation of experimental conditions

Many studies have identified LRRK2 kinase substrates, mostly from in vitro kinase assays, or systems where LRRK2 is overexpressed (Section 1.3.4). Only two studies, conducted in mouse embryonic fibroblasts (MEFs), and human peripheral blood mononuclear cells (PBMCs), have taken an unbiased approach towards identifying LRRK2 kinase substrates in a system where LRRK2 is present at physiological levels (Steger et al. 2016; Thirstrup et al. 2017). No such studies have previously been undertaken in vmDA neurons.

The successful identification of pathways that are disrupted by the LRRK2-G2019S mutation in vmDA-neuron cultures (Section 5.4), demonstrated the utility of these cultures as relevant model for PD. Therefore, an experiment was designed, combining iPSC-derived vmDA-neuron cultures with different LRRK2 genotypes, and LRRK2 inhibitors, to identify *bone fide* LRRK2 kinase substrates.

Suitable iPSC lines were identified for use in the experiment (Table 5.5). A LRRK2-KO line had recently been developed and validated by our collaborator, Dr. Sally Cowley, at the Sir William Dunn School of Pathology (University of Oxford). This line (SFC840-3 C11), and its parental control line (SFC840-3) were selected for the experiment. No LRRK2-G2019S isogenic line was available to match to this control and KO pair; therefore, efforts were made to choose the most closely matched G2019S line possible. The KO and its parental control were derived from a 67-year-old female donor, using the Cytotune reprogramming kit; therefore, a LRRK2-G2019S line (SFC832-

19) that was derived from a 77-year-old female, using the same reprogramming method, was selected.

Table 5.5. iPSC lines for phosphoproteomics experiment.

#	Cell line	Age/Sex	LRRK2 Genotype	Reprogramming method
1	SFC840-3	67/F	WT	Cytotune (Sendai virus)
2	SFC840-3 C11	67/F	KO	Cytotune (Sendai virus)
3	SFC832-19	77/F	G2019S	Cytotune (Sendai virus)

Phosphorylation of LRRK2 at its S935 residue is mediated by LRRK2 kinase activity (Dzamko et al. 2010); therefore, this phosphorylation site was assayed using Western blotting with a pS935-LRRK2-specific antibody for identification of suitable LRRK2 inhibitor concentrations. As previously demonstrated (section 3.5), LRRK2 protein levels are low in the vmDA-neuron cultures. It was therefore not possible to detect phosphorylation of this residue in these cells (data not shown). A surrogate model was therefore adopted for this optimisation step. Primary mixed neuronal cultures, derived from non-transgenic rat cortices at postnatal day one, were provided by Rebecca Wallings (University of Oxford) after 14 days of maturation. Two LRRK2 inhibitors, PF06447475 (referred to as PF475 from here onwards), developed by Pfizer Ltd (Henderson et al. 2015), and mLi-2, developed by Merck & Co. (Fell et al. 2015) (Figure 5.14A), were selected for use in this experiment. The IC50s of PF475 and mLi-2 are in the range of 8-15 nM (Henderson et al. 2015) and 0.8-3.4 nM (Fell et al. 2015) respectively, depending on the assay used. These values were taken into consideration and two concentrations, one just above the IC50 and one 5X higher, were selected for each compound (20 and 100nM for PF475, and 5 and 25 nM for mLi-2). Cells were treated with each concentration of the inhibitors for 30, 60, or 90 min, before harvesting. Short incubation times were selected to allow for detection of a reduction

in phosphorylation of LRRK2 kinase substrates, but to limit the number of downstream phosphorylation events that would be detected by the study. Western blot analysis of LRRK2-S935 phosphorylation was then conducted on the lysates (Figure 5.14B, C). All inhibitor treatments resulted in decreased levels of LRRK2-S935 phosphorylation. For PF475, phosphorylation was lowest after 90 min of treatment at the 100 nM concentration, which was selected for the phosphoproteomics experiment. Phosphorylation levels were similarly decreased by all concentrations and durations of mLi-2 treatment; therefore, an incubation time of 90 minutes and a concentration of 25 nM was chosen, to align with the treatment duration and concentration (relative to IC50) chosen for PF475.

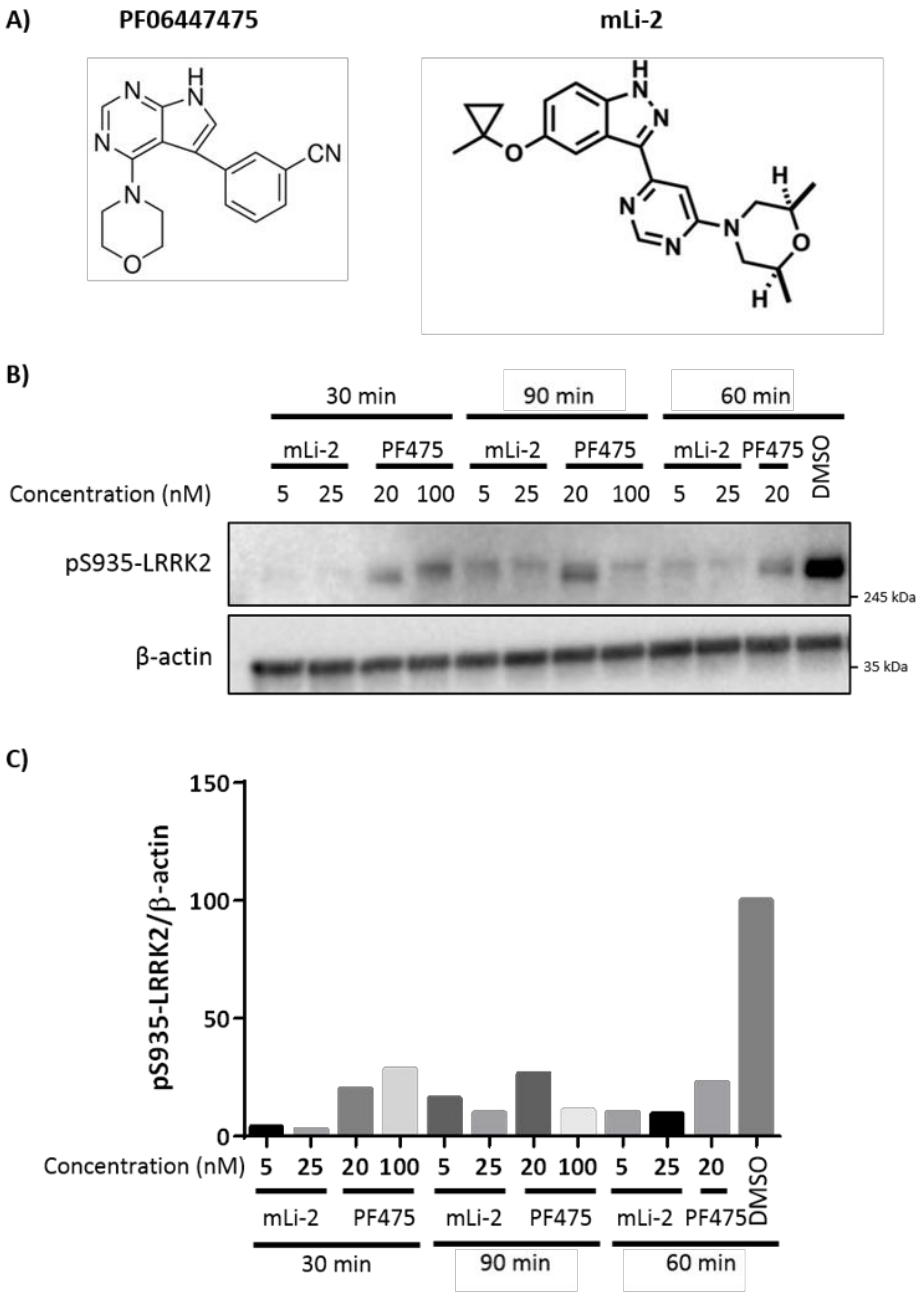

Figure 5.14. Selection of optimal LRRK2 inhibitor concentrations.
LRRK2 inhibitors were tested on primary cortical neuronal cultures from non-transgenic rats. A) Chemical structures of LRRK2 inhibitors PF06447475 (PF475) and mLi-2. B) Western blot analysis of pS935-LRRK2 and β-actin loading control. C) Quantification of blots.

5.6.2. Identification of candidate LRRK2 kinase substrates

Once iPSC lines and compound concentrations had been selected, iPSCs were differentiated to vmDA-neurons and matured until 35 DIV (Figure 5.15), at which point they were treated with PF475 (100 nM), mLi-2 (25 nM), or DMSO control for 90 min (Figure 5.16A). Cells were harvested in quadruplicate for analysis of phosphosites by LC-MS/MS. A total of 38,923 phosphosites were detected across the four replicates, including 13,470 sites that were replicated across at least three of the replicates (Figure 5.16B). These 13,470 sites were used for analysis. Sites that were differentially phosphorylated between genotypes were identified, then filtered to identify candidate LRRK2 kinase substrates (Figure 5.16C). Off-target effects of each inhibitor were excluded from the analysis by only considering sites where phosphorylation was modulated by both inhibitors in the same direction, in both the LRRK2-G2019S line and in the control line. Any sites that were also modulated in the same direction in the LRRK2-KO line were then removed from the analysis. Although this method excluded sites that were phosphorylated exclusively by LRRK2-WT or LRRK2-G2019S, it was chosen for analysis of the data as it provided the highest stringency for identification of LRRK2 kinase substrates.

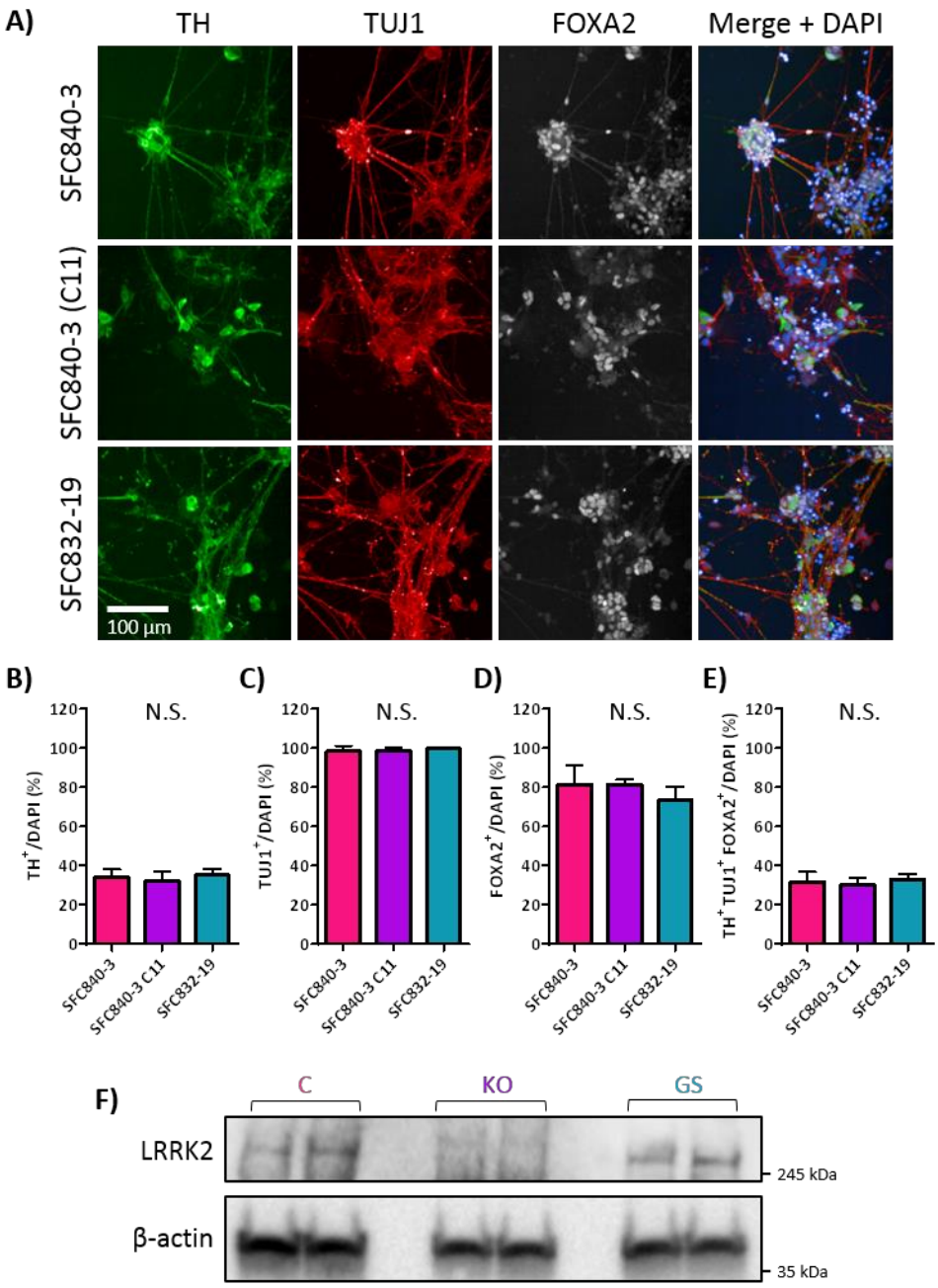

Figure 5.15. Differentiation of iPSC-lines for phosphoproteomics analysis.
iPSC lines (one control: SFC840-3, one LRRK2-KO: SFC840-3 C11, one LRRK2-G2019S: SFC832-19) were differentiated to vmDA neurons. A) Cells were fixed after 35 DIV and immunostained for TH (green), TUJ1 (red), FOXA2 (white), and costained with DAPI (blue). B-E) Quantification of cells that were positive for B) TH, C) TUJ1, D) FOXA2, and E) TH, TUJ1, and FOXA2, from one differentiation. F) Western blot analysis demonstrating that LRRK2 is not expressed in the KO line. (Graphs show mean ± SD from three images per line. Significance was assessed using a one-way ANOVA, N.S. = not significant).

A)

Genotype	Treatment	Sample
Control	Vehicle	1a
		1b
		1c
		1d
	mLi2 25nM	2a
		2b
		2c
		2d
	PF-475 100nM	3a
		3b
		3c
		3d
LRRK2 KO	Vehicle	4a
		4b
		4c
		4d
	mLi2 25nM	5a
		5b
		5c
		5d
	PF-475 100nM	6a
		6b
		6c
		6d
LRRK2 G2019S	Vehicle	7a
		7b
		7c
		7d
	mLi2 25nM	8a
		8b
		8c
		8d
	PF-475 100nM	9a
		9b
		9c
		9d

B)

Parameter	Total
Treatment conditions	9
TMT sets	4
Total identified phosphosites	38,923
Overlap in at least 3 TMT Sets	13,470
Overlap in at least 2 TMT Sets	19,196
Identified TMT phosphosites, Set 1	15,657
Identified TMT phosphosites, Set 2	21,545
Identified TMT phosphosites, Set 3	22,536
Identified TMT phosphosites, Set 4	22,248

C)

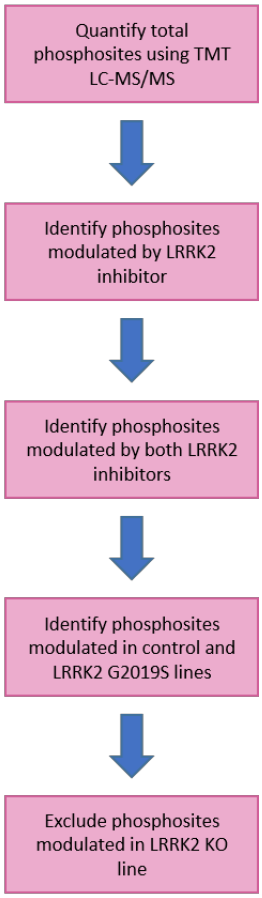

Figure 5.16. Phosphoproteomics experimental design, workflow, and results.
A) Experimental design for phosphoproteomics. B) Experimental parameters and phosphosite identification results. C) Data analysis workflow.

Phosphorylation of eleven peptides was significantly downregulated in both the control and G2019S line, but not the KO line (*p*-value cut-off $p<0.001$) (Table 5.6). These peptides are candidates for classification as true LRRK2 kinase substrates, as they are modulated by both inhibitors, in two LRRK2 genotypes, and are not modulated in cells lacking LRRK2. The peptides were mapped to eleven distinct proteins (Table 5.6), six of which (ABL-interactor 2 (ABI-2),

Collapsin-Response Mediator Protein 1 (CRMP1), Coiled-Coil Domain Containing 120 (CCDC120), P21-Activated Kinase 3 (PAK3); Liprin-α3 (PPFIA3), and Hyperpolarization Activated Cyclic Nucleotide Gated Potassium Channel 3 (HCN3)) have been previously implicated in various aspects of neuronal function. ABI2 is a member of the Wiskott-Aldrich syndrome protein family member 2 (WAVE2) complex and localises to neurite growth cones and synaptosomes (Courtney et al. 2000; Xie et al. 2013). CRMP1 is necessary for neurite extension, and its phosphorylation by Cyclin-Dependent Kinase 5 (CDK5) promotes dendritic spine development (Yamashita et al. 2007; Quach et al. 2004). CCDC120 has been shown to be necessary for neurite outgrowth and for microtubule anchoring on centrosomes, and is transported along microtubules in vesicles (Torii et al. 2014; Huang et al. 2017). PAK3 also regulates dendritic spine length (Boda et al. 2008), and has been shown to regulate recycling of the Alpha-Amino-3-Hydroxy-5-Methyl-4-Isoxazole Propionate Receptor (AMPAR), via phosphorylation of the AMPAR subunit Glutamate Receptor 1 (GLUR1) (Hussain et al. 2015). PPFIA3 belongs to the Liprin-α protein family; members of this family have been shown to negatively regulate dendritic spine and synapse development, to localise to synapses and growth cones, and to target AMPARs to the synapse (Spangler and Hoogenraad 2007; Wyszynski et al. 2002). HCN3 is a channel that produces hyperpolarisation-activated (I_h) currents (Mistrik et al. 2005), which play a key role in autonomous pacemaking in dopaminergic neurons in the SNc (Chan et al. 2007; Guzman et al. 2009).

The five other proteins that exhibited decreased phosphorylation have been implicated in a variety of pathways. Clathrin Interactor 1 (CLINT1—also known as EpsinR) has been shown to interact with Clathrin and its adaptor, Adaptor Protein 1 (AP1), in the region of the trans-golgi network (TGN), suggesting that it may play a role in vesicle trafficking from the TGN to the

endosome (Kalthoff et al. 2002). LIM domain and actin-binding protein 1 (LIMA1—also known as EPLIN) is an actin-binding protein (Maul et al. 2003), and Pleckstrin Homology Domain Containing A5 (PLEKHA5), has been shown to interact with phosphoinositide lipids on the internal side of the cell membrane (Yamada et al. 2012). Serine/Arginine Repetitive Matrix 2 (SRRM2) is an RNA-splice factor, which has been previously identified as a potential blood biomarker for PD (Shehadeh et al. 2010), and Family with Sequence Similarity 107 B (FAM107B) has been characterised as a tumour suppressor (Nakajima et al. 2010).

Table 5.6. Proteins with reduced phosphorylation in the presence of LRRK2 inhibitors.
Table lists proteins and the position of phosphosites that were modulated by LRRK2 inhibitors, along with the probability of phosphorylation at each site, the peptide where the site was identified, and how many sites were phosphorylated on the identified peptide. In the peptide column, probable phosphorylation sites are highlighted in bold and underlined.

Protein	Phosphosite position (probability)	Peptide	Number of phosphorylated sites
ABI2	S37(1)	GTLGRH**S**PYR	1
CCDC120	S302(1)	**S**VPATPVLTR	1
CLINT1	S441(1)	**S**QPLQNVSTVLQK	1
CRMP1	S54(1)	TIDFDAY**S**VGRR	1
FAM107B	T135(1)	PSIID**T**PK	1
HCN3	S591(0.984)/T592(0.016)	GRAP**ST**GAQLSGK	1
LIMA1	S698(1)	QQ**S**PQEPK	1
PAK3	S138(0.994)/T140(0.002)/S141(0.004)	YM**S**F**TS**GDK	1
PLEKHA5	S913(1)/T926(1)	**S**PTPESSTIASYV**T**LRK	2
PPFIA3	S1155(1)	SAAAGALG**S**PGLPLRK	1
SRRM2	T2420(0.184)/S2421(0.816)/ S2426(0.001)	M**TS**ERAP**S**PSSR	1

Table 5.7. Proteins with increased phosphorylation in the presence of LRRK2 inhibitors.
Table lists proteins and the position of phosphosites that were modulated by LRRK2 inhibitors, along with the probability of phosphorylation at each site, the peptide where the site was identified, and how many sites were phosphorylated on the identified peptide. In the peptide column, probable phosphorylation sites are highlighted in bold and underlined.

Protein	Phosphosite position (probability)	Peptide	Number of phosphorylated sites
ADD1	S464(0.636)/S465 (0.364)	GDEASEEGQNG**SS**PK	1
ARMC10	S45(1)	**S**AGALEEGTSEGQLCGR	1
C9orf78	S15(1)/S17(0.121)/S24(0.879)	RRGD**S**E**S**EEDEQD**S**EEVR	1
DCK	T72(0.024)/S74(0.976)	WCNVQSTQDEFEEL**T**M**S**QK	1
HACD3	S114(1)	WLDE**S**DAEMELR	1
HMGA2	S105(1)	KPAQEETEETSSQE**S**AEED	1
MARCKSL1	S135(1)	EGGGDSSASSPTEEEQEQGEIGAC**S**DEGTAQEGK	1
NUCKS1	S119(1)/S234(1)/S240(1)	**S**GDEG**S**EDEAP**S**GED	3
PRMT6	T21(1)	LESGGGGEGGEG**T**EEEDGAEREAALERPR	1
SRCIN1	S654(0.01)/S655(0.01)/T658(0.979)/S661(0.002)	**SS**GA**T**PV**S**GPPPPSASSTPAGQPTAVSR	1
THRAP3	S928(1)	WAHDKF**S**GEEGEIEDDESGTENREEK	1

Phosphorylation of a total of eleven peptides was upregulated in the presence of both LRRK2 inhibitors, in both the control and LRRK2-G2019S cultures, but not in the LRRK2-KO cultures (*p*-value cut-off $p<0.001$) (Table 5.7). These peptides mapped to eleven distinct proteins, four of which (Alpha-adducin (ADD1), MARCKS-Related Protein (MARCKSL1), SRC Kinase Signaling Inhibitor 1 (SRCIN1—also known as P140Cap), and Armadillo repeat-containing protein 10 (ARMC10)) have previously been demonstrated to play a role in neuronal function. ADD1 binds to actin and regulates axon diameter (Leite et al. 2016). MARCKSL1 is expressed in the brain and has been shown to bundle and stabilise F-Actin when phosphorylated, resulting in inhibition of cellular migration (Bjorkblom et al. 2012). SRCIN1 has been shown to localise to dendritic spines and synapses, and to regulate their morphologies (Jaworski et al. 2009). ARMC10 regulates

mitochondrial trafficking in neurons (Serrat et al. 2014; Lopez-Domenech et al. 2012). Of the other identified phosphoproteins, Very-long-chain (3R)-3-hydroxyacyl-CoA dehydratase 3 (HACD3—also known as PTPLAD1), has been implicated in fatty-acid synthesis (Ikeda et al. 2008), and the remainder were all annotated as being involved in transcriptional regulation. The detection of upregulated phosphorylation of these proteins in response to the inhibitors suggests that phosphorylation events downstream of LRRK2 inhibition are also captured in our analysis.

5.7. Discussion and conclusions

In this chapter, an unbiased approach was taken to investigate the effects of the pathogenic LRRK2-G2019S mutation on cellular functions in iPSC-derived vmDA neurons and MP astrocytes, and to investigate PD-relevant LRRK2 kinase substrates in iPSC-derived vmDA-neurons. LC-MS/MS for proteomic analysis, and RNA-seq for transcriptomic analysis were combined to provide a robust analysis of the total proteome and transcriptome of these cells. In iPSC-derived vmDA neurons, widespread proteomic and transcriptomic dysregulation was detected as a result of the LRRK2-G2019S mutation. However, in iPSC-derived MP-astrocytes, no significant changes to the proteome were detected, and both transcriptome and proteome data were found to cluster by the sex of the cells rather than by their genotype (Section 5.5). Further investigation found that the second X-chromosome of the two female LRRK2-G2019S lines had been reactivated. X-chromosome reactivation has been previously demonstrated by others to be a stochastic event that can occur during long-term passaging of iPSCs (Mekhoubad et al. 2012). In our study, X-reactivation is thought to have occurred during MP astrocyte differentiation, as no reactivation was detected in the vmDA-neuron omics dataset (Section 5.4), which was produced using cells derived from the same vials of iPSCs. The MP-astrocyte differentiation protocol involves regular passaging of highly proliferative progenitor cells, whereas the vmDA-neuron differentiation protocol does not. As X-chromosome reactivation has been previously shown to occur during passaging of iPSCs (Mekhoubad et al. 2012), it is likely that this event occurred during the passaging phase of MP-astrocyte differentiation. Numerous genes are regulated by the X-chromosome, and it has previously been shown that X-chromosome reactivation can significantly affect disease phenotypes in differentiated cultures (Mekhoubad et al. 2012). For

this reason, no further analysis was conducted on the MP-astrocyte dataset. Collection of experimental replicates for the hypothesis-driven analysis of these cells (Section 4.4), was also halted at this point, as all cells were differentiated from the same bank of MP progenitors, which had been frozen at 90 DIV.

The data from the iPSC-derived vmDA-neuron cultures suggested that the LRRK2-G2019S mutation had a significant effect on these cells (Section 5.4). EGSEA pathway enrichment analysis identified 92 pathways that were significantly dysregulated (p<0.05) (Appendix (ii)), suggesting that LRRK2 may act upstream of multiple cellular functions. The two most significantly perturbed pathways were identified as endocytosis and axon guidance, which were both predicted to be impaired in our model.

Phosphoproteomics analysis of iPSC-derived vmDA-neuron cultures identified potential LRRK2 kinase substrates that participate in these pathways, providing mechanistic insight into their impairment by LRRK2 mutations (Section 5.6). Phosphorylation of eleven proteins was found to be significantly inhibited in the presence of LRRK2 inhibitors in both control and LRRK2-G2019S iPSC-derived vmDA-neuron cultures, but not in LRRK2 KO cells (Figure 5.17). These proteins point to a role for LRRK2 in direct regulation of neurite growth, synapse formation and function, and vesicle trafficking (Figure 5.17). Phosphorylation of a further eleven proteins was found to be significantly upregulated as a result of LRRK2 inhibition. Of these, four have been previously demonstrated to play a role in cytoskeletal dynamics, neurite growth, synaptic morphology, and organelle trafficking. The majority of the remainder have been implicated in transcriptional regulation. The identification of proteins that exhibited increased phosphorylation in the

presence of LRRK2 inhibitors suggests that phosphorylation events downstream of LRRK2 inhibition have been captured by our phosphoproteomics analysis. This raises the possibility that some of the potential LRRK2 kinase substrates may not in fact be direct substrates, but may be downstream responders to LRRK2 inhibition. Further experiments will therefore be necessary to determine which of the eleven identified proteins that exhibited a decrease in phosphorylation in response to LRRK2 inhibitors are true LRRK2 kinase substrates, and which are downstream of these.

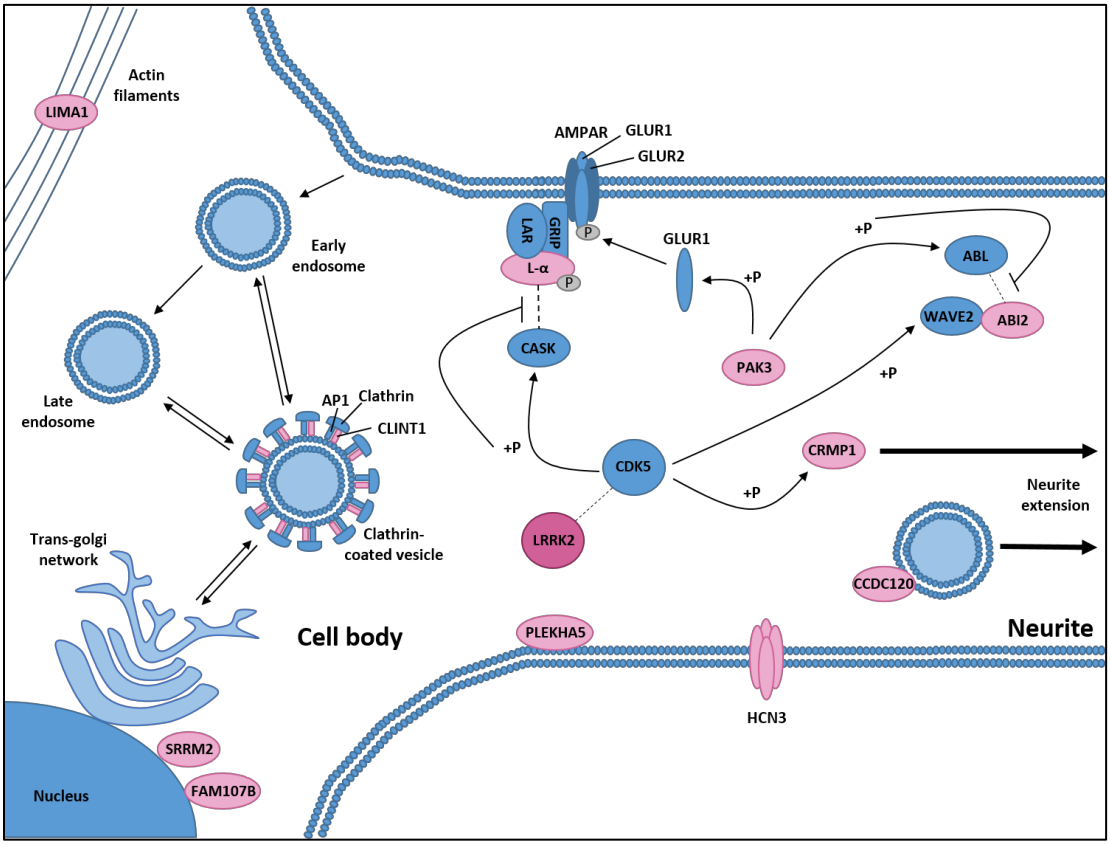

Figure 5.17. Candidate LRRK2 kinase substrates and their interactions.

Eleven potential LRRK2 kinase substrates (in light pink) were identified by phosphoproteomic analysis of iPSC-derived vmDA-neuron cultures in the presence of LRRK2 inhibitors. A number of these proteins (or their family members) participate in the same pathways. Phosphorylation by proteins other than LRRK2 is indicated with solid black arrows. Protein interactions are indicated by proximity of proteins, or by dashed lines. Inhibition of interactions is indicated by blunt-ended solid arrows. Phosphorylation-dependent complexes are denoted by the addition of (P) to the appropriate complex member. Abbreviations: Lα3: Liprin-α3.

LRRK2 participates in the endocytic pathway and vesicle trafficking

The results described in this chapter strongly implicate LRRK2 in the endocytic/endosomal pathway and vesicle trafficking. Thirty-four proteins/genes that contribute to endocytosis according to the *Kyoto Encyclopaedia of Genes and Genome*s (KEGG) pathway database were differentially expressed in the dual-omics study of iPSC-derived vmDA-neuron cultures (Section 5.4.3). These were distributed across most aspects of the pathway, although many of the changes were concentrated around clathrin-dependent endocytosis. Levels of four proteins that contribute to the pathway were assessed to provide confirmation of the omics study results. Endophilin I-III, and Dynamin-1, which are both involved in clathrin-dependent synaptic vesicle endocytosis were confirmed to be downregulated in both G2019S and R1441C cultures in comparison to controls. RAB5B and RAB7A, which participate downstream of endocytosis, at the early and late endosome respectively, were also downregulated by LRRK2 mutations. LRRK2 has previously been implicated in the endocytosis-endosomal pathway, and has been shown to interact with, and to phosphorylate Endophilin proteins (Matta et al. 2012; Arranz et al. 2015), to interact with Dynamin-1 (Piccoli et al. 2014), to colocalise with RAB7 in the late endosome, and to regulate RAB5 and RAB7 levels (Gomez-Suaga et al. 2014; Dodson et al. 2012; Higashi et al. 2009). Furthermore, SRCIN1, which was identified downstream of LRRK2 inhibition in our phosphoproteomics study, has previously been shown to interact with Endophilin I, to modulate dendritic spine and synapse morphology (Yang et al. 2015).

Two potential LRRK2 kinase substrates identified in our study (Section 5.6.2), CLINT1 and PLEKHA5, have both been implicated in phosphoinositide binding (Hirst et al. 2004; Yamada et

al. 2012), suggesting that they may play a role in cellular signalling or membrane trafficking (Figure 5.17). Furthermore, CLINT1 has been implicated in vesicle trafficking; it localises to the TGN, and interacts with Clathrin and its adaptor AP1 (Hirst et al. 2004; Kalthoff et al. 2002). CLINT1 has been suggested to mediate formation of clathrin-coated vesicles between the TGN and the endosomal system (Kalthoff et al. 2002), and has been demonstrated to be an adaptor for the endosomal SNARE protein VTI1B (Chidambaram et al. 2004; Hirst et al. 2004). In the dual omics study (Section 5.4), the AP1 subunit APBP1, was upregulated 1.5-fold, and VTI1B was downregulated 1.2-fold, suggesting that this pathway may be perturbed by LRRK2 mutations. Another potential LRRK2 kinase substrate identified in our study, CCDC120, has also been implicated in vesicle trafficking. Little is known about CCDC120; however, it has been found in vesicles that participate in neurite growth (Torii et al. 2014) (Figure 5.17). Together, the findings of the dual-omics study and the phosphoproteomics analysis of iPSC-derived vmDA-neuron cultures confirm for the first time that LRRK2 regulates the endocytic pathway, when it is expressed at physiological levels in a human context, and in a PD-relevant cell type.

LRRK2 plays a role in synaptic function

Synaptic function is closely linked to the endocytic pathway, as synaptic vesicles are taken up by endocytosis and recycled through the endosome. The findings of our phosphoproteomics study (Section 5.6.2) provide evidence to support synaptic phenotypes that have been found in other LRRK2-mutant models. Liprin-α3 (PPFIA3), was identified as a potential LRRK2 kinase substrate in our phosphoproteomics study; CDK5 phosphorylation of Peripheral Plasma Membrane Protein CASK (CASK), a presynaptic scaffolding protein, has been shown to regulate synapse formation by inhibiting its interaction with Liprin-α family members at the synapse (Samuels et al. 2007)

(Figure 5.17). Furthermore, LRRK2 has recently been identified as a potential CDK5 interactor, providing further evidence for its role in this pathway (Shanley et al. 2015; Shu et al. 2016).

Members of the Liprin-α family, and PAK3, another potential LRRK2 kinase substrate identified in our study, have been demonstrated to play a role in localisation of the excitatory synaptic receptor, AMPAR, to the synapse, and in regulating its recycling (Figure 5.17). PAK3 phosphorylates the GLUR1 AMPAR subunit, promoting its assembly into the cell membrane (Hussain et al. 2015). Liprin-α also forms a complex with LAR Transmembrane Tyrosine Phosphatase (LAR-RPTP), Glutamate Receptor-Interacting Protein (GRIP), and the AMPAR subunit GLUR2, stabilising AMPARs at the synapse (Wyszynski et al. 2002). The interaction between Liprin-α and LAR-RPTP in this complex is modulated by Liprin-α phosphorylation (Serra-Pages et al. 2005). AMPARs are important for excitatory synaptic activity, which has been previously been shown to be elevated in LRRK2-mutant expressing rodent neurons (Piccoli et al. 2011, Plowey, et al. 2014; Beccano-Kelly et al. 2014; Maas et al. 2017). Our finding that LRRK2 may directly phosphorylate Liprin-α3 and PAK3, suggests that LRRK2 kinase activity may be important for regulation of AMPARs. AMPAR recycling is mediated through endocytosis and endocytic recycling (Henley et al. 2013), and provides a further link to the changes seen in the endocytosis pathway in our model.

HCN3, which is involved in electrophysiological neuronal activity, is another potential LRRK2 kinase substrate that was identified in our study (Figure 5.17). The HCN family of proteins are responsible for the production of synaptic I_h currents, which are necessary for autonomic pacemaking—a key characteristic of dopaminergic neurons in the SNc (Mistrik et al. 2005; Chan

et al. 2007; Guzman et al. 2009). Phosphorylation of HCN channels has been shown to affect their activity (Jung et al. 2010), suggesting that LRRK2 may play a direct role in dopaminergic pacemaking. It has previously been demonstrated that the frequency of dopaminergic neuron action potential firing is altered in LRRK2-R1441C BAC-transgenic rats (Sloan et al. 2016), resulting in fewer high-frequency bursts of firing. HCN3 has also been found to be upregulated in the basal ganglia in the rat 6-OHDA model of PD (Meurers et al. 2009), supporting the hypothesis that it plays a role in disease pathogenesis. Furthermore, inhibition of the I_h current has differential effects in SNc and VTA vmDA neurons, and leads to preferential degeneration of SNc neurons (Masi et al. 2015; Carbone et al. 2017). The phosphorylation of HCN3, either directly by, or downstream of LRRK2, may therefore be key to understanding the role of LRRK2 mutations in PD pathogenesis.

LRRK2 regulates neurite growth

Neurite growth deficits have been previously found in many studies of LRRK2 mutations (Section 1.3.4.i). The results of this chapter confirm these findings, and provide novel insight into the mechanisms of LRRK2-mediated neurite growth. Thirty-five proteins/genes that contribute to axon guidance/neurite growth according to the KEGG pathway database were differentially expressed in our dual-omics study of iPSC-derived vmDA-neuron cultures (Section 5.4.4). These were distributed across different regions of the pathway, with a mild concentration of changes around Semaphorin 3A (SEMA3A)-mediated axon guidance signalling. Expression levels of NRP1, which is a key node in SEMA3A signalling; FYN, which contributes to SEMA3A and Ephrin signalling; EPHA5, which contributes to Ephrin and MAPK signalling; K-RAS, which contributes to Mitogen-Activated Protein Kinase (MAPK) signalling; and GNAI1, which contributes to C-X-C

chemokine receptor type 4 (CXCR4) signalling, were assessed with the aim of confirming the results of the dual omics study. Downregulation of GNAI1 protein levels was confirmed at 56 DIV in both G2019S and R1441C cultures, and a strong trend towards downregulation of NRP1 protein levels was also detected at this timepoint. No changes in EPHA5 and FYN protein levels were detected. At the gene expression level, significant downregulation of *NRP1*, *GNAI1*, *EPHA5*, and *KRAS* was confirmed in the LRRK2 mutant genotypes. Furthermore, functional confirmation of a reduction axon guidance was achieved using a neurite regrowth assay, which revealed a deficit in LRRK2-G2019S and -R1441C iPSC-derived vmDA-neuron cultures, confirming the neurite growth deficits seen by others, albeit using a different assay (Section 1.3.4.i).

The identification of ABI2, CRMP1, CCDC120, PAK3, and Liprin-α3 (PPFIA3) as potential LRRK2 kinase substrates (Section 5.6.2) provides mechanistic insight into this phenotype (Figure 5.17). PAK3 is a member of the p21-activated kinase (PAK) family, which also includes PAK6. LRRK2 has been previously found by others to regulate neurite growth through its interaction with PAK6, although the same study also found that LRRK2 did not interact with PAK3 on a protoarray (Civiero et al. 2015). The discrepancy between the Civiero study and the results presented here suggests that interaction of LRRK2 with PAK3, and the subsequent phosphorylation of PAK3 may require the presence of other proteins or cellular membranes. Interestingly, another PAK family member, PAK2, has been previously demonstrated to phosphorylate Abelson murine leukaemia viral oncogene homolog 1 (ABL1) (Jung et al. 2008), disrupting its interaction with ABI2, which we have also identified here as a potential LRRK2 kinase substrate. ABI2 is a component of the WAVE2 complex, which localises to neurite growth cones (Courtney et al. 2000; Xie et al. 2013). In this complex, ABI2 interacts with WAVE2, which is phosphorylated by CDK5 (Xie et al. 2013).

CDK5 has also been shown to regulate neurite growth via phosphorylation of CRMP1 (Yamashita et al. 2007), another of our potential LRRK2 kinase substrates.

Previous studies have demonstrated that LRRK2 phosphorylates other cytoskeletal proteins including ERM proteins (Jaleel et al. 2007; Parisiadou et al. 2009), Tubulins, (Gandhi et al. 2008, Law et al. 2014), Tau (Kawakami et al. 2012), VIM, and SCFD1 (Daschel et al. 2007) using in-vitro assays or LRRK2-overexpression systems. So far, we have found no evidence that LRRK2 phosphorylates any of these proteins, apart from Tau, in our iPSC-derived vmDA-neuron cultures. In our phosphoproteomics study we found that phosphorylation of Tau was downregulated in the presence of both LRRK2 inhibitors, in the control and LRRK2-G2019S cells, but not LRRK2-KO cells; however, this finding did not meet our significance cut-off of $p<0.001$. Tau phosphorylation regulates its binding to microtubules (Lindwall and Cole 1984; Bramblett et al. 1993; Biernat et al. 1993), which is important for neurite growth and trafficking of cellular components (Caceres and Kosik 1990; Stamer et al. 2002; Magnani et al. 2007). One previous study has demonstrated that LRRK2 directly phosphorylates tubulin-associated Tau (Kawakami et al. 2012); however, other studies suggest that LRRK2 regulates Tau phosphorylation by other kinases, such as GSK3β or CDK5 (Lin et al. 2010; Ohta et al. 2015; Shanley et al. 2015). If further work were to confirm that Tau phosphorylation status is modified either directly or indirectly by LRRK2 in iPSC-derived vmDA-neurons, this would support the findings of these previous studies, and provide further insight into the mechanism by which LRRK2 regulates neurite growth.

LRRK2 mutations may disrupt chaperone-mediated autophagy

The lysosomal protein LAMP2 was significantly upregulated in the dual omics study (Section 5.4.5). This was unexpected, due to data presented in Chapter 4 (Section 4.3.4) indicating that the lysosomal protein LAMP1 did not change in iPSC-derived vmDA neurons expressing the LRRK2-G2019S mutation. However, the changes in LAMP2 expression were confirmed by Western blotting at 35 DIV in G2019S and R1441C cultures. Analysis of the LAMP2 isoform LAMP2A, which is involved in chaperone-mediated autophagy, showed that this was also increased in these cultures, reaching statistical significance in the R1441C cultures. A significant increase in the number of LAMP2A puncta, and their size, was also detected across all cells in the cultures. When these parameters were assessed solely in vmDA neurons, there was a non-significant trend towards increased puncta number per cell. Due to culture availability, only a limited number of vmDA-neurons were assessed for LAMP2A puncta, and further replication may be necessary to add statistical strength to this finding. Overall, these findings suggest that LRRK2 mutations may result in perturbation of chaperone-mediated autophagy across the cell types present iPSC-derived vmDA-neuron cultures, and that this contributes in part to the changes in total LAMP2 levels. It is possible however, that other LAMP2 splice variants also contribute to the measured change, as total LAMP2 appears to be upregulated to a greater extent than LAMP2A alone. These findings are consistent with a previous study that demonstrated that the LRRK2-G2019S mutation caused a blockage in chaperone-mediated autophagy across a variety of models, and showed an increase in LAMP2A, but not LAMP1, puncta in post-mortem LRRK2-G2019S PD patient brains (Orenstein et al. 2013).

LRRK2 intersects with other PD risk genes

Expression levels of PD-risk genes were assessed in the dual omics study of iPSC-derived vmDA-neuron cultures. α-Synuclein and Tau were both significantly downregulated at 35 DIV in this study (Section 5.4.6). This was unexpected, especially in the case of α-Synuclein, which has previously been shown to be upregulated in iPSC-derived cultures expressing LRRK2 mutations (Section 1.3.4.vi). No evidence of increased α-Synuclein accumulation or secretion was found, suggesting that the decreased levels were simply due to lower α-Synuclein expression. It has been shown that α-Synuclein and Tau levels increase throughout development (Zhong et al. 2010; Kosik et al. 1989), and that Tau levels increase with maturity of iPSC-derived vmDA-neuron cultures (Beevers et al. 2017). The decreased expression of α-Synuclein and Tau in LRRK2-G2019S cultures at 35 DIV but not at 56 DIV may therefore suggest that the LRRK2-G2019S mutation results in a delay in iPSC-derived vmDA-neuron maturity. As discussed earlier, Tau is involved in microtubule binding; therefore, the decrease in Tau levels at this timepoint may also contribute to the deficits in neurite growth in the LRRK2-mutant lines.

In addition to these findings, the results of our phosphoproteomics study identified the transcriptional regulator Nuclear Casein Kinase and Cyclin Dependent Kinase Substrate 1 (NUCKS1) as being phosphorylated downstream of LRRK2 inhibition (Section 5.6.2). A single nucleotide polymorphism in the intergenic region between NUCKS1 and RAB7L1 has previously been identified as a risk variant for PD (Nalls et al. 2014). Our results suggest that this variant may act on the same pathway as LRRK2 mutations.

LRRK2 kinase activity is responsible for widespread transcriptional regulation

Eight of the proteins that exhibited upregulation of phosphorylation downstream of LRRK2 inhibition are transcriptional regulators (Section 5.6.2), suggesting that modulation of LRRK2 kinase activity has a broad effect on transcription within the cell. This is in agreement with the findings from the dual omics experiment (Section 5.4) comparing iPSC-derived vmDA neurons from LRRK2-G2019S lines and controls, where ~18% of detected proteins and ~14% of detected transcripts were dysregulated in the G2019S cells.

LRRK2 kinase substrates differ depending on cellular context

Two previous phosphoproteomics studies have utilised LRRK2 kinase inhibitors in order to identify *bone fide* LRRK2 substrates. One study was conducted in MEFs and confirmed in whole mouse brain samples (Steger et al. 2016), and the second was conducted in human PBMCs (Thirstrup et al. 2017). Both studies identified RAB10 and RAB12 as LRRK2 kinase substrates, and Steger et al. also identified RAB8. However, none of these phosphoproteins were identified as LRRK2 kinase substrates in our study, although the proteins themselves were detected. Similar to our study, the publication by Steger et al. identified LRRK2 kinase substrates that were phosphorylated by both LRRK2-WT and LRRK2-G2019S proteins (Steger et al. 2016). Conversely, the study by Thirstrup et al. only identified substrates phosphorylated by LRRK2-WT protein (Thirstrup et al. 2017). Neither of these studies included a LRRK2-KO line to account for off-target effects of the inhibitors; however, Steger et al. used a drug-resistant mutant of LRRK2 as a control to exclude off-target effects of the LRRK2 inhibitor, whilst retaining the presence of LRRK2 in the cell.

Phosphorylation of RAB8, RAB10, and RAB12 was not regulated by LRRK2 inhibitors in any of the genotypes that we included in our analysis. The difference between our results and those of these previous studies may therefore be due to differential substrate phosphorylation in different cellular contexts. The majority of the LRRK2 substrates identified in our study exhibit neuron-specific functions; it may be the case that when these proteins are present, LRRK2 preferentially phosphorylates them over RAB proteins. As vmDA neurons preferentially degenerate in PD, it is likely that the interaction of LRRK2 with neuronal proteins plays a key role in disease pathogenesis, and that it is these neuron specific-substrates that hold the key to understanding and treating PD.

Chapter 6: General discussion

6.1. Discussion

vmDA neurons in the SNc preferentially degenerate in PD (Kordower et al. 2013). Genetic mutations account for ~30% of familial and 3-5% of sporadic cases (Kumar et al. 2011), the most common of which are found in LRRK2 (Saiki et al. 2012). LRRK2 is expressed in neurons and astrocytes, as well as other cell types in the human brain (Zhang et al. 2016), and may therefore contribute to vmDA-neuron degeneration through cell-autonomous, or non-cell autonomous mechanisms. This thesis set out to optimise and validate protocols for the differentiation of vmDA neurons and MP astrocytes from human iPSCs, with the goal of investigating the effects of the PD related LRRK2-G2019S mutation in these cell types.

In Chapter 3, a previously published protocol for the differentiation of vmDA neurons from human embryonic stem cells (Kriks et al. 2011) was optimised for use with iPSCs, while a protocol for differentiation of cortical astrocytes from iPSCs (Rinaldi, unpublished) was modified for the differentiation of MP astrocytes. The optimised protocols provided a yield of vmDA neurons (30%) that was higher than has been used in previous studies of LRRK2 mutations, and a high yield of MP astrocytes (48%). Additionally, both differentiated cell types were demonstrated to be functionally active.

In Chapters 4 and 5, these protocols were used to differentiate iPSCs derived from PD patients carrying the LRRK2-G2019S mutation into vmDA neurons and MP astrocytes. In Chapter 4, hypothesis-driven, functional analysis was conducted on these cultures, with the aim of

confirming cellular phenotypes that have previously been associated with LRRK2 mutations, and identifying hypothesised novel phenotypes. Several pathways were investigated, including autophagy and mitochondrial function; however, no phenotypic changes were detected in the presence of the LRRK2-G2019S mutation in either cell type. In Chapter 5, proteomics and transcriptomics methods were used in combination, to study the effects of the LRRK2-G2019S mutation across all cellular pathways in these cell types in an unbiased manner. This approach identified stochastic X-chromosome reactivation in the two female LRRK2-G2019S iPSC-derived MP astrocyte lines. X-chromosome reactivation has previously been demonstrated to affect disease phenotypes in iPSC-derived cells (Mekhoubad et al. 2012) therefore no further analysis was conducted on MP-astrocyte cultures. This effect was not seen in iPSC-derived vmDA-neuron cultures, where a large number of proteins and genes were differentially regulated by the LRRK2-G2019S mutation. Two major pathways—endocytosis and axon guidance—were significantly disrupted by the LRRK2-G2019S mutation in these cells. Perturbation of these pathways was confirmed by Western blotting, qPCR, and functional analysis of neurite regrowth. Furthermore, these findings were also confirmed in iPSC-derived vmDA neurons carrying the LRRK2-R1441C mutation, demonstrating that despite their differential effects on LRRK2 kinase and GTPase activity, these mutations lead to PD pathology through similar pathways.

In order to understand how LRRK2 interacts with the pathways identified in the dual omics study, phosphoproteomics analysis was conducted on vmDA-neuron cultures in the presence or absence of LRRK2 inhibitors, with the aim of identifying LRRK2 kinase substrates. This study, discussed in Chapter 5, is the first to use an unbiased approach to identify substrates of LRRK2 in DA neurons. Eleven distinct proteins were identified as potential LRRK2 kinase substrates. In

contrast with two similar studies conducted in MEFs and PBMCs (Steger et al. 2016; Thirstrup et al. 2017), no RAB proteins were identified by the analysis described here, suggesting that LRRK2 may phosphorylate different substrates in different cellular contexts. Further support of this hypothesis comes from the fact that the majority of the potential LRRK2 kinase substrates identified in our study exhibit neuron-specific functions.

Together, the results of the dual omics study and the phosphoproteomics analysis point to key roles for LRRK2 in endocytosis and endosomal vesicle trafficking, and regulation of synapses and neurite growth. These pathways are intrinsically linked to one another, and are integral for many other cellular functions. The endosome is involved in synaptic vesicle recycling (Cousin 2015), and converges with autophagy at the lysosome, and neurite extension requires endosomal vesicles for transport of cellular material to the growing neurites (Sann et al. 2009).

Previous studies have been conducted in cultures derived from iPSCs using differing differentiation protocols, where percentages of vmDA neurons are lower than in the model used here. Different phenotypes have been identified across these studies, likely due to variations in culture conditions. The phenotype that has been most consistently observed across these studies is impairment of neurite growth (Sanchez-Danes et al. 2012a; Su et al. 2013; Reinhardt et al. 2013; Borgs et al. 2016), and this is the only phenotype that could be confirmed in this study, albeit using a neurite regrowth assay rather than by Sholl analysis. LRRK2 mutations have been widely demonstrated to disrupt autophagy and/or mitochondrial function (Section 1.3.4.2–1.3.4.3), and a selection of different phenotypes in these pathways have also been shown in studies utilising iPSC-derived cultures containing vmDA or DA neurons (Sanchez-Danes et al. 2012a; Cooper et al. 2012; Orenstein et al. 2013; Su et al. 2013; Sanders et al. 2014; Ohta et al.

2015; Hsieh et al. 2016). Although no evidence of mitochondrial dysfunction, and minimal evidence of autophagic dysfunction were detected in iPSC-derived vmDA-neuron cultures in this thesis, it is highly probable that these phenotypes could arise due to perturbation of the pathways that have been identified in the omics studies presented here. Lysosomal enzymes are supplied by endosomal vesicles (Staudt et al. 2016); therefore, if endosomal vesicle trafficking is disrupted, then lysosomes may become dysfunctional, resulting in a blockage of autophagy. Degradation of dysfunctional mitochondria also occurs through this pathway via mitophagy; if autophagy is disrupted, and mitophagy cannot occur, then a build-up of damaged, dysfunctional mitochondria may occur. A hypothesis can therefore be made that the iPSC-derived vmDA-neuron model used in this thesis reflects an earlier stage of PD pathogenesis than those used in some of the previously published studies.

One of the questions that this thesis set out to answer was whether LRRK2 mutations result in neuronal degeneration in PD through cell-autonomous or non-cell-autonomous mechanisms. Although the study of MP astrocytes was unsuccessful, the identification of neuron-specific LRRK2 kinase substrates, and G2019S-mediated dysfunction in neuron-specific pathways in iPSC-derived vmDA neurons strongly suggests that LRRK2 acts through a cell-autonomous pathway. Furthermore, disruption of the pathways that are affected in these cultures can lead to a cascade of cellular events that may result in dopamine neuron death, as seen in PD. This study has not ruled out a role for LRRK2 in other cell types such as astrocytes; however, it has outlined a key role for neuronal LRRK2 in disease pathogenesis.

6.2. Future directions

The work presented in this thesis has provided further evidence for LRRK2's role in neurite growth and endocytosis, and points to a role for LRRK2 in regulation of synaptic machinery. Colleagues in the Wade-Martins Laboratory, and collaborators at Biogen Inc., are continuing to follow this work up in a number of ways. Experiments are currently underway using the FM1-43 dye (Betz and Bewick 1992) to study synaptic-vesicle endocytosis in iPSC-derived vmDA-neuron cultures. These experiments should identify whether a functional deficit in endocytosis is measurable in LRRK2 mutant cells. Furthermore, iPSC-derived vmDA-neuron cultures have been harvested for analysis of endosomal compartments and synaptic vesicle pools by electron microscopy.

Phosphoproteomics analysis of iPSC-derived vmDA-neuron cultures treated with LRRK2 inhibitors identified eleven potential LRRK2 kinase substrates. However, due to the duration of inhibitor treatment, and the fact that upregulation of other phosphosites were detected, it is believed that some of these may be modulated downstream of LRRK2 kinase activity. To identify which of these proteins are true LRRK2 kinase substrates, in vitro kinase assays, and potentially co-immunoprecipitation experiments will be conducted. Further bioinformatics analyses are also underway to investigate LRRK2 kinase substrates that are specifically phosphorylated by either the LRRK2-WT or -G2019S protein, but not by both. These might provide insight into any loss or gain of function of the LRRK2-G2019S mutation.

In addition to these planned experiments, LRRK2 inhibitors could be used in LRRK2-mutant iPSC-derived vmDA-neuron cultures to assess their effects on the functional readouts of neurite

outgrowth, endocytosis, and electrophysiological activity. It would be especially interesting to determine whether LRRK2 inhibitors reverse the altered protein levels seen in LRRK2-R1441C iPSC-derived vmDA-neuron cultures, as these are generally considered to have unaltered kinase activity. These functional assays may also be developed as screening tools for identification of other small-molecule modulators of these phenotypes, which may prove to be more suitable for treatment of non-LRRK2 PD.

Finally, electrophysiological analysis of LRRK2-G2019S and -R1441C iPSC-derived vmDA neurons should be explored. The results described in this thesis suggest that LRRK2, through phosphorylation, regulates recruitment and retention of AMPA receptors at the synapse, and the activity of the hyperpolarisation-activated HCN3 channel. AMPA receptors are involved in excitatory synaptic activity, which is upregulated in LRRK2-mutant primary neuronal cultures from rodents (Plowey et al. 2014; Beccano-Kelly et al. 2014; Maas et al. 2017). The HCN channel family produce I_h currents, which are necessary for autonomic pacemaking. Their activity is regulated by phosphorylation, and as HCN3 was identified as a potential LRRK2 kinase substrate, this indicates that LRRK2 may play a direct role in dopaminergic pacemaking. Furthermore, I_h current inhibition has been shown to result in preferential degeneration of vmDA neurons in the SNc compared to those in the ventral tegmental area (VTA) (Carbone et al. 2017). Assessment of the I_h current in iPSC-derived vmDA neurons should therefore be a priority, as whether HCN3 is phosphorylated by LRRK2 or a kinase downstream of LRRK2, this interaction could be key to understanding why vmDA neurons specifically degenerate in PD.

References

Aasly J. O., C. Vilariño-Güell, J. C. Dachsel, P. J. Webber, A. B. West, K. Haugarvoll, K. K. Johansen, M. Toft, J. G. Nutt, H. Payami, J. M. Kachergus, S. J. Lincoln, A. Felic, C. Wider, A. I. Soto-Ortolaza, S. A. Cobb, L. R. White, O. A. Ross and M. J. Farrer (2010). "Novel pathogenic LRRK2 p.Asn1437His substitution in familial Parkinson's disease." Mov Disord **25**(13): 2156-63.

Alegre-Abarrategui, J., H. Christian, M. M. Lufino, R. Mutihac, L. L. Venda, O. Ansorge and R. Wade-Martins (2009). "LRRK2 regulates autophagic activity and localizes to specific membrane microdomains in a novel human genomic reporter cellular model." Hum Mol Genet **18**(21): 4022-4034.

Alfei, L., M. Aita, B. Caronti, R. De Vita, V. Margotta, L. Medolago Albani and A. M. Valente (1999). "Hyaluronate receptor CD44 is expressed by astrocytes in the adult chicken and in astrocyte cell precursors in early development of the chick spinal cord." Eur J Histochem **43**(1): 29-38.

Alhamdoosh, M., M. Ng, N. J. Wilson, J. M. Sheridan, H. Huynh, M. J. Wilson and M. E. Ritchie (2017). "Combining multiple tools outperforms individual methods in gene set enrichment analyses." Bioinformatics **33**(3): 414-424.

Anand, V. S., L. J. Reichling, K. Lipinski, W. Stochaj, W. Duan, K. Kelleher, P. Pungaliya, E. L. Brown, P. H. Reinhart, R. Somberg, W. D. Hirst, S. M. Riddle and S. P. Braithwaite (2009). "Investigation of leucine-rich repeat kinase 2 : enzymological properties and novel assays." FEBS J **276**(2): 466-478.

Andersson, E., U. Tryggvason, Q. Deng, S. Friling, Z. Alekseenko, B. Robert, T. Perlmann and J. Ericson (2006). "Identification of intrinsic determinants of midbrain dopamine neurons." Cell **124**(2): 393-405.

Arias, E. and A. M. Cuervo (2011). "Chaperone-mediated autophagy in protein quality control." Curr Opin Cell Biol **23**(2): 184-189.

Arranz, A. M., L. Delbroek, K. Van Kolen, M. R. Guimaraes, W. Mandemakers, G. Daneels, S. Matta, S. Calafate, H. Shaban, P. Baatsen, P. J. De Bock, K. Gevaert, P. Vanden Berghe, P. Verstreken, B. De Strooper and D. Moechars (2015). "LRRK2 functions in synaptic vesicle endocytosis through a kinase-dependent mechanism." J Cell Sci **128**(3): 541-552.

Arriza, J. L., W. A. Fairman, J. I. Wadiche, G. H. Murdoch, M. P. Kavanaugh and S. G. Amara (1994). "Functional comparisons of three glutamate transporter subtypes cloned from human motor cortex." J Neurosci **14**(9): 5559-5569.

Ashley, A. K., A. I. Hinds, W. H. Hanneman, R. B. Tjalkens and M. E. Legare (2016). "DJ-1 mutation decreases astroglial release of inflammatory mediators." Neurotoxicology **52**: 198-203.

Badger, J. L., O. Cordero-Llana, E. M. Hartfield and R. Wade-Martins (2014). "Parkinson's disease in a dish - Using stem cells as a molecular tool." Neuropharmacology **76 Pt A**: 88-96.

Bakalarski, C. E. and D. S. Kirkpatrick (2016). "A Biologist's Field Guide to Multiplexed Quantitative Proteomics." Mol Cell Proteomics **15**(5): 1489-1497.

Ballard, P. A., J. W. Tetrud and J. W. Langston (1985). "Permanent human parkinsonism due to 1-methyl-4-phenyl-1,2,3,6-tetrahydropyridine (MPTP): seven cases." Neurology **35**(7): 949-956.

Barnabe-Heider, F., J. A. Wasylnka, K. J. Fernandes, C. Porsche, M. Sendtner, D. R. Kaplan and F. D. Miller (2005). "Evidence that embryonic neurons regulate the onset of cortical gliogenesis via cardiotrophin-1." Neuron **48**(2): 253-265.

Beccano-Kelly, D. A., N. Kuhlmann, I. Tatarnikov, M. Volta, L. N. Munsie, P. Chou, L. P. Cao, H. Han, L. Tapia, M. J. Farrer and A. J. Milnerwood (2014). "Synaptic function is modulated by LRRK2 and glutamate release is increased in cortical neurons of G2019S LRRK2 knock-in mice." Front Cell Neurosci **8**: 301.

Beevers, J. E., M. C. Lai, E. Collins, H. D. E. Booth, F. Zambon, L. Parkkinen, J. Vowles, S. A. Cowley, R. Wade-Martins and T. M. Caffrey (2017). "MAPT Genetic Variation and Neuronal Maturity Alter Isoform Expression Affecting Axonal Transport in iPSC-Derived Dopamine Neurons." Stem Cell Reports **9**(2): 587-599.

Beilina, A., I. N. Rudenko, A. Kaganovich, L. Civiero, H. Chau, S. K. Kalia, L. V. Kalia, E. Lobbestael, R. Chia, K. Ndukwe, J. Ding, M. A. Nalls, C. International Parkinson's Disease Genomics, C. North American Brain Expression, M. Olszewski, D. N. Hauser, R. Kumaran, A. M. Lozano, V. Baekelandt, L. E. Greene, J. M. Taymans, E. Greggio and M. R. Cookson (2014). "Unbiased screen for interactors of leucine-rich repeat kinase 2 supports a common pathway for sporadic and familial Parkinson disease." Proc Natl Acad Sci U S A **111**(7): 2626-2631.

Bellou, V., L. Belbasis, I. Tzoulaki, E. Evangelou and J. P. Ioannidis (2016). "Environmental risk factors and Parkinson's disease: An umbrella review of meta-analyses." Parkinsonism Relat Disord **23**: 1-9.

Bengoa-Vergniory, N., R. F. Roberts, R. Wade-Martins and J. Alegre-Abarrategui (2017). "Alpha-synuclein oligomers: a new hope." Acta Neuropathol.

Benjamini, Y. and Y. Hochberg (1995). "Controlling the False Discovery Rate - a Practical and Powerful Approach to Multiple Testing." Journal of the Royal Statistical Society Series B-Methodological **57**(1): 289-300.

Bentley, D. R., S. Balasubramanian, H. P. Swerdlow, G. P. Smith, J. Milton, C. G. Brown, K. P. Hall, D. J. Evers, C. L. Barnes, H. R. Bignell, J. M. Boutell, J. Bryant, R. J. Carter, R. Keira Cheetham, A. J. Cox, D. J. Ellis, M. R. Flatbush, N. A. Gormley, S. J. Humphray, L. J. Irving, M. S. Karbelashvili, S. M. Kirk, H. Li, X. Liu, K. S. Maisinger, L. J. Murray, B. Obradovic, T. Ost, M. L. Parkinson, M. R. Pratt, I. M. Rasolonjatovo, M. T. Reed, R. Rigatti, C. Rodighiero, M. T. Ross, A. Sabot, S. V. Sankar, A. Scally, G. P. Schroth, M. E. Smith, V. P. Smith, A. Spiridou, P. E. Torrance, S. S. Tzonev, E. H. Vermaas, K. Walter, X. Wu, L. Zhang, M. D. Alam, C. Anastasi, I. C. Aniebo, D. M. Bailey, I. R.

Bancarz, S. Banerjee, S. G. Barbour, P. A. Baybayan, V. A. Benoit, K. F. Benson, C. Bevis, P. J. Black, A. Boodhun, J. S. Brennan, J. A. Bridgham, R. C. Brown, A. A. Brown, D. H. Buermann, A. A. Bundu, J. C. Burrows, N. P. Carter, N. Castillo, E. C. M. Chiara, S. Chang, R. Neil Cooley, N. R. Crake, O. O. Dada, K. D. Diakoumakos, B. Dominguez-Fernandez, D. J. Earnshaw, U. C. Egbujor, D. W. Elmore, S. S. Etchin, M. R. Ewan, M. Fedurco, L. J. Fraser, K. V. Fuentes Fajardo, W. Scott Furey, D. George, K. J. Gietzen, C. P. Goddard, G. S. Golda, P. A. Granieri, D. E. Green, D. L. Gustafson, N. F. Hansen, K. Harnish, C. D. Haudenschild, N. I. Heyer, M. M. Hims, J. T. Ho, A. M. Horgan, K. Hoschler, S. Hurwitz, D. V. Ivanov, M. Q. Johnson, T. James, T. A. Huw Jones, G. D. Kang, T. H. Kerelska, A. D. Kersey, I. Khrebtukova, A. P. Kindwall, Z. Kingsbury, P. I. Kokko-Gonzales, A. Kumar, M. A. Laurent, C. T. Lawley, S. E. Lee, X. Lee, A. K. Liao, J. A. Loch, M. Lok, S. Luo, R. M. Mammen, J. W. Martin, P. G. McCauley, P. McNitt, P. Mehta, K. W. Moon, J. W. Mullens, T. Newington, Z. Ning, B. Ling Ng, S. M. Novo, M. J. O'Neill, M. A. Osborne, A. Osnowski, O. Ostadan, L. L. Paraschos, L. Pickering, A. C. Pike, A. C. Pike, D. Chris Pinkard, D. P. Pliskin, J. Podhasky, V. J. Quijano, C. Raczy, V. H. Rae, S. R. Rawlings, A. Chiva Rodriguez, P. M. Roe, J. Rogers, M. C. Rogert Bacigalupo, N. Romanov, A. Romieu, R. K. Roth, N. J. Rourke, S. T. Ruediger, E. Rusman, R. M. Sanches-Kuiper, M. R. Schenker, J. M. Seoane, R. J. Shaw, M. K. Shiver, S. W. Short, N. L. Sizto, J. P. Sluis, M. A. Smith, J. Ernest Sohna Sohna, E. J. Spence, K. Stevens, N. Sutton, L. Szajkowski, C. L. Tregidgo, G. Turcatti, S. Vandevondele, Y. Verhovsky, S. M. Virk, S. Wakelin, G. C. Walcott, J. Wang, G. J. Worsley, J. Yan, L. Yau, M. Zuerlein, J. Rogers, J. C. Mullikin, M. E. Hurles, N. J. McCooke, J. S. West, F. L. Oaks, P. L. Lundberg, D. Klenerman, R. Durbin and A. J. Smith (2008). "Accurate whole human genome sequencing using reversible terminator chemistry." Nature **456**(7218): 53-59.

Berger, Z., K. A. Smith and M. J. Lavoie (2010). "Membrane localization of LRRK2 is associated with increased formation of the highly active LRRK2 dimer and changes in its phosphorylation." Biochemistry **49**(26): 5511-5523.

Betz, W. J. and G. S. Bewick (1992). "Optical analysis of synaptic vesicle recycling at the frog neuromuscular junction." Science **255**(5041): 200-203.

Biernat, J., N. Gustke, G. Drewes, E. M. Mandelkow and E. Mandelkow (1993). "Phosphorylation of Ser262 strongly reduces binding of tau to microtubules: distinction between PHF-like immunoreactivity and microtubule binding." Neuron **11**(1): 153-163.

Bignami, A., L. F. Eng, D. Dahl and C. T. Uyeda (1972). "Localization of the glial fibrillary acidic protein in astrocytes by immunofluorescence." Brain Res **43**(2): 429-435.

Biosa, A., A. Trancikova, L. Civiero, L. Glauser, L. Bubacco, E. Greggio and D. J. Moore (2013). "GTPase activity regulates kinase activity and cellular phenotypes of Parkinson's disease-associated LRRK2." Hum Mol Genet **22**(6): 1140-1156.

Bjorkblom, B., A. Padzik, H. Mohammad, N. Westerlund, E. Komulainen, P. Hollos, L. Parviainen, A. C. Papageorgiou, K. Iljin, O. Kallioniemi, M. Kallajoki, M. J. Courtney, M. Magard, P. James and E. T. Coffey (2012). "c-Jun N-terminal kinase phosphorylation of MARCKSL1 determines actin stability and migration in neurons and in cancer cells." Mol Cell Biol **32**(17): 3513-3526.

Blandini, F. and M. T. Armentero (2014). "Dopamine receptor agonists for Parkinson's disease." Expert Opin Investig Drugs **23**(3): 387-410.

Boda, B., L. Jourdain and D. Muller (2008). "Distinct, but compensatory roles of PAK1 and PAK3 in spine morphogenesis." Hippocampus **18**(9): 857-861.

Boland, D. F. and M. Stacy (2012). "The economic and quality of life burden associated with Parkinson's disease: a focus on symptoms." Am J Manag Care **18**(7 Suppl): S168-175.

Bonifacino, J. S. and J. H. Hurley (2008). "Retromer." Curr Opin Cell Biol **20**(4): 427-436.

Bonni, A., Y. Sun, M. Nadal-Vicens, A. Bhatt, D. A. Frank, I. Rozovsky, N. Stahl, G. D. Yancopoulos and M. E. Greenberg (1997). "Regulation of gliogenesis in the central nervous system by the JAK-STAT signaling pathway." Science **278**(5337): 477-483.

Booth, H. D. E., W. D. Hirst and R. Wade-Martins (2017). "The Role of Astrocyte Dysfunction in Parkinson's Disease Pathogenesis." Trends Neurosci **40**(6): 358-370.

Borgs, L., E. Peyre, P. Alix, K. Hanon, B. Grobarczyk, J. D. Godin, A. Purnelle, N. Krusy, P. Maquet, P. Lefebvre, V. Seutin, B. Malgrange and L. Nguyen (2016). "Dopaminergic neurons differentiating from LRRK2 G2019S induced pluripotent stem cells show early neuritic branching defects." Sci Rep **6**: 33377.

Bose, A. and M. F. Beal (2016). "Mitochondrial dysfunction in Parkinson's disease." J Neurochem **139 Suppl 1**: 216-231.

Braak, H. and K. Del Tredici (2004). "Poor and protracted myelination as a contributory factor to neurodegenerative disorders." Neurobiol Aging **25**(1): 19-23.

Braak, H., K. Del Tredici, U. Rub, R. A. de Vos, E. N. Jansen Steur and E. Braak (2003). "Staging of brain pathology related to sporadic Parkinson's disease." Neurobiol Aging **24**(2): 197-211.

Bramblett, G. T., M. Goedert, R. Jakes, S. E. Merrick, J. Q. Trojanowski and V. M. Lee (1993). "Abnormal tau phosphorylation at Ser396 in Alzheimer's disease recapitulates development and contributes to reduced microtubule binding." Neuron **10**(6): 1089-1099.

Bravo-San Pedro, J. M., M. Niso-Santano, R. Gomez-Sanchez, E. Pizarro-Estrella, A. Aiastui-Pujana, A. Gorostidi, V. Climent, R. Lopez de Maturana, R. Sanchez-Pernaute, A. Lopez de Munain, J. M. Fuentes and R. A. Gonzalez-Polo (2013). "The LRRK2 G2019S mutant exacerbates basal autophagy through activation of the MEK/ERK pathway." Cell Mol Life Sci **70**(1): 121-136.

Brodsky, F. M., C. Y. Chen, C. Knuehl, M. C. Towler and D. E. Wakeham (2001). "Biological basket weaving: formation and function of clathrin-coated vesicles." Annu Rev Cell Dev Biol **17**: 517-568.

Cabezas, R., M. Avila, J. Gonzalez, R. S. El-Bacha, E. Baez, L. M. Garcia-Segura, J. C. Jurado Coronel, F. Capani, G. P. Cardona-Gomez and G. E. Barreto (2014). "Astrocytic modulation of blood brain barrier: perspectives on Parkinson's disease." Front Cell Neurosci **8**: 211.

Caceres, A. and K. S. Kosik (1990). "Inhibition of neurite polarity by tau antisense oligonucleotides in primary cerebellar neurons." Nature **343**(6257): 461-463.

Carbone, C., A. Costa, G. Provensi, G. Mannaioni and A. Masi (2017). "The Hyperpolarization-Activated Current Determines Synaptic Excitability, Calcium Activity and Specific Viability of Substantia Nigra Dopaminergic Neurons." Front Cell Neurosci **11**: 187.

Carpenter, A. E., T. R. Jones, M. R. Lamprecht, C. Clarke, I. H. Kang, O. Friman, D. A. Guertin, J. H. Chang, R. A. Lindquist, J. Moffat, P. Golland and D. M. Sabatini (2006). "CellProfiler: image analysis software for identifying and quantifying cell phenotypes." Genome Biol **7**(10): R100.

Castillo, S. O., J. S. Baffi, M. Palkovits, D. S. Goldstein, I. J. Kopin, J. Witta, M. A. Magnuson and V. M. Nikodem (1998). "Dopamine biosynthesis is selectively abolished in substantia nigra/ventral tegmental area but not in hypothalamic neurons in mice with targeted disruption of the Nurr1 gene." Mol Cell Neurosci **11**(1-2): 36-46.

Chan, C. S., J. N. Guzman, E. Ilijic, J. N. Mercer, C. Rick, T. Tkatch, G. E. Meredith and D. J. Surmeier (2007). "'Rejuvenation' protects neurons in mouse models of Parkinson's disease." Nature **447**(7148): 1081-1086.

Chan, S. L. and E. K. Tan (2017). "Targeting LRRK2 in Parkinson's disease: an update on recent developments." Expert Opin Ther Targets **21**(6): 601-610.

Chen, C., P. Jiang, H. Xue, S. E. Peterson, H. T. Tran, A. E. McCann, M. M. Parast, S. Li, D. E. Pleasure, L. C. Laurent, J. F. Loring, Y. Liu and W. Deng (2014). "Role of astroglia in Down's syndrome revealed by patient-derived human-induced pluripotent stem cells." Nat Commun **5**: 4430.

Chen, L., J. Jin, J. Davis, Y. Zhou, Y. Wang, J. Liu, P. J. Lockhart and J. Zhang (2007). "Oligomeric alpha-synuclein inhibits tubulin polymerization." Biochem Biophys Res Commun **356**(3): 548-553.

Chen, L., S. Zhang, Y. Liu, H. Hong, H. Wang, Y. Zheng, H. Zhou, J. Chen, W. Xian, Y. He, J. Li, Z. Liu, Z. Pei and J. Zeng (2011). "LRRK2 R1398H polymorphism is associated with decreased risk of Parkinson's disease in a Han Chinese population." Parkinsonism Relat Disord **17**(4): 291-292.

Cherra, S. J., 3rd, E. Steer, A. M. Gusdon, K. Kiselyov and C. T. Chu (2013). "Mutant LRRK2 elicits calcium imbalance and depletion of dendritic mitochondria in neurons." Am J Pathol **182**(2): 474-484.

Chidambaram, S., N. Mullers, K. Wiederhold, V. Haucke and G. F. von Mollard (2004). "Specific interaction between SNAREs and epsin N-terminal homology (ENTH) domains of epsin-related proteins in trans-Golgi network to endosome transport." J Biol Chem **279**(6): 4175-4179.

Chiu, F. C., W. T. Norton and K. L. Fields (1981). "The cytoskeleton of primary astrocytes in culture contains actin, glial fibrillary acidic protein, and the fibroblast-type filament protein, vimentin." J Neurochem **37**(1): 147-155.

Choi, I., J. Kim, H. K. Jeong, B. Kim, I. Jou, S. M. Park, L. Chen, U. J. Kang, X. Zhuang and E. H. Joe (2013). "PINK1 deficiency attenuates astrocyte proliferation through

mitochondrial dysfunction, reduced AKT and increased p38 MAPK activation, and downregulation of EGFR." Glia **61**(5): 800-812.

Choi, I., J. H. Woo, I. Jou and E. H. Joe (2016). "PINK1 Deficiency Decreases Expression Levels of mir-326, mir-330, and mir-3099 during Brain Development and Neural Stem Cell Differentiation." Exp Neurobiol **25**(1): 14-23.

Civiero, L., M. D. Cirnaru, A. Beilina, U. Rodella, I. Russo, E. Belluzzi, E. Lobbestael, L. Reyniers, G. Hondhamuni, P. A. Lewis, C. Van den Haute, V. Baekelandt, R. Bandopadhyay, L. Bubacco, G. Piccoli, M. R. Cookson, J. M. Taymans and E. Greggio (2015). "Leucine-rich repeat kinase 2 interacts with p21-activated kinase 6 to control neurite complexity in mammalian brain." J Neurochem **135**(6): 1242-1256.

Collomb-Clerc, A. and M. L. Welter (2015). "Effects of deep brain stimulation on balance and gait in patients with Parkinson's disease: A systematic neurophysiological review." Neurophysiol Clin **45**(4-5): 371-388.

Cooper, O., H. Seo, S. Andrabi, C. Guardia-Laguarta, J. Graziotto, M. Sundberg, J. R. McLean, L. Carrillo-Reid, Z. Xie, T. Osborn, G. Hargus, M. Deleidi, T. Lawson, H. Bogetofte, E. Perez-Torres, L. Clark, C. Moskowitz, J. Mazzulli, L. Chen, L. Volpicelli-Daley, N. Romero, H. Jiang, R. J. Uitti, Z. Huang, G. Opala, L. A. Scarffe, V. L. Dawson, C. Klein, J. Feng, O. A. Ross, J. Q. Trojanowski, V. M. Lee, K. Marder, D. J. Surmeier, Z. K. Wszolek, S. Przedborski, D. Krainc, T. M. Dawson and O. Isacson (2012). "Pharmacological rescue of mitochondrial deficits in iPSC-derived neural cells from patients with familial Parkinson's disease." Sci Transl Med **4**(141): 141ra190.

Courtney, K. D., M. Grove, H. Vandongen, A. Vandongen, A. S. LaMantia and A. M. Pendergast (2000). "Localization and phosphorylation of Abl-interactor proteins, Abi-1 and Abi-2, in the developing nervous system." Mol Cell Neurosci **16**(3): 244-257.

Cousin, M. A. (2015). "Synaptic Vesicle Endocytosis and Endosomal Recycling in Central Nerve Terminals: Discrete Trafficking Routes?" Neuroscientist **21**(4): 413-423.

Cuervo, A. M. and J. F. Dice (2000). "Unique properties of lamp2a compared to other lamp2 isoforms." J Cell Sci **113 Pt 24**: 4441-4450.

Dachsel, J. C., B. Behrouz, M. Yue, J. E. Beevers, H. L. Melrose and M. J. Farrer (2010). "A comparative study of Lrrk2 function in primary neuronal cultures." Parkinsonism Relat Disord **16**(10): 650-655.

Dachsel, J. C. and M. J. Farrer (2010). "LRRK2 and Parkinson disease." Arch Neurol **67**(5): 542-547.

Dachsel, J. C., J. P. Taylor, S. S. Mok, O. A. Ross, K. M. Hinkle, R. M. Bailey, J. H. Hines, J. Szutu, B. Madden, L. Petrucelli and M. J. Farrer (2007). "Identification of potential protein interactors of Lrrk2." Parkinsonism Relat Disord **13**(7): 382-385.

DaCosta Byfield, S., C. Major, N. J. Laping and A. B. Roberts (2004). "SB-505124 is a selective inhibitor of transforming growth factor-beta type I receptors ALK4, ALK5, and ALK7." Mol Pharmacol **65**(3): 744-752.

Danielian, P. S. and A. P. McMahon (1996). "Engrailed-1 as a target of the Wnt-1 signalling pathway in vertebrate midbrain development." Nature **383**(6598): 332-334.

Daniels, V., R. Vancraenenbroeck, B. M. Law, E. Greggio, E. Lobbestael, F. Gao, M. De Maeyer, M. R. Cookson, K. Harvey, V. Baekelandt and J. M. Taymans (2011). "Insight into the mode of action of the LRRK2 Y1699C pathogenic mutant." J Neurochem **116**(2): 304-315.

Danzer, K. M., D. Haasen, A. R. Karow, S. Moussaud, M. Habeck, A. Giese, H. Kretzschmar, B. Hengerer and M. Kostka (2007). "Different species of alpha-synuclein oligomers induce calcium influx and seeding." J Neurosci **27**(34): 9220-9232.

Davis, C. A. and A. L. Joyner (1988). "Expression patterns of the homeo box-containing genes En-1 and En-2 and the proto-oncogene int-1 diverge during mouse development." Genes Dev **2**(12B): 1736-1744.

Davis, G. C., A. C. Williams, S. P. Markey, M. H. Ebert, E. D. Caine, C. M. Reichert, and I. J. Kopin (1979). "Chronic Parkinsonism Secondary to Intravenous Injection of Meperidine Analogues" Psychiatry Res **1**(3): 249-54.

Dayon, L., A. Hainard, V. Licker, N. Turck, K. Kuhn, D. F. Hochstrasser, P. R. Burkhard and J. C. Sanchez (2008). "Relative quantification of proteins in human cerebrospinal fluids by MS/MS using 6-plex isobaric tags." Anal Chem **80**(8): 2921-2931.

De Duve, C. (1963). "The lysosome." Sci Am **208**: 64-72.

De Duve, C. and R. Wattiaux (1966). "Functions of lysosomes." Annu Rev Physiol **28**: 435-492.

de Sampaio e Spohr, T. C., R. Martinez, E. F. da Silva, V. M. Neto and F. C. Gomes (2002). "Neuro-glia interaction effects on GFAP gene: a novel role for transforming growth factor-beta1." Eur J Neurosci **16**(11): 2059-2069.

Deuschl, G., S. Paschen and K. Witt (2013). "Clinical outcome of deep brain stimulation for Parkinson's disease." Handb Clin Neurol **116**: 107-128.

Di Fonzo, A., Y. H. Wu-Chou, C. S. Lu, M. van Doeselaar, E. J. Simons, C. F. Rohe, H. C. Chang, R. S. Chen, Y. H. Weng, N. Vanacore, G. J. Breedveld, B. A. Oostra and V. Bonifati (2006). "A common missense variant in the LRRK2 gene, Gly2385Arg, associated with Parkinson's disease risk in Taiwan." Neurogenetics **7**(3): 133-138.

Dodson, M. W., T. Zhang, C. Jiang, S. Chen and M. Guo (2012). "Roles of the Drosophila LRRK2 homolog in Rab7-dependent lysosomal positioning." Hum Mol Genet **21**(6): 1350-1363.

Doherty, K. M. and J. Hardy (2013). "Parkin disease and the Lewy body conundrum." Mov Disord **28**(6): 702-704.

Driver-Dunckley, E., C. H. Adler, J. G. Hentz, B. N. Dugger, H. A. Shill, J. N. Caviness, M. N. Sabbagh, T. G. Beach and C. Arizona Parkinson Disease (2014). "Olfactory dysfunction in incidental Lewy body disease and Parkinson's disease." Parkinsonism Relat Disord **20**(11): 1260-1262.

Duan, D., Y. Fu, G. Paxinos and C. Watson (2013). "Spatiotemporal expression patterns of Pax6 in the brain of embryonic, newborn, and adult mice." Brain Struct Funct **218**(2): 353-372.

Duty, S. (2012). "Targeting glutamate receptors to tackle the pathogenesis, clinical symptoms and levodopa-induced dyskinesia associated with Parkinson's disease." CNS Drugs **26**(12): 1017-1032.

Dzamko N., M. Deak, F. Hentati, A. D. Reith, A. R. Prescott, D. R. Alessi and R. J. Nichols (2010). "Inhibition of LRRK2 kinase activity leads to dephosphorylation of Ser(910)/Ser(935), disruption of 14-3-3 binding and altered cytoplasmic localization." Biochem J **430**(3): 405-13.

Eiyama, A. and K. Okamoto (2015). "PINK1/Parkin-mediated mitophagy in mammalian cells." Curr Opin Cell Biol **33**: 95-101.

Emdad, L., S. L. D'Souza, H. P. Kothari, Z. A. Qadeer and I. M. Germano (2012). "Efficient differentiation of human embryonic and induced pluripotent stem cells into functional astrocytes." Stem Cells Dev **21**(3): 404-410.

Evans, M. J. and M. H. Kaufman (1981). "Establishment in culture of pluripotential cells from mouse embryos." Nature **292**(5819): 154-156.

Fahn, S. (2015). "The medical treatment of Parkinson disease from James Parkinson to George Cotzias." Mov Disord **30**(1): 4-18.

Fell, M. J., C. Mirescu, K. Basu, B. Cheewatrakoolpong, D. E. DeMong, J. M. Ellis, L. A. Hyde, Y. Lin, C. G. Markgraf, H. Mei, M. Miller, F. M. Poulet, J. D. Scott, M. D. Smith, Z. Yin, X. Zhou, E. M. Parker, M. E. Kennedy and J. A. Morrow (2015). "MLi-2, a Potent, Selective, and Centrally Active Compound for Exploring the Therapeutic Potential and Safety of LRRK2 Kinase Inhibition." J Pharmacol Exp Ther **355**(3): 397-409.

Fellner, L., R. Irschick, K. Schanda, M. Reindl, L. Klimaschewski, W. Poewe, G. K. Wenning and N. Stefanova (2013). "Toll-like receptor 4 is required for alpha-synuclein dependent activation of microglia and astroglia." Glia **61**(3): 349-360.

Fernandes, H. J., E. M. Hartfield, H. C. Christian, E. Emmanoulidou, Y. Zheng, H. Booth, H. Bogetofte, C. Lang, B. J. Ryan, S. P. Sardi, J. Badger, J. Vowles, S. Evetts, G. K. Tofaris, K. Vekrellis, K. Talbot, M. T. Hu, W. James, S. A. Cowley and R. Wade-Martins (2016). "ER Stress and Autophagic Perturbations Lead to Elevated Extracellular alpha-Synuclein in GBA-N370S Parkinson's iPSC-Derived Dopamine Neurons." Stem Cell Reports **6**(3): 342-356.

Fernandez-Santiago, R., I. Carballo-Carbajal, G. Castellano, R. Torrent, Y. Richaud, A. Sanchez-Danes, R. Vilarrasa-Blasi, A. Sanchez-Pla, J. L. Mosquera, J. Soriano, J. Lopez-Barneo, J. M. Canals, J. Alberch, A. Raya, M. Vila, A. Consiglio, J. I. Martin-Subero, M. Ezquerra and E. Tolosa (2015). "Aberrant epigenome in iPSC-derived dopaminergic neurons from Parkinson's disease patients." EMBO Mol Med **7**(12): 1529-1546.

Ferri, A. L., W. Lin, Y. E. Mavromatakis, J. C. Wang, H. Sasaki, J. A. Whitsett and S. L. Ang (2007). "Foxa1 and Foxa2 regulate multiple phases of midbrain dopaminergic

neuron development in a dosage-dependent manner." Development **134**(15): 2761-2769.

Friling, S., E. Andersson, L. H. Thompson, M. E. Jonsson, J. B. Hebsgaard, E. Nanou, Z. Alekseenko, U. Marklund, S. Kjellander, N. Volakakis, O. Hovatta, A. El Manira, A. Bjorklund, T. Perlmann and J. Ericson (2009). "Efficient production of mesencephalic dopamine neurons by Lmx1a expression in embryonic stem cells." Proc Natl Acad Sci U S A **106**(18): 7613-7618.

Fujioka, S. and Z. K. Wszolek (2012). "Update on genetics of parkinsonism." Neurodegener Dis **10**(1-4): 257-260.

Funayama, M., K. Hasegawa, H. Kowa, M. Saito, S. Tsuji and F. Obata (2002). "A new locus for Parkinson's disease (PARK8) maps to chromosome 12p11.2-q13.1." Ann Neurol **51**(3): 296-301.

Funayama, M., K. Hasegawa, E. Ohta, N. Kawashima, M. Komiyama, H. Kowa, S. Tsuji and F. Obata (2005). "An LRRK2 mutation as a cause for the parkinsonism in the original PARK8 family." Ann Neurol **57**(6): 918-921.

Fusaki, N., H. Ban, A. Nishiyama, K. Saeki and M. Hasegawa (2009). "Efficient induction of transgene-free human pluripotent stem cells using a vector based on Sendai virus, an RNA virus that does not integrate into the host genome." Proc Jpn Acad Ser B Phys Biol Sci **85**(8): 348-362.

Gai, W. P., H. X. Yuan, X. Q. Li, J. T. Power, P. C. Blumbergs and P. H. Jensen (2000). "In situ and in vitro study of colocalization and segregation of alpha-synuclein, ubiquitin, and lipids in Lewy bodies." Exp Neurol **166**(2): 324-333.

Gaig, C., M. J. Marti, M. Ezquerra, M. J. Rey, A. Cardozo and E. Tolosa (2007). "G2019S LRRK2 mutation causing Parkinson's disease without Lewy bodies." J Neurol Neurosurg Psychiatry **78**(6): 626-628.

Gandhi, P. N., X. Wang, X. Zhu, S. G. Chen and A. L. Wilson-Delfosse (2008). "The Roc domain of leucine-rich repeat kinase 2 is sufficient for interaction with microtubules." J Neurosci Res **86**(8): 1711-1720.

Gao, X., H. Chen, M. A. Schwarzschild and A. Ascherio (2011). "Use of ibuprofen and risk of Parkinson disease." Neurology **76**(10): 863-869.

Garcia-Miralles, M., J. Coomaraswamy, K. Habig, M. C. Herzig, N. Funk, F. Gillardon, M. Maisel, M. Jucker, T. Gasser, D. Galter and S. Biskup (2015). "No dopamine cell loss or changes in cytoskeleton function in transgenic mice expressing physiological levels of wild type or G2019S mutant LRRK2 and in human fibroblasts." PLoS One **10**(4): e0118947.

Gibb, W. R. and A. J. Lees (1988). "The relevance of the Lewy body to the pathogenesis of idiopathic Parkinson's disease." J Neurol Neurosurg Psychiatry **51**(6): 745-752.

Gloeckner, C. J., N. Kinkl, A. Schumacher, R. J. Braun, E. O'Neill, T. Meitinger, W. Kolch, H. Prokisch and M. Ueffing (2006). "The Parkinson disease causing LRRK2 mutation I2020T is associated with increased kinase activity." Hum Mol Genet **15**(2): 223-232.

Godena, V. K., N. Brookes-Hocking, A. Moller, G. Shaw, M. Oswald, R. M. Sancho, C. C. Miller, A. J. Whitworth and K. J. De Vos (2014). "Increasing microtubule acetylation rescues axonal transport and locomotor deficits caused by LRRK2 Roc-COR domain mutations." Nat Commun **5**: 5245.

Goldwurm, S., S. Tunesi, S. Tesei, M. Zini, F. Sironi, P. Primignani, C. Magnani and G. Pezzoli (2011). "Kin-cohort analysis of LRRK2-G2019S penetrance in Parkinson's disease." Mov Disord **26**(11): 2144-2145.

Gomez-Suaga, P., B. Luzon-Toro, D. Churamani, L. Zhang, D. Bloor-Young, S. Patel, P. G. Woodman, G. C. Churchill and S. Hilfiker (2012). "Leucine-rich repeat kinase 2 regulates autophagy through a calcium-dependent pathway involving NAADP." Hum Mol Genet **21**(3): 511-525.

Gomez-Suaga, P., P. Rivero-Rios, E. Fdez, M. Blanca Ramirez, I. Ferrer, A. Aiastui, A. Lopez De Munain and S. Hilfiker (2014). "LRRK2 delays degradative receptor trafficking by impeding late endosomal budding through decreasing Rab7 activity." Hum Mol Genet **23**(25): 6779-6796.

Gray, M. T. and J. M. Woulfe (2015). "Striatal blood-brain barrier permeability in Parkinson's disease." J Cereb Blood Flow Metab **35**(5): 747-750.

Gronostajski, R. M. and A. B. Pardee (1984). "Protein degradation in 3T3 cells and tumorigenic transformed 3T3 cells." J Cell Physiol **119**(1): 127-132.

Grunewald, A., B. Arns, B. Meier, K. Brockmann, V. Tadic and C. Klein (2014). "Does uncoupling protein 2 expression qualify as marker of disease status in LRRK2-associated Parkinson's disease?" Antioxid Redox Signal **20**(13): 1955-1960.

Gu, X. L., C. X. Long, L. Sun, C. Xie, X. Lin and H. Cai (2010). "Astrocytic expression of Parkinson's disease-related A53T alpha-synuclein causes neurodegeneration in mice." Mol Brain **3**: 12.

Gurdon, J. B. (1962). "The developmental capacity of nuclei taken from intestinal epithelium cells of feeding tadpoles." J Embryol Exp Morphol **10**: 622-640.

Gutierrez, H. and A. M. Davies (2007). "A fast and accurate procedure for deriving the Sholl profile in quantitative studies of neuronal morphology." J Neurosci Methods **163**(1): 24-30.

Guzman, J. N., J. Sanchez-Padilla, C. S. Chan and D. J. Surmeier (2009). "Robust pacemaking in substantia nigra dopaminergic neurons." J Neurosci **29**(35): 11011-11019.

Gygi, S. P., B. Rist, S. A. Gerber, F. Turecek, M. H. Gelb and R. Aebersold (1999). "Quantitative analysis of complex protein mixtures using isotope-coded affinity tags." Nat Biotechnol **17**(10): 994-999.

Hackam, D. G. and D. A. Redelmeier (2006). "Translation of research evidence from animals to humans." JAMA **296**(14): 1731-1732.

Hamza, T. H., C. P. Zabetian, A. Tenesa, A. Laederach, J. Montimurro, D. Yearout, D. M. Kay, K. F. Doheny, J. Paschall, E. Pugh, V. I. Kusel, R. Collura, J. Roberts, A. Griffith, A. Samii, W. K. Scott, J. Nutt, S. A. Factor and H. Payami (2010). "Common genetic

variation in the HLA region is associated with late-onset sporadic Parkinson's disease." Nat Genet **42**(9): 781-785.

Hartfield, E. M., M. Yamasaki-Mann, H. J. Ribeiro Fernandes, J. Vowles, W. S. James, S. A. Cowley and R. Wade-Martins (2014). "Physiological characterisation of human iPS-derived dopaminergic neurons." PLoS One **9**(2): e87388.

Hartmann, A. (2004). "Postmortem studies in Parkinson's disease." Dialogues Clin Neurosci **6**(3): 281-293.

Hegarty, S. V., A. M. Sullivan and G. W. O'Keeffe (2013). "Midbrain dopaminergic neurons: a review of the molecular circuitry that regulates their development." Dev Biol **379**(2): 123-138.

Hemmati-Brivanlou, A., O. G. Kelly and D. A. Melton (1994). "Follistatin, an antagonist of activin, is expressed in the Spemann organizer and displays direct neuralizing activity." Cell **77**(2): 283-295.

Henderson, J. L., B. L. Kormos, M. M. Hayward, K. J. Coffman, J. Jasti, R. G. Kurumbail, T. T. Wager, P. R. Verhoest, G. S. Noell, Y. Chen, E. Needle, Z. Berger, S. J. Steyn, C. Houle, W. D. Hirst and P. Galatsis (2015). "Discovery and preclinical profiling of 3-[4-(morpholin-4-yl)-7H-pyrrolo[2,3-d]pyrimidin-5-yl]benzonitrile (PF-06447475), a highly potent, selective, brain penetrant, and in vivo active LRRK2 kinase inhibitor." J Med Chem **58**(1): 419-432.

Henley, J. M. and K. A. Wilkinson (2013). "AMPA receptor trafficking and the mechanisms underlying synaptic plasticity and cognitive aging." Dialogues Clin Neurosci **15**(1): 11-27.

Henry, A. G., S. Aghamohammadzadeh, H. Samaroo, Y. Chen, K. Mou, E. Needle and W. D. Hirst (2015). "Pathogenic LRRK2 mutations, through increased kinase activity, produce enlarged lysosomes with reduced degradative capacity and increase ATP13A2 expression." Hum Mol Genet **24**(21): 6013-6028.

Hernandez-Chan, N. G., M. J. Bannon, C. E. Orozco-Barrios, L. Escobedo, S. Zamudio, F. De la Cruz, J. L. Gongora-Alfaro, J. Armendariz-Borunda, D. Reyes-Corona, A. J. Espadas-Alvarez, Y. M. Flores-Martinez, J. Ayala-Davila, M. E. Hernandez-Gutierrez, L. Pavon, R. Garcia-Villegas, R. Nadella and D. Martinez-Fong (2015). "Neurotensin-polyplex-mediated brain-derived neurotrophic factor gene delivery into nigral dopamine neurons prevents nigrostriatal degeneration in a rat model of early Parkinson's disease." J Biomed Sci **22**: 59.

Hernandez, D. G., C. Paisan-Ruiz, A. McInerney-Leo, S. Jain, A. Meyer-Lindenberg, E. W. Evans, K. F. Berman, J. Johnson, G. Auburger, A. A. Schaffer, G. J. Lopez, R. L. Nussbaum and A. B. Singleton (2005). "Clinical and positron emission tomography of Parkinson's disease caused by LRRK2." Ann Neurol **57**(3): 453-456.

Hernandez, D. G., X. Reed and A. B. Singleton (2016). "Genetics in Parkinson disease: Mendelian versus non-Mendelian inheritance." J Neurochem **139 Suppl 1**: 59-74.

Herzig, M. C., C. Kolly, E. Persohn, D. Theil, T. Schweizer, T. Hafner, C. Stemmelen, T. J. Troxler, P. Schmid, S. Danner, C. R. Schnell, M. Mueller, B. Kinzel, A. Grevot, F.

Bolognani, M. Stirn, R. R. Kuhn, K. Kaupmann, P. H. van der Putten, G. Rovelli and D. R. Shimshek (2011). "LRRK2 protein levels are determined by kinase function and are crucial for kidney and lung homeostasis in mice." Hum Mol Genet **20**(21): 4209-4223.

Heytler, P. G. and W. W. Prichard (1962). "A new class of uncoupling agents--carbonyl cyanide phenylhydrazones." Biochem Biophys Res Commun **7**: 272-275.

Higashi, S., D. J. Moore, R. Yamamoto, M. Minegishi, K. Sato, T. Togo, O. Katsuse, H. Uchikado, Y. Furukawa, H. Hino, K. Kosaka, P. C. Emson, K. Wada, V. L. Dawson, T. M. Dawson, H. Arai and E. Iseki (2009). "Abnormal localization of leucine-rich repeat kinase 2 to the endosomal-lysosomal compartment in lewy body disease." J Neuropathol Exp Neurol **68**(9): 994-1005.

Hirst, J., S. E. Miller, M. J. Taylor, G. F. von Mollard and M. S. Robinson (2004). "EpsinR is an adaptor for the SNARE protein Vti1b." Mol Biol Cell **15**(12): 5593-5602.

Hochstim, C., B. Deneen, A. Lukaszewicz, Q. Zhou and D. J. Anderson (2008). "Identification of positionally distinct astrocyte subtypes whose identities are specified by a homeodomain code." Cell **133**(3): 510-522.

Hockey, L. N., B. S. Kilpatrick, E. R. Eden, Y. Lin-Moshier, G. C. Brailoiu, E. Brailoiu, C. E. Futter, A. H. Schapira, J. S. Marchant and S. Patel (2015). "Dysregulation of lysosomal morphology by pathogenic LRRK2 is corrected by TPC2 inhibition." J Cell Sci **128**(2): 232-238.

Holmqvist, S., M. Brouwer, M. Djelloul, A. G. Diaz, M. J. Devine, A. Hammarberg, K. Fog, T. Kunath and L. Roybon (2015). "Generation of human pluripotent stem cell reporter lines for the isolation of and reporting on astrocytes generated from ventral midbrain and ventral spinal cord neural progenitors." Stem Cell Res **15**(1): 203-220.

Hong, L., H. W. Ko, B. J. Gwag, E. Joe, S. Lee, Y. T. Kim and Y. H. Suh (1998). "The cDNA cloning and ontogeny of mouse alpha-synuclein." Neuroreport **9**(6): 1239-1243.

Horvath P., N. Aulner, M. Bickle, A. M. Davies, E. D. Nery, D. Ebner, M. C. Montoya, P. Östling P, V. Pietiäinen, L. S. Price, S. L. Shorte, G. Turcatti, C. von Schantz and N. O. Carragher (2016). "Screening out irrelevant cell-based models of disease." Nat Rev Drug Discov **15**(11): 751-769.

Hsieh, C. H., A. Shaltouki, A. E. Gonzalez, A. Bettencourt da Cruz, L. F. Burbulla, E. St Lawrence, B. Schule, D. Krainc, T. D. Palmer and X. Wang (2016). "Functional Impairment in Miro Degradation and Mitophagy Is a Shared Feature in Familial and Sporadic Parkinson's Disease." Cell Stem Cell **19**(6): 709-724.

Hsu, J. L., S. Y. Huang, N. H. Chow and S. H. Chen (2003). "Stable-isotope dimethyl labeling for quantitative proteomics." Anal Chem **75**(24): 6843-6852.

Hu, B. Y., J. P. Weick, J. Yu, L. X. Ma, X. Q. Zhang, J. A. Thomson and S. C. Zhang (2010). "Neural differentiation of human induced pluripotent stem cells follows developmental principles but with variable potency." Proc Natl Acad Sci U S A **107**(9): 4335-4340.

Hu, J., H. Ge, M. Newman and K. Liu (2012). "OSA: a fast and accurate alignment tool for RNA-Seq." Bioinformatics **28**(14): 1933-1934.

Huang, N., Y. Xia, D. Zhang, S. Wang, Y. Bao, R. He, J. Teng and J. Chen (2017). "Hierarchical assembly of centriole subdistal appendages via centrosome binding proteins CCDC120 and CCDC68." Nat Commun **8**: 15057.

Hube F. and C. Francastel (2015). "Mammalian introns: when the junk generates molecular diversity." Int J Mol Sci **16**(3): 4429-52.

Hussain, N. K., G. M. Thomas, J. Luo and R. L. Huganir (2015). "Regulation of AMPA receptor subunit GluA1 surface expression by PAK3 phosphorylation." Proc Natl Acad Sci U S A **112**(43): E5883-5890.

Hyman, C., M. Hofer, Y. A. Barde, M. Juhasz, G. D. Yancopoulos, S. P. Squinto and R. M. Lindsay (1991). "BDNF is a neurotrophic factor for dopaminergic neurons of the substantia nigra." Nature **350**(6315): 230-232.

Hynes, M., J. A. Porter, C. Chiang, D. Chang, M. Tessier-Lavigne, P. A. Beachy and A. Rosenthal (1995). "Induction of midbrain dopaminergic neurons by Sonic hedgehog." Neuron **15**(1): 35-44.

Hynes, M., D. M. Stone, M. Dowd, S. Pitts-Meek, A. Goddard, A. Gurney and A. Rosenthal (1997). "Control of cell pattern in the neural tube by the zinc finger transcription factor and oncogene Gli-1." Neuron **19**(1): 15-26.

Ikeda, M., Y. Kanao, M. Yamanaka, H. Sakuraba, Y. Mizutani, Y. Igarashi and A. Kihara (2008). "Characterization of four mammalian 3-hydroxyacyl-CoA dehydratases involved in very long-chain fatty acid synthesis." FEBS Lett **582**(16): 2435-2440.

Ito, G., T. Okai, G. Fujino, K. Takeda, H. Ichijo, T. Katada and T. Iwatsubo (2007). "GTP binding is essential to the protein kinase activity of LRRK2, a causative gene product for familial Parkinson's disease." Biochemistry **46**(5): 1380-1388.

Jaleel, M., R. J. Nichols, M. Deak, D. G. Campbell, F. Gillardon, A. Knebel and D. R. Alessi (2007). "LRRK2 phosphorylates moesin at threonine-558: characterization of how Parkinson's disease mutants affect kinase activity." Biochem J **405**(2): 307-317.

Jaworski, J., L. C. Kapitein, S. M. Gouveia, B. R. Dortland, P. S. Wulf, I. Grigoriev, P. Camera, S. A. Spangler, P. Di Stefano, J. Demmers, H. Krugers, P. Defilippi, A. Akhmanova and C. C. Hoogenraad (2009). "Dynamic microtubules regulate dendritic spine morphology and synaptic plasticity." Neuron **61**(1): 85-100.

Jiang, C., T. R. Cummins and G. G. Haddad (1994). "Membrane ionic currents and properties of freshly dissociated rat brainstem neurons." Exp Brain Res **100**(3): 407-420.

Jiang, W., C. Ju, H. Jiang and D. Zhang (2014). "Dairy foods intake and risk of Parkinson's disease: a dose-response meta-analysis of prospective cohort studies." Eur J Epidemiol **29**(9): 613-619.

Jost, W. H. (2003). "Autonomic dysfunctions in idiopathic Parkinson's disease." J Neurol **250 Suppl 1**: I28-30.

Jost, W. H. and V. F. Eckardt (2003). "Constipation in idiopathic Parkinson's disease." Scand J Gastroenterol **38**(7): 681-686.

Jung, J. H., A. M. Pendergast, P. A. Zipfel and J. A. Traugh (2008). "Phosphorylation of c-Abl by protein kinase Pak2 regulates differential binding of ABI2 and CRK." Biochemistry **47**(3): 1094-1104.

Jung, S., J. B. Bullis, I. H. Lau, T. D. Jones, L. N. Warner and N. P. Poolos (2010). "Downregulation of dendritic HCN channel gating in epilepsy is mediated by altered phosphorylation signaling." J Neurosci **30**(19): 6678-6688.

Juopperi, T. A., W. R. Kim, C. H. Chiang, H. Yu, R. L. Margolis, C. A. Ross, G. L. Ming and H. Song (2012). "Astrocytes generated from patient induced pluripotent stem cells recapitulate features of Huntington's disease patient cells." Mol Brain **5**: 17.

Kachergus, J., I. F. Mata, M. Hulihan, J. P. Taylor, S. Lincoln, J. Aasly, J. M. Gibson, O. A. Ross, T. Lynch, J. Wiley, H. Payami, J. Nutt, D. M. Maraganore, K. Czyzewski, M. Styczynska, Z. K. Wszolek, M. J. Farrer and M. Toft (2005). "Identification of a novel LRRK2 mutation linked to autosomal dominant parkinsonism: evidence of a common founder across European populations." Am J Hum Genet **76**(4): 672-680.

Kalf, J. G., G. F. Borm, B. J. de Swart, B. R. Bloem, M. J. Zwarts and M. Munneke (2011). "Reproducibility and validity of patient-rated assessment of speech, swallowing, and saliva control in Parkinson's disease." Arch Phys Med Rehabil **92**(7): 1152-1158.

Kalthoff, C., S. Groos, R. Kohl, S. Mahrhold and E. J. Ungewickell (2002). "Clint: a novel clathrin-binding ENTH-domain protein at the Golgi." Mol Biol Cell **13**(11): 4060-4073.

Kang, K. and M. R. Song (2010). "Diverse FGF receptor signaling controls astrocyte specification and proliferation." Biochem Biophys Res Commun **395**(3): 324-329.

Kawakami, F., T. Yabata, E. Ohta, T. Maekawa, N. Shimada, M. Suzuki, H. Maruyama, T. Ichikawa and F. Obata (2012). "LRRK2 phosphorylates tubulin-associated tau but not the free molecule: LRRK2-mediated regulation of the tau-tubulin association and neurite outgrowth." PLoS One **7**(1): e30834.

Kelly, C. M., P. Tyers, M. T. Borg, C. N. Svendsen, S. B. Dunnett and A. E. Rosser (2005). "EGF and FGF-2 responsiveness of rat and mouse neural precursors derived from the embryonic CNS." Brain Res Bull **68**(1-2): 83-94.

Kern, A., I. Dikic and C. Behl (2015). "The integration of autophagy and cellular trafficking pathways via RAB GAPs." Autophagy **11**(12): 2393-2397.

Kett, L. R., D. Boassa, C. C. Ho, H. J. Rideout, J. Hu, M. Terada, M. Ellisman and W. T. Dauer (2012). "LRRK2 Parkinson disease mutations enhance its microtubule association." Hum Mol Genet **21**(4): 890-899.

Khasnavis, S. and K. Pahan (2014). "Cinnamon treatment upregulates neuroprotective proteins Parkin and DJ-1 and protects dopaminergic neurons in a mouse model of Parkinson's disease." J Neuroimmune Pharmacol **9**(4): 569-581.

Kiecker, C., T. Bates and E. Bell (2016). "Molecular specification of germ layers in vertebrate embryos." Cell Mol Life Sci **73**(5): 923-947.

Kim, J. H., D. J. Choi, H. K. Jeong, J. Kim, D. W. Kim, S. Y. Choi, S. M. Park, Y. H. Suh, I. Jou and E. H. Joe (2013b). "DJ-1 facilitates the interaction between STAT1 and its phosphatase, SHP-1, in brain microglia and astrocytes: A novel anti-inflammatory function of DJ-1." Neurobiol Dis **60**: 1-10.

Kim, J. M., S. H. Cha, Y. R. Choi, I. Jou, E. H. Joe and S. M. Park (2016). "DJ-1 deficiency impairs glutamate uptake into astrocytes via the regulation of flotillin-1 and caveolin-1 expression." Sci Rep **6**: 28823.

Kim, K. S., J. S. Kim, J. Y. Park, Y. H. Suh, I. Jou, E. H. Joe and S. M. Park (2013a). "DJ-1 associates with lipid rafts by palmitoylation and regulates lipid rafts-dependent endocytosis in astrocytes." Hum Mol Genet **22**(23): 4805-4817.

Kirkeby, A., S. Grealish, D. A. Wolf, J. Nelander, J. Wood, M. Lundblad, O. Lindvall and M. Parmar (2012). "Generation of regionally specified neural progenitors and functional neurons from human embryonic stem cells under defined conditions." Cell Rep **1**(6): 703-714.

Kitchens, D. L., E. Y. Snyder and D. I. Gottlieb (1994). "FGF and EGF are mitogens for immortalized neural progenitors." J Neurobiol **25**(7): 797-807.

Klegeris, A., B. I. Giasson, H. Zhang, J. Maguire, S. Pelech and P. L. McGeer (2006). "Alpha-synuclein and its disease-causing mutants induce ICAM-1 and IL-6 in human astrocytes and astrocytoma cells." FASEB J **20**(12): 2000-2008.

Kordower, J. H., C. W. Olanow, H. B. Dodiya, Y. Chu, T. G. Beach, C. H. Adler, G. M. Halliday and R. T. Bartus (2013). "Disease duration and the integrity of the nigrostriatal system in Parkinson's disease." Brain **136**(Pt 8): 2419-2431.

Kornblum, H. I., R. Hussain, J. Wiesen, P. Miettinen, S. D. Zurcher, K. Chow, R. Derynck and Z. Werb (1998). "Abnormal astrocyte development and neuronal death in mice lacking the epidermal growth factor receptor." J Neurosci Res **53**(6): 697-717.

Kosik, K. S., L. D. Orecchio, S. Bakalis and R. L. Neve (1989). "Developmentally regulated expression of specific tau sequences." Neuron **2**(4): 1389-1397.

Koutsilieri, E. and P. Riederer (2007). "Excitotoxicity and new antiglutamatergic strategies in Parkinson's disease and Alzheimer's disease." Parkinsonism Relat Disord **13 Suppl 3**: S329-331.

Krashia, P., A. Martini, A. Nobili, D. Aversa, M. D'Amelio, N. Berretta, E. Guatteo and N. B. Mercuri (2017). "On the properties of identified dopaminergic neurons in the mouse substantia nigra and ventral tegmental area." Eur J Neurosci **45**(1): 92-105.

Krencik, R. and S. C. Zhang (2011). "Directed differentiation of functional astroglial subtypes from human pluripotent stem cells." Nat Protoc **6**(11): 1710-1717.

Kriks, S., J. W. Shim, J. Piao, Y. M. Ganat, D. R. Wakeman, Z. Xie, L. Carrillo-Reid, G. Auyeung, C. Antonacci, A. Buch, L. Yang, M. F. Beal, D. J. Surmeier, J. H. Kordower, V. Tabar

and L. Studer (2011). "Dopamine neurons derived from human ES cells efficiently engraft in animal models of Parkinson's disease." Nature **480**(7378): 547-551.

Kumar, K. R., A. Djarmati-Westenberger and A. Grunewald (2011). "Genetics of Parkinson's disease." Semin Neurol **31**(5): 433-440.

Lamb, T. M., A. K. Knecht, W. C. Smith, S. E. Stachel, A. N. Economides, N. Stahl, G. D. Yancopolous and R. M. Harland (1993). "Neural induction by the secreted polypeptide noggin." Science **262**(5134): 713-718.

Lang, Y., D. Gong and Y. Fan (2015). "Calcium channel blocker use and risk of Parkinson's disease: a meta-analysis." Pharmacoepidemiol Drug Saf **24**(6): 559-566.

Langston J. W., P. Ballard, J. W. Tetrud and I. Irwin (1983). "Chronic Parkinsonism in humans due to a product of meperidine-analog synthesis." Science **219**(4587): 979-80.

Larsen, N. J., G. Ambrosi, S. J. Mullett, S. B. Berman and D. A. Hinkle (2011). "DJ-1 knock-down impairs astrocyte mitochondrial function." Neuroscience **196**: 251-264.

Law, B. M., V. A. Spain, V. H. Leinster, R. Chia, A. Beilina, H. J. Cho, J. M. Taymans, M. K. Urban, R. M. Sancho, M. Blanca Ramirez, S. Biskup, V. Baekelandt, H. Cai, M. R. Cookson, D. C. Berwick and K. Harvey (2014). "A direct interaction between leucine-rich repeat kinase 2 and specific beta-tubulin isoforms regulates tubulin acetylation." J Biol Chem **289**(2): 895-908.

Lee, A. J., Y. Wang, R. N. Alcalay, H. Mejia-Santana, R. Saunders-Pullman, S. Bressman, J. C. Corvol, A. Brice, S. Lesage, G. Mangone, E. Tolosa, C. Pont-Sunyer, D. Vilas, B. Schule, F. Kausar, T. Foroud, D. Berg, K. Brockmann, S. Goldwurm, C. Siri, R. Asselta, J. Ruiz-Martinez, E. Mondragon, C. Marras, T. Ghate, N. Giladi, A. Mirelman, K. Marder and J. F. L. C. C. Michael (2017). "Penetrance estimate of LRRK2 p.G2019S mutation in individuals of non-Ashkenazi Jewish ancestry." Mov Disord.

Lehre, K. P., L. M. Levy, O. P. Ottersen, J. Storm-Mathisen and N. C. Danbolt (1995). "Differential expression of two glial glutamate transporters in the rat brain: quantitative and immunocytochemical observations." J Neurosci **15**(3 Pt 1): 1835-1853.

Leite, S. C., P. Sampaio, V. F. Sousa, J. Nogueira-Rodrigues, R. Pinto-Costa, L. L. Peters, P. Brites and M. M. Sousa (2016). "The Actin-Binding Protein alpha-Adducin Is Required for Maintaining Axon Diameter." Cell Rep **15**(3): 490-498.

Lesage, S., A. Durr and A. Brice (2007). "LRRK2: a link between familial and sporadic Parkinson's disease?" Pathol Biol (Paris) **55**(2): 107-110.

Lev, N., Y. Barhum, T. Ben-Zur, E. Melamed, I. Steiner and D. Offen (2013). "Knocking out DJ-1 attenuates astrocytes neuroprotection against 6-hydroxydopamine toxicity." J Mol Neurosci **50**(3): 542-550.

Lewis, P. A., E. Greggio, A. Beilina, S. Jain, A. Baker and M. R. Cookson (2007). "The R1441C mutation of LRRK2 disrupts GTP hydrolysis." Biochem Biophys Res Commun **357**(3): 668-671.

Li, B. and C. N. Dewey (2011). "RSEM: accurate transcript quantification from RNA-Seq data with or without a reference genome." BMC Bioinformatics **12**: 323.

Li, X., Y. C. Tan, S. Poulose, C. W. Olanow, X. Y. Huang and Z. Yue (2007). "Leucine-rich repeat kinase 2 (LRRK2)/PARK8 possesses GTPase activity that is altered in familial Parkinson's disease R1441C/G mutants." J Neurochem **103**(1): 238-247.

Li, Y., W. Liu, T. F. Oo, L. Wang, Y. Tang, V. Jackson-Lewis, C. Zhou, K. Geghman, M. Bogdanov, S. Przedborski, M. F. Beal, R. E. Burke and C. Li (2009). "Mutant LRRK2(R1441G) BAC transgenic mice recapitulate cardinal features of Parkinson's disease." Nat Neurosci **12**(7): 826-828.

Liao, J., C. X. Wu, C. Burlak, S. Zhang, H. Sahm, M. Wang, Z. Y. Zhang, K. W. Vogel, M. Federici, S. M. Riddle, R. J. Nichols, D. Liu, M. R. Cookson, T. A. Stone and Q. Q. Hoang (2014). "Parkinson disease-associated mutation R1441H in LRRK2 prolongs the "active state" of its GTPase domain." Proc Natl Acad Sci U S A **111**(11): 4055-4060.

Lieu, P. T., A. Fontes, M. C. Vemuri and C. C. Macarthur (2013). "Generation of induced pluripotent stem cells with CytoTune, a non-integrating Sendai virus." Methods Mol Biol **997**: 45-56.

Lin, C. H., P. I. Tsai, R. M. Wu and C. T. Chien (2010). "LRRK2 G2019S mutation induces dendrite degeneration through mislocalization and phosphorylation of tau by recruiting autoactivated GSK3ss." J Neurosci **30**(39): 13138-13149.

Lin, L. F., D. H. Doherty, J. D. Lile, S. Bektesh and F. Collins (1993). "GDNF: a glial cell line-derived neurotrophic factor for midbrain dopaminergic neurons." Science **260**(5111): 1130-1132.

Lin, W., E. Metzakopian, Y. E. Mavromatakis, N. Gao, N. Balaskas, H. Sasaki, J. Briscoe, J. A. Whitsett, M. Goulding, K. H. Kaestner and S. L. Ang (2009). "Foxa1 and Foxa2 function both upstream of and cooperatively with Lmx1a and Lmx1b in a feedforward loop promoting mesodiencephalic dopaminergic neuron development." Dev Biol **333**(2): 386-396.

Lindwall, G. and R. D. Cole (1984). "Phosphorylation affects the ability of tau protein to promote microtubule assembly." J Biol Chem **259**(8): 5301-5305.

Linhart, R., S. A. Wong, J. Cao, M. Tran, A. Huynh, C. Ardrey, J. M. Park, C. Hsu, S. Taha, R. Peterson, S. Shea, J. Kurian and K. Venderova (2014). "Vacuolar protein sorting 35 (Vps35) rescues locomotor deficits and shortened lifespan in Drosophila expressing a Parkinson's disease mutant of Leucine-Rich Repeat Kinase 2 (LRRK2)." Mol Neurodegener **9**: 23.

Lopez-Domenech, G., R. Serrat, S. Mirra, S. D'Aniello, I. Somorjai, A. Abad, N. Vitureira, E. Garcia-Arumi, M. T. Alonso, M. Rodriguez-Prados, F. Burgaya, A. L. Andreu, J. Garcia-Sancho, R. Trullas, J. Garcia-Fernandez and E. Soriano (2012). "The Eutherian Armcx genes regulate mitochondrial trafficking in neurons and interact with Miro and Trak2." Nat Commun **3**: 814.

Lopez de Maturana, R., V. Lang, A. Zubiarrain, A. Sousa, N. Vazquez, A. Gorostidi, J. Aguila, A. Lopez de Munain, M. Rodriguez and R. Sanchez-Pernaute (2016). "Mutations in LRRK2 impair NF-kappaB pathway in iPSC-derived neurons." J Neuroinflammation **13**(1): 295.

Love, M. I., W. Huber and S. Anders (2014). "Moderated estimation of fold change and dispersion for RNA-seq data with DESeq2." Genome Biol **15**(12): 550.

Maas, J. W., J. Yang and R. H. Edwards (2017). "Endogenous Leucine-Rich Repeat Kinase 2 Slows Synaptic Vesicle Recycling in Striatal Neurons." Front Synaptic Neurosci **9**: 5.

Mabie, P. C., M. F. Mehler and J. A. Kessler (1999). "Multiple roles of bone morphogenetic protein signaling in the regulation of cortical cell number and phenotype." J Neurosci **19**(16): 7077-7088.

Mackenzie, I. R. A. (2001). "The pathology of Parkinson's disease." BCMJ **43**(3): 142-147.

MacLeod, D., J. Dowman, R. Hammond, T. Leete, K. Inoue and A. Abeliovich (2006). "The familial Parkinsonism gene LRRK2 regulates neurite process morphology." Neuron **52**(4): 587-93.

MacLeod, D. A., H. Rhinn, T. Kuwahara, A. Zolin, G. Di Paolo, B. D. McCabe, K. S. Marder, L. S. Honig, L. N. Clark, S. A. Small and A. Abeliovich (2013). "RAB7L1 interacts with LRRK2 to modify intraneuronal protein sorting and Parkinson's disease risk." Neuron **77**(3): 425-439.

Magnani, E., J. Fan, L. Gasparini, M. Golding, M. Williams, G. Schiavo, M. Goedert, L. A. Amos and M. G. Spillantini (2007). "Interaction of tau protein with the dynactin complex." EMBO J **26**(21): 4546-4554.

Manzoni, C., A. Mamais, S. Dihanich, P. McGoldrick, M. J. Devine, J. Zerle, E. Kara, J. W. Taanman, D. G. Healy, J. F. Marti-Masso, A. H. Schapira, H. Plun-Favreau, S. Tooze, J. Hardy, R. Bandopadhyay and P. A. Lewis (2013a). "Pathogenic Parkinson's disease mutations across the functional domains of LRRK2 alter the autophagic/lysosomal response to starvation." Biochem Biophys Res Commun **441**(4): 862-866.

Manzoni, C., A. Mamais, S. Dihanich, R. Abeti, M. P. M. Soutar, H. Plun-Favreau, P. Giunti, S. A. Tooze, R. Bandopadhyay and P. A. Lewis (2013b). "Inhibition of LRRK2 kinase activity stimulates macroautophagy." Biochim Biophys Acta **1833**(12): 2900-2910.

Manzoni, C., A. Mamais, D. A. Roosen, S. Dihanich, M. P. Soutar, H. Plun-Favreau, R. Bandopadhyay, J. Hardy, S. A. Tooze, M. R. Cookson and P. A. Lewis (2016). "mTOR independent regulation of macroautophagy by Leucine Rich Repeat Kinase 2 via Beclin-1." Sci Rep **6**: 35106.

Margolin W. (2012). "The price of tags in protein localization studies." J Bacteriol **194**(23): 6369-71.

Martin, G. R. (1981). "Isolation of a pluripotent cell line from early mouse embryos cultured in medium conditioned by teratocarcinoma stem cells." Proc Natl Acad Sci U S A **78**(12): 7634-7638.

Masi, A., R. Narducci, F. Resta, C. Carbone, K. Kobayashi and G. Mannaioni (2015). "Differential contribution of Ih to the integration of excitatory synaptic inputs in substantia nigra pars compacta and ventral tegmental area dopaminergic neurons." Eur J Neurosci **42**(9): 2699-2706.

Matikainen-Ankney, B. A., N. Kezunovic, R. E. Mesias, Y. Tian, F. M. Williams, G. W. Huntley and D. L. Benson (2016). "Altered Development of Synapse Structure and Function in Striatum Caused by Parkinson's Disease-Linked LRRK2-G2019S Mutation." J Neurosci **36**(27): 7128-7141.

Matta, S., K. Van Kolen, R. da Cunha, G. van den Bogaart, W. Mandemakers, K. Miskiewicz, P. J. De Bock, V. A. Morais, S. Vilain, D. Haddad, L. Delbroek, J. Swerts, L. Chavez-Gutierrez, G. Esposito, G. Daneels, E. Karran, M. Holt, K. Gevaert, D. W. Moechars, B. De Strooper and P. Verstreken (2012). "LRRK2 controls an EndoA phosphorylation cycle in synaptic endocytosis." Neuron **75**(6): 1008-1021.

Maul, R. S., Y. Song, K. J. Amann, S. C. Gerbin, T. D. Pollard and D. D. Chang (2003). "EPLIN regulates actin dynamics by cross-linking and stabilizing filaments." J Cell Biol **160**(3): 399-407.

Maxwell, S. L., H. Y. Ho, E. Kuehner, S. Zhao and M. Li (2005). "Pitx3 regulates tyrosine hydroxylase expression in the substantia nigra and identifies a subgroup of mesencephalic dopaminergic progenitor neurons during mouse development." Dev Biol **282**(2): 467-479.

McGrew, L. L., K. Takemaru, R. Bates and R. T. Moon (1999). "Direct regulation of the Xenopus engrailed-2 promoter by the Wnt signaling pathway, and a molecular screen for Wnt-responsive genes, confirm a role for Wnt signaling during neural patterning in Xenopus." Mech Dev **87**(1-2): 21-32.

Mekhoubad, S., C. Bock, A. S. de Boer, E. Kiskinis, A. Meissner and K. Eggan (2012). "Erosion of dosage compensation impacts human iPSC disease modeling." Cell Stem Cell **10**(5): 595-609.

Melrose, H. L., J. C. Dachsel, B. Behrouz, S. J. Lincoln, M. Yue, K. M. Hinkle, C. B. Kent, E. Korvatska, J. P. Taylor, L. Witten, Y. Q. Liang, J. E. Beevers, M. Boules, B. N. Dugger, V. A. Serna, A. Gaukhman, X. Yu, M. Castanedes-Casey, A. T. Braithwaite, S. Ogholikhan, N. Yu, D. Bass, G. Tyndall, G. D. Schellenberg, D. W. Dickson, C. Janus and M. J. Farrer (2010). "Impaired dopaminergic neurotransmission and microtubule-associated protein tau alterations in human LRRK2 transgenic mice." Neurobiol Dis **40**(3): 503-517.

Mena, M. A., M. J. Casarejos, A. Bonin, J. A. Ramos and J. Garcia Yebenes (1995). "Effects of dibutyryl cyclic AMP and retinoic acid on the differentiation of dopamine neurons: prevention of cell death by dibutyryl cyclic AMP." J Neurochem **65**(6): 2612-2620.

Meurers, B. H., G. Dziewczapolski, A. Bittner, T. Shi, F. Kamme and C. W. Shults (2009). "Dopamine depletion induced up-regulation of HCN3 enhances rebound excitability of basal ganglia output neurons." Neurobiol Dis **34**(1): 178-188.

Migliore, M. M., R. Ortiz, S. Dye, R. B. Campbell, M. M. Amiji and B. L. Waszczak (2014). "Neurotrophic and neuroprotective efficacy of intranasal GDNF in a rat model of Parkinson's disease." Neuroscience **274**: 11-23.

Miklossy, J., T. Arai, J. P. Guo, A. Klegeris, S. Yu, E. G. McGeer and P. L. McGeer (2006). "LRRK2 expression in normal and pathologic human brain and in human cell lines." J Neuropathol Exp Neurol **65**(10): 953-963.

Mistrik, P., R. Mader, S. Michalakis, M. Weidinger, A. Pfeifer and M. Biel (2005). "The murine HCN3 gene encodes a hyperpolarization-activated cation channel with slow kinetics and unique response to cyclic nucleotides." J Biol Chem **280**(29): 27056-27061.

Mitchell, P. (1961). "Coupling of phosphorylation to electron and hydrogen transfer by a chemi-osmotic type of mechanism." Nature **191**: 144-148.

Moore, I. and A. Murphy (2009). "Validating the Location of Fluorescent Protein Fusions in the Endomembrane System" Plant Cell **21**(6): 1632-1636.

Mortiboys, H., R. Furmston, G. Bronstad, J. Aasly, C. Elliott and O. Bandmann (2015). "UDCA exerts beneficial effect on mitochondrial dysfunction in LRRK2(G2019S) carriers and in vivo." Neurology **85**(10): 846-852.

Mortiboys, H., K. K. Johansen, J. O. Aasly and O. Bandmann (2010). "Mitochondrial impairment in patients with Parkinson disease with the G2019S mutation in LRRK2." Neurology **75**(22): 2017-2020.

Mortimer, J. A., A. R. Borenstein and L. M. Nelson (2012). "Associations of welding and manganese exposure with Parkinson disease: review and meta-analysis." Neurology **79**(11): 1174-1180.

Muller, T. (2015). "Catechol-O-methyltransferase inhibitors in Parkinson's disease." Drugs **75**(2): 157-174.

Mullett, S. J. and D. A. Hinkle (2009). "DJ-1 knock-down in astrocytes impairs astrocyte-mediated neuroprotection against rotenone." Neurobiol Dis **33**(1): 28-36.

Mullett, S. J. and D. A. Hinkle (2011). "DJ-1 deficiency in astrocytes selectively enhances mitochondrial Complex I inhibitor-induced neurotoxicity." J Neurochem **117**(3): 375-387.

Nakajima, H., Y. Ishigaki, Q. S. Xia, T. Ikeda, Y. Yoshitake, H. Yonekura, T. Nojima, T. Tanaka, H. Umehara, N. Tomosugi, T. Takata, T. Shimasaki, N. Nakaya, I. Sato, K. Kawakami, K. Koizumi, T. Minamoto and Y. Motoo (2010). "Induction of HITS, a newly identified family with sequence similarity 107 protein (FAM107B), in cancer cells by heat shock stimulation." Int J Oncol **37**(3): 583-593.

Nakashima, K., M. Yanagisawa, H. Arakawa and T. Taga (1999). "Astrocyte differentiation mediated by LIF in cooperation with BMP2." FEBS Lett **457**(1): 43-46.

Nalls, M. A., N. Pankratz, C. M. Lill, C. B. Do, D. G. Hernandez, M. Saad, A. L. DeStefano, E. Kara, J. Bras, M. Sharma, C. Schulte, M. F. Keller, S. Arepalli, C. Letson, C. Edsall, H. Stefansson, X. Liu, H. Pliner, J. H. Lee, R. Cheng, C. International Parkinson's Disease Genomics, G. I. Parkinson's Study Group Parkinson's Research: The Organized,

andMe, GenePd, C. NeuroGenetics Research, G. Hussman Institute of Human, I. Ashkenazi Jewish Dataset, H. Cohorts for, E. Aging Research in Genetic, C. North American Brain Expression, C. United Kingdom Brain Expression, C. Greek Parkinson's Disease, G. Alzheimer Genetic Analysis, M. A. Ikram, J. P. Ioannidis, G. M. Hadjigeorgiou, J. C. Bis, M. Martinez, J. S. Perlmutter, A. Goate, K. Marder, B. Fiske, M. Sutherland, G. Xiromerisiou, R. H. Myers, L. N. Clark, K. Stefansson, J. A. Hardy, P. Heutink, H. Chen, N. W. Wood, H. Houlden, H. Payami, A. Brice, W. K. Scott, T. Gasser, L. Bertram, N. Eriksson, T. Foroud and A. B. Singleton (2014). "Large-scale meta-analysis of genome-wide association data identifies six new risk loci for Parkinson's disease." Nat Genet **46**(9): 989-993.

Nam, J. H., E. Leem, M. T. Jeon, K. H. Jeong, J. W. Park, U. J. Jung, N. Kholodilov, R. E. Burke, B. K. Jin and S. R. Kim (2015). "Induction of GDNF and BDNF by hRheb(S16H) transduction of SNpc neurons: neuroprotective mechanisms of hRheb(S16H) in a model of Parkinson's disease." Mol Neurobiol **51**(2): 487-499.

Namihira, M., J. Kohyama, K. Semi, T. Sanosaka, B. Deneen, T. Taga and K. Nakashima (2009). "Committed neuronal precursors confer astrocytic potential on residual neural precursor cells." Dev Cell **16**(2): 245-255.

Nguyen, H. N., B. Byers, B. Cord, A. Shcheglovitov, J. Byrne, P. Gujar, K. Kee, B. Schule, R. E. Dolmetsch, W. Langston, T. D. Palmer and R. R. Pera (2011). "LRRK2 mutant iPSC-derived DA neurons demonstrate increased susceptibility to oxidative stress." Cell Stem Cell **8**(3): 267-280.

Nico, B., A. Frigeri, G. P. Nicchia, F. Quondamatteo, R. Herken, M. Errede, D. Ribatti, M. Svelto and L. Roncali (2001). "Role of aquaporin-4 water channel in the development and integrity of the blood-brain barrier." J Cell Sci **114**(Pt 7): 1297-1307.

Nielsen, S., E. A. Nagelhus, M. Amiry-Moghaddam, C. Bourque, P. Agre and O. P. Ottersen (1997). "Specialized membrane domains for water transport in glial cells: high-resolution immunogold cytochemistry of aquaporin-4 in rat brain." J Neurosci **17**(1): 171-180.

Nikonova, E. V., Y. Xiong, K. Q. Tanis, V. L. Dawson, R. L. Vogel, E. M. Finney, D. J. Stone, I. J. Reynolds, J. T. Kern and T. M. Dawson (2012). "Transcriptional responses to loss or gain of function of the leucine-rich repeat kinase 2 (LRRK2) gene uncover biological processes modulated by LRRK2 activity." Hum Mol Genet **21**(1): 163-174.

Niranjan, R. (2014). "The role of inflammatory and oxidative stress mechanisms in the pathogenesis of Parkinson's disease: focus on astrocytes." Mol Neurobiol **49**(1): 28-38.

Niu, J., M. Yu, C. Wang and Z. Xu (2012). "Leucine-rich repeat kinase 2 disturbs mitochondrial dynamics via Dynamin-like protein." J Neurochem **122**(3): 650-658.

Nixon-Abell, J., D. C. Berwick, S. Granno, V. A. Spain, C. Blackstone and K. Harvey (2016). "Protective LRRK2 R1398H Variant Enhances GTPase and Wnt Signaling Activity." Front Mol Neurosci **9**: 18.

Noyce, A. J., J. P. Bestwick, L. Silveira-Moriyama, C. H. Hawkes, G. Giovannoni, A. J. Lees and A. Schrag (2012). "Meta-analysis of early nonmotor features and risk factors for Parkinson disease." Ann Neurol **72**(6): 893-901.

O'Sullivan, S. S., D. R. Williams, D. A. Gallagher, L. A. Massey, L. Silveira-Moriyama and A. J. Lees (2008). "Nonmotor symptoms as presenting complaints in Parkinson's disease: a clinicopathological study." Mov Disord **23**(1): 101-106.

Ochiai, W., M. Yanagisawa, T. Takizawa, K. Nakashima and T. Taga (2001). "Astrocyte differentiation of fetal neuroepithelial cells involving cardiotrophin-1-induced activation of STAT3." Cytokine **14**(5): 264-271.

Ogura, A., A. Morizane, Y. Nakajima, S. Miyamoto and J. Takahashi (2013). "gamma-secretase inhibitors prevent overgrowth of transplanted neural progenitors derived from human-induced pluripotent stem cells." Stem Cells Dev **22**(3): 374-382.

Ohta, E., T. Nihira, A. Uchino, Y. Imaizumi, Y. Okada, W. Akamatsu, K. Takahashi, H. Hayakawa, M. Nagai, M. Ohyama, M. Ryo, M. Ogino, S. Murayama, A. Takashima, K. Nishiyama, Y. Mizuno, H. Mochizuki, F. Obata and H. Okano (2015). "I2020T mutant LRRK2 iPSC-derived neurons in the Sagamihara family exhibit increased Tau phosphorylation through the AKT/GSK-3beta signaling pathway." Hum Mol Genet **24**(17): 4879-4900.

Ong, S. E., B. Blagoev, I. Kratchmarova, D. B. Kristensen, H. Steen, A. Pandey and M. Mann (2002). "Stable isotope labeling by amino acids in cell culture, SILAC, as a simple and accurate approach to expression proteomics." Mol Cell Proteomics **1**(5): 376-386.

Orenstein, S. J., S. H. Kuo, I. Tasset, E. Arias, H. Koga, I. Fernandez-Carasa, E. Cortes, L. S. Honig, W. Dauer, A. Consiglio, A. Raya, D. Sulzer and A. M. Cuervo (2013). "Interplay of LRRK2 with chaperone-mediated autophagy." Nat Neurosci **16**(4): 394-406.

Osellame, L. D. and M. R. Duchen (2013). "Defective quality control mechanisms and accumulation of damaged mitochondria link Gaucher and Parkinson diseases." Autophagy **9**(10): 1633-1635.

Pagano, G., G. Rengo, G. Pasqualetti, G. D. Femminella, F. Monzani, N. Ferrara and M. Tagliati (2015). "Cholinesterase inhibitors for Parkinson's disease: a systematic review and meta-analysis." J Neurol Neurosurg Psychiatry **86**(7): 767-773.

Pagonabarraga, J., S. Martinez-Horta, R. Fernandez de Bobadilla, J. Perez, R. Ribosa-Nogue, J. Marin, B. Pascual-Sedano, C. Garcia, A. Gironell and J. Kulisevsky (2016). "Minor hallucinations occur in drug-naive Parkinson's disease patients, even from the premotor phase." Mov Disord **31**(1): 45-52.

Paisan-Ruiz, C., S. Jain, E. W. Evans, W. P. Gilks, J. Simon, M. van der Brug, A. Lopez de Munain, S. Aparicio, A. M. Gil, N. Khan, J. Johnson, J. R. Martinez, D. Nicholl, I. M. Carrera, A. S. Pena, R. de Silva, A. Lees, J. F. Marti-Masso, J. Perez-Tur, N. W. Wood and A. B. Singleton (2004). "Cloning of the gene containing mutations that cause PARK8-linked Parkinson's disease." Neuron **44**(4): 595-600.

Pankratz, N., J. B. Wilk, J. C. Latourelle, A. L. DeStefano, C. Halter, E. W. Pugh, K. F. Doheny, J. F. Gusella, W. C. Nichols, T. Foroud, R. H. Myers, P. Psg, C. GenePd Investigators and L. Molecular Genetic (2009). "Genomewide association study for susceptibility genes contributing to familial Parkinson disease." Hum Genet **124**(6): 593-605.

Papkovskaia, T. D., K. Y. Chau, F. Inesta-Vaquera, D. B. Papkovsky, D. G. Healy, K. Nishio, J. Staddon, M. R. Duchen, J. Hardy, A. H. Schapira and J. M. Cooper (2012). "G2019S leucine-rich repeat kinase 2 causes uncoupling protein-mediated mitochondrial depolarization." Hum Mol Genet **21**(19): 4201-4213.

Parisiadou, L., C. Xie, H. J. Cho, X. Lin, X. L. Gu, C. X. Long, E. Lobbestael, V. Baekelandt, J. M. Taymans, L. Sun and H. Cai (2009). "Phosphorylation of ezrin/radixin/moesin proteins by LRRK2 promotes the rearrangement of actin cytoskeleton in neuronal morphogenesis." J Neurosci **29**(44): 13971-13980.

Parisiadou, L., J. Yu, C. Sgobio, C. Xie, G. Liu, L. Sun, X. L. Gu, X. Lin, N. A. Crowley, D. M. Lovinger and H. Cai (2014). "LRRK2 regulates synaptogenesis and dopamine receptor activation through modulation of PKA activity." Nat Neurosci **17**(3): 367-376.

Park, C. H., Y. K. Minn, J. Y. Lee, D. H. Choi, M. Y. Chang, J. W. Shim, J. Y. Ko, H. C. Koh, M. J. Kang, J. S. Kang, D. J. Rhie, Y. S. Lee, H. Son, S. Y. Moon, K. S. Kim and S. H. Lee (2005). "In vitro and in vivo analyses of human embryonic stem cell-derived dopamine neurons." J Neurochem **92**(5): 1265-1276.

Park, S., S. Han, I. Choi, B. Kim, S. P. Park, E. H. Joe and Y. H. Suh (2016). "Interplay between Leucine-Rich Repeat Kinase 2 (LRRK2) and p62/SQSTM-1 in Selective Autophagy." PLoS One **11**(9): e0163029.

Parkinson, J. (2002). "An essay on the shaking palsy. 1817." J Neuropsychiatry Clin Neurosci **14**(2): 223-236; discussion 222.

Parkkinen, L., T. Pirttila, M. Tervahauta and I. Alafuzoff (2005). "Widespread and abundant alpha-synuclein pathology in a neurologically unimpaired subject." Neuropathology **25**(4): 304-314.

Peng, C., L. Aron, R. Klein, M. Li, W. Wurst, N. Prakash and W. Le (2011). "Pitx3 is a critical mediator of GDNF-induced BDNF expression in nigrostriatal dopaminergic neurons." J Neurosci **31**(36): 12802-12815.

Penny, G. D., G. F. Kay, S. A. Sheardown, S. Rastan and N. Brockdorff (1996). "Requirement for Xist in X chromosome inactivation." Nature **379**(6561): 131-137.

Perel, P., I. Roberts, E. Sena, P. Wheble, C. Briscoe, P. Sandercock, M. Macleod, L. E. Mignini, P. Jayaram and K. S. Khan (2007). "Comparison of treatment effects between animal experiments and clinical trials: systematic review." BMJ **334**(7586): 197.

Perrett, R. M., Z. Alexopoulou and G. K. Tofaris (2015). "The endosomal pathway in Parkinson's disease." Mol Cell Neurosci **66**(Pt A): 21-28.

Perrier, A. L., V. Tabar, T. Barberi, M. E. Rubio, J. Bruses, N. Topf, N. L. Harrison and L. Studer (2004). "Derivation of midbrain dopamine neurons from human embryonic stem cells." Proc Natl Acad Sci U S A **101**(34): 12543-12548.

Pezzoli, G. and E. Cereda (2013). "Exposure to pesticides or solvents and risk of Parkinson disease." Neurology **80**(22): 2035-2041.

Pfeffer, S. R. (2005). "Structural clues to Rab GTPase functional diversity." J Biol Chem **280**(16): 15485-15488.

Piccoli, G., S. B. Condliffe, M. Bauer, F. Giesert, K. Boldt, S. De Astis, A. Meixner, H. Sarioglu, D. M. Vogt-Weisenhorn, W. Wurst, C. J. Gloeckner, M. Matteoli, C. Sala and M. Ueffing (2011). "LRRK2 controls synaptic vesicle storage and mobilization within the recycling pool." J Neurosci **31**(6): 2225-2237.

Piccoli, G., F. Onofri, M. D. Cirnaru, C. J. Kaiser, P. Jagtap, A. Kastenmuller, F. Pischedda, A. Marte, F. von Zweydorf, A. Vogt, F. Giesert, L. Pan, F. Antonucci, C. Kiel, M. Zhang, S. Weinkauf, M. Sattler, C. Sala, M. Matteoli, M. Ueffing and C. J. Gloeckner (2014). "Leucine-rich repeat kinase 2 binds to neuronal vesicles through protein interactions mediated by its C-terminal WD40 domain." Mol Cell Biol **34**(12): 2147-2161.

Picconi, B., G. Piccoli and P. Calabresi (2012). "Synaptic dysfunction in Parkinson's disease." Adv Exp Med Biol **970**: 553-572.

Pieri, L., K. Madiona and R. Melki (2016). "Structural and functional properties of prefibrillar alpha-synuclein oligomers." Sci Rep **6**: 24526.

Pissadaki, E. K. and J. P. Bolam (2013). "The energy cost of action potential propagation in dopamine neurons: clues to susceptibility in Parkinson's disease." Front Comput Neurosci **7**: 13.

Plowey, E. D., S. J. Cherra, 3rd, Y. J. Liu and C. T. Chu (2008). "Role of autophagy in G2019S-LRRK2-associated neurite shortening in differentiated SH-SY5Y cells." J Neurochem **105**(3): 1048-1056.

Plowey, E. D. and C. T. Chu (2011). "Synaptic dysfunction in genetic models of Parkinson's disease: a role for autophagy?" Neurobiol Dis **43**(1): 60-67.

Plowey, E. D., J. W. Johnson, E. Steer, W. Zhu, D. A. Eisenberg, N. M. Valentino, Y. J. Liu and C. T. Chu (2014). "Mutant LRRK2 enhances glutamatergic synapse activity and evokes excitotoxic dendrite degeneration." Biochim Biophys Acta **1842**(9): 1596-1603.

Polymeropoulos, M. H., C. Lavedan, E. Leroy, S. E. Ide, A. Dehejia, A. Dutra, B. Pike, H. Root, J. Rubenstein, R. Boyer, E. S. Stenroos, S. Chandrasekharappa, A. Athanassiadou, T. Papapetropoulos, W. G. Johnson, A. M. Lazzarini, R. C. Duvoisin, G. Di Iorio, L. I. Golbe and R. L. Nussbaum (1997). "Mutation in the alpha-synuclein gene identified in families with Parkinson's disease." Science **276**(5321): 2045-2047.

Poewe W., K. Seppi, C. M. Tanner, G. M. Halliday, P. Brundin, J. Volkmann, A. Schrag and A. E. Lang (2017). "Parkinson Disease." Nat Rev Dis Primers **3**: 17013.

Pont-Sunyer, C., A. Hotter, C. Gaig, K. Seppi, Y. Compta, R. Katzenschlager, N. Mas, D. Hofeneder, T. Brucke, A. Bayes, K. Wenzel, J. Infante, H. Zach, W. Pirker, I. J. Posada, R. Alvarez, L. Ispierto, O. De Fabregues, A. Callen, A. Palasi, M. Aguilar, M. J. Marti, F. Valldeoriola, M. Salamero, W. Poewe and E. Tolosa (2015). "The onset of

nonmotor symptoms in Parkinson's disease (the ONSET PD study)." Mov Disord **30**(2): 229-237.

Poulsen, K. T., M. P. Armanini, R. D. Klein, M. A. Hynes, H. S. Phillips and A. Rosenthal (1994). "TGF beta 2 and TGF beta 3 are potent survival factors for midbrain dopaminergic neurons." Neuron **13**(5): 1245-1252.

Pringsheim, T., N. Jette, A. Frolkis and T. D. Steeves (2014). "The prevalence of Parkinson's disease: a systematic review and meta-analysis." Mov Disord **29**(13): 1583-1590.

Pylypenko, O., A. Rak, R. Reents, A. Niculae, V. Sidorovitch, M. D. Cioaca, E. Bessolitsyna, N. H. Thoma, H. Waldmann, I. Schlichting, R. S. Goody and K. Alexandrov (2003). "Structure of Rab escort protein-1 in complex with Rab geranylgeranyltransferase." Mol Cell **11**(2): 483-494.

Qiao, C., N. Yin, H. Y. Gu, J. L. Zhu, J. H. Ding, M. Lu and G. Hu (2016). "Atp13a2 Deficiency Aggravates Astrocyte-Mediated Neuroinflammation via NLRP3 Inflammasome Activation." CNS Neurosci Ther **22**(6): 451-460.

Quach, T. T., A. M. Duchemin, V. Rogemond, M. Aguera, J. Honnorat, M. F. Belin and P. E. Kolattukudy (2004). "Involvement of collapsin response mediator proteins in the neurite extension induced by neurotrophins in dorsal root ganglion neurons." Mol Cell Neurosci **25**(3): 433-443.

Ramonet, D., J. P. Daher, B. M. Lin, K. Stafa, J. Kim, R. Banerjee, M. Westerlund, O. Pletnikova, L. Glauser, L. Yang, Y. Liu, D. A. Swing, M. F. Beal, J. C. Troncoso, J. M. McCaffery, N. A. Jenkins, N. G. Copeland, D. Galter, B. Thomas, M. K. Lee, T. M. Dawson, V. L. Dawson and D. J. Moore (2011). "Dopaminergic neuronal loss, reduced neurite complexity and autophagic abnormalities in transgenic mice expressing G2019S mutant LRRK2." PLoS One **6**(4): e18568.

Rannikko, E. H., S. S. Weber and P. J. Kahle (2015). "Exogenous alpha-synuclein induces toll-like receptor 4 dependent inflammatory responses in astrocytes." BMC Neurosci **16**: 57.

Raponi, E., F. Agenes, C. Delphin, N. Assard, J. Baudier, C. Legraverend and J. C. Deloulme (2007). "S100B expression defines a state in which GFAP-expressing cells lose their neural stem cell potential and acquire a more mature developmental stage." Glia **55**(2): 165-177.

Rappold, P. M. and K. Tieu (2010). "Astrocytes and therapeutics for Parkinson's disease." Neurotherapeutics **7**(4): 413-423.

Ray, S., S. Bender, S. Kang, R. Lin, M. A. Glicksman and M. Liu (2014). "The Parkinson disease-linked LRRK2 protein mutation I2020T stabilizes an active state conformation leading to increased kinase activity." J Biol Chem **289**(19): 13042-13053.

Razgado-Hernandez, L. F., A. J. Espadas-Alvarez, P. Reyna-Velazquez, A. Sierra-Sanchez, V. Anaya-Martinez, I. Jimenez-Estrada, M. J. Bannon, D. Martinez-Fong and J. Aceves-Ruiz (2015). "The transfection of BDNF to dopamine neurons potentiates the effect of dopamine D3 receptor agonist recovering the striatal innervation, dendritic

spines and motor behavior in an aged rat model of Parkinson's disease." PLoS One **10**(2): e0117391.

Reijnders, J. S., U. Ehrt, W. E. Weber, D. Aarsland and A. F. Leentjens (2008). "A systematic review of prevalence studies of depression in Parkinson's disease." Mov Disord **23**(2): 183-189; quiz 313.

Reinhardt, P., B. Schmid, L. F. Burbulla, D. C. Schondorf, L. Wagner, M. Glatza, S. Hoing, G. Hargus, S. A. Heck, A. Dhingra, G. Wu, S. Muller, K. Brockmann, T. Kluba, M. Maisel, R. Kruger, D. Berg, Y. Tsytsyura, C. S. Thiel, O. E. Psathaki, J. Klingauf, T. Kuhlmann, M. Klewin, H. Muller, T. Gasser, H. R. Scholer and J. Sterneckert (2013). "Genetic correction of a LRRK2 mutation in human iPSCs links parkinsonian neurodegeneration to ERK-dependent changes in gene expression." Cell Stem Cell **12**(3): 354-367.

Rhinn, M. and M. Brand (2001). "The midbrain--hindbrain boundary organizer." Curr Opin Neurobiol **11**(1): 34-42.

Ristevski, S. (2005). "Making better transgenic models: conditional, temporal, and spatial approaches." Mol Biotechnol **29**(2): 153-163.

Ritchie, M. E., B. Phipson, D. Wu, Y. Hu, C. W. Law, W. Shi and G. K. Smyth (2015). "limma powers differential expression analyses for RNA-sequencing and microarray studies." Nucleic Acids Res **43**(7): e47.

Robakis, D. and S. Fahn (2015). "Defining the Role of the Monoamine Oxidase-B Inhibitors for Parkinson's Disease." CNS Drugs **29**(6): 433-441.

Ross, O. A., Y. R. Wu, M. C. Lee, M. Funayama, M. L. Chen, A. I. Soto, I. F. Mata, G. J. Lee-Chen, C. M. Chen, M. Tang, Y. Zhao, N. Hattori, M. J. Farrer, E. K. Tan and R. M. Wu (2008). "Analysis of Lrrk2 R1628P as a risk factor for Parkinson's disease." Ann Neurol **64**(1): 88-92.

Ross, P. L., Y. N. Huang, J. N. Marchese, B. Williamson, K. Parker, S. Hattan, N. Khainovski, S. Pillai, S. Dey, S. Daniels, S. Purkayastha, P. Juhasz, S. Martin, M. Bartlet-Jones, F. He, A. Jacobson and D. J. Pappin (2004). "Multiplexed protein quantitation in Saccharomyces cerevisiae using amine-reactive isobaric tagging reagents." Mol Cell Proteomics **3**(12): 1154-1169.

Roy, N. S., C. Cleren, S. K. Singh, L. Yang, M. F. Beal and S. A. Goldman (2006). "Functional engraftment of human ES cell-derived dopaminergic neurons enriched by coculture with telomerase-immortalized midbrain astrocytes." Nat Med **12**(11): 1259-1268.

Roybon, L., N. J. Lamas, A. D. Garcia, E. J. Yang, R. Sattler, V. J. Lewis, Y. A. Kim, C. A. Kachel, J. D. Rothstein, S. Przedborski, H. Wichterle and C. E. Henderson (2013). "Human stem cell-derived spinal cord astrocytes with defined mature or reactive phenotypes." Cell Rep **4**(5): 1035-1048.

Saez-Atienzar, S., L. Bonet-Ponce, J. R. Blesa, F. J. Romero, M. P. Murphy, J. Jordan and M. F. Galindo (2014). "The LRRK2 inhibitor GSK2578215A induces protective autophagy in SH-SY5Y cells: involvement of Drp-1-mediated mitochondrial fission and mitochondrial-derived ROS signaling." Cell Death Dis **5**: e1368.

Saha, S., L. Liu-Yesucevitz and B. Wolozin (2014). "Regulation of autophagy by LRRK2 in Caenorhabditis elegans." Neurodegener Dis **13**(2-3): 110-113.

Saiki, S., S. Sato and N. Hattori (2012). "Molecular pathogenesis of Parkinson's disease: update." J Neurol Neurosurg Psychiatry **83**(4): 430-436.

Samuels, B. A., Y. P. Hsueh, T. Shu, H. Liang, H. C. Tseng, C. J. Hong, S. C. Su, J. Volker, R. L. Neve, D. T. Yue and L. H. Tsai (2007). "Cdk5 promotes synaptogenesis by regulating the subcellular distribution of the MAGUK family member CASK." Neuron **56**(5): 823-837.

Sanalkumar, R., S. Vidyanand, C. Lalitha Indulekha and J. James (2010). "Neuronal vs. glial fate of embryonic stem cell-derived neural progenitors (ES-NPs) is determined by FGF2/EGF during proliferation." J Mol Neurosci **42**(1): 17-27.

Sanchez-Danes, A., Y. Richaud-Patin, I. Carballo-Carbajal, S. Jimenez-Delgado, C. Caig, S. Mora, C. Di Guglielmo, M. Ezquerra, B. Patel, A. Giralt, J. M. Canals, M. Memo, J. Alberch, J. Lopez-Barneo, M. Vila, A. M. Cuervo, E. Tolosa, A. Consiglio and A. Raya (2012a). "Disease-specific phenotypes in dopamine neurons from human iPS-based models of genetic and sporadic Parkinson's disease." EMBO Mol Med **4**(5): 380-395.

Sanchez-Danes, A., A. Consiglio, Y. Richaud, I. Rodriguez-Piza, B. Dehay, M. Edel, J. Bove, M. Memo, M. Vila, A. Raya and J. C. Izpisua Belmonte (2012b). "Efficient generation of A9 midbrain dopaminergic neurons by lentiviral delivery of LMX1A in human embryonic stem cells and induced pluripotent stem cells." Hum Gene Ther **23**(1): 56-69.

Sanders, L. H., J. Laganiere, O. Cooper, S. K. Mak, B. J. Vu, Y. A. Huang, D. E. Paschon, M. Vangipuram, R. Sundararajan, F. D. Urnov, J. W. Langston, P. D. Gregory, H. S. Zhang, J. T. Greenamyre, O. Isacson and B. Schule (2014). "LRRK2 mutations cause mitochondrial DNA damage in iPSC-derived neural cells from Parkinson's disease patients: reversal by gene correction." Neurobiol Dis **62**: 381-386.

Sandor, C., P. Robertson, C. Lang, A. Heger, H. Booth, J. Vowles, L. Witty, R. Bowden, M. Hu, S. A. Cowley, R. Wade-Martins and C. Webber (2017). "Transcriptomic profiling of purified patient-derived dopamine neurons identifies convergent perturbations and therapeutics for Parkinson's disease." Hum Mol Genet **26**(3): 552-566.

Sann, S., Z. Wang, H. Brown and Y. Jin (2009). "Roles of endosomal trafficking in neurite outgrowth and guidance." Trends Cell Biol **19**(7): 317-324.

Satake, W., Y. Nakabayashi, I. Mizuta, Y. Hirota, C. Ito, M. Kubo, T. Kawaguchi, T. Tsunoda, M. Watanabe, A. Takeda, H. Tomiyama, K. Nakashima, K. Hasegawa, F. Obata, T. Yoshikawa, H. Kawakami, S. Sakoda, M. Yamamoto, N. Hattori, M. Murata, Y. Nakamura and T. Toda (2009). "Genome-wide association study identifies common variants at four loci as genetic risk factors for Parkinson's disease." Nat Genet **41**(12): 1303-1307.

Sattler, R., M. P. Charlton, M. Hafner and M. Tymianski (1998). "Distinct influx pathways, not calcium load, determine neuronal vulnerability to calcium neurotoxicity." J Neurochem **71**(6): 2349-2364.

Scaduto, R. C., Jr. and L. W. Grotyohann (1999). "Measurement of mitochondrial membrane potential using fluorescent rhodamine derivatives." Biophys J **76**(1 Pt 1): 469-477.

Schaar, D. G., B. A. Sieber, C. F. Dreyfus and I. B. Black (1993). "Regional and cell-specific expression of GDNF in rat brain." Exp Neurol **124**(2): 368-371.

Schmidt, S., B. Linnartz, S. Mendritzki, T. Sczepan, M. Lubbert, C. C. Stichel and H. Lubbert (2011). "Genetic mouse models for Parkinson's disease display severe pathology in glial cell mitochondria." Hum Mol Genet **20**(6): 1197-1211.

Schousboe, A., G. Svenneby and L. Hertz (1977). "Uptake and metabolism of glutamate in astrocytes cultured from dissociated mouse brain hemispheres." J Neurochem **29**(6): 999-1005.

Schreij, A. M. A., M. Chaineau, W. Ruan, S. Lin, P. A. Barker, E. A. Fon and P. S. McPherson (2015). "LRRK2 localizes to endosomes and interacts with clathrin-light chains to limit Rac1 activation." EMBO Rep **16**(1): 79-86.

Seki, T., S. Yuasa, M. Oda, T. Egashira, K. Yae, D. Kusumoto, H. Nakata, S. Tohyama, H. Hashimoto, M. Kodaira, Y. Okada, H. Seimiya, N. Fusaki, M. Hasegawa and K. Fukuda (2010). "Generation of induced pluripotent stem cells from human terminally differentiated circulating T cells." Cell Stem Cell **7**(1): 11-14.

Sen, S., P. J. Webber and A. B. West (2009). "Dependence of leucine-rich repeat kinase 2 (LRRK2) kinase activity on dimerization." J Biol Chem **284**(52): 36346-36356.

Sepulveda, B., R. Mesias, X. Li, Z. Yue and D. L. Benson (2013). "Short- and long-term effects of LRRK2 on axon and dendrite growth." PLoS One **8**(4): e61986.

Serio, A., B. Bilican, S. J. Barmada, D. M. Ando, C. Zhao, R. Siller, K. Burr, G. Haghi, D. Story, A. L. Nishimura, M. A. Carrasco, H. P. Phatnani, C. Shum, I. Wilmut, T. Maniatis, C. E. Shaw, S. Finkbeiner and S. Chandran (2013). "Astrocyte pathology and the absence of non-cell autonomy in an induced pluripotent stem cell model of TDP-43 proteinopathy." Proc Natl Acad Sci U S A **110**(12): 4697-4702.

Serra-Pages, C., M. Streuli and Q. G. Medley (2005). "Liprin phosphorylation regulates binding to LAR: evidence for liprin autophosphorylation." Biochemistry **44**(48): 15715-15724.

Serrat, R., S. Mirra, J. Figueiro-Silva, E. Navas-Perez, M. Quevedo, G. Lopez-Domenech, P. Podlesniy, F. Ulloa, J. Garcia-Fernandez, R. Trullas and E. Soriano (2014). "The Armc10/SVH gene: genome context, regulation of mitochondrial dynamics and protection against Abeta-induced mitochondrial fragmentation." Cell Death Dis **5**: e1163.

Shaltouki, A., J. Peng, Q. Liu, M. S. Rao and X. Zeng (2013). "Efficient generation of astrocytes from human pluripotent stem cells in defined conditions." Stem Cells **31**(5): 941-952.

Shanley, M. R., D. Hawley, S. Leung, N. F. Zaidi, R. Dave, K. A. Schlosser, R. Bandopadhyay, S. A. Gerber and M. Liu (2015). "LRRK2 Facilitates tau Phosphorylation through Strong Interaction with tau and cdk5." Biochemistry **54**(33): 5198-5208.

Sharon, R., I. Bar-Joseph, M. P. Frosch, D. M. Walsh, J. A. Hamilton and D. J. Selkoe (2003). "The formation of highly soluble oligomers of alpha-synuclein is regulated by fatty acids and enhanced in Parkinson's disease." Neuron **37**(4): 583-595.

Shehadeh, L. A., K. Yu, L. Wang, A. Guevara, C. Singer, J. Vance and S. Papapetropoulos (2010). "SRRM2, a potential blood biomarker revealing high alternative splicing in Parkinson's disease." PLoS One **5**(2): e9104.

Shen, Q., Y. Wang, J. T. Dimos, C. A. Fasano, T. N. Phoenix, I. R. Lemischka, N. B. Ivanova, S. Stifani, E. E. Morrisey and S. Temple (2006). "The timing of cortical neurogenesis is encoded within lineages of individual progenitor cells." Nat Neurosci **9**(6): 743-751.

Sholl, D. A. (1953). "Dendritic organization in the neurons of the visual and motor cortices of the cat." J Anat **87**(4): 387-406.

Sholl, D. A. (1956). "The measurable parameters of the cerebral cortex and their significance in its organization." Prog Neurobiol(2): 324-333.

Shu, Y., J. Ming, P. Zhang, Q. Wang, F. Jiao and B. Tian (2016). "Parkinson-Related LRRK2 Mutation R1628P Enables Cdk5 Phosphorylation of LRRK2 and Upregulates Its Kinase Activity." PLoS One **11**(3): e0149739.

Sibilia, M., J. P. Steinbach, L. Stingl, A. Aguzzi and E. F. Wagner (1998). "A strain-independent postnatal neurodegeneration in mice lacking the EGF receptor." EMBO J **17**(3): 719-731.

Siller R., S. Greenhough, I. H. Park and G. J. Sullivan (2013). "Modelling human disease with pluripotent stem cells." Curr Gene Ther **13**(2): 99-110.

Simon-Sanchez, J., C. Schulte, J. M. Bras, M. Sharma, J. R. Gibbs, D. Berg, C. Paisan-Ruiz, P. Lichtner, S. W. Scholz, D. G. Hernandez, R. Kruger, M. Federoff, C. Klein, A. Goate, J. Perlmutter, M. Bonin, M. A. Nalls, T. Illig, C. Gieger, H. Houlden, M. Steffens, M. S. Okun, B. A. Racette, M. R. Cookson, K. D. Foote, H. H. Fernandez, B. J. Traynor, S. Schreiber, S. Arepalli, R. Zonozi, K. Gwinn, M. van der Brug, G. Lopez, S. J. Chanock, A. Schatzkin, Y. Park, A. Hollenbeck, J. Gao, X. Huang, N. W. Wood, D. Lorenz, G. Deuschl, H. Chen, O. Riess, J. A. Hardy, A. B. Singleton and T. Gasser (2009). "Genome-wide association study reveals genetic risk underlying Parkinson's disease." Nat Genet **41**(12): 1308-1312.

Simon, H. H., H. Saueressig, W. Wurst, M. D. Goulding and D. D. O'Leary (2001). "Fate of midbrain dopaminergic neurons controlled by the engrailed genes." J Neurosci **21**(9): 3126-3134.

Sloan, M., J. Alegre-Abarrategui, D. Potgieter, A. K. Kaufmann, R. Exley, T. Deltheil, S. Threlfell, N. Connor-Robson, K. Brimblecombe, R. Wallings, M. Cioroch, D. M. Bannerman, J. P. Bolam, P. J. Magill, S. J. Cragg, P. D. Dodson and R. Wade-Martins (2016). "LRRK2 BAC transgenic rats develop progressive, L-DOPA-responsive motor impairment, and deficits in dopamine circuit function." Hum Mol Genet **25**(5): 951-963.

Smith, J. R., L. Vallier, G. Lupo, M. Alexander, W. A. Harris and R. A. Pedersen (2008). "Inhibition of Activin/Nodal signaling promotes specification of human embryonic stem cells into neuroectoderm." Dev Biol **313**(1): 107-117.

Sofroniew, M. V. and H. V. Vinters (2010). "Astrocytes: biology and pathology." Acta Neuropathol **119**(1): 7-35.

Solano, R. M., M. J. Casarejos, J. Menendez-Cuervo, J. A. Rodriguez-Navarro, J. Garcia de Yebenes and M. A. Mena (2008). "Glial dysfunction in parkin null mice: effects of aging." J Neurosci **28**(3): 598-611.

Solano, R. M., J. Menendez, M. J. Casarejos, J. A. Rodriguez-Navarro, J. Garcia de Yebenes and M. A. Mena (2006). "Midbrain neuronal cultures from parkin mutant mice are resistant to nitric oxide-induced toxicity." Neuropharmacology **51**(2): 327-340.

Spangler, S. A. and C. C. Hoogenraad (2007). "Liprin-alpha proteins: scaffold molecules for synapse maturation." Biochem Soc Trans **35**(Pt 5): 1278-1282.

Spillantini, M. G., R. A. Crowther, R. Jakes, M. Hasegawa and M. Goedert (1998). "alpha-Synuclein in filamentous inclusions of Lewy bodies from Parkinson's disease and dementia with lewy bodies." Proc Natl Acad Sci U S A **95**(11): 6469-6473.

Stamer, K., R. Vogel, E. Thies, E. Mandelkow and E. M. Mandelkow (2002). "Tau blocks traffic of organelles, neurofilaments, and APP vesicles in neurons and enhances oxidative stress." J Cell Biol **156**(6): 1051-1063.

Staudt, C., E. Puissant and M. Boonen (2016). "Subcellular Trafficking of Mammalian Lysosomal Proteins: An Extended View." Int J Mol Sci **18**(1).

Steen, H. and M. Mann (2004). "The ABC's (and XYZ's) of peptide sequencing." Nat Rev Mol Cell Biol **5**(9): 699-711.

Steger, M., F. Tonelli, G. Ito, P. Davies, M. Trost, M. Vetter, S. Wachter, E. Lorentzen, G. Duddy, S. Wilson, M. A. Baptista, B. K. Fiske, M. J. Fell, J. A. Morrow, A. D. Reith, D. R. Alessi and M. Mann (2016). "Phosphoproteomics reveals that Parkinson's disease kinase LRRK2 regulates a subset of Rab GTPases." Elife **5**.

Stenmark, H. (2009). "Rab GTPases as coordinators of vesicle traffic." Nat Rev Mol Cell Biol **10**(8): 513-525.

Stipursky, J. and F. C. Gomes (2007). "TGF-beta1/SMAD signaling induces astrocyte fate commitment in vitro: implications for radial glia development." Glia **55**(10): 1023-1033.

Strokin, M., M. Sergeeva and G. Reiser (2011). "Proinflammatory treatment of astrocytes with lipopolysaccharide results in augmented Ca2+ signaling through increased expression of via phospholipase A2 (iPLA2)." Am J Physiol Cell Physiol **300**(3): C542-549.

Su, Y. C. and X. Qi (2013). "Inhibition of excessive mitochondrial fission reduced aberrant autophagy and neuronal damage caused by LRRK2 G2019S mutation." Hum Mol Genet **22**(22): 4545-4561.

Sudhof, T. C. (2004). "The synaptic vesicle cycle." Annu Rev Neurosci **27**: 509-547.

Sulzer, D. and D. J. Surmeier (2013). "Neuronal vulnerability, pathogenesis, and Parkinson's disease." Mov Disord **28**(6): 715-724.

Surmacz, B., H. Fox, A. Gutteridge, P. Fish, S. Lubitz and P. Whiting (2012). "Directing differentiation of human embryonic stem cells toward anterior neural ectoderm using small molecules." Stem Cells **30**(9): 1875-1884.

Takahashi, K., K. Tanabe, M. Ohnuki, M. Narita, T. Ichisaka, K. Tomoda and S. Yamanaka (2007). "Induction of pluripotent stem cells from adult human fibroblasts by defined factors." Cell **131**(5): 861-872.

Takahashi, K. and S. Yamanaka (2006). "Induction of pluripotent stem cells from mouse embryonic and adult fibroblast cultures by defined factors." Cell **126**(4): 663-676.

Takakusaki, K. and S. T. Kitai (1997). "Ionic mechanisms involved in the spontaneous firing of tegmental pedunculopontine nucleus neurons of the rat." Neuroscience **78**(3): 771-794.

Tang, Q. and M. Edidin (2001). "Vesicle trafficking and cell surface membrane patchiness." Biophys J **81**(1): 196-203.

Tereshchenko, J., A. Maddalena, M. Bahr and S. Kugler (2014). "Pharmacologically controlled, discontinuous GDNF gene therapy restores motor function in a rat model of Parkinson's disease." Neurobiol Dis **65**: 35-42.

Thirstrup, K., J. C. Dachsel, F. S. Oppermann, D. S. Williamson, G. P. Smith, K. Fog and K. V. Christensen (2017). "Selective LRRK2 kinase inhibition reduces phosphorylation of endogenous Rab10 and Rab12 in human peripheral mononuclear blood cells." Sci Rep **7**(1): 10300.

Thompson, A., J. Schafer, K. Kuhn, S. Kienle, J. Schwarz, G. Schmidt, T. Neumann, R. Johnstone, A. K. Mohammed and C. Hamon (2003). "Tandem mass tags: a novel quantification strategy for comparative analysis of complex protein mixtures by MS/MS." Anal Chem **75**(8): 1895-1904.

Thomson, J. A., J. Itskovitz-Eldor, S. S. Shapiro, M. A. Waknitz, J. J. Swiergiel, V. S. Marshall and J. M. Jones (1998). "Embryonic stem cell lines derived from human blastocysts." Science **282**(5391): 1145-1147.

Tokuda, T., M. M. Qureshi, M. T. Ardah, S. Varghese, S. A. Shehab, T. Kasai, N. Ishigami, A. Tamaoka, M. Nakagawa and O. M. El-Agnaf (2010). "Detection of elevated levels of alpha-synuclein oligomers in CSF from patients with Parkinson disease." Neurology **75**(20): 1766-1772.

Torii, T., Y. Miyamoto, K. Tago, K. Sango, K. Nakamura, A. Sanbe, A. Tanoue and J. Yamauchi (2014). "Arf6 guanine nucleotide exchange factor cytohesin-2 binds to CCDC120 and is transported along neurites to mediate neurite growth." J Biol Chem **289**(49): 33887-33903.

Tropepe, V., M. Sibilia, B. G. Ciruna, J. Rossant, E. F. Wagner and D. van der Kooy (1999). "Distinct neural stem cells proliferate in response to EGF and FGF in the developing mouse telencephalon." Dev Biol **208**(1): 166-188.

Tsai, H. H., H. Li, L. C. Fuentealba, A. V. Molofsky, R. Taveira-Marques, H. Zhuang, A. Tenney, A. T. Murnen, S. P. Fancy, F. Merkle, N. Kessaris, A. Alvarez-Buylla, W. D. Richardson and D. H. Rowitch (2012). "Regional astrocyte allocation regulates CNS synaptogenesis and repair." Science **337**(6092): 358-362.

van der Mark, M., M. Brouwer, H. Kromhout, P. Nijssen, A. Huss and R. Vermeulen (2012). "Is pesticide use related to Parkinson disease? Some clues to heterogeneity in study results." Environ Health Perspect **120**(3): 340-347.

Vangipuram, M., D. Ting, S. Kim, R. Diaz and B. Schule (2013). "Skin punch biopsy explant culture for derivation of primary human fibroblasts." J Vis Exp(77): e3779.

Vermilyea, S. C. and M. E. Emborg (2015). "alpha-Synuclein and nonhuman primate models of Parkinson's disease." J Neurosci Methods **255**: 38-51.

Vitner, E. B., H. Dekel, H. Zigdon, T. Shachar, T. Farfel-Becker, R. Eilam, S. Karlsson and A. H. Futerman (2010). "Altered expression and distribution of cathepsins in neuronopathic forms of Gaucher disease and in other sphingolipidoses." Hum Mol Genet **19**(18): 3583-3590.

von Stechow, L., C. Francavilla and J. V. Olsen (2015). "Recent findings and technological advances in phosphoproteomics for cells and tissues." Expert Rev Proteomics **12**(5): 469-487.

Waak, J., S. S. Weber, A. Waldenmaier, K. Gorner, M. Alunni-Fabbroni, H. Schell, D. Vogt-Weisenhorn, T. T. Pham, V. Reumers, V. Baekelandt, W. Wurst and P. J. Kahle (2009). "Regulation of astrocyte inflammatory responses by the Parkinson's disease-associated gene DJ-1." FASEB J **23**(8): 2478-2489.

Wang, X., M. H. Yan, H. Fujioka, J. Liu, A. Wilson-Delfosse, S. G. Chen, G. Perry, G. Casadesus and X. Zhu (2012). "LRRK2 regulates mitochondrial dynamics and function through direct interaction with DLP1." Hum Mol Genet **21**(9): 1931-1944.

Waschbusch, D., H. Michels, S. Strassheim, E. Ossendorf, D. Kessler, C. J. Gloeckner and A. Barnekow (2014). "LRRK2 transport is regulated by its novel interacting partner Rab32." PLoS One **9**(10): e111632.

Watanabe, K., M. Ueno, D. Kamiya, A. Nishiyama, M. Matsumura, T. Wataya, J. B. Takahashi, S. Nishikawa, S. Nishikawa, K. Muguruma and Y. Sasai (2007). "A ROCK inhibitor permits survival of dissociated human embryonic stem cells." Nat Biotechnol **25**(6): 681-686.

Webber, P. J., A. D. Smith, S. Sen, M. B. Renfrow, J. A. Mobley and A. B. West (2011). "Autophosphorylation in the leucine-rich repeat kinase 2 (LRRK2) GTPase domain modifies kinase and GTP-binding activities." J Mol Biol **412**(1): 94-110.

Wichmann, T. and M. R. DeLong (2016). "Deep Brain Stimulation for Movement Disorders of Basal Ganglia Origin: Restoring Function or Functionality?" Neurotherapeutics **13**(2): 264-283.

Williams-Gray, C. H., T. Foltynie, S. J. Lewis and R. A. Barker (2006). "Cognitive deficits and psychosis in Parkinson's disease: a review of pathophysiology and therapeutic options." CNS Drugs **20**(6): 477-505.

Williams, J. T., R. A. North, S. A. Shefner, S. Nishi and T. M. Egan (1984). "Membrane properties of rat locus coeruleus neurones." Neuroscience **13**(1): 137-156.

Wilson, L. and M. Maden (2005). "The mechanisms of dorsoventral patterning in the vertebrate neural tube." Dev Biol **282**(1): 1-13.

Winner, B., H. L. Melrose, C. Zhao, K. M. Hinkle, M. Yue, C. Kent, A. T. Braithwaite, S. Ogholikhan, R. Aigner, J. Winkler, M. J. Farrer and F. H. Gage (2011). "Adult neurogenesis and neurite outgrowth are impaired in LRRK2 G2019S mice." Neurobiol Dis **41**(3): 706-716.

Wood, B. H., J. A. Bilclough, A. Bowron and R. W. Walker (2002). "Incidence and prediction of falls in Parkinson's disease: a prospective multidisciplinary study." J Neurol Neurosurg Psychiatry **72**(6): 721-725.

Wu, C. K. and A. D. Hohler (2015). "Management of orthostatic hypotension in patients with Parkinson's disease." Pract Neurol **15**(2): 100-104.

Wyszynski, M., E. Kim, A. W. Dunah, M. Passafaro, J. G. Valtschanoff, C. Serra-Pages, M. Streuli, R. J. Weinberg and M. Sheng (2002). "Interaction between GRIP and liprin-alpha/SYD2 is required for AMPA receptor targeting." Neuron **34**(1): 39-52.

Xie, M. J., H. Yagi, K. Kuroda, C. C. Wang, M. Komada, H. Zhao, A. Sakakibara, T. Miyata, K. Nagata, Y. Oka, T. Iguchi and M. Sato (2013). "WAVE2-Abi2 complex controls growth cone activity and regulates the multipolar-bipolar transition as well as the initiation of glia-guided migration." Cereb Cortex **23**(6): 1410-1423.

Xiong, Y., C. E. Coombes, A. Kilaru, X. Li, A. D. Gitler, W. J. Bowers, V. L. Dawson, T. M. Dawson and D. J. Moore (2010). "GTPase activity plays a key role in the pathobiology of LRRK2." PLoS Genet **6**(4): e1000902.

Yakhine-Diop, S. M., J. M. Bravo-San Pedro, R. Gomez-Sanchez, E. Pizarro-Estrella, M. Rodriguez-Arribas, V. Climent, A. Aiastui, A. Lopez de Munain, J. M. Fuentes and R. A. Gonzalez-Polo (2014). "G2019S LRRK2 mutant fibroblasts from Parkinson's disease patients show increased sensitivity to neurotoxin 1-methyl-4-phenylpyridinium dependent of autophagy." Toxicology **324**: 1-9.

Yamada, K., N. Nomura, A. Yamano, Y. Yamada and N. Wakamatsu (2012). "Identification and characterization of splicing variants of PLEKHA5 (Plekha5) during brain development." Gene **492**(1): 270-275.

Yamashita, N., A. Morita, Y. Uchida, F. Nakamura, H. Usui, T. Ohshima, M. Taniguchi, J. Honnorat, N. Thomasset, K. Takei, T. Takahashi, P. Kolattukudy and Y. Goshima (2007). "Regulation of spine development by semaphorin3A through cyclin-dependent kinase 5 phosphorylation of collapsin response mediator protein 1." J Neurosci **27**(46): 12546-12554.

Yamazoe, H., M. Kobori, Y. Murakami, K. Yano, M. Satoh, K. Mizuseki, Y. Sasai and H. Iwata (2006). "One-step induction of neurons from mouse embryonic stem cells in serum-free media containing vitamin B12 and heparin." Cell Transplant **15**(2): 135-145.

Yan, C. H., M. Levesque, S. Claxton, R. L. Johnson and S. L. Ang (2011). "Lmx1a and lmx1b function cooperatively to regulate proliferation, specification, and differentiation of midbrain dopaminergic progenitors." J Neurosci **31**(35): 12413-12425.

Yan, J., L. Studer and R. D. McKay (2001). "Ascorbic acid increases the yield of dopaminergic neurons derived from basic fibroblast growth factor expanded mesencephalic precursors." J Neurochem **76**(1): 307-311.

Yang, Y., M. Wei, Y. Xiong, X. Du, S. Zhu, L. Yang, C. Zhang and J. J. Liu (2015). "Endophilin A1 regulates dendritic spine morphogenesis and stability through interaction with p140Cap." Cell Res **25**(4): 496-516.

Yeger-Lotem E. and R. Sharan 2015. "Human protein interaction networks across tissues and diseases." Front Genet **6**: 257.

Yue, M., K. M. Hinkle, P. Davies, E. Trushina, F. C. Fiesel, T. A. Christenson, A. S. Schroeder, L. Zhang, E. Bowles, B. Behrouz, S. J. Lincoln, J. E. Beevers, A. J. Milnerwood, A. Kurti, P. J. McLean, J. D. Fryer, W. Springer, D. W. Dickson, M. J. Farrer and H. L. Melrose (2015). "Progressive dopaminergic alterations and mitochondrial abnormalities in LRRK2 G2019S knock-in mice." Neurobiol Dis **78**: 172-195.

Yun, H. J., H. Kim, I. Ga, H. Oh, D. H. Ho, J. Kim, H. Seo, I. Son and W. Seol (2015). "An early endosome regulator, Rab5b, is an LRRK2 kinase substrate." J Biochem **157**(6): 485-495.

Yun, H. J., J. Park, D. H. Ho, H. Kim, C. H. Kim, H. Oh, I. Ga, H. Seo, S. Chang, I. Son and W. Seol (2013). "LRRK2 phosphorylates Snapin and inhibits interaction of Snapin with SNAP-25." Exp Mol Med **45**: e36.

Zabetian, C. P., A. Samii, A. D. Mosley, J. W. Roberts, B. C. Leis, D. Yearout, W. H. Raskind and A. Griffith (2005). "A clinic-based study of the LRRK2 gene in Parkinson disease yields new mutations." Neurology **65**(5): 741-744.

Zeng, X., J. Cai, J. Chen, Y. Luo, Z. B. You, E. Fotter, Y. Wang, B. Harvey, T. Miura, C. Backman, G. J. Chen, M. S. Rao and W. J. Freed (2004). "Dopaminergic differentiation of human embryonic stem cells." Stem Cells **22**(6): 925-940.

Zhang, D., H. Jiang and J. Xie (2014). "Alcohol intake and risk of Parkinson's disease: a meta-analysis of observational studies." Mov Disord **29**(6): 819-822.

Zhang, H., C. Duan and H. Yang (2015). "Defective autophagy in Parkinson's disease: lessons from genetics." Mol Neurobiol **51**(1): 89-104.

Zhang, Y., K. Chen, S. A. Sloan, M. L. Bennett, A. R. Scholze, S. O'Keeffe, H. P. Phatnani, P. Guarnieri, C. Caneda, N. Ruderisch, S. Deng, S. A. Liddelow, C. Zhang, R. Daneman, T. Maniatis, B. A. Barres and J. Q. Wu (2014). "An RNA-sequencing transcriptome and splicing database of glia, neurons, and vascular cells of the cerebral cortex." J Neurosci **34**(36): 11929-11947.

Zhang, Y., S. A. Sloan, L. E. Clarke, C. Caneda, C. A. Plaza, P. D. Blumenthal, H. Vogel, G. K. Steinberg, M. S. Edwards, G. Li, J. A. Duncan, 3rd, S. H. Cheshier, L. M. Shuer, E. F. Chang, G. A. Grant, M. G. Gephart and B. A. Barres (2016). "Purification and Characterization of Progenitor and Mature Human Astrocytes Reveals Transcriptional and Functional Differences with Mouse." Neuron **89**(1): 37-53.

Zhong, S. C., X. Luo, X. S. Chen, Q. Y. Cai, J. Liu, X. H. Chen and Z. X. Yao (2010). "Expression and subcellular location of alpha-synuclein during mouse-embryonic development." Cell Mol Neurobiol **30**(3): 469-482.

Zhou, W. and C. R. Freed (2009). "Adenoviral gene delivery can reprogram human fibroblasts to induced pluripotent stem cells." Stem Cells **27**(11): 2667-2674.

Zhu, Y., C. Wang, M. Yu, J. Cui, L. Liu and Z. Xu (2013). "ULK1 and JNK are involved in mitophagy incurred by LRRK2 G2019S expression." Protein Cell **4**(9): 711-721.

Zimprich, A., S. Biskup, P. Leitner, P. Lichtner, M. Farrer, S. Lincoln, J. Kachergus, M. Hulihan, R. J. Uitti, D. B. Calne, A. J. Stoessl, R. F. Pfeiffer, N. Patenge, I. C. Carbajal, P. Vieregge, F. Asmus, B. Muller-Myhsok, D. W. Dickson, T. Meitinger, T. M. Strom, Z. K. Wszolek and T. Gasser (2004). "Mutations in LRRK2 cause autosomal-dominant parkinsonism with pleomorphic pathology." Neuron **44**(4): 601-607.

Appendix

Appendix (i)

All iPSC lines were previously genotyped by staff at the Oxford Martin Stem Cell Facility (University of Oxford). Assays to confirm genotyping were conducted for the LRRK2-G2019S and -R1441C mutations in at least one iPSC clone per patient. DNA was extracted and then amplified by PCR, before digestion with a restriction enzyme, then agarose gel electrophoresis. In both assays, two bands are detected on the gel when the mutation is absent, and a third band is detected when the mutation is present.

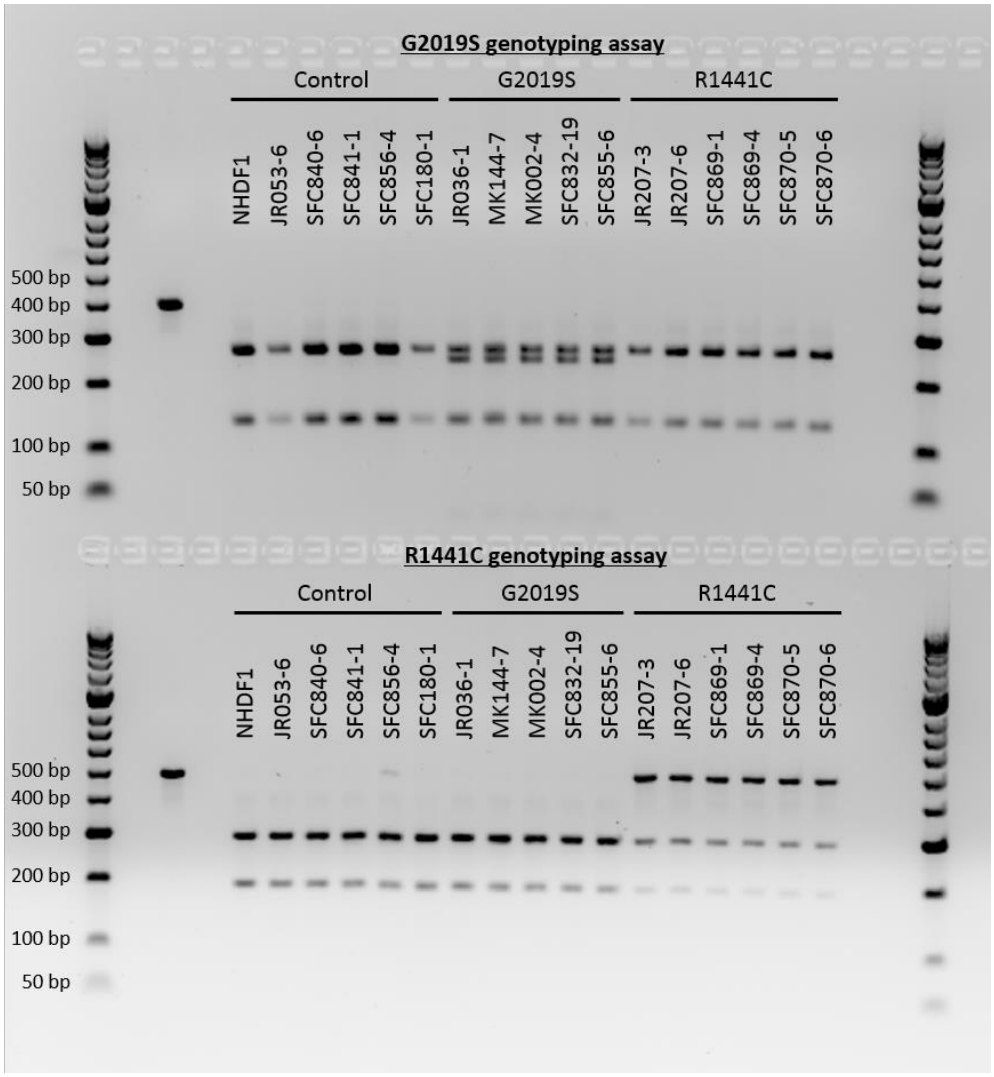

Appendix (ii)

Significantly differentially expressed pathways (p.adj<0.05) as identified by EGSEA analysis of the integrated omics dataset. p-values were adjusted for false-discovery rate. FC=fold change. Direction refers to the predicted direction of change of the pathway, down=downregulation of pathway, up=upregulation of pathway.

EGSEA Pathway	*p*.value	*p*.adj	avg.logFC	Direction
hsa04144 Endocytosis	6.32E-11	8.85E-09	5.15E-01	Down
hsa04360 Axon guidance	4.86E-11	8.85E-09	5.01E-01	Down
hsa05100 Bacterial invasion of epithelial cells	1.62E-09	1.51E-07	5.14E-01	Down
hsa03010 Ribosome	2.65E-09	1.85E-07	2.66E-01	Up
hsa04062 Chemokine signaling pathway	6.61E-07	2.06E-05	5.35E-01	Down
hsa04530 Tight junction	4.09E-07	2.06E-05	5.62E-01	Down
hsa04660 T cell receptor signaling pathway	6.31E-07	2.06E-05	5.97E-01	Down
hsa04728 Dopaminergic synapse	5.63E-07	2.06E-05	5.02E-01	Down
hsa05161 Hepatitis B	5.60E-07	2.06E-05	5.59E-01	Down
hsa04261 Adrenergic signaling in cardiomyocytes	9.48E-07	2.65E-05	5.34E-01	Down
hsa04666 Fc gamma R-mediated phagocytosis	1.71E-06	4.35E-05	5.71E-01	Down
hsa04520 Adherens junction	2.54E-06	5.94E-05	5.01E-01	Down
hsa04014 Ras signaling pathway	2.99E-06	6.34E-05	5.76E-01	Down
hsa04510 Focal adhesion	3.17E-06	6.34E-05	6.21E-01	Down
hsa04810 Regulation of actin cytoskeleton	4.18E-06	7.80E-05	4.96E-01	Down
hsa04725 Cholinergic synapse	5.26E-06	9.21E-05	5.57E-01	Down
hsa04010 MAPK signaling pathway	6.48E-06	1.07E-04	5.77E-01	Down
hsa05132 Salmonella infection	9.37E-06	1.46E-04	4.63E-01	Down
hsa04670 Leukocyte transendothelial migration	9.92E-06	1.46E-04	7.00E-01	Down
hsa04722 Neurotrophin signaling pathway	1.25E-05	1.75E-04	4.28E-01	Down
hsa04921 Oxytocin signaling pathway	1.62E-05	2.16E-04	5.51E-01	Down
hsa05203 Viral carcinogenesis	1.98E-05	2.52E-04	5.72E-01	Down
hsa04664 Fc epsilon RI signaling pathway	3.12E-05	3.79E-04	6.07E-01	Down
hsa04015 Rap1 signaling pathway	3.42E-05	3.96E-04	5.80E-01	Down
hsa04662 B cell receptor signaling pathway	3.53E-05	3.96E-04	5.84E-01	Down
hsa05210 Colorectal cancer	4.59E-05	4.95E-04	4.90E-01	Down
hsa05200 Pathways in cancer	4.92E-05	5.10E-04	5.73E-01	Down
hsa05205 Proteoglycans in cancer	6.17E-05	6.17E-04	5.54E-01	Up
hsa05213 Endometrial cancer	8.07E-05	7.79E-04	4.79E-01	Down
hsa04390 Hippo signaling pathway	9.75E-05	9.10E-04	6.01E-01	Down
hsa04911 Insulin secretion	1.32E-04	1.19E-03	5.48E-01	Down
hsa04919 Thyroid hormone signaling pathway	1.47E-04	1.29E-03	5.08E-01	Down
hsa05160 Hepatitis C	1.55E-04	1.31E-03	6.20E-01	Up
hsa04727 GABAergic synapse	1.68E-04	1.34E-03	5.77E-01	Down
hsa04960 Aldosterone-regulated sodium reabsorption	1.67E-04	1.34E-03	6.99E-01	Down
hsa04151 PI3K-Akt signaling pathway	1.87E-04	1.45E-03	6.52E-01	Down
hsa04724 Glutamatergic synapse	2.08E-04	1.57E-03	5.07E-01	Down
hsa04012 ErbB signaling pathway	2.29E-04	1.68E-03	5.43E-01	Down
hsa04514 Cell adhesion molecules (CAMs)	2.78E-04	1.94E-03	7.87E-01	Down

hsa04650 Natural killer cell mediated cytotoxicity	2.77E-04	1.94E-03	6.75E-01	Down
hsa04915 Estrogen signaling pathway	3.41E-04	2.33E-03	4.87E-01	Down
hsa04721 Synaptic vesicle cycle	3.64E-04	2.37E-03	4.17E-01	Down
hsa05120 Epithelial cell signaling in Helicobacter pylori infection	3.61E-04	2.37E-03	3.54E-01	Down
hsa04611 Platelet activation	4.28E-04	2.72E-03	6.71E-01	Down
hsa04210 Apoptosis	4.40E-04	2.74E-03	4.85E-01	Down
hsa05412 Arrhythmogenic right ventricular cardiomyopathy (ARVC)	4.55E-04	2.77E-03	5.82E-01	Down
hsa04370 VEGF signaling pathway	5.05E-04	2.89E-03	5.46E-01	Down
hsa05206 MicroRNAs in cancer	5.07E-04	2.89E-03	5.60E-01	Down
hsa05215 Prostate cancer	5.06E-04	2.89E-03	5.80E-01	Down
hsa05220 Chronic myeloid leukemia	6.22E-04	3.48E-03	4.69E-01	Down
hsa04962 Vasopressin-regulated water reabsorption	6.60E-04	3.63E-03	4.60E-01	Down
hsa04022 cGMP-PKG signaling pathway	6.74E-04	3.63E-03	4.84E-01	Down
hsa04723 Retrograde endocannabinoid signaling	8.77E-04	4.57E-03	5.64E-01	Down
hsa04917 Prolactin signaling pathway	8.80E-04	4.57E-03	5.56E-01	Down
hsa01212 Fatty acid metabolism	9.77E-04	4.92E-03	4.62E-01	Up
hsa05030 Cocaine addiction	9.84E-04	4.92E-03	5.42E-01	Down
hsa05166 HTLV-I infection	1.22E-03	5.90E-03	5.50E-01	Up
hsa05212 Pancreatic cancer	1.21E-03	5.90E-03	4.95E-01	Down
hsa00071 Fatty acid degradation	1.31E-03	6.04E-03	4.62E-01	Up
hsa00650 Butanoate metabolism	1.32E-03	6.04E-03	5.80E-01	Up
hsa03320 PPAR signaling pathway	1.29E-03	6.04E-03	4.80E-01	Down
hsa00280 Valine, leucine and isoleucine degradation	1.37E-03	6.20E-03	4.46E-01	Up
hsa05130 Pathogenic Escherichia coli infection	1.82E-03	8.10E-03	4.11E-01	Down
hsa04668 TNF signaling pathway	2.05E-03	8.96E-03	5.15E-01	Down
hsa04024 cAMP signaling pathway	2.10E-03	9.03E-03	6.27E-01	Down
hsa05211 Renal cell carcinoma	2.15E-03	9.14E-03	4.48E-01	Down
hsa05032 Morphine addiction	2.33E-03	9.73E-03	5.40E-01	Down
hsa04145 Phagosome	2.39E-03	9.86E-03	5.44E-01	Down
hsa04152 AMPK signaling pathway	2.71E-03	1.10E-02	3.99E-01	Down
hsa05031 Amphetamine addiction	2.79E-03	1.11E-02	5.55E-01	Down
hsa04910 Insulin signaling pathway	2.84E-03	1.12E-02	4.09E-01	Down
hsa04070 Phosphatidylinositol signaling system	3.09E-03	1.18E-02	4.62E-01	Down
hsa05231 Choline metabolism in cancer	3.09E-03	1.18E-02	4.90E-01	Down
hsa00562 Inositol phosphate metabolism	3.37E-03	1.28E-02	4.24E-01	Down
hsa00512 Mucin type O-Glycan biosynthesis	3.57E-03	1.33E-02	9.36E-01	Up
hsa04141 Protein processing in endoplasmic reticulum	3.89E-03	1.43E-02	3.98E-01	Up
hsa04071 Sphingolipid signaling pathway	4.49E-03	1.63E-02	4.09E-01	Down
hsa05222 Small cell lung cancer	5.01E-03	1.80E-02	5.04E-01	Down
hsa04380 Osteoclast differentiation	5.23E-03	1.85E-02	6.26E-01	Down
hsa04713 Circadian entrainment	5.28E-03	1.85E-02	5.30E-01	Down

hsa05142 Chagas disease (American trypanosomiasis)	5.68E-03	1.94E-02	5.15E-01	Down
hsa05221 Acute myeloid leukemia	5.69E-03	1.94E-02	4.71E-01	Down
hsa04350 TGF-beta signaling pathway	5.77E-03	1.95E-02	5.62E-01	Up
hsa00100 Steroid biosynthesis	9.87E-03	3.25E-02	7.95E-01	Down
hsa04550 Signaling pathways regulating pluripotency of stem cells	9.87E-03	3.25E-02	6.15E-01	Down
hsa05131 Shigellosis	1.01E-02	3.29E-02	3.26E-01	Down
hsa05414 Dilated cardiomyopathy	1.16E-02	3.73E-02	5.77E-01	Down
hsa03420 Nucleotide excision repair	1.18E-02	3.74E-02	3.11E-01	Up
hsa04114 Oocyte meiosis	1.19E-02	3.74E-02	4.75E-01	Down
hsa04726 Serotonergic synapse	1.29E-02	4.01E-02	7.06E-01	Down
hsa05034 Alcoholism	1.38E-02	4.24E-02	5.92E-01	Down
hsa00072 Synthesis and degradation of ketone bodies	1.56E-02	4.76E-02	5.80E-01	Down